

# Robust 3D Quantitative Phase Imaging

*Regina Eckert*



Electrical Engineering and Computer Sciences  
University of California, Berkeley

Technical Report No. UCB/EECS-2022-29

<http://www2.eecs.berkeley.edu/Pubs/TechRpts/2022/EECS-2022-29.html>

May 1, 2022

Copyright © 2022, by the author(s).  
All rights reserved.

Permission to make digital or hard copies of all or part of this work for personal or classroom use is granted without fee provided that copies are not made or distributed for profit or commercial advantage and that copies bear this notice and the full citation on the first page. To copy otherwise, to republish, to post on servers or to redistribute to lists, requires prior specific permission.

Robust 3D Quantitative Phase Imaging

by

Regina Frances Eckert

A dissertation submitted in partial satisfaction of the

requirements for the degree of

Doctor of Philosophy

in

Engineering - Electrical Engineering and Computer Sciences

in the

Graduate Division

of the

University of California, Berkeley

Committee in charge:

Associate Professor Laura Waller, Chair

Associate Professor Ren Ng

Associate Professor Na Ji

Summer 2021

Robust 3D Quantitative Phase Imaging

Copyright 2021  
by  
Regina Frances Eckert

## Abstract

## Robust 3D Quantitative Phase Imaging

by

Regina Frances Eckert

Doctor of Philosophy in Engineering - Electrical Engineering and Computer Sciences

University of California, Berkeley

Associate Professor Laura Waller, Chair

Biomedical research relies upon quantitative imaging methods to measure functional and structural data about microscopic organisms. Recently-developed quantitative phase imaging (QPI) methods use jointly designed optical and computational systems to recover structural quantitative phase information for biological samples. However, these methods have not seen wide adoption in biological research because the optical systems can be difficult to use and the computational algorithms often require expert operation for consistently high-quality results. QPI systems are usually developed under a computational imaging framework, where the optical measurement system is jointly designed with the computational reconstruction algorithm. Designing QPI systems for robust and practical real-world use is often difficult, however, because each imaging and computational configuration has unique and difficult-to-quantify practical implications for the end-user.

In this dissertation, I present three frameworks for increasing the robustness and practicality of computational imaging systems, and I demonstrate the usefulness of these three frameworks by applying them to 2D and 3D quantitative phase imaging systems. First, algorithmic self-calibration directly recovers imaging system parameters from data measurements, doing away with the need for extensive pre-calibration steps and ensuring greater calibration accuracy for non-ideal, real-world systems. I present a robust and efficient self-calibration algorithm for angled coherent illumination, which has enabled new QPI system designs for 2D Fourier ptychographic microscopy (FPM) and 3D intensity optical diffraction tomography (ODT) that would have otherwise been infeasible. Second, increased measurement diversity better encodes useful information across measurements, which can reduce imaging system complexity, data requirements, and computation time. I present a novel pupil-coded intensity ODT system designed to increase measurement diversity of 3D refractive index (RI) information by including joint illumination- and detection-side coding for improved volumetric RI reconstructions. Finally, physics-based machine learning uses a data-driven approach to directly optimize imaging system parameters, which can improve imaging reconstructions

and build intuition for better designs of complicated computational imaging systems. I show results from a physics-based machine learning algorithm to optimize pupil coding masks for 3D RI reconstructions of thick cell clusters in the pupil-coded intensity ODT system.

In addition, I provide practical methods for the design, calibration, and operation of Fourier ptychography, intensity-only ODT, and pupil-coded intensity ODT microscopes to aid in the future development of robust QPI systems. I additionally present a validation of joint system pupil recovery using FPM and a comparison of the accuracy and computational complexity of coherent light propagation models that are commonly used in 3D quantitative phase imaging. I also compare field-based 3D RI reconstructions to intensity-based RI reconstructions, concluding that the proposed pupil-coded intensity ODT system captures similarly diverse phase information to field-based ODT microscopes.

Throughout this work, I demonstrate that by using the frameworks of algorithmic self-calibration, increased system measurement diversity, and physics-based machine learning for computational imaging system design, we can develop more robust quantitative phase imaging systems that are practical for real-world use.

To my family  
You made this possible.

# Contents

<b>Contents</b>	<b>ii</b>
<b>List of Figures</b>	<b>iv</b>
<b>1 Introduction</b>	<b>1</b>
1.1 Computational Microscopy . . . . .	2
1.2 Biological Microscopy . . . . .	3
1.3 3D Biological Microscopy . . . . .	5
1.4 Quantitative Phase Imaging . . . . .	8
1.5 Design of Computational Imaging Systems . . . . .	11
1.6 Dissertation Outline . . . . .	15
<b>2 Practical Fourier Ptychography Systems</b>	<b>18</b>
2.1 Introduction to Fourier Ptychography . . . . .	18
2.2 Fourier Ptychography Microscope Design . . . . .	23
2.3 FPM Reconstruction Methods . . . . .	29
2.4 Joint Pupil Reconstruction . . . . .	35
<b>3 Efficient Illumination Angle Self-Calibration in Fourier Ptychography</b>	<b>37</b>
3.1 Introduction . . . . .	38
3.2 Methods . . . . .	40
3.3 Results . . . . .	47
3.4 Discussion . . . . .	50
3.5 Conclusion . . . . .	51
<b>4 Practical 3D Refractive Index Imaging Systems</b>	<b>52</b>
4.1 Introduction to 3D Refractive Index Imaging . . . . .	52
4.2 Intensity-only Optical Diffraction Tomography . . . . .	54
4.3 3D Coherent Light Propagation Models . . . . .	55
4.4 Intensity-only ODT System Design and Alignment . . . . .	61
4.5 Comparison of Field- and Amplitude-Based 3D RI Reconstructions . . . . .	66
<b>5 Measurement Diversity for Improved 3D Refractive Index Imaging</b>	<b>69</b>

5.1	Introduction . . . . .	70
5.2	Methods . . . . .	71
5.3	Simulation Results . . . . .	77
5.4	Experimental Results . . . . .	86
5.5	Analysis . . . . .	96
5.6	Conclusion . . . . .	105
<b>6</b>	<b>Machine Learning for Pupil-Coded 3D Refractive Index Imaging</b>	<b>107</b>
6.1	Introduction . . . . .	108
6.2	Methods . . . . .	110
6.3	Results . . . . .	116
6.4	Analysis . . . . .	126
6.5	Conclusion . . . . .	128
<b>7</b>	<b>Conclusion</b>	<b>130</b>
7.1	Funding Information . . . . .	132
	<b>Bibliography</b>	<b>133</b>

# List of Figures

2.1	Example wide field of view, high resolution phase image of a mouse brain . . . . .	20
2.2	Another example wide field of view, high resolution phase images of a mouse brain	21
2.3	Four illumination systems for Fourier ptychography . . . . .	23
2.4	Increased illumination coherence leads to sharper phase reconstructions . . . . .	26
2.5	Example FPM calibration steps . . . . .	28
2.6	Artifacts due to improper background subtraction . . . . .	30
2.7	Example vignetted images in FPM . . . . .	33
2.8	Methods for correcting for vignetting in FPM . . . . .	34
2.9	Verification of joint pupil estimation in FPM . . . . .	36
3.1	Illumination angle calibration overview. . . . .	39
3.2	Circular edge detection algorithm for illumination angle correction . . . . .	42
3.3	Combined bright-field and dark-field illumination calibration . . . . .	43
3.4	FPM results with illumination angle calibration (LED array microscope) . . . . .	45
3.5	FPM results with illumination angle calibration (scanned laser and quasi-dome LED array microscopes) . . . . .	47
3.6	3D FPM results with illumination calibration (LED array microscope) . . . . .	49
3.7	Analysis of illumination angle calibration algorithm . . . . .	50
4.1	Four forward models for coherent light propagation . . . . .	57
4.2	Forward model comparison across illumination angle . . . . .	60
4.3	Forward model comparison across $\Delta n$ . . . . .	61
4.4	Comparison of model computation time and overall error . . . . .	62
4.5	Intensity-only ODT system overview . . . . .	63
4.6	Comparison of simulated field- and amplitude-based 3D RI reconstructions . . . . .	66
5.1	Joint illumination- and detection-side coding captures diverse measurements for improved 3D refractive index reconstructions . . . . .	72
5.2	Example SLM phase masks and simulated images . . . . .	73
5.3	Simulation of a 3D refractive index 40 cell cluster . . . . .	79
5.4	Reconstructed simulated volumes for full and limited illumination cases, compar- ing intensity-only ODT and pupil-coded intensity ODT . . . . .	81

5.5	Reconstructed simulated 3D RI volumes for limited computation and high noise cases . . . . .	83
5.6	Reconstructed simulated 3D RI volumes for different numbers of distinct pupil coding masks under a limited illumination condition . . . . .	85
5.7	Pupil-coded intensity ODT system calibration . . . . .	88
5.8	Pupil-coded intensity ODT SLM phase verification via Fourier ptychography . .	90
5.9	Polystyrene bead experimental reconstructions . . . . .	94
5.10	Fabrication phase object experimental reconstructions . . . . .	95
5.11	A transfer function weight matrix reveals the measurement system's frequency space weighting . . . . .	97
5.12	Transfer function weight matrix analysis of objective glass aberrations . . . . .	99
5.13	Transfer function analysis shows encoding of diverse phase information . . . . .	101
5.14	Spatial entropy across measurements is used to calculate measurement diversity	103
6.1	Overview of pupil-coded intensity ODT system . . . . .	111
6.2	Overview of physics-based machine learning algorithm . . . . .	112
6.3	Training results for different system parameters . . . . .	115
6.4	Map of learned masks across pupil bases for ideal system and aberrated system with SLM shifts . . . . .	117
6.5	Comparison of learned masks across pupil bases and training system parameters	119
6.6	Simulated reconstruction results with learned masks . . . . .	121
6.7	Experimental results on fabricated phase object . . . . .	123
6.8	Experimental results on stack of 8 $\mu\text{m}$ polystyrene beads . . . . .	125
6.9	Transfer function analysis of learned and random pupil coding masks . . . . .	127

## Acknowledgments

At the end of a long journey, it is a privilege to look back across the space of years to acknowledge those who made the journey possible. I was extremely fortunate to have the support of family, friends, and colleagues, and fellow co-agitators throughout my time at UC Berkeley. While I will attempt here to acknowledge them all, I know that the support I received was part of a dense network of connections that would be infeasible to detail in its entirety. To those who are left unnamed, know that I deeply appreciate your help and support in improving both my experience and the experiences of other graduate students at UC Berkeley.

Thank you to my advisor, Prof. Laura Waller, who gave me space and resources to explore a broad array of computational imaging research topics, as well as to lead a student organization, Bias Busters, for the majority of my time in graduate school. I appreciate that you never questioned my efforts for social change inside the Electrical Engineering and Computer Sciences (EECS) department and wider tech community through Bias Busters, even when it took time away from my research. Thank you as well to my committee members, Prof. Ren Ng and Prof. Na Ji, as well as my additional qualifying exam committee member, Prof. Ming Wu. Your feedback at a critical point in graduate school proved useful in guiding my steps towards my journey's end. Many thanks also go to my early scientific mentors, including Megan Slinkard and Seethambal Mani from Sandia National Laboratories and Prof. Sanjay Krishna from the University of New Mexico.

Many thanks must of course be given to the Waller Lab, especially to all of my co-authors and collaborators. The optics and computation knowledge I gained in graduate school was in large part due to the excellent group of people around me who were always striving to understand the best way to use computational imaging. In particular, many thanks to Emma Alexander, post-doc extraordinaire whose encouragement helped me through rough research times; Grace Kuo, whose enthusiasm brightened the entirety of my graduate experience; Zack Phillips, Li-Hao Yeh, Michael Chen, and Herbert Liu, who were infinitely supportive as I delved into phase imaging and scattering research; Lei Tian, whose mentorship in the first six months of my time in graduate school was invaluable; as well as Kristina Monakhova, Linda Liu, Henry Pinkard, Michael Kellman, Ruiming Cao, and the rest of the Waller Lab group members, who were always happy to discuss optics, optimization, and machine learning methods with me.

Bias Busters was as much a part of my graduate school experience as my research in the Waller Lab, from founding the group in November 2016 to handing it off to new leadership in August 2020. Huge thanks go to Vasuki Narasimha Swamy for also believing we could create positive change in the EECS department through Bias Busters by engaging our community on the effects of implicit bias on the experiences of underrepresented groups in STEM fields, and for her grit and determination in making the group a reality. Many thanks go to the Google Bias Busting @ Work team and the Carnegie Mellon University's Bias Busters group, who sparked our enthusiasm and gathered the initial research around implicit bias, and to Prof. Marcia Linn, Marquita Ellis, and Grace Kuo, who helped drive

additional early research for Bias Busters in Spring 2017. Since volunteering for community-involved groups such as Bias Busters often goes unrecognized, I will attempt to name all of the Bias Busters members who worked very hard over many years to create positive changes in the UC Berkeley climate. My deep and abiding thanks to Roel Dobbe and Aditya Devarakonda, who worked alongside Vasuki and me to bring together the first Bias Busters presentations in Spring 2017; to Laura Brink, Emily Naviasky, Nate Weinman, Sandra Hui, Gabe Fierro, Hani Gomez, Kelly Fernandez, Josh Sanz, J.P. Llinas, Akshay Pattabi, and Nicole Cotton, who formed a dedicated core of Bias Busters folks from 2017 and beyond; to Rudy Corona Rodriguez, Jake Sporrer, Carol Baumbauer, Arya Reais-Parsi, and Kieran Peleaux, who brought fresh perspectives and energy to the group in 2019; and to Alexander Alvara, Eyes Robson, and Rachel Rex, who joined in 2020, just in time to help steer the group in new directions. Margaret Mead once said, “Never doubt that a small group of thoughtful, committed, citizens can change the world. Indeed, it is the only thing that ever has.” This has certainly been a guiding principle of Bias Busters since its inception. It was a pleasure to work with all of you in our endeavor to drive social change both at UC Berkeley and in the wider tech world.

Bias Busters was also made possible by the hard work and support of the EECS and College of Engineering (COE) staff, without whom none of our work would have been possible. Warm thanks go to Tiffany Reardon and Shirley Salanio, who first shepherded Bias Busters into being, as well as Audrey Sillers, Susanne Kauer, Heather Levien, Charlene Duncan, Christopher Hunn, and Patrick Hernan, who supported us at every step of the way. Huge thanks also go to Sheila Humphreys for her expert advice and warm support over the years, and to Fatima Alleyne, who brought Bias Busters work to the College of Engineering level. Besides their support of Bias Busters, these EECS and COE staff members also work tirelessly to improve the student experience at UC Berkeley, for which I could not be more grateful. Thanks also to Prof. Tsu-Jae King-Liu, who has been an inspiring and approachable leader of both the EECS department and the College of Engineering, and to Prof. Jeff Bokor and Prof. John Canny, EE and CS department chairs, who listened and worked to act on our ideas about how to improve the EECS department climate many times over the years.

Additional thanks goes to the Women in Computer Science and Engineering (WICSE) group, the EE and CS Graduate Student Associations, EEGSA Basis Outreach, and the Science Policy Group at Berkeley. Each of these organizations have been driven by incredible people over the years, and they have enhanced my graduate school experience greatly.

My life in Berkeley was greatly enriched by all of the wonderful people I had the privilege to know. Many warm thanks to Samantha Vega and Han Hee Yu, who first made me feel welcome in Berkeley and whose love and support made it more than worth living next to a frat house for two years. Many thanks to all of my roommates over the years who helped make life bearable, especially during the COVID-19 pandemic when work and home became deeply and inexplicably intertwined.

To the incomparable Mindy Liu Perkins, who has driven me to look at the world from every angle, and whose listening ear and thoughtful advice has gotten me through many tough

times. To Grace Kuo, Ben Mildenhall, and Coline Devin, whose friendship was a mainstay from Game of Thrones Season 6 through Season 8 and beyond, with many intervening sushi, dim sum, and mac 'n' cheese-related adventures. To Alyssa Morrow, who laughed with me so many times, especially the hard ones. To Vasuki Narasimha Swamy, whose drive and determination have always an inspiration, and who asked me to go to Turkey and did not bat an eye when I immediately said yes. To all those who hiked, camped, and adventured with me, including Hani Gomez, Carol Baumbauer, Kristina Monakhova, Linda Liu, Justin Yim, Stephanie Wang, and Danny Lazar. And finally, to Emma Alexander, Sarah Sterman, Emily Naviasky, Mindy Liu Perkins, and Laurel Estes, who kindled my long love of writing into a steady flame. I am forever grateful for all of you.

Many warm thanks to Megan Ehrhart, whose laughter and advice on our weekly video calls made life infinitely more bearable, along with the rest of the Sandia High School crew, including Reina Buenconsejo, Yung Jones, Chloe Vaughn, and Elaine Stamp. I always look forward to spending time with you in New Mexico, even as life has taken us on very different paths.

Huge thanks also go to my teachers at every step along the way. I have been the beneficiary of so many dedicated and passionate public school teachers along the way, and I am deeply indebted to all of you. Thank you all for your hard work and dedication on the part of every student who passes through your door.

None of this journey would be possible without the steadfast support of my family. My parents, Sandy and Marty Eckert, have always been an unfailing source of love and support, for which I could not be more grateful. They were always there to buoy my losses, celebrate my successes, listen to my frustrations, and support me in anything I wanted to achieve. The degree to which they have enabled me to make this journey cannot be overstated. Many thanks also go to my sister Aubrey Eckert and brother-in-law Andrew Clark, who have always offered a listening ear and relentless support. Thanks as well to Aunt Patty and Uncle Dick Maguire, as well as the rest of my extended family, for all of their love and support over the years.

Finally, thanks to my grandparents, all of whom deeply valued education and instilled that love in us. To Grandma Jere and Grandpa Martin, who would call just to recommend an interesting documentary and who brought much joy into all our lives. To Grandma Jo, whose fierce pursuit of education and sage advice made a strong impact on me even as a young child. And to Grandpa Bob, who gave me my first black and white film camera, which sparked my love of optics many years ago. He was here as I started this journey, and his absence now is sorely felt.

# Chapter 1

## Introduction

A thick, unstained slice of a mouse's brain is a desert landscape under the microscope. Unmyelinated axons mesh into smooth grey plains that buffer between the bright ridged canyons of sulci and the wilder regions of white matter, snarled through with myelin and tree-like dendrites. Spinal tissue is the surface of a melting glacier, with sudden holes and bright ridges that meet and part unexpectedly. Individual cells catch the light at the edge of an organoid's embryonic cell cluster like the crescent moon reflects sunlight: only a fingernail of light to show what is there. The cluster's center is a field of speckle where the light is scrambled by the profusion of cells as through churning ocean waves, hiding secrets deep within.

Each sample is a different line of poetry under the microscope, an expression of knotted creation, formed from cells unique in conformation but not in underlying principle and structure. To look through the microscope is to ask fundamental questions about life. The microscope is not simply a tool, but a method of expression, of interrogation. The power of the lenses, the field of view, the depth of focus, the working distance, the imaging contrast: they all define the bounds of the scientific questions we can ask and the certainty with which we can answer.

In this dissertation, the microscope itself is the object of focus. Throughout my PhD, I have sought to answer how microscopes might best be designed to answer biological researchers' questions about the many forms of embodied life. Specifically, I have focused on creating robust computational imaging systems for 2D and 3D quantitative phase imaging (QPI). Quantitative phase imaging has the potential to be extremely useful to biological researchers, as it provides quantitative structural data about biological samples without requiring labor-intensive labeling processes. However, in order for QPI systems to be widely adopted for biological imaging, they must be made more robust and usable across a wide variety of applications. Achieving system robustness and usability in computational imaging systems is not straightforward, though, as it requires that both the physical optical system and the computational reconstruction algorithm be robust to system noise and practical for an end-user.

In this work, I present three methods for building more robust and practical 2D and 3D

quantitative phase imaging systems, including algorithmic self-calibration, increased measurement diversity for improved system robustness, and use of physics-based machine learning for the optimization of imaging parameters. The QPI systems presented under these three frameworks have increased robustness compared to previous systems, enabling novel imaging designs with reduced physical constraints and increasing QPI system practicality. Moreover, these design frameworks can be extended beyond QPI to provide useful guidance for the design of robust computational imaging systems across imaging domains.

The majority of this thesis will explore these frameworks and QPI systems in detail. However, in this introduction, I focus on the larger space of microscope design and development, especially that of the more recent field of computational microscopy. I review the wide range of functional and structural imaging systems for biological research. I additionally discuss the development of 3D imaging for biological samples and review quantitative phase imaging methods. Finally, I present an overview of design methods typically used for computational imaging systems. By providing a strong foundation in both biological microscopy applications and computational imaging system design, I hope to provide context for the work presented throughout this dissertation.

## 1.1 Computational Microscopy

Microscopes have a long history, with the first compound microscope built in the late 1500s by Dutch inventors Hans and Zacharias Janssen. Later improvements to optical microscopes lead to important biological discoveries in the late 1600s by English scientist Robert Hooke and Dutch scientist Antony van Leeuwenhoek [176]. Over centuries of innovation in optics, visible light microscopes, which operate at wavelengths  $\lambda$  from 380 nm to 750 nm, have become masterpieces of engineering, enabling humans, whose eyes only resolve down to  $\sim 90 \mu\text{m}$  [153] on a 13 ms timescale [177], to see objects as small as  $\sim 200 \text{ nm}$  [152] on a 1  $\mu\text{s}$  timescale.<sup>1</sup> This neglects the amazing advances in the extreme ultra-violet (EUV) wavelengths and electron microscopy, which offer imaging resolutions as low as 50 pm [61]. In traditional visible light microscopes, this has been achieved by designing compound objective lenses and other compound lens systems that magnify and relay high resolution information through the optical system. With use of high-quality optical lenses, *traditional optical microscopes* have allowed biologists to easily view microscopic samples in a laboratory setting. *Traditional non-optical microscopes*, such as early electron microscopes in the 1930s [191], relied upon photographic film rather than the human eye to perceive and record the image of the sample at hand.

With the advent of digital cameras recorded the electromagnetic signal through the microscope, rather than relying on the human eye to view and record the microscope's output, microscopes began to enter a new age. With modern, high-quantum efficiency scientific cameras, the photons received at the camera sensor can be converted into low-noise digital

---

<sup>1</sup>As judged by the Phantom v2512, which offers 25,700 frames per second imaging for high throughput imaging and up to 1 million frames per second for smaller image sizes [169].

signals that can be analyzed computationally. Computation has also increasingly become a part of microscope automation, including autofocus controls [119, 174] and control of multi-wavelength fluorescence systems [11]. This has led to *computationally-assisted microscopes* that are optimized for use with a digital camera and computer, rather than a human operator. In both *traditional*, human-operated microscopes and *computationally-assisted* microscopes, the output of the optical system is a well-formed image that can be analyzed directly by a human user, whether that output is captured by a human eye, photographic film, or digital camera sensor.

In contrast, *computational microscopes* require both an optical system and a computational algorithm to create a useful data output from the microscope. This might be a well-formed image that can be visually understood by the end-user or quantitative sample data. Perhaps the simplest form of computational microscope is one where the measured image is improved by removing the effects of well-characterized lens aberrations via a deconvolution algorithm [205]. More complicated systems include quantitative phase or 3D refractive index reconstructions, where the recovered object must be reconstructed from multiple captured images. In these *computational microscopes*, the optical system encodes a signal into the measured images which the computational algorithm then decodes, recovering the desired sample information from the measured images.

## 1.2 Biological Microscopy

While microscopes have been useful across many domains, from verification of semiconductor chip fabrication processes [193] to material characterization [196], one of the largest application spaces is biological imaging. In general, biological imaging seeks to capture *functional* and *structural* information microscopic samples, from single cells, such as cancer cells, up to large biological systems, such as the brain. While cell function and structure are deeply interconnected, *functional* imaging involves understanding the function of each cell or system component, while *structural* imaging seeks to capture the physical morphology of the sample at hand. Both of these components are useful for researchers across a wide range of application spaces, from those seeking to understand how the brain works [166], how organs grow [123], how bacteria react to antibiotic treatment [154], or analyze phytoplankton properties for oceanic studies [44, 114].

Functional imaging generally involves labeling cell components based on their underlying chemistry to reveal the interaction of different cell components inside the larger system. The most common functional imaging method used today is done with fluorescent labeling [184]. Fluorescent labels are engineered to attach to certain binding sites in a cell. They contain fluorophores that, when illuminated with a certain wavelength of light, emit light at a different wavelength that can be detected at the imaging plane. Multiple cell components can be labeled with tags that fluoresce at different wavelengths of light so many functional components can be imaged simultaneously. While fluorescence imaging can create beautiful images, the fluorescence labeling process is very time-intensive, the fluorescence degrades,

or “bleaches”, over time as it is illuminated, and the labels only bind to a small percentage of the desired cell components. In addition, unless the cell walls are labeled with their own fluorescent tag, the overall cell structure can be difficult to discern from sparse fluorescent labels. However, other label-free methods are also available for functional imaging, including methods based on cell auto-fluorescence, Raman scattering, and second harmonic generation (SHG) properties.

A prime example of functional imaging is optogenetics, where mice have been genetically modified to attach a fluorescent label to neuronal calcium ion channels in the brain [47]. If the fluorescent tag is illuminated through a thinned skull, optical fiber, or skull window when the neuron fires, the tag emits light, which can be imaged through the brain tissue. The neurons can also be stimulated optically through the light-sensitive ion channels, allowing read/write control of the fluorescence-expressing neurons. By correlating the measured fluorescence with stimuli to the mouse, researchers are attempting to understand brain functionality at a much deeper level than ever before.

Structural imaging, on the other hand, focuses on imaging the overall cell morphology. Since biological tissue is often transparent, this has traditionally been accomplished by staining the cell with dyes [10]. As with fluorescent imaging, this can be a time-intensive process and requires altering the sample prior to imaging, which might destroy the cell structure before it can be captured. Starting in 1934 with Frits Zernike’s invention [237], phase contrast microscopes have been developed that used the phase delay of light through the sample to image its structure. Since it is the cell structure itself that creates the image contrast in phase contrast imaging, the cell does not have to be altered for phase contrast imaging microscopes. More recently, quantitative phase imaging techniques have been designed from a computational imaging framework. Quantitative phase imaging (QPI) seeks to quantify the phase delay of light through the sample, which relates to the sample’s thickness and refractive index. QPI systems can be used to image cell structure and can quantify cell dry mass [6] and other important cell properties [7]. QPI methods are discussed in detail below.

Most practical imaging methods are, at their base, two-dimensional (2D) data capture systems that measure 2D spatial information, but many multi-dimensional imaging methodologies exist for both functional and structural imaging. Fast imaging systems capture images as the sample evolves over time, adding a time dimension to the captured data [93, 206]. Three-dimensional (3D) imaging methods seek to reconstruct the full 3D sample volume that resulted in multiple measured 2D images [36, 215, 217]. Hyperspectral imaging captures data at multiple wavelengths, beyond that of a typical red-green-blue (RGB) digital camera [180]. Polarization imaging captures the polarization properties of the sample by measuring the polarization change in light transmitted through the sample [144]. This list is not exhaustive and only attempts to convey the breadth of multi-dimensional imaging methods that are useful for biological imaging.

In general, each system described here must be designed specifically for the task at hand. Trade-offs in the system design must be made to capture higher-dimensional data beyond 2D spatial information. For example, capturing high-resolution 3D information often requires that many images must be captured of the sample, and so time-resolved imaging capabilities

are discarded in order to recover 3D information. Traditional optical design also often involves a trade-off between resolution and field of view (FOV). It is difficult and costly to design and build lens systems that image very fine, high resolution features over a large field of view. For this reason, optical systems are often evaluated on their space-bandwidth product (SBP), which accounts for the amount of space (or field of view) and Fourier domain bandwidth (related to resolution) that can be captured through the imaging system [134]. However, the SBP metric does not easily extend to comparisons between multi-dimensional systems, as the comparison between the information captured by, for example, spatial 3D imaging and hyperspectral imaging is not straightforward. Therefore, while traditional 2D optical systems might be designed to optimize for SBP, the design of multi-dimensional capture systems is less well-understood.

### 1.3 3D Biological Microscopy

Most biological tissue and cells are inherently spatial, three-dimensional objects. However, since digital cameras capture 2D, not 3D, spatial information and microscope systems have a limited depth of field (axial region in which the object is in focus) it is difficult to capture 3D information in biological microscopy. This difficulty is enhanced by increased scattering of light inside thicker biological tissues, which distorts the measured images of thick, 3D samples.

There are two basic ways to account for the 3D, scattering nature of biological samples in microscopy. First, imaging methods can correct for the distortions caused by the microscope's limited depth of field or by the sample's scattering in order to capture undistorted images. This includes optical clearing methods, where the sample is chemically treated to reduce or eliminate sample scattering by delipidization, decoloration, or other methods so that the sample is clear and easy to image with either 2D or 3D methods [220]. This also includes systems that increase the microscope's depth of field so that the entire axial region of interest is in focus on the camera plane [132, 178]. Finally, incoherent illumination can be used to create better depth sectioning inside thick, scattering objects, so that each 2D plane inside the object is measured with a minimum of distortions from off-focus planes inside the volume. While these methods allow for thick samples to be imaged, they often throw away valuable axial spatial information.

The second method of imaging 3D samples is to build systems that reconstruct the entire 3D sample volume. This is beneficial because it allows the entire 3D structure of the sample to be viewed and analyzed. However, these systems often require multiple captures, so they cannot image fast phenomena. Additionally, they can have large data requirements, long computation times, and can be difficult to build and design. In general, some 3D imaging systems are commonly used in tandem with fluorescent labeling to capture 3D information, including confocal and light sheet microscopes, and more recently developed sparsity-based microscopes.<sup>2</sup> In addition, other 3D imaging systems capture a thick sample's structural

---

<sup>2</sup>We note that the fluorescence is not intrinsically necessary to the concept of confocal and light sheet

information through manipulation of the illumination light and detection system encoding, including systems such as optical coherence tomography (OCT) [90], focal stack methods [29, 135], computed tomography (CT) [155], and optical diffraction tomography (ODT) [225]. We call these *3D phase imaging methods*, as they generally rely upon the phase delay of light through the sample to provide 3D information.

### 1.3.1 3D Fluorescent Imaging Methods

One of the earliest 3D imaging methods was confocal imaging, where a small focused beam is scanned across the entire sample volume in tandem with a detection pinhole that filters out all out-of-focus light [45, 168, 203]. Confocal microscopes are commonly used today because they are relatively easy to build and use. However, the imaging process can be time-intensive, since the entire volume must be scanned. In addition, the scanned light beam and attendant excitation of off-focus fluorophores means the sample is exposed to a large amount of high-powered light, which often bleaches the fluorophores and damages the sample during capture.

More recently, light sheet microscopy has been developed to answer these deficiencies by scanning a planar sheet of light through the object. Instead of capturing data at each point in the volume, light sheet microscopy captures images at each plane the light sheet moves through the volume, enabling a 3D capture built from multiple images [222]. This decreases the capture time and light exposure to the sample, thereby decreasing bleaching of the fluorophores and increasing the overall amount of time a sample can be imaged. Light sheet microscopes are more difficult to build, but have come into common commercial use since the mid-2010s.

A main benefit of imaging fluorescence in 3D is that the fluorophore tags are often sparse in 3D space, which is leveraged in various imaging methods. One method to leverage the sparsity of fluorescent imaging is to engineer the point spread function (PSF) of the imaging system to create different patterns for fluorophores at different depth planes. Since the fluorophores are generally sparse, these patterns can be imaged with enough fidelity for a deconvolution algorithm to reconstruct an undistorted 3D volume. Example systems often used for 3D fluorescent imaging include the double-helix PSF microscope [165], light field microscopy [115], the DiffuserCam microscope [12, 230], and various other coded aperture microscopes [3, 127, 128]. Additionally, the native axial variation in the system PSF can be measured and used to reconstruct the 3D volume in the same way [179, 199]. Multi-focal imaging [48, 84] is another common method for recovering 3D information for fluorescent samples.

---

microscopes, but since most of these microscopes are built to image fluorescent samples, we discuss them in that context here.

### 1.3.2 3D Phase Imaging Methods

3D phase imaging systems are label-free methods that reconstruct a sample's 3D structural volume using information from the delay of light through the sample. There are four main ways that 3D phase information is captured in microscope imaging systems: by 1) leveraging coherence properties [90, 100, 150, 231], 2) focal scanning [29, 48, 66, 68, 94, 141, 143, 200, 204, 226, 244], 3) sample rotation [14, 27, 80, 155, 190], or 4) illumination angle scanning [33, 36, 65, 105, 113, 150, 213, 215, 225]. All of these systems involve the capture of multiple images and require a computational algorithm to reconstruct the output volume, which is generally not sparse and can be defined in terms of reflectivity, phase contrast, quantitative phase, or refractive index values.

The coherence of light transmitted through the sample can be leveraged to determine depth information by interference with a reference arm at a known axial position, as in optical coherence tomography (OCT) [90]; at a known time delay, as in CLASS microscopy [100]; or at a known spatial shift and phase delay, as in gradient light interference microscopy (GLIM) [150]. OCT can also be formulated in the Fourier (frequency) domain, where multi-spectral illumination is used to reconstruct 3D depth [231]. In these systems, off-focus and multiply scattered light are coherence-gated by the interference mechanism. This limits the volume that can be recovered using OCT in particular, as deep regions where multiple scattering make up most of the sample's reflected light will have little to no single-scattered signal detected at the camera plane.

Another way to capture 3D phase information is by capturing images at different focal planes. The simplest way to do this is to have an imaging system with a very small depth of field, thus blurring out most off-focus light, and capturing images while moving the sample at very small  $\Delta z$  axial intervals to scan through the volume [141, 143, 200]. However, this system has long capture times, distortion from off-focus light, and low contrast for transparent phase objects, if a brightfield illumination scheme is used. Multi-focal imaging [48, 226], where different focal planes are relayed onto one camera plane, decreases the imaging time of this method, but does not address off-focus or contrast issues. By illuminating with specifically designed partially-incoherent illumination patterns and scanning through focus, 3D differential phase contrast (DPC) imaging [29] increases the phase contrast in the measured images, and additionally uses a model-based optimization reconstruction to account for off-focus light in the reconstruction. Transport of intensity equation-based (TIE) methods [94, 244] also involve focal-scanning, and particularly uses the high contrast defocus patterns of transparent phase objects (such as biological cells) to reconstruct 3D phase information [68, 204].

Sample rotation provides 3D information by capturing the transmission of light through the sample at many different rotation angles. One of the most well-known 3D imaging systems that uses relative rotation of the sample and imaging system is a computed tomography (CT) scanner, commonly used in medical imaging [155, 190]. Similar to CT, microscopic tomography methods rotate either the sample itself [14, 27, 80] or the imaging system around

the sample<sup>3</sup> to measure the transmission of light through the sample at different angles. In the case where direct transmission is measured and multiply scattered light is rejected, as in medical CT imaging, the transmission of light through the sample is equivalent to a projection through the sample. Classically, the 3D volume can be reconstructed using a filtered back-projection algorithm [195]. As they require large but consistent changes in either sample location or imaging system configuration, these systems can be difficult to build and use in a microscopy setting.

Finally, scanning the incident angle of coherent plane wave illumination through a sample also provides 3D phase information about a sample. Optical diffraction tomography (ODT) uses scanned illumination angle in tandem with an interferometric detection system to directly capture phase information in the intensity measurements [113, 150, 213, 225]. Recently, intensity-only ODT [36, 126], which is conceptually equivalent to 3D Fourier ptychographic microscopy (FPM) [88, 215], has done away with the reference arm for interferometric detection to reconstruct 3D volumes directly from the intensity measurements using an optimization algorithm, which simplifies the imaging system.

One way to compare these 3D phase imaging methods is to compare the 3D Fourier space information captured by each system. To do this, the Ewald sphere formulation [62, 63] can be used, which describes the envelope of spatial frequencies in the single-scattered coherent wave transmitted through an optic of a certain numerical aperture (NA). For each of the tomography methods described above, the envelope of 3D Fourier space coverage for each captured measurement can be combined to determine the maximum 3D Fourier coverage for each imaging method, as in [163]. From this formulation, we see that angled illumination provides higher lateral resolution than the other methods, but has poor low-spatial frequency coverage, in what is commonly called the “missing cone problem” in diffraction tomography [124].

## 1.4 Quantitative Phase Imaging

Quantitative phase imaging captures the phase delay of light through a biological sample, capturing rich structural information. Transparent or nearly-transparent biological samples can be well-described by a complex 3D refractive index volume, where the refractive index  $n = \frac{c}{v}$  describes the delay of light from the speed of light  $c$  to the (slower) phase velocity  $v$  inside a material. When  $n$  is complex, it can be written as

$$n = n_r + jn_i, \quad (1.1)$$

where real part,  $n_r$ , describes the phase delay and the imaginary part,  $n_i$ , called the extinction coefficient, describes the amplitude attenuation of light through the object. The refractive index and the distance  $d$  light propagates in a material is used to calculate the optical path length (OPL) of light,

$$OPL = nd \quad (1.2)$$

---

<sup>3</sup>Theoretically, anyway; this would be difficult to implement experimentally for microscopic imaging.

which determines the relative phase of light in the material. The phase delay of light that has propagated a physical distance  $d$  through a material of refractive index  $n$  relative to light transmitted the same distance through vacuum, where  $n_0 = 1$ , is given by

$$\Delta\phi = \frac{2\pi nd}{\lambda_0}, \quad (1.3)$$

where  $\lambda_0$  is the wavelength of the light in vacuum. The phase delay of light through an object is thus deeply interconnected with that object's refractive index and thickness properties. 2D quantitative phase imaging seeks to recover the 2D quantitative phase delay of the light through the sample,  $\Delta\phi$ , while 3D quantitative phase imaging generally reconstructs the volumetric refractive index (RI) distribution,  $n$ , of the 3D sample, or another related property. For this reason, 3D QPI systems are also referred to as 3D RI imaging systems.

Investigation into 2D quantitative phase imaging systems began with phase-shifting interferometric systems and defocus-based systems based on the transport of intensity equation (TIE) [164, 245]. 3D QPI systems were first developed with the introduction of illumination angle-scanning optical diffraction tomography (ODT) [113, 225] and tomographic phase microscopy (TPM) [33]. We refer to [164] for a thorough review of the development of QPI systems. Overall, most QPI systems involve capturing multiple images of a biological sample with different illumination- or detection-side encoding of the optical signal, which are then used by a computational reconstruction algorithm to recover the quantitative phase delay of the electric field through the sample.

Given that current technology only allows measurement of the intensity of the electric field for visible wavelengths, rather than complex amplitude and phase, QPI systems require illumination- or detection-side optical manipulation to encode phase information into intensity measurements. Many QPI systems capture phase information using an interferometric<sup>4</sup> detection system, where the light exiting from the sample is interfered with a reference beam. The complex amplitude and phase of the electric field at the camera can be recovered from this interferometric measurement. Common interferometric systems include phase-shifting interferometry and off-axis interferometry, as described in [164]. In phase-shifting interferometry, the complex field is recovered from four measurements with reference beam phase delayed by  $\theta = 0, \pi/2, \pi, 3\pi/2$ , respectively, with the measured intensity at the detector given by:

$$I(\mathbf{r}) = I_r + I_1(\mathbf{r}) + 2\sqrt{I_r I_1(\mathbf{r})} \cos(\phi(\mathbf{r}) + \theta) \quad (1.4)$$

---

<sup>4</sup>Interferometric systems are also often called holographic systems, and thus interferometry and holography can be regarded somewhat interchangeably when referring to camera-based imaging systems. However, this is not to be confused with holographic displays or storage. While both use the principle of interference to record a complex electric field, holographic displays *directly* display a complex visible electric field that is, in principle, indistinguishable to a human viewer from light perceived from the world. In contrast, holographic (interferometric) detection at a camera plane encodes phase information in an intensity measurement and requires processing to extract complex field information. While holographic (interferometric) detection is relatively mature, it cannot reconstruct the phase in all circumstances, especially when the object is thick and the phase has many wrapping artifacts. These systems *indirectly* detect the complex field, and thus are distinct from holographic displays and storage which *directly* display or store the complex field.

and the wrapped electric field phase  $\phi(\mathbf{r})$  recovered by

$$\phi(\mathbf{r}) = \arctan\left(\frac{I_{3\pi/2} - I_{\pi/2}}{I_0 - I_\pi}\right), \quad (1.5)$$

where  $\mathbf{r} = (x, y)$  denotes the spatial coordinates, and  $I_r$  and  $I_1(\mathbf{r})$  are the intensities of the reference and detection arm, respectively. In contrast, off-axis interferometry is a single-shot method where a constant plane wave reference beam is interfered at angle  $\theta_\alpha$ , giving the measured interferogram intensity as:

$$I(\mathbf{r}) = I_r + I_1(\mathbf{r}) + 2\sqrt{I_r I_1(\mathbf{r})} \cos\left(\phi(\mathbf{r}) + \frac{2\pi \sin \theta_\alpha}{\lambda} x\right), \quad (1.6)$$

where  $\lambda$  is the wavelength of the light. This effectively shifts the interference term  $\sqrt{I_r I_1(\mathbf{r})}$  to a side-lobe in the Fourier transform of the image  $I$  centered at spatial angular frequency  $\alpha = 2\pi \sin \theta_\alpha / \lambda$ . This side-lobe can be selected via filtering and inverse Fourier transformed to recover the (wrapped) complex field; however, this comes with a loss of measurement resolution [164]. Thick samples often require a phase unwrapping algorithm, which can be unstable or difficult to use because phase unwrapping is an ill-posed problem [32, 236].

3D QPI algorithms that involve interferometric detection often first reconstruct the 2D complex field of multiple interferometric intensity measurements, then use those recovered field values from to reconstruct 3D quantitative phase or refractive index. For example, ODT systems capture multiple phase-shifted interferometric measurements of the sample illuminated with coherent plane waves at different incident angles. The complex field of each of these measurements is recovered, and then these recovered field values are used to reconstruct the complex 3D scattering potential,  $V(\mathbf{r}, z)$  [113]. The reconstruction methods used often require accurate phase recovery from the interferograms and are formulated solely for use with complex field measurements. Instabilities in the field recovery can lead to error in the reconstruction. In addition, interferometric systems can be difficult to build and use, and the commonly used methods require a trade-off between imaging speed, in the case of phase-shifting interferometry, or resolution, in the case of off-axis interferometry.

Recent QPI methods have been developed that directly process the measured intensity images to recover 2D quantitative phase or 3D refractive index values. This includes differential phase contrast (DPC) microscopes [82, 216], which encode phase information into four intensity measurements with specifically-designed partially-coherent illumination patterns. Ptychography [138, 186, 187] captures far-field intensity diffraction patterns as a focused beam is scanned across an object plane. Fourier ptychographic microscopy (FPM) [240] is essentially a Fourier-transformed ptychography system, where images are captured at different incident angles of plane wave illumination. All of these methods use intensity-only measurements to directly reconstruct quantitative phase values. DPC systems can recover 2D quantitative phase with fewer measurements<sup>5</sup> and with less computational complexity than FPM and ptychography, both of which use an iterative, model-based reconstruction algorithm. Both ptychography and FPM reconstruct high-resolution amplitude and phase

<sup>5</sup>DPC can be single-shot if a multiplexed color-based illumination scheme is used [171].

by capturing high spatial frequency information in multiple low-resolution measurements, breaking the traditional optical trade-off between resolution and field of view.

Similarly, many intensity-only 3D QPI methods have been developed in recent years. DPC, ptychography, and FPM systems have all been extended to 3D reconstructions. In the case of 3D DPC, the designed partially-coherent illumination patterns are augmented by focal stack scanning to capture 3D information [29]. The 3D DPC algorithm relies upon a first-order linear Born approximation to calculate system transfer functions for reconstruction. Both 3D ptychography [69, 118, 136] and 3D FPM [88, 215] formulate a 3D reconstruction problem based on the same measurement systems for their equivalent 2D formulations. 3D FPM has the same physical illumination angle-scanning system as intensity-only ODT [36, 88, 126, 215], but a different processing algorithm. Intensity-only ODT formulates the reconstruction to reconstruct sample refractive index (RI), and can be used with any forward light propagation method.

While we make the distinction here between *interferometric* and *intensity-only* QPI systems, we note that all methods capture intensity images at the camera plane. In the case of *interferometric* systems, there is then an intermediate processing step where the complex field of the measurement is recovered before the final result is reconstructed. In contrast, in *intensity-only* systems, phase information is still encoded into the intensity measurements, but there may be no intermediate processing step where the complex field is reconstructed; instead, the final result is often reconstructed directly from the intensity measurements using a model-based optimization algorithm. So while many make distinctions between the two types of systems, this is largely a historic artifact due to the earlier development of interferometric QPI systems. It is important to note that both interferometric and intensity-only systems are merely different choices in how to design a QPI system that can optimally encode multi-dimensional phase information into intensity measurements such that a computational algorithm can be used to recover 3D quantitative phase information. These different system design choices have practical implications for the physical system’s cost, ease of use, and robustness in real-world settings, as well as the computational algorithm’s speed, accuracy, and stability, among other factors, which are not easy to compare across systems.

## 1.5 Design of Computational Imaging Systems

Computational microscopy is a subset of computational imaging and lies at the boundary of signal processing and traditional optical design. Computational imaging seeks to reframe traditional imaging domains from a signal processing perspective. A few of the many computational imaging systems in common use are ultrasound, magnetic resonance imaging (MRI), computed tomography (CT), high-dynamic range (HDR) cell phone cameras, synthetic aperture radar (SAR), and radio telescopes, such as the very-long baseline interferometry (VLBI) telescope recently used to image a black hole [5]. Computational imaging includes systems from across the electromagnetic spectrum for a wide variety of imaging scales and applications.

Many computational imaging systems have specifically formulated algorithms developed in tandem with the imaging system for the desired reconstruction process. However, most systems can also be formulated in a model-based optimization framework, where the imaging system is modeled as operator  $\mathcal{A}\{\cdot\}$  on the desired object  $\mathbf{x}$  to produce estimates of the measurements  $\mathbf{y}$ . In this general framework, the desired object  $\mathbf{x}$  can be reconstructed by an optimization procedure that optimizes a cost function, such as given by:

$$\mathbf{x}^* = \underset{\mathbf{x}}{\operatorname{argmin}} \|\mathcal{A}\{\mathbf{x}\} - \mathbf{y}\|_2^2 + \mathcal{P}(\mathbf{x}) \quad (1.7)$$

where  $\mathcal{P}(\mathbf{x})$  represents a prior penalty where prior knowledge about the object  $\mathbf{x}$  can be included in the optimization algorithm to drive the reconstruction  $\mathbf{x}^*$  to be physically realistic. An example is that a certain cell might be known to have a refractive index that is strictly higher than the background RI, in which case a positivity penalty would be used to enforce that  $\mathbf{x}^*$  have RI greater than the background. In practice, a proximal operator version of the prior is often used, which is more computationally efficient to calculate [162]. Eq. 1.7 includes an  $\ell_2$  norm loss function, but other norms can be used in computational imaging. In particular, compressed sensing systems specifically rely upon the sparsity-enforcing  $\ell_1$  norm to reconstruct sparse signals from data captured using systems that can operate below the Nyquist sampling rate [23].

In linear systems, the system model  $\mathcal{A}\{\mathbf{x}\}$  can be written in linear algebraic terms,

$$\mathbf{y} = \mathbf{A}\mathbf{x}, \quad (1.8)$$

where  $\mathbf{A}$  is a linear system matrix. This linear equation often has a closed-form solution and so the estimate of the object,  $\mathbf{x}^*$  can be recovered in a single step from measurements  $\mathbf{y}$ , given knowledge of  $\mathbf{A}$ . However, in the case where  $\mathbf{A}$  is large and the analytical solution is therefore computationally complex, or in the case where  $\mathcal{A}\{\mathbf{x}\}$  represents a nonlinear system, iterative algorithms are used to solve Eq. 1.7. First-order gradient descent methods rely upon calculation of the gradient to iteratively converge upon the estimate  $\mathbf{x}^*$  that best satisfies the data consistency and prior penalty. Second-order methods utilize the second-derivative Hessian matrix for optimization. Many optimization algorithms exist, with trade-offs in speed, stability, and ease of implementation. These include methods such as: conjugate gradient, FISTA [15], ADMM [21], maximum likelihood, and Newton's method, among many others.

These algorithms are usually formulated to guarantee recovery of a global minimum of the cost function for convex problems. However, many imaging problems are not only nonlinear and high-dimensional, but non-convex as well. When applied to non-convex problems, convex optimization algorithms may return an estimate  $\mathbf{x}^*$  from a local minimum of the optimization problem in Eq. 1.7. Local minima can be avoided by introducing stronger prior knowledge  $\mathcal{P}(\mathbf{x})$  to eliminate non-physical answers for  $\mathbf{x}^*$ . However, especially in high-dimensional, nonlinear, non-convex problems like 2D and 3D QPI, many local minima exist, and thus the algorithm, initialization, and calibration must be chosen correctly for consistently stable reconstruction results.

One goal of computational imaging is to jointly design the imaging system and the computational algorithm to capture and reconstruct the desired signal in the most efficient and robust manner possible. However, it is often difficult to identify the optical and computational trade-offs that can be leveraged to make a system more robust and practical. The physical arrangement, ease of alignment, cost, ease of use, optical quality, noise, imaging speed, stability over time, and other characteristics must be considered in the optical design, all of which is difficult to quantify. Simultaneously, the computational complexity, speed, data requirements, stability, signal-to-noise ratio (SNR) requirements, and accuracy must be accounted for. All of these qualities can be optimized over, but there are many inherent trade-offs between them. The optimal trade-off between all of these factors will depend on the system's application space.

Generally speaking, computational imaging system design has followed three phases. The oldest computational imaging systems were designed using intuition and physical understanding to determine how to capture information relevant to the desired application. For example, we can understand the use of coherence gating, focal scanning, sample rotation, and closely-related illumination angle rotation for 3D imaging by intuitively considering how these different optical operations will capture 3D information about the object, as described above. The computational representation of this optical operation is conceived, and then a specific reconstruction algorithm is designed and deemed to be feasible given the computational constraints. Then, given hardware constraints and resolution requirements of the microscope, an optical system is built that allows the specifically-designed computational algorithm to function stably. In this way, the computational and optical practicality are both considered in the system design. However, while these designs are robust and practical, they are not necessarily the best design with the most efficient use of the available optical and computational resources. For example, computed tomography (CT) scanners were created from the observation that collecting *only* the transmitted light through a sample is equivalent to a mathematical 2D projection operator, which enables use of the filtered back-projection algorithm for 3D reconstruction with few errors [95]. In order to allow use of this computational algorithm, medical CT scanners typically include an anti-scatter grid (ASG) to absorb multiply scattered light [67]. More recent work [67], following from previous work in x-ray diffraction CT [83], has shown that by removing this component and using a new, optimization-based algorithm, conventional CT scanners can use multiply scattered light for better reconstructions with lowered radiation dose for patients. This example shows that these traditional systems, while robust and practical, are not fully leveraging the currently available optical and computational power.

In the second phase, computational imaging system design has been framed as a direct trade-off between the *optics* and the *computation*. In these designs, designers have sought to re-implement typically-optical operations as computational operations or vice versa in order to simplify either the optics or the computation. For example, a low-aberration microscope can be implemented traditionally by designing an expensive and difficult-to-build objective lens system. Equivalently, a computational deconvolution algorithm can be paired with a less expensive, easier-to-build, higher-aberration objective lens to produce equiva-

lent deblurred images [205]. In this way, difficult optical operations are traded off for an added computational element. Difficult computations can also be simplified by adding optical elements to the system. For example, work has been done to optically implement deep neural network classification algorithms [26, 117, 125]. Other work has used a biomimetic framework to build systems with optical elements that reduce computational requirements, as inspired by the eyes of jumping spiders [9, 79]. However, this design framework generally focuses upon optimizing a preexisting system rather than creating an entirely new system design. For example, in the example case of building a low-aberration microscope, perhaps doing away with a lensed system completely and instead modulating light through scattering media might produce even higher resolution results [34, 35, 182, 234]<sup>6</sup>. When considering the direct trade-off between optics and computation, these more unconventional ideas are much less likely to be considered, though they might represent useful ways to address certain application needs.

In the most recent phase of computational imaging design, many works have focused on the joint design of optical and computational systems through either *model-based optimization* [12, 64, 142, 140] or *data-driven machine learning* [51, 87, 102, 149, 185]. In this design regime, a general optical and computational system design is known and can be computationally modeled with some tunable optical and computational parameters that can be optimized for an improved system design. In *model-based optimization*, the optical and computational system parameters are optimized to improve some predetermined metric, such as system condition number, resolution, SNR, or other metrics [12, 64, 142, 140, 181]. In general, these systems tend to optimize the optical system to work best with the predetermined computational algorithm, and require a useful metric to optimize the system parameters, which is not always straight-forward to design. In *data-driven machine learning*, the tunable parameters are instead optimized to improve the fidelity of the final reconstruction to a ground truth comparison object [51, 87, 102, 149, 185]. These systems can optimize both optical and computational parameters and are fairly easy to apply across different optical systems thanks to modern computational tools and advancements, doing away with the need for specifically-designed optimization metrics. However, the computational cost and data requirements can be very high for these algorithms. They additionally require knowledge of the ground truth object, which often means system optimization must be done completely on simulated data. In this case, real-world nonidealities like noise, system misalignments, and spurious reflections will not be (easily) captured in the machine learning algorithm. Therefore, the systems designed using this method might not be robust to these real-world nonidealities. Both *model-based optimization* and *data-driven machine learning* design moreover explicitly optimize a pre-existing system to create more optimal imaging parameters. While these methods may produce more non-intuitive designs that

---

<sup>6</sup>Though in most applications, a high-quality objective lens can be bought off the shelf and, due to many years of standardized optical design, fitted easily into a microscope system, and so is usually preferable. However, specific applications exist where a scattering lens-based design would be more useful than an off-the-shelf lens, as detailed in [34, 35, 182, 234]. In addition, many diffractive [1] and metalens [28, 227] optical designs have been proposed to replace refractive lens systems for certain applications.

better leverage the available optical and computational power, they do not usually provide a useful framework for thinking about wholly new computational imaging systems. In addition, they generally do not account for the practicality of the optical system, as this can be difficult to include in the optimization or learning algorithm, either due to computational limitations, lack of a good model, or difficult-to-optimize discrete parameters.<sup>7</sup>

## 1.6 Dissertation Outline

In this dissertation, I focus on three methods for approaching computational imaging design with an emphasis on robustness and practicality. I focus in particular on 2D and 3D quantitative phase imaging systems; specifically, 2D Fourier ptychography and 3D intensity-only optical diffraction tomography. Overall, QPI systems were chosen because they are an exciting new imaging modality that has not yet seen wide adoption in the biological research community, and so represent a space where better computational imaging designs could have a large impact on biological research processes. FPM and intensity-only ODT were chosen because they explicitly process intensity images, rather than relying upon the intermediate creation of recovered field measurements, as in interferometry-based systems, widening the available system design space considerably and eliminating the need for interference reference arms. I present work on self-calibration algorithms, increased measurement diversity, and physics-based machine learning for more robust system design through the lens of these systems. I additionally give practical advice for designing, building, and using FPM and intensity-only ODT systems based on my own experience, which I hope will be helpful to those who want to use these systems in a research setting.

Fourier ptychographic microscopy (FPM) uses multiple low-resolution images from a low-cost, low numerical aperture (NA), and wide field of view objective lens to reconstruct a high-resolution object amplitude and phase, breaking the traditional optical trade-off between imaging resolution and field of view. This has proved exciting for many application spaces where cheap, high resolution amplitude and phase imaging across a wide field of view would be beneficial, such as *in vitro* cell culture studies [218] and white blood cell counts [39]. In comparison to ptychography, an equivalent high-resolution phase system implemented in Fourier space, FPM is easy to implement in a conventional microscope by replacing the condenser lens with a programmable LED array [240]. However, high-quality FPM reconstructions require system parameters such as illumination angle to be well-known for a good reconstruction.

In Chapter 2, I discuss practical considerations for FPM optical and reconstruction parameter design, including illumination system design, background removal and initialization options, methods to account for system vignetting, and joint system pupil reconstruction stability. In Chapter 3, I present work on a self-calibration algorithm that directly recovers illu-

---

<sup>7</sup>For example, only certain objective lenses are available for purchase, with pre-determined parameters such as NA, field of view, working distance, and cost. As these parameters do not exist on a continuum, it is difficult to represent them inside the algorithm for optimization.

mination angle parameters from measured data for more robust FPM system operation [56, 57]. This algorithm has enabled multiple new optical systems to be used for FPM [4, 96, 173] and intensity-only ODT [36], as well as to enable aberration correction methods [76] that would not have been previously possible. I discuss how the self-calibration framework can be useful for overall computational imaging system design.

Intensity-only ODT reconstructs 3D refractive index (RI) volumes from intensity images captured at multiple incident plane-wave illumination angles. The intensity-only ODT framework is easy to use with many forward light propagation models, including models that account for multiple scattering and therefore can reconstruct thicker, more complex samples than single-scattering models. High-resolution systems can provide gorgeous 3D RI reconstructions [36], but are difficult to align and use, require large amounts of data and long computations times, and additionally have many local minima in the reconstruction algorithm, so are sensitive to algorithm parameters.

In Chapter 4, I introduce intensity-only ODT and compare the accuracy and computational complexity for three common 3D coherent light propagation models that can be used for 3D RI imaging [58]: the first Born approximation [18], the multislice (or beam propagation) algorithm [42], and an optimization-based series-expanded Born method called SEAGLE [129]. I discuss techniques for intensity-only ODT system design and alignment, including illumination and objective lens design choices, alignment methods, and hardware synchronization. I also present a comparison between intensity-based and complex field-based ODT reconstructions.

In Chapter 5, I present a novel 3D RI imaging system design called *pupil-coded intensity ODT* which was designed to increase the ODT system's measurement diversity. The pupil-coded intensity ODT system captures 3D RI data by scanning incident plane-wave illumination angle in tandem with dynamic Fourier-plane phase pupil coding. I show that this joint illumination- and detection-side coding technique increases the diversity of 3D RI information in the measured images, leading to a reduction in the computational processing time and data requirements needed to reconstruct high-quality 3D refractive index volumes. This system additionally reduces design constraints on the illumination system for ODT by eliminating the need for high-NA illumination angles, which were needed in intensity-only ODT systems for high-quality reconstructions. Using a transfer function analysis of the system, I show that the proposed system better encodes the low-spatial frequency components of the 3D RI across all measured images compared to traditional intensity-only ODT. While in general, pupil-coded intensity ODT requires dynamic phase coding, I also show that a single, well-designed pupil aberration can be used for similar results. I present a highly non-intuitive result of this finding, which is that an uncorrected objective lens with high aberrations due to glass in the imaging path can be used through the pupil-coded intensity ODT framework to produce better 3D RI reconstructions than a corrected, aberration-free objective lens for a limited illumination condition, which eliminates the need for a dynamic pupil modulation element such as a spatial light modulator (SLM) for pupil-coded intensity ODT, further reducing ODT system complexity. Through this work, I show that increasing measurement diversity is a useful design principle for developing more robust and effective

computational imaging systems.

In Chapter 6, I present results from a physics-based machine learning algorithm for pupil-coded intensity ODT that optimizes the system's dynamic pupil coding masks for imaging of thick cell clusters. While initial results show promise for reconstruction improvements, implementation of specific system constraints due to use of a liquid crystal on silicon (LCOS) SLM in the Fourier plane of the system means that the optimized pupil coding designs under this algorithm have equivalent performance when compared to the randomly-weighted pupil coding designs discussed in Chapter 5. I discuss opportunities for future optimization of the pupil-coded intensity ODT design system. Additionally, I discuss the benefits and drawbacks of using machine learning to optimize computational imaging system designs.

Overall, my aim is to present useful frameworks for the design of robust computational imaging systems, through the lens of specific quantitative phase imaging systems. I also aim to provide guidance for the practical operation of Fourier ptychographic microscopes and intensity optical diffraction tomography systems, so that these quantitative phase imaging systems can be useful to a wide variety of applications in the future.

## Chapter 2

# Practical Fourier Ptychography Systems

Fourier ptychographic microscopy (FPM) is an exciting framework for computational imaging in general and quantitative phase imaging specifically, as it showcases how combining a model-based computational algorithm with cheap, cleverly-designed optics can break traditional boundaries in optical microscopy. In particular, Fourier ptychography uses angled illumination to scan the Fourier space of a sample, enabling high-resolution quantitative phase imaging across a wide field of view with low-cost objective lenses. The literature since the inception of the Fourier ptychographic microscope [240] is extensive, reflecting the research community’s search for the best implementation of FPM for a wide variety of applications. This includes an illumination angle self-calibration algorithm for FPM presented in Chapter 3, which has made FPM systems more robust and has enabled the use of novel imaging systems for FPM.

In this chapter, I present a brief review of Fourier ptychography, with practical notes from my experiences in aligning and using various FPM systems to image samples with different characteristics. Recent works have also been published which attempt to cover the basics of FPM systems [109, 242], which I hope to augment here with my own knowledge in building robust and practical FPM systems. I begin with an introduction to Fourier ptychography, discuss microscope and reconstruction algorithm design considerations, including a discussion of vignetting effects in FPM, and conclude with a demonstration of the efficacy of joint system pupil recovery with FPM. It is my hope that this guidance will prove useful in the wide adoption of FPM systems for biological applications.

### 2.1 Introduction to Fourier Ptychography

Fourier ptychographic microscopy is a recently developed quantitative phase imaging method that uses intensity-only measurements to reconstruct high-resolution amplitude and phase of a 2D object  $O(\mathbf{r})$  across a wide field of view [240], where  $\mathbf{r} = (x, y)$  denotes the spatial

coordinates. This is accomplished by illuminating the sample with spatially coherent plane waves from diverse angles up to the maximum illumination angle of  $NA_{illum,max}$ . The sample is imaged with a low-resolution, wide field of view objective lens with numerical aperture  $NA_{obj}$ , which defines a low-pass filter pupil support  $\tilde{P}(\mathbf{k})$ , where  $\mathbf{k} = (k_x, k_y)$  are the spatial frequency coordinates. The FPM reconstruction algorithm computationally combines these measurements to build up a high-resolution image with numerical aperture

$$NA_{sys} = NA_{obj} + NA_{illum,max}. \quad (2.1)$$

Since low-resolution objective lenses typically have much wider field of views than high-resolution objectives, FPM therefore increases the available system space-bandwidth product (SBP) by providing high-resolution across the entire field of view of the low-resolution objective lens. This is useful for a variety of biological applications, including *in vitro* cell culture studies [218] and white blood cell counts [39]. Example FPM results can be seen in Fig. 2.1 and Fig. 2.2, where two regions of a mouse brain slice have been imaged in high resolution across a wide field of view.

For illumination at wavelength  $\lambda$  in a medium of refractive index  $n$ , the  $i^{th}$  illumination of object  $O(\mathbf{r})$  by a coherent plane wave at angle  $\theta_i = (\theta_{x,i}, \theta_{y,i})$  can be described as multiplication by a phase ramp at spatial frequency  $\mathbf{k}_i = \frac{2\pi\mathbf{N}\mathbf{A}_i}{\lambda} = \frac{2\pi n \sin \theta_i}{\lambda}$ , giving the  $i^{th}$  intensity measurement

$$I_i(\mathbf{r}) = |O(\mathbf{r})e^{-j\mathbf{k}_i\mathbf{r}} * P(\mathbf{r})|^2 \quad (2.2)$$

where  $*$  denotes convolution and  $P(\mathbf{r})$  is the system's point spread function, the real-space version for the complex Fourier-space pupil function  $\tilde{P}(\mathbf{k})$ . By the Fourier shift theorem, this is equivalent to shifting the object spectrum  $\tilde{O}(\mathbf{k})$  by  $\mathbf{k}_i$  in the Fourier domain, giving the equivalent formulation

$$I_i(\mathbf{r}) = |\mathcal{F}^{-1}(\tilde{O}(\mathbf{k} - \mathbf{k}_i)\tilde{P}(\mathbf{k}))|^2. \quad (2.3)$$

The angled illumination in FPM shifts high spatial frequency (and therefore high spatial resolution) information into the pass-band of the objective lens. The shifted pupils must generally have large overlap in Fourier space between measurements for a good FPM reconstruction [53, 212]. When the  $i^{th}$  angle of illumination's NA  $|\mathbf{N}\mathbf{A}_i| \leq NA_{obj}$ , the DC component of the object spectrum passes through the pass-band of the objective lens, giving brightfield images with high intensity values in transmissive regions of the object. When  $|\mathbf{N}\mathbf{A}_i| > NA_{obj}$ , the object spectrum is blocked by the objective pupil, resulting in darkfield images that typically have little to no light in transmissive object regions. Darkfield images generally have lower SNR, but contain important high resolution information. A high-resolution image is built up from these measurements with a computational reconstruction algorithm, as in synthetic aperture imaging [50, 221]. The successful transfer of the FPM algorithm to new imaging domains (*e.g.*, reflection-mode rather than transmission-

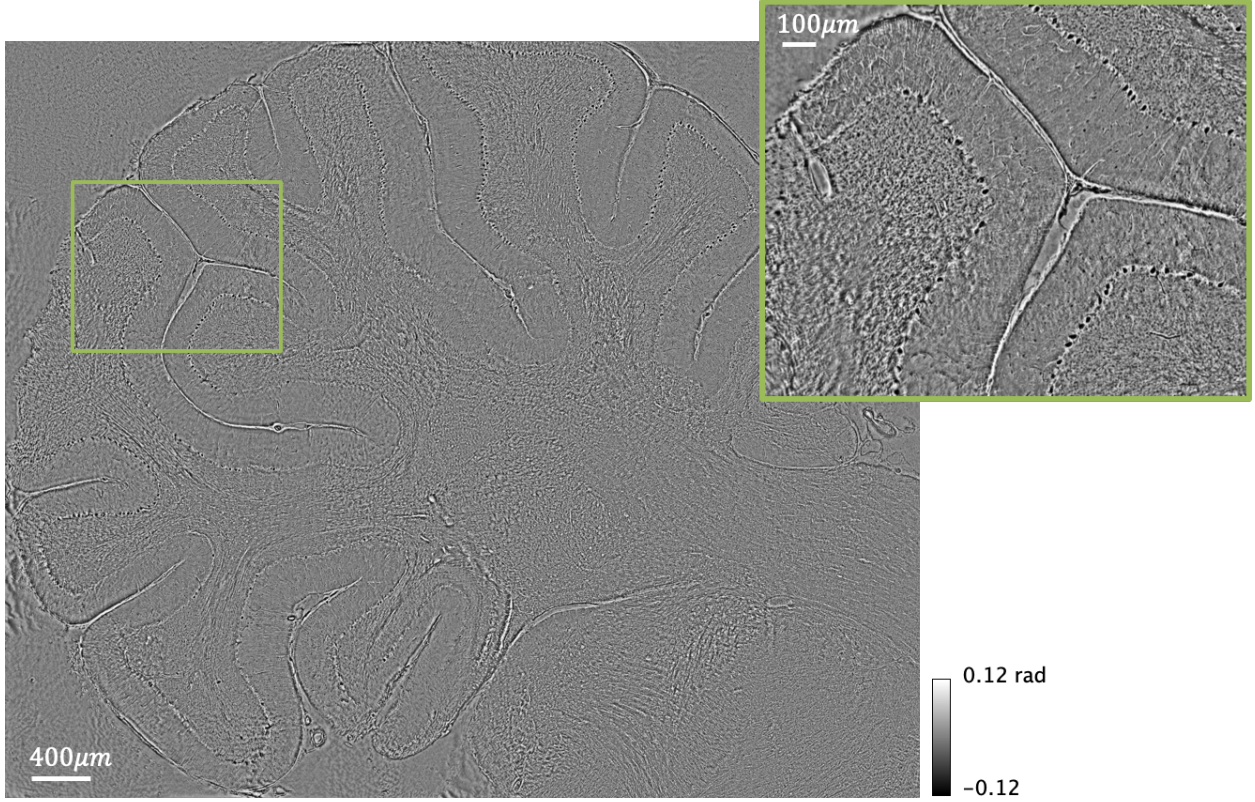


Figure 2.1: Example wide field of view ( $8.9\text{ mm}\times 10.78\text{ mm}$ ), high resolution ( $r_{\text{Rayleigh}} = 0.732\text{ }\mu\text{m}$ ) phase image of a  $20\text{ }\mu\text{m}$  thick mouse brain slice reconstructed using Fourier ptychography.

mode) hinges upon whether the interaction of the plane wave illumination with the object is properly described by the forward model in Eq. 2.2.<sup>1</sup>

We formulate the FPM reconstruction algorithm as a minimization problem on the amplitude of the measured images to better account for Poisson noise statistics in the measurements [233], giving

$$O^*(\mathbf{r}) = \operatorname{argmin}_{O(\mathbf{r})} \sum_i \left\| \left| \mathcal{F}^{-1}(\tilde{O}(\mathbf{k} - \mathbf{k}_i)\tilde{P}(\mathbf{k})) \right| - \sqrt{I_i(\mathbf{r})} \right\|_2^2. \quad (2.4)$$

Many improvements on the FPM algorithm have been proposed [53, 54, 56, 109, 158, 156, 219, 218, 233, 240, 242]. One especially important set of improvements for FPM centers

<sup>1</sup>For example, if a sample is highly scattering, this model might no longer be accurate and good reconstruction results may not be achieved. In general, this is why we say FPM is *object-dependent*, as some samples may not fit this simplified imaging model, leading to incorrect reconstructions with many artifacts.

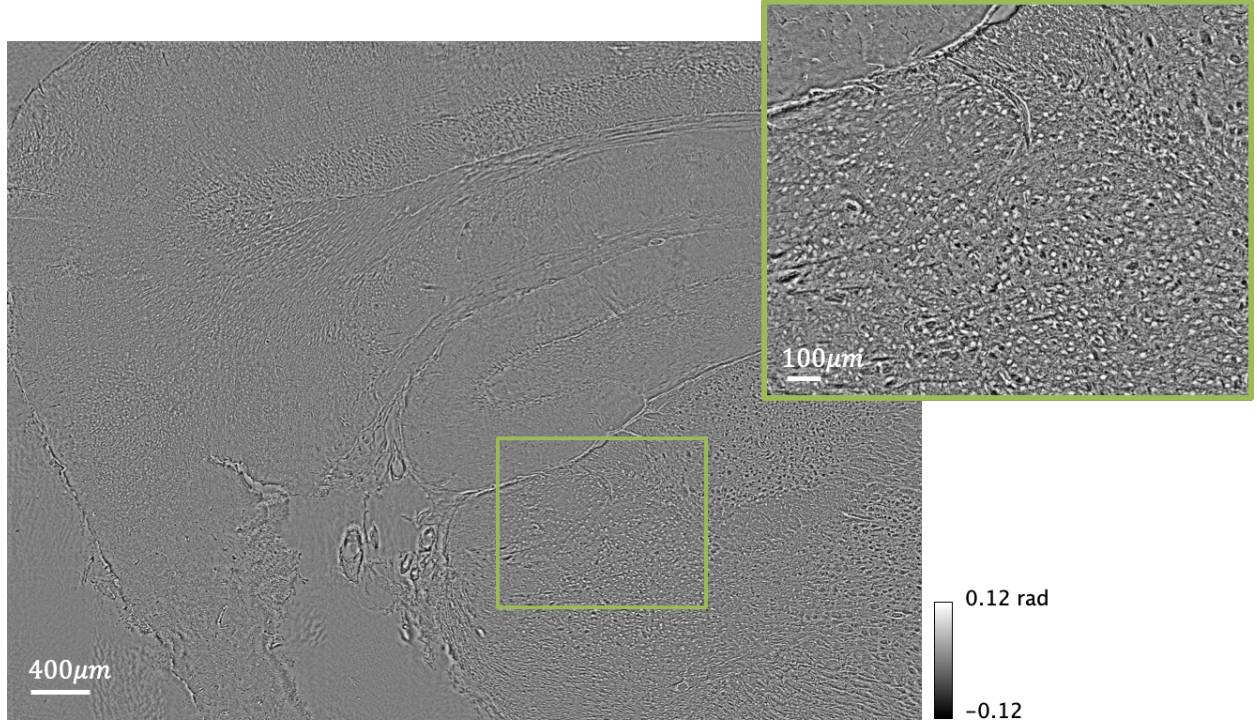


Figure 2.2: Example wide field of view (7.93 mm × 10.71 mm), high resolution ( $r_{\text{Rayleigh}} = 0.732 \mu\text{m}$ ) phase image of a 20  $\mu\text{m}$  thick mouse brain slice reconstructed using Fourier ptychography.

around the calibration of the system pupil  $\tilde{P}(\mathbf{k})$  [89, 156, 214] and illumination angles [4, 56, 57, 130, 137, 210, 233, 238], among other system parameters [17, 16, 54, 194, 160], which are essential for a high-quality reconstruction. These improvements, and especially the self-calibration of illumination angles, are discussed in detail in Chapter 3.

In practice, we find that calibrating the illumination angles as in [56] and jointly estimating the pupil function as in [156] provide consistently high-quality FPM reconstructions using the algorithm described in Algorithm 1. Important system characteristics include the camera pixel pitch  $d_{\text{cam}}$ , system magnification  $mag$ , and image patch size  $N_{im} \times N_{im}$  pixels, as well as the NA of the objective lens  $NA_{obj}$ , and angles of illumination for each measurement,  $\mathbf{NA}_i$ . In the initialization steps, the background of the intensity images is removed as described in Sec. 2.3.1, giving images  $I(\mathbf{r})$ . We initialize the object estimate  $O_0(\mathbf{r})$  as described in Sec. 2.3.2 and the pupil estimate  $\tilde{P}_0(\mathbf{k})$  to the binary low-pass filter support  $\tilde{P}_{support}(\mathbf{k})$ , which is unity where  $|\mathbf{k}| \leq (\frac{2\pi NA_{obj}}{\lambda})$  and zero everywhere else. Since the final system NA,  $NA_{sys}$ , is larger than the objective  $NA_{obj}$ , the number of pixels in the FPM reconstruction is usually increased to avoid aliasing of the high-resolution result. The upsampled number of pixels,  $N_{sys} \times N_{sys}$ , is defined to be the smallest integer multiple of the image size  $N_{im} \times N_{im}$

to prevent aliasing and avoid other upsampling artifacts.<sup>2</sup> The minimum requirement for  $N_{sys}$  to avoid aliasing is

$$N_{sys,min} = \frac{4NA_{sys} N_{im} d_{cam}}{\lambda \cdot mag}. \quad (2.5)$$

Accounting for the integer multiplication of  $N_{im}$ , the final system reconstruction size is given by

$$N_{sys} = \text{ceil} \left( \frac{N_{sys,min}}{N_{im}} \right) N_{im} = \text{ceil} \left( \frac{4NA_{sys} d_{cam}}{\lambda \cdot mag} \right) N_{im}. \quad (2.6)$$

The illumination angles are sorted in order of increasing magnitude of numerical aperture,  $|\mathbf{NA}_i| \equiv NA_{illum, i}$ , for best results. Additional parameters include  $eps$ , the minimum value that can be represented computationally by the data type to avoid division by zero, as well as  $\alpha$  and  $\beta$ , the respective regularization parameters for the object and pupil reconstruction. We find that  $\alpha = 10$  and  $\beta = 1$  are usually good choices. The best way to search for the optimal values of  $\alpha$  and  $\beta$  for a certain object is to vary them by orders of magnitude across different reconstructions. The update steps in Algorithm 1 are drawn from previous work in ptychography's PIE algorithm [75, 186], as well as multiplexed and 3D FPM [215, 219], where they have been shown to be robust. Many other formulations of the FPM update steps are available and are given in detail in [109, 233, 242].

---

**Algorithm 1** Fourier ptychography reconstruction

---

- 1:  $\tilde{O}^{[N_{sys} \times N_{sys}]} \leftarrow \mathcal{F}(O_0)$  ▷ Initialize variables
  - 2:  $\tilde{P}^{[N_{im} \times N_{im}]} \leftarrow \tilde{P}_0$
  - 3:  $\text{pupilshift}_i \leftarrow \text{round}(\mathbf{k}_i \frac{N_{im} d_{cam}}{2\pi mag})$  ▷ Define shift and crop of pupil by  $i^{th}$  illumination
  - 4:  $\text{roiCoord}_i \leftarrow \text{pupilshift}_i + \text{floor}(N_{sys}/2) \pm \text{floor}(N_{im}/2)$
  - 5: **while**  $iter < iter_{max}$  **do**
  - 6:     **for**  $i$  image **do**
  - 7:          $\tilde{O}_{roi}^{[N_{im} \times N_{im}]} \leftarrow \tilde{O}|_{\text{roiCoord}_i}$  ▷ Crop object spectrum around  $i^{th}$  illumination shift
  - 8:          $O_{fwd} \leftarrow \mathcal{F}^{-1}(\tilde{O}_{roi} \tilde{P})$  ▷ Forward imaging model for  $i^{th}$  angle
  - 9:          $\tilde{O}_{up} \leftarrow \mathcal{F} \left( \frac{\sqrt{I_i} O_{fwd}}{|O_{fwd} + eps|} \right)$  ▷ Update with  $i^{th}$  measured image amplitude
  - 10:          $\tilde{P} \leftarrow \tilde{P} + \frac{|\tilde{O}_{roi}| \text{conj}(\tilde{O}_{roi})(\tilde{O}_{up} - \mathcal{F}(O_{fwd}))}{|\tilde{O}|_{\max}(|\tilde{O}_{roi}|^2 + \beta)} \tilde{P}_{support}$  ▷ Update pupil
  - 11:          $\tilde{O}|_{\text{roiCoord}_i} \leftarrow \tilde{O}_{roi} + \frac{|\tilde{P}| \text{conj}(\tilde{P})(\tilde{O}_{up} - \mathcal{F}(O_{fwd}))}{|\tilde{P}|_{\max}(|\tilde{P}|^2 + \alpha)} \tilde{P}_{support}$  ▷ Update object spectrum
  - 12:     **end for**
  - 13: **end while**
- 

<sup>2</sup>Though  $N_{sys}$  can be chosen to be an arbitrarily large number, restricting its size reduces the computing needs of the algorithm.

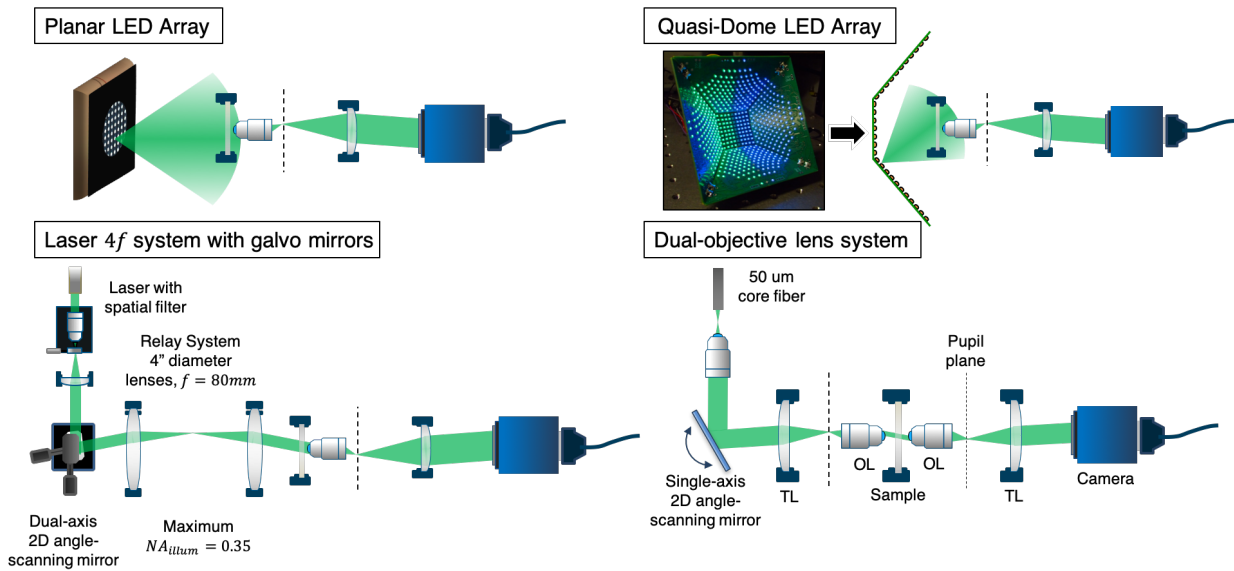


Figure 2.3: Four illumination systems for Fourier ptychography. In all examples, a sample is imaged by an objective lens (OL) and tube lens (TL) onto a camera. The maximum illumination angle for the planar and quasi-dome LED arrays is limited by simple geometry. The dual-objective lens system’s maximum illumination angle is limited by the NA of the illumination-side objective lens.

## 2.2 Fourier Ptychography Microscope Design

FPM imaging systems are typically easier to design and build than their Fourier-conjugate system of ptychography, since in their simplest form, they can be implemented by replacing the condenser lens on a traditional microscope with a low-cost programmable LED array [53, 158, 218, 219, 240]. However, a low-cost programmable LED array might not be the best illumination system for FPM applications that need fast, reliable, or extremely high-resolution imaging. This section discusses design considerations for the illumination system and the detection objective lens and camera for FPM.

### 2.2.1 Light Sources

The simplest way to implement a FPM system is to replace the condenser lens of a traditional microscope with a programmable LED array, such as an Adafruit LED array [240]. However, off-the-shelf LED arrays are often slow, low-power (thus either leading to increased measurement noise, increased camera exposure time, or both), and can be difficult to control. In addition, they often have a diffusive film deposited on top of the LEDs which destroys the LED light’s spatial coherence, which must be removed for proper FPM functionality. There-

fore, custom LED arrays and other illumination systems designed specifically for FPM are important for practical FPM systems. Many custom LED arrays have been demonstrated for FPM, including planar grid-like arrays [133, 215, 218, 219], circular arrays [78], and domed arrays [159, 173, 172, 198]. Systems have also been designed for high-NA illumination [157, 159, 173] for extremely high-resolution reconstructions. In particular, a quasi-dome array was developed to allow fast, multiplexed Fourier ptychography captures with illumination up to 0.98 NA [173], as shown in Fig. 2.3. As of this writing, these quasi-dome arrays are some of the only commercially available LED arrays specifically designed for FPM and other computational microscopes.<sup>3</sup>

FPM requires coherent light sources to properly function. LEDs, which emit light in an approximately spherical wave, have a coherence area  $A_c = \frac{\lambda z_{\text{LED}}}{d_{\text{LED}}}$  by the van Cittert-Zernike theorem, where  $z_{\text{LED}}$  is the distance from the LED to the sample plane and  $d_{\text{LED}}$  is the size of the LED's active emitting region ( $d_{\text{LED}} = 120 \mu\text{m} \times 120 \mu\text{m}$  is one example size) [215]. LED illumination is approximately planar within this area, but reconstructions can be slightly improved by increasing the illumination coherence by shrinking the LED size, moving the LED further away, or using a more coherent light source, as seen in Fig. 2.4. We note that the observed loss of reconstruction sharpness is slight, and that many very successful FPM systems have been built using LED array-based illumination sources. Common high-coherence light sources are lasers and fiber-coupled LEDs, where a fiber with few optical modes effectively filters the partially incoherent LED, increasing its coherence. Lasers are higher power than LEDs, allowing for lower exposure times and lower measurement noise. However, the extremely high coherence of lasers means laser-illuminated systems can have many ringing artifacts from dust in the optical path, which often makes fiber-coupled LEDs preferable for practical imaging. Arrays of lasers or fiber-coupled LEDs are not currently available on the market, so other methods for creating dynamic angled illumination must be used for these higher-coherence sources, as seen in Fig. 2.3. Systems using steerable mirrors [36, 41, 56], digital micromirror devices (DMDs) [111], and liquid crystal displays [77] have been used for this purpose.

Steerable mirrors might be galvanometer-, motor-, or piezo-driven, with galvanometric mirror systems generally having a larger angle range and piezo-driven mirrors having the fastest operation. The main problem with using steerable mirrors is that the system needs to relay a non-moving, angled illumination spot from the mirror surface to the sample plane. This can be accomplished through lensed relay systems [36, 56] or mirror systems [41]. Note that using a dual-axis steerable mirror where the  $x$ - and  $y$ -coordinate controls are physically offset, such as the Thorlabs GVS012 as in [56], means that the ideal sample planes where the illumination beam does not move laterally will be different for the  $x$  and  $y$  directions. Thus the illumination spot will have to be physically large enough to still illuminate the desired sample field of view when placed between these two planes across all angles of illumination.

---

<sup>3</sup>These LED arrays were developed by Zachary F. Phillips and Michael Chen as graduate students in Prof. Laura Waller's lab at UC Berkeley. They are available to purchase through SCI Microscopy at <https://www.sci-microscopy.com/>.

It is therefore preferable to use a steerable mirror that rotates in  $x$  and  $y$  around a single rotation axis, as done in [36].

A relay lens system can be used to relay a coherent, non-moving illumination beam to the sample plane. If a simple  $4f$  system is used, where the sample plane is 4 focal lengths  $f$  from the mirror plane, there is a practical limit to the maximum angle of illumination geometrically given by the lens diameter  $d_{\text{lens}}$  and the focal length  $f$ , as well as the illumination beam diameter  $d_{\text{beam}}$ . In this case, the maximum illumination angle is  $\theta = \arctan(\frac{R}{f})$ , where the maximum radial distance on the lens with a clear aperture is given by  $R = (d_{\text{lens}} - d_{\text{beam}})/2$ . We used large  $f = 80$  mm,  $d_{\text{lens}} = 4$  inch relay lenses in combination with a dual-axis galvanometric mirror control (Thorlabs GVS012) with a  $d_{\text{beam}} = 10$  mm laser beam, as seen in Fig. 2.3, for high-quality laser-based FPM results, shown in Fig. 2.4. While the system was high-speed due to the fast galvanometric mirrors and high laser illumination intensity (and thus low exposure time), the maximum practical illumination NA of the system was  $NA_{\text{illum,max}} \approx 0.35$ . We searched for larger relay lenses with shorter focal lengths, but all available options were condenser lenses, which created extreme aberrations in the laser beam that destroyed the desired plane wave illumination. After extensive searching, we concluded that the maximum  $NA_{\text{illum}}$  for a simple  $4f$  relay system is  $\approx 0.35$  with readily available commercial lenses at this time.

Another option for a steerable mirror design with a lensed relay system is to use an objective lens to obtain high-angle illumination. We call this system a *dual objective system*, since it pairs an illumination objective lens with the objective lens used to image the sample, as seen in Fig. 2.3. In this system, the steerable mirror is placed in the back focal plane of an illumination objective tube lens, as shown in [36]. This system effectively steers a small focal spot around the back focal plane of the objective lens, creating collimated illumination at the sample plane at angles up to the NA of the objective lens. These systems can create high-power illumination at high angles, but create many system design constraints, especially for high NA objectives. First of all, the spot size exiting the objective can be very small, so precise alignment and optical stability is important for high-quality results. Second, since the working distance of an objective generally decreases with increasing NA, the axial space available for the sample might be very small for high-NA illumination systems, making the system difficult to align and use. Additionally, axial alignment of the imaging objective is difficult. If the illumination-side tube lens is removed, a shearing plate interferometer could reveal when the imaging objective is correctly placed to output a collimated beam. However, this method doesn't work well for high-NA objectives, which are not optimized to work without a tube lens, and so exhibit many aberrations. Therefore, in practice, the imaging objective is iteratively aligned by observing if a feature in the beam-path does not move as the illumination angle is changed.

Another option for steering collimated light is a mirror array, which can be bulky and costly [41]. A DMD [111] or liquid crystal spatial light modulator [77] can be used to create angled illumination by placing it in the back focal plane of an illumination lens. The DMD system reported in [111] uses a dual-objective illumination system, with the DMD effectively

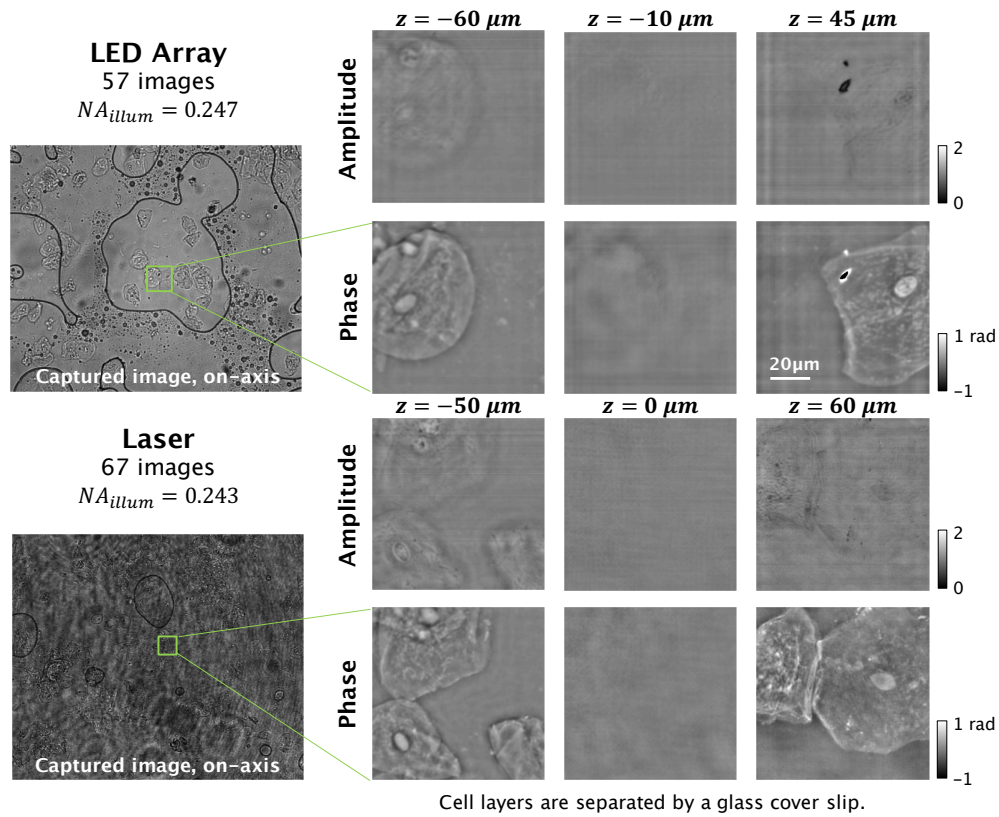


Figure 2.4: Increased illumination coherence leads to sharper phase reconstructions. 3D FPM reconstructions of cheek cells on either side of a glass coverslip, captured with an LED array (less coherent) and laser (more coherent) illumination source with similar numbers of images. While the on-axis laser image is much noisier due to coherent ringing from off-focus dust and system reflections, the reconstructed phase edges appear crisper with the laser illumination. Both datasets were captured with  $NA_{obj} = 0.25$ .

selecting the illumination angle by transmitting light from a single pixel only, which leads to large light losses. The liquid crystal display system reported in [77] places an LCD in front of a commercial microscope’s backlight, using it as a transparent phase spatial light modulator to change the angle of illumination. Additional FPM systems have used a multi-aperture configuration to further extend the system resolution [107, 108], or have been engineered for low-cost, portable form-factors [4, 52, 172].

In FPM, the maximum  $NA_{illum,max}$  is chosen to complement the objective  $NA_{obj}$  to produce the desired final system  $NA_{sys}$ , typically with  $NA_{illum,max} \gg NA_{obj}$  to fully leverage the wide field of view of the low-NA objective lens with the high-resolution features provided by the high-NA illumination source and the computational reconstruction. It is therefore

best to measure as many darkfield images as possible in FPM (where  $NA_{illum, i} > NA_{obj}$ ) to build up the reconstruction resolution, though since the camera must capture both high-intensity brightfield images (where  $NA_{illum, i} < NA_{obj}$ ) and low-intensity darkfield images, the dynamic range of the camera should be considered. When many darkfield images are included, the noise statistics in the low-intensity darkfield images should be considered in the algorithm formulation for higher-quality reconstructions [233]. The light intensity fall-off at extreme angles should also be accounted for, and has spurred the creation of domed and quasi-domed LED arrays [173, 172, 198] and multi-aperture systems [107, 108].

While these light sources have been discussed here in the context of FPM, they are applicable to any computational imaging system where the incident angle of plane-wave illumination is changed to capture diverse information about the sample at hand. This includes 3D RI imaging ODT systems. While the light source options are the same for both systems, the choice of optimal light source might varies based on the application space. Dual-objective lens systems have so far proven useful for these 3D quantitative phase imaging systems [36], though they come with many constraints. See Sec. 4.4.1 for more details on ODT illumination system design.

### 2.2.2 System Design and Calibration

The FPM imaging objective lens is generally chosen under field of view and cost constraints, since the numerical aperture (*i.e.*, resolution) of the system can be built up via the system's angled illumination. Depending on the illumination system chosen, the imaging objective  $NA_{obj}$  should be chosen to provide the required final  $NA_{sys}$  when considering the available maximum illumination  $NA_{illum, max}$ , as shown by Eq. 2.1. Flat-field corrected Plan Apochromatic objective lenses that are rated as well-suited for brightfield operation are good choices for FPM. If high-NA lenses are used, care should also be taken to select an objective that is corrected for the spherical aberrations introduced by glass coverslips if samples with coverslips are expected in the system.

The choice of camera may also be important for consistently high-quality FPM reconstructions, especially if  $NA_{illum, max} \gg NA_{obj}$  and many darkfield images will be measured. In this case, a low-noise, high quantum efficiency scientific camera should be used, such as an sCMOS camera. All results presented here use a monochromatic 16-bit PCO Edge 5.5 sCMOS air-cooled camera with a  $d_{cam} = 6.5 \mu\text{m}$  pixel pitch.

Ideally, the imaging system would be designed to avoid aliasing of the optical signal on the camera plane. Following the Nyquist sampling rate, this means the camera's spatial sampling rate must be double the maximum system spatial frequency. This implies that the system must obey

$$mag \geq \frac{4NA_{obj}d_{cam}}{\lambda} \quad (2.7)$$

to avoid aliasing, where  $mag$  is the total system magnification and  $d_{cam}$  is the camera pixel size. The FPM algorithm can account for aliasing artifacts, so this is not strictly necessary. However, it is practically much simpler to tell if a sample is at or very near focus if the

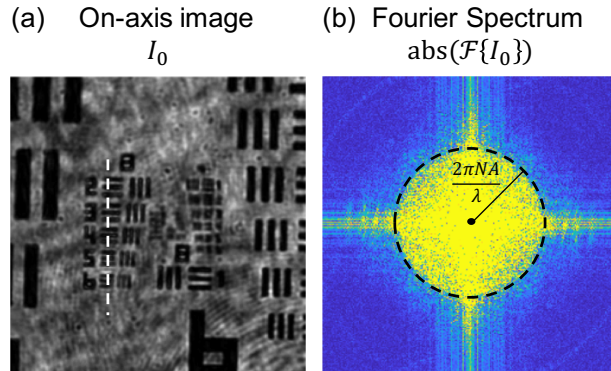


Figure 2.5: Example FPM calibration steps. (a) Compare the frequency of USAF resolution target bars in an on-axis image along a vertical axis (dashed white line) to the expected period to verify the system magnification. (b) Verify objective NA by viewing the contrast-stretched or log plot of the Fourier transform amplitude and estimating the pupil radius.

imaging system is not aliased, which is necessary for high-quality results, since aliasing artifacts distort high-resolution features at focus. Therefore, it is practically better to ensure that the imaging system is not aliased, if possible.

Once the system is designed and built, the final system magnification and NA should be verified to check that the system has been properly aligned. The system magnification can be checked by imaging a USAF resolution target with on-axis illumination, as seen in Fig 2.5. The USAF target's resolution are given in terms of line pairs per millimeter ( $lpmm_{\text{USAF}}$ ) or, equivalently, line width  $w_{\text{USAF}}$  for each three-bar element of each group. The line pairs per millimeter  $lpmm_{\text{meas}}$  or line width  $w_{\text{meas}}$  at the camera for a set of elements within a group can be measured using knowledge of the camera pixel size  $d_{\text{cam}}$ . A white dotted line shows the potential for using horizontal elements 2-6 of group 8 in Fig. 2.5(a) for calibration. The system magnification  $mag$  will then be given by

$$mag = \frac{lpmm_{\text{USAF}}}{lpmm_{\text{meas}}} = \frac{w_{\text{meas}}}{w_{\text{USAF}}}. \quad (2.8)$$

It is best to take an average over many elements and line pairs to average out noise when calibrating the magnification, and preprocessing of the image can also be done to ensure that the USAF bars are perfectly horizontal and vertical before the magnification calibration. The objective NA can be verified by looking at the Fourier transform of the measured calibration image, as seen in Fig. 2.5(b). For on-axis illumination, the low-pass filtering by the objective lens will create a circular pass-band in the center of the image's Fourier transform magnitude. Note that either contrast-stretching or taking the log of the Fourier transform amplitude might be needed to view the circular pass-band. The radius of this circle in  $\mathbf{k}$ -space is given by  $2\pi NA_{\text{obj}}/\lambda$ . If the physical radius in the captured data is different than expected, there

may be misalignments in the system. In general, viewing the Fourier transform amplitude of measured images can be useful for debugging FPM systems.

Correct system operation can additionally be verified by reconstructing a high-resolution image of a USAF target using FPM by comparing the highest resolvable reconstruction features to the expected final system  $NA_{sys}$ . Different resolution criteria define the minimum resolvable line width  $r$ , all with some multiple of  $\frac{\lambda}{NA}$ . The Rayleigh criterion states  $r_{Rayleigh} = \frac{0.61\lambda}{NA}$ ; another commonly used value is the Abbe Resolution  $r_{Abbe} = \frac{\lambda}{2NA}$ . In practice, the highest resolution USAF element that can be discerned as three separate bars in the final reconstruction should have a line width  $w_{USAF}$  in the approximate range of  $r_{Rayleigh}$  and  $r_{Abbe}$ . If the system is not functioning well, there will usually be many artifacts and the finest line width that can be resolved will be much wider than these two resolution definitions.

## 2.3 FPM Reconstruction Methods

While the FPM optical system design and alignment is important to consider for system functionality and robustness, the reconstruction parameters are also important to consider. Background removal and object initialization are particularly important for high-quality reconstructions. Additionally, two computational models exist for implementations of the Fourier shift theorem, one involving cropping in the Fourier domain, the other involving multiplication by a phase ramp, resulting in different reconstruction artifacts. Practical considerations for these algorithmic design choices are discussed. The effect of vignetting inside the objective lens is also discussed, along with mechanisms for avoiding reconstruction vignetting artifacts. Another common source of error in FPM reconstructions is misestimation of the angles of illumination, which is separately addressed in Chapter 3.

### 2.3.1 Background Removal

Background removal is important for removing the effects of dark current noise and off-focus dust artifacts, as well as for normalization of background values across illumination angles to better match the forward model, which expects uniform illumination intensity across all angles. Two main methods for background removal are *background subtraction* and *background division*.

*Background subtraction* generally involves estimating the background dark current level from user-designated background regions in the captured darkfield images  $I_{raw}$ . Since there should be zero signal in the background regions of darkfield images, the average intensity of designated background regions,  $\text{mean}(I_{bk,region})$ , can be assumed to approximately equal the dark current noise level of the camera system under the measurement scheme. The background-subtracted intensity images are given by  $I_{sub} = I_{raw} - \text{mean}(I_{bk,region})$ , with  $I_{sub}$  set equal to 0 in all regions where  $(I_{raw} - \text{mean}(I_{bk,region})) < 0$ . Background subtraction is beneficial because it allows for correction of background without having to capture separate background frames and empirically provides more stable reconstructions; however, it does

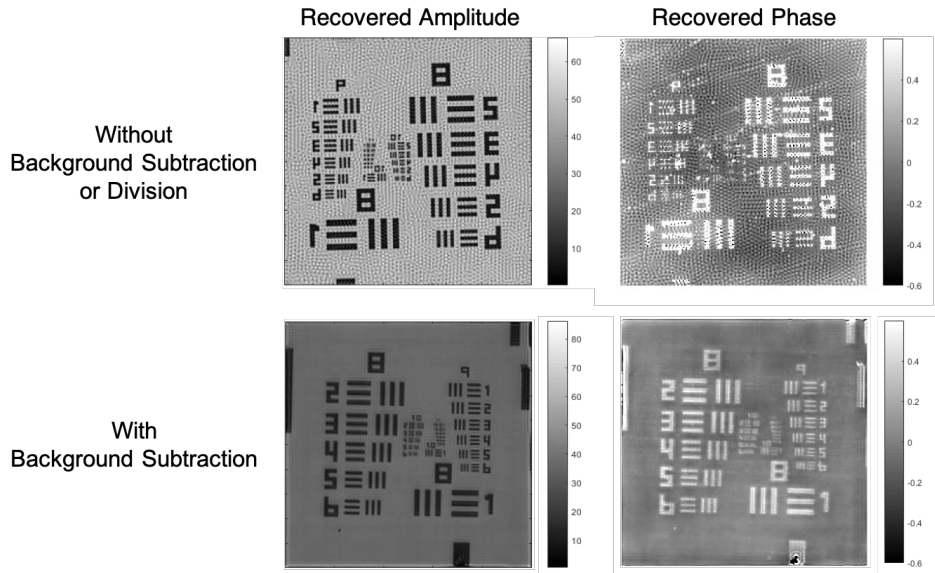


Figure 2.6: FPM artifacts due to improper background subtraction present as a high spatial frequency “dimpling” of both the object amplitude and phase (top row). With proper background subtraction parameters, the reconstruction background is smooth (bottom row).

not account for illumination intensity variation or off-focus dust artifacts and leads to incorrect scaling of jointly recovered pupil phases, as discussed below. Common reconstruction artifacts due to improper background subtraction appear as high-spatial frequency dimpling of the reconstruction as seen in Fig. 2.6.

*Background division* instead requires that a separate set of background images,  $I_{bk,images}$  be captured across all illumination angles. The background-divided images are given by a pointwise division of the data measurements by the background measurements,  $I_{div} = I_{raw}/I_{bk,images}$ . This has the benefit of accounting for intensity illumination variation and off-focus dust artifacts, as well as correct scaling of the recovered pupil phase. However, it is inaccurate and unstable for darkfield images and, experimentally, has less stable FPM reconstructions than images processed using background subtraction.<sup>4</sup>

### 2.3.2 Initialization

As FPM is a nonlinear optimization algorithm, there are many local minima that satisfy the minimization algorithm given by Eq. 2.4 but that may not represent the best possible object reconstruction at the optimization problem’s global minimum. In order to reconstruct objects with local minima near the global minimum, the object  $O(\mathbf{r})$  must be properly

<sup>4</sup>That is, the FPM algorithm diverges more often when the background division method is used, though still converges a majority of the time.

initialized. The simplest method is to initialize the object as a *constant value* with unity amplitude and zero phase; however, this may take longer to converge to a good solution or may lead to less desirable minima. The *average over all measurements* might be taken as the object amplitude, again with zero phase. This method effectively initializes the object to a low-contrast version of the final high-resolution reconstruction. However, if the majority of measurements are darkfield, this method will bias the initial background value to be too low. The *on-axis image* might also be taken as the object amplitude with zero phase, providing a decent initialization of the object's low-resolution features. This will not include the high-resolution information gained by averaging all measurements, but will no longer face biases of the background due to the darkfield measurements. All of these methods are suitable for objects that are expected to be primarily amplitude objects, since they initialize the phase to a constant zero value.

Alternatively, a *differential phase contrast (DPC)* algorithm [216] can initialize both the object amplitude and phase to non-constant values, providing by far the best initialization for phase-only objects [41]. DPC measurements are taken with partially incoherent half-circles of illumination and so can be synthesized from the individual coherent measurements of FPM. The synthesized DPC measurements are created by summing the FPM measurements whose angles of illumination are in the top ( $NA_y > 0$ ), bottom ( $NA_y \leq 0$ ), left ( $NA_x > 0$ ), and right ( $NA_x \leq 0$ ) half planes of the illumination angle space. These measurements are then processed with the linear DPC reconstruction algorithm given in [216] to return an initial object amplitude and phase for FPM. This initialization method provides more consistent and stable FPM reconstructions for phase-only objects.

All of these initialization schemes will produce an initial object that is the same image size and pixel pitch as the measured data (*i.e.*,  $[N_{im} \times N_{im}]$  pixels), rather than the larger image size (and smaller pixels) of the higher-resolution reconstruction. Therefore, all of these images must be upsampled to the system reconstruction size  $[N_{sys} \times N_{sys}]$  pixels. All methods of upsampling introduce artifacts into the initialization that can affect the reconstruction. The preferred method of upsampling is by padding the Fourier transform of the initialization with zeros to the correct image size, then inverse Fourier transforming to retrieve the upsampled image. While this also introduces initialization artifacts, they generally exhibit fewer artifacts than other upsampling methods.

### 2.3.3 Crop- and Phase Ramp-Based Fourier Shift

Fourier ptychography relies upon the Fourier shift theorem, whereby a phase ramp (*i.e.*, an angled plane wave) applied in the image domain corresponds to a coordinate shift in the Fourier transform domain (*i.e.*, the shift of the object's spectrum in the imaging system's pupil plane), as discussed above. In the FPM algorithm, this Fourier shift can be represented in one of two ways: 1) by directly applying a phase ramp at each given illumination angle in image space, or 2) by shifting the Fourier transform of the intensity image by the amount dictated by the angle of illumination. The latter method is shown in Algorithm 1.

While both of these reconstruction algorithms can create impressive results, their reconstruction artifacts will differ from each other, even with the same input data and initialization. The phase ramp-based method generally has more low-spatial frequency artifacts and edge artifacts due to the circular boundary conditions of the computationally efficient FFT implementation of a Fourier transform. Therefore, the shift-based algorithm is generally preferred, as it explicitly enforces integer pixel shifts of the spectrum, which eliminates many of these FFT boundary condition-based artifacts.

### 2.3.4 Vignetting

Vignetting is an imaging artifact due to natural and opto-mechanical mechanisms that result in high-angle light beams being attenuated and potentially physically blocked in an optical system. In systems with incoherent illumination, such as photographic cameras, this manifests as lower intensity light at the edge of the field of view, also called “light fall-off” [2]. Natural vignetting results in a  $\cos^4(\theta)$  illumination intensity fall-off across light angle  $\theta$  due to three sources. The angled projection of high-angle light onto the lens and the camera sensor planes each contribute a  $\cos(\theta)$  fall-off term. High-angle light additionally propagates a longer distance inside the lens system, contributing an additional  $\cos^2(\theta)$  fall-off term [223].<sup>5</sup> Opto-mechanical vignetting occurs due to blockage of the light inside the lens system, where a portion of the high-angle light beam falls outside of the projection of the aperture stop, and thus a portion of the light is clipped [2, 223].

Low-cost objective lenses are typically built to work in traditional microscopes, where a condenser lens directs wide-field, incoherent light at illumination angles up to and beyond the objective NA onto the sample, which is imaged by the objective lens. In this case, vignetting appears as a gradual fall-off of intensity at the edge of the field of view. While this intensity fall-off is a metric in the objective lens design process, it is difficult and expensive to achieve a flat intensity across an objective’s entire field of view. For FPM systems, where angled coherent plane-wave illumination is used instead of incoherent illumination, this means that the angles of illumination near the objective NA,  $NA_{illum,i} \approx NA_{obj}$ , will generally be vignetted in most commonly used objective lenses. We can therefore see significant opto-mechanical vignetting in angles near the objective NA in typical FPM systems, as seen in Fig. 2.7.

While natural vignetting can be accounted for in FPM by including the  $\cos^4(\theta)$  fall-off term in forward model’s light intensity for each illumination angle, opto-mechanical vignetting is not so easily accounted for. By definition, vignetting clips the optical ray at a separate plane from the system pupil plane, so can be thought of as applying an angle-dependent amplitude filter at a partial Fourier transform plane. Fresnel-diffraction based

---

<sup>5</sup>We note that  $\cos^4(\theta)$  is an approximation, since the angle of light incident upon the lens,  $\theta_{lens}$ , will generally be different than the angle incident upon the camera sensor plane,  $\theta_{sensor}$ . With this, the natural fall-off term is closer to  $\cos(\theta_{lens}) \cos^3(\theta_{sensor})$ , assuming the angle of light inside the camera  $\approx \theta_{sensor}$ . However, since  $\theta_{lens}$  is generally small for normal camera lenses, and thus  $\theta_{lens} \approx \theta_{sensor}$ ,  $\cos^4(\theta)$  is usually a good approximation [223].

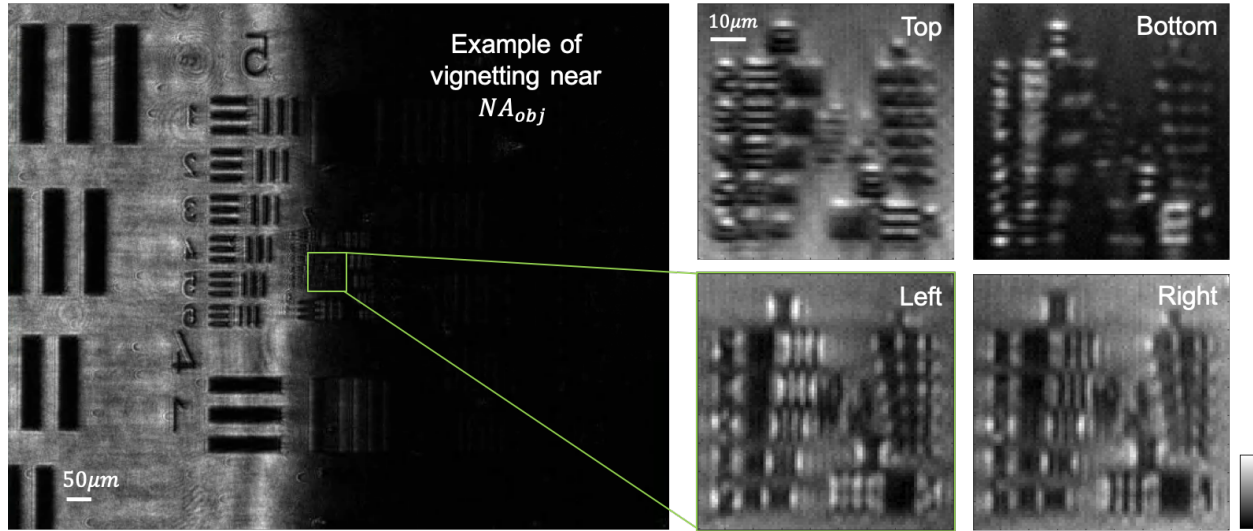


Figure 2.7: Example vignettted images when  $NA_{illum,i} \approx NA_{obj}$ . Overall vignetting is easy to see in large field of view image (left image), but appears as an average between a brightfield and darkfield image in the small, reconstruction field of view (right images). Example vignettted small field of views are shown for illumination angles from the system’s top, bottom, left, and right.

methods have been proposed to deal with this problem in FPM reconstructions [161]. However, this is not computationally simple to model, especially because the objective lens designs are usually proprietary and therefore unavailable for modeling the precise location of vignetting planes. This makes it more difficult to develop a simpler vignetting model for use inside the FPM reconstruction. Therefore, we must use more heuristic methods for dealing with this system nonideality.

In Fig. 2.8, we present several processing options to account for vignetting in FPM systems. Without accounting for the vignetting, the reconstruction has many artifacts due to the model mismatch in the vignettted images. Since vignetting results in low-spatial frequency mismatch in the measured images (*i.e.*, the background intensity is lower than expected), the reconstruction artifacts are low-spatial frequency ripples in the background of the amplitude and phase reconstructions. Judging by the lack of low-spatial frequency reconstruction artifacts, the two best methods for dealing with the vignetting are to 1) exclude vignettted images and 2) use the joint pupil calibration algorithm described above [156] with a slightly larger effective objective NA support,  $NA_{obj, eff} \approx NA_{obj} + 0.015$ , where the additional 0.015 is a heuristically chosen value. In this second option, the pupil amplitude will be updated to weight the high-NA angle images appropriately, self-calibrating away the vignetting artifacts, though we note that this means the reconstructed pupil amplitude will no longer strictly describe the physical system pupil, since it will include additional vignetting model

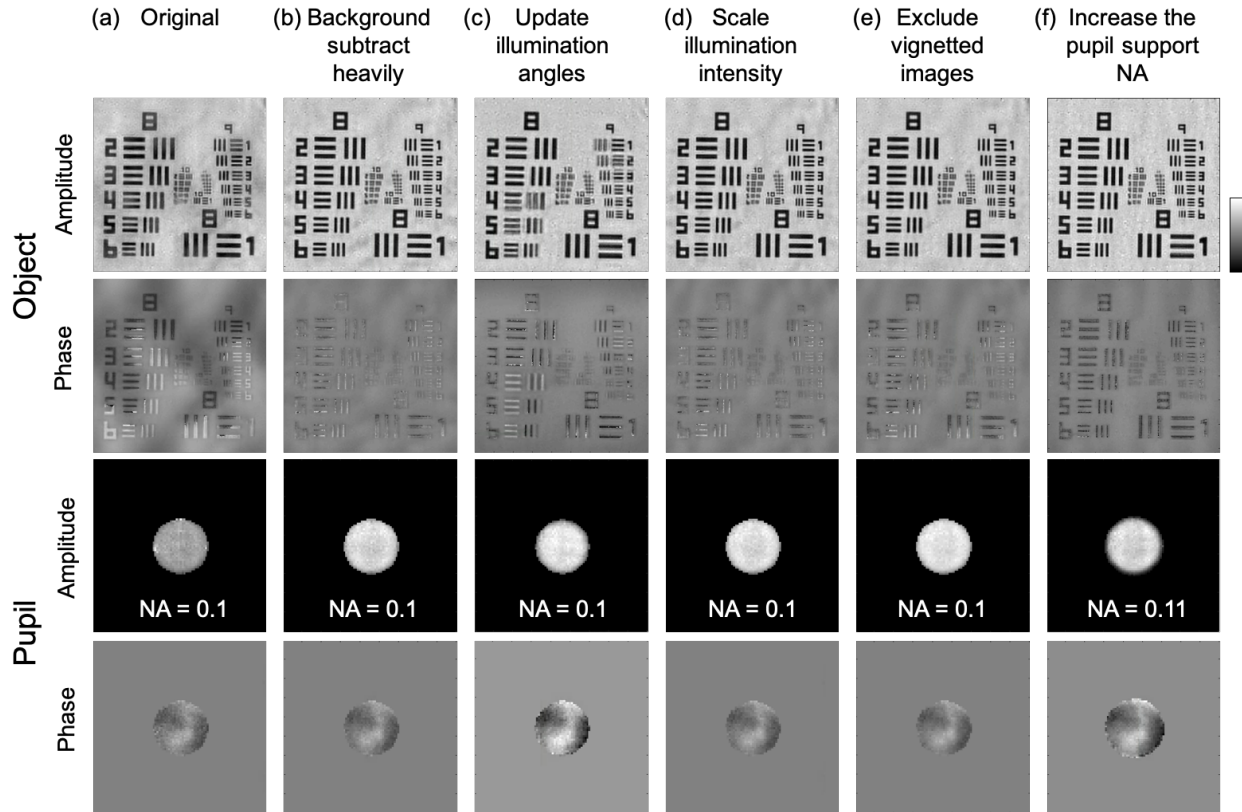


Figure 2.8: Methods for correcting for vignetting in FPM. (a) Vignetting causes low spatial frequency artifacts. (b) Heavy background subtraction, (c) dynamic updating of the illumination angles, and (d) heuristically scaling the illumination intensity corrects for some of the artifacts, but still has problems. (e) Excluding the vignetted images and (f) increasing the pupil support NA in the reconstruction (in tandem with joint pupil estimation) correct for the vignetting best. The joint reconstructed complex object and pupil are shown for all methods.

mismatch.

Additional methods for accounting for system vignetting include: 3) heavily background subtracting the vignetted images, effectively making them darkfield images; 4) allowing the illumination angles to be updated inside the algorithm, which allows the algorithm to “move” the angles to a pupil location with the appropriate weighting; and 5) heuristically modeling the reduced illumination intensity for the vignetted images, accounting for the lower background. All of these are shown in Fig. 2.8. All reconstructions shown included a joint pupil estimation step, which often results in improved reconstructions since it increases the degrees of freedom in the reconstruction. However, both the third and fourth options introduce significant model mismatch of their own, and the fifth would ideally include a separate algo-

rithm to model and calibrate the illumination intensity under vignetting. Therefore, these options do not work as well as the first two mentioned options in correcting for vignetting in FPM reconstructions.

## 2.4 Joint Pupil Reconstruction

Joint estimation of system pupil via the EPRY algorithm [156] is often essential for high-quality FPM object reconstructions. We note here and in Chapter 5 that accurate pupil recovery can be equally useful for microscopy applications as FPM’s recovery of high-resolution information, as the pupil recovery enables novel lens design [4, 96] and expedites deconvolution methods for fluorescence imaging [40, 202]. We present validation of pupil recovery via FPM using a system with a phase spatial light modulator (SLM) in the conjugate Fourier plane of an FPM system shown in Fig. 5.1. We show that the system pupil phase recovered via FPM has high fidelity to displayed phase values on the SLM.

The system uses a 50  $\mu\text{m}$  fiber-coupled LED source (Thorlabs M530F2) with wavelength  $\lambda = 530\text{ nm}$  which is beam-expanded and collimated by a 0.1 NA objective, as seen in Fig. 5.1. A mirror mount with a single rotation axis is driven by DC servo motors to steer the collimated beam in  $\theta_x$  and  $\theta_y$  at a conjugate imaging plane. The angled beam is relayed through a dual-objective system with 0.8 NA,  $50\times$ , working distance 1 mm objectives (Olympus M Plan Fluorite air objective, tube lens  $f = 180\text{ mm}$ ). A linear polarizer is placed close to the tube lens to linearly polarize the collimated light in the same direction as the SLM’s modulation axis. A 300 mm lens Fourier transforms the light between the imaging plane and the pupil plane at the LCOS SLM (Hamamatsu X13138-01) surface, where the pupil phase is displayed. The modulated light is reflected, Fourier transformed again by the 300 mm lens, and relayed by a beamsplitter (Thorlabs BS031) to the camera (PCO Edge 5.5), where the intensity image is measured. Calibration steps for the SLM phase are discussed in Sec. 5.4.1.

In order to jointly verify the SLM’s displayed phase and the FPM pupil reconstruction, we imaged and reconstructed well-understood planar phase objects with a DPC-initialized FPM algorithm. In these results, we imaged a phase USAF resolution target (Benchmark Technologies<sup>6</sup>, target #3). We first imaged the sample with the SLM displaying zero phase in order to recover the aberrations of the imaging objective, then imaged the sample with the random SLM patterns on different bases seen in Fig. 2.9(a). We ran the FPM algorithm described above for 250 iterations with a simple binary pupil support initialization for the pupil function  $\tilde{P}$  with *background subtracted* images to produce the initial pupil reconstruction  $\tilde{P}_{initial}$ . We then restarted the FPM algorithm, re-initializing the object with a DPC initialization and using *background divided* images. We initialized this second FPM reconstruction with a binary pupil support amplitude and the phase of the initial pupil reconstruction,  $\angle\tilde{P}_{initial} = \phi_{initial}$ , again running the algorithm for 250 iterations. We found

<sup>6</sup>See a detailed user report at <https://www.benchmarktech.com/sites/default/files/UserReport.pdf> [170].

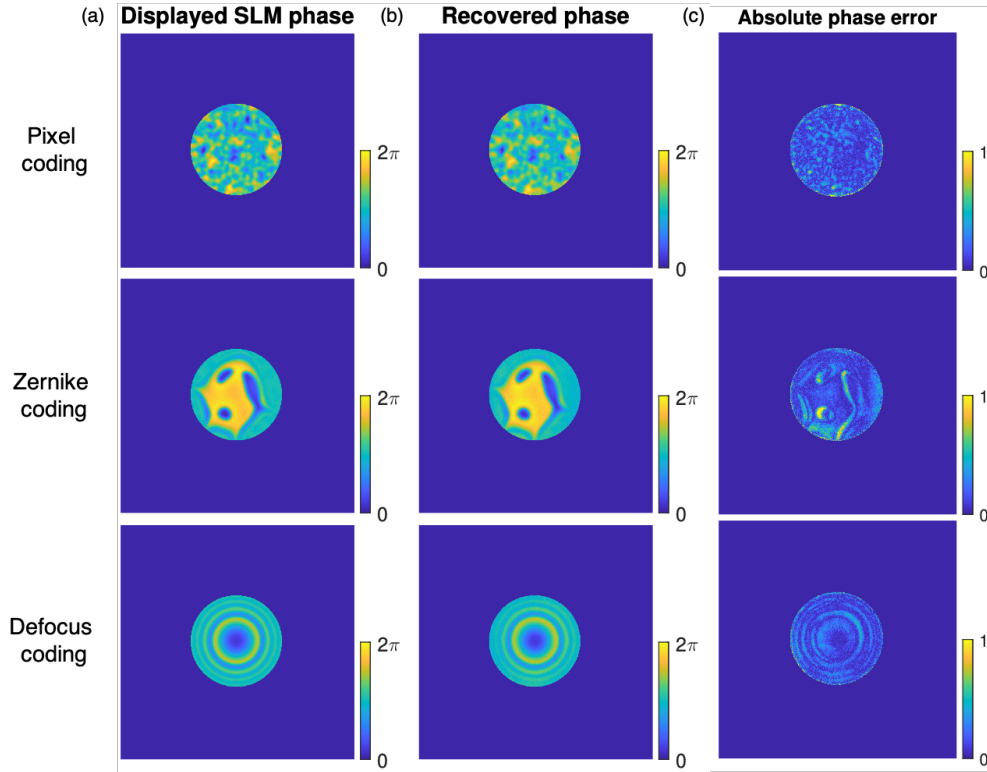


Figure 2.9: Verification of joint pupil estimation in FPM using a spatial light modulator (SLM) in the conjugate Fourier plane of the imaging system. The (a) expected, displayed phase on the SLM is compared to the (b) recovered pupil phase from an FPM reconstruction of a phase resolution target with joint pupil estimation. (c) RMSE maps are shown comparing the recovered to the expected pupil phase.

that the initial *background subtracted* step provided reconstruction stability, giving a good initial estimation for the pupil phase, while the *background divided* reconstruction gave highly accurate pupil phase values  $\tilde{P}_{recon}$  when compared to the expected results.

The reconstructed pupil phase without SLM coding,  $\phi_{recon, no\ coding}$ , represents the objective lens aberrations. We subtracted this lens aberration phase from the reconstructed pupil phases with SLM coding, giving  $\phi_{final} = \phi_{recon, SLM\ coding} - \phi_{recon, no\ coding}$ . The final reconstructed phase values  $\phi_{final}$  are shown in Fig. 2.9(b). We see that the reconstructed FPM phase results match the expected SLM phase values well with low absolute phase errors, as shown in Fig. 2.9(c). These results suggest that the FPM pupil recovery can be highly accurate and a useful tool for imaging system calibration.

## Chapter 3

# Efficient Illumination Angle Self-Calibration in Fourier Ptychography

Fourier ptychography captures intensity images with varying source patterns (illumination angles) in order to computationally reconstruct large space-bandwidth-product images. Accurate knowledge of the illumination angles is necessary for good image quality; hence, calibration methods are crucial, despite often being impractical or slow. Here, we propose a fast, robust and accurate self-calibration algorithm that uses only experimentally-collected data and general knowledge of the illumination setup.<sup>1</sup> First, our algorithm makes a fast direct estimate of the brightfield illumination angles based on image processing. Then, a more computationally-intensive spectral correlation method is used inside the iterative solver to further refine the angle estimates of both brightfield and darkfield images. We demonstrate our method for correcting large and small misalignment artifacts in both 2D and 3D Fourier ptychography with different source types: an LED array, a galvo-steered laser, and a high-NA quasi-dome LED illuminator.

Self-calibration is a useful principle for designing robust optical systems. Self-calibration algorithms retrieve important system parameters directly from the measured data, rather than requiring additional pre-calibration procedures that are vulnerable to system instabilities over time. The illumination angle self-calibration algorithm presented in this chapter has enabled multiple novel optical systems to be used for FPM [4, 96, 173], for intensity-only ODT [36], and for novel aberration correction methods [76]. This work shows the importance of considering the inclusion of self-calibration algorithms when designing robust

---

<sup>1</sup>Chapter 3 represents work done in collaboration with Zachary F. Phillips. It is primarily drawn from [56] Regina Eckert, Zachary F. Phillips, and Laura Waller, "Efficient illumination angle self-calibration in Fourier ptychography," *Appl. Opt.* 57, 5434-5442 (2018). The work was initially published as a conference paper [57] Regina Eckert, Lei Tian, and Laura Waller, "Algorithmic self-calibration of illumination angles in Fourier ptychographic microscopy," in *Imaging and Applied Optics 2016*, OSA Technical Digest (online) (Optical Society of America, 2016), paper CT2D.3.

computational imaging systems.

### 3.1 Introduction

Computational imaging leverages the power of both optical hardware and computational algorithms to reconstruct images from indirect measurements. In optical microscopy, programmable sources have been used for computational illumination techniques including multi-contrast [133, 241], quantitative phase [29, 216, 217, 240] and super-resolution [53, 158, 218, 219, 240]. Implementation is simple, requiring only an inexpensive source attachment for a commercial microscope. However, these methods are also sensitive to experimental misalignment errors and can suffer severe artifacts due to model mismatch. Extensive system calibration is needed to ensure that the inverse algorithm is consistent with the experimental setup, which can be time- and labor-intensive. This often requires significant user expertise, making the setup less accessible to reproduction by non-experts and undermining the simplicity of the scheme. Further, pre-calibration methods are not robust to changes in the system (e.g. bumping the setup, changing objectives, sample-induced aberrations) and require precise knowledge of a ground-truth test object.

Algorithmic self-calibration methods [16, 17, 40, 54, 57, 89, 130, 137, 156, 160, 194, 210, 214, 233, 238] eliminate the need for pre-calibration and precise test objects by making calibration part of the inverse problem. These methods jointly solve two inverse problems: one for the reconstructed image of the object and the other for the calibration parameters. By recovering system calibration information directly from captured data, the system becomes robust to dynamic changes in the system.

Here, we focus on *illumination angle* self-calibration for Fourier Ptychographic Microscopy (FPM) [240]. FPM is a coherent computational imaging method that reconstructs high-resolution amplitude and phase across a wide field-of-view (FoV) from intensity images captured with a low-resolution objective lens and a dynamically-coded illumination source. Images captured with different illumination angles are combined computationally in an iterative phase retrieval algorithm that constrains the measured intensity in the image domain and pupil support in the Fourier domain. This algorithm can be described as stitching together different sections of Fourier space (synthetic aperture imaging [50, 221]) coupled with iterative phase retrieval. FPM has enabled fast *in vitro* capture via multiplexing [218, 219], fluorescence imaging [40], and 3D microscopy [88, 215]. It requires significant redundancy (pupil overlap) in the dataset [53, 212], making it suitable for joint estimation self-calibration.

Self-calibration routines have previously been developed to solve for pupil aberrations [89, 156, 214], illumination angles [130, 137, 210, 233, 238], LED intensity [17], sample motion [16], and auto-focusing [54] in FPM. The state-of-the-art self-calibration method for illumination angles is simulated annealing [210, 233], a joint estimation solution which (under proper initialization) removes LED misalignment artifacts that usually manifest as low-frequency noise. Unfortunately, because the simulated annealing procedure operates inside the FPM algorithm iterative loop, it slows the run-time of the solver by an order of magni-

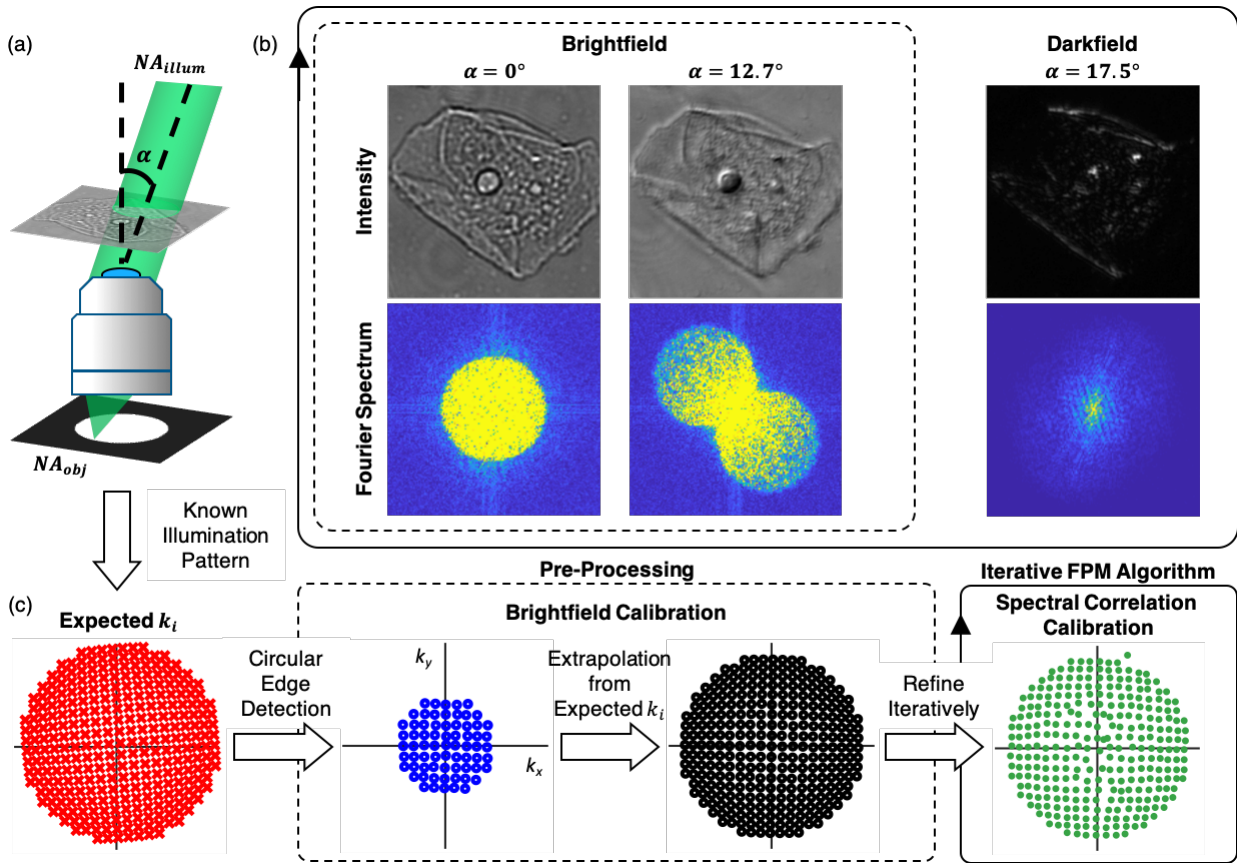


Figure 3.1: Illumination angles are calibrated by analyzing Fourier spectra. (a) A cheek cell is illuminated at angle  $\alpha$  and imaged with  $NA_{obj}$ . (b) Brightfield images contain overlapping circles in their Fourier spectra; darkfield images do not. (c) We perform a fast and efficient brightfield calibration in pre-processing, then extrapolate the correction to darkfield images and, finally, iteratively calibrate angles inside the FPM algorithm using a spectral correlation calibration.

tude or more. For 3D FPM (which is particularly sensitive to angle calibration [215]), the computational costs become infeasible.

Moreover, most self-calibration algorithms require a relatively close initial guess for the calibration parameters. This is especially true when the problem is non-convex or if multiple calibration variables are to be solved for (*e.g.* object, pupil, and angles of illumination). Of the relevant calibration variables for FPM, illumination angles are the most prone to error, due to shifts or rotations of the LED array [78], source instabilities [57, 111], non-planar illuminator arrangements [41, 173, 172, 198], or sample-induced aberrations [86, 101]. Sample-induced aberrations can also change the effective illumination angles dynamically, such as when the sample is in a moving aqueous solution.

We propose here a two-pronged angle self-calibration method that uses both pre-processing (*brightfield calibration*) and iterative joint estimation (*spectral correlation calibration*) that is quicker and more robust to system changes than state-of-the-art calibration methods. A circle-finding step prior to the FPM solver accurately identifies the angles of illumination in the brightfield (BF) region. A transformation between the expected and BF calibrated angles extrapolates the correction to illuminations in the darkfield (DF) region. Then, a local grid-search-based algorithm inside the FPM solver further refines the angle estimates, with an optional prior based on the illuminator geometry (Fig. 3.1). Our method is object-independent, robust to coherent noise, and time-efficient, adding only seconds to the processing time. We demonstrate on-line angle calibration for 2D and 3D FPM with 3 different source types: an LED array, a galvanometer-steered laser, and a high-NA ( $\max NA_{illum} = 0.98$ ) quasi-dome illuminator [173].

## 3.2 Methods

The image formation process for a thin sample under off-axis spatially coherent plane wave illumination can be described by:

$$I_i(\mathbf{r}) = |O(\mathbf{r})e^{-j\mathbf{k}_i\mathbf{r}} * P(\mathbf{r})|^2 = |\mathcal{F}^{-1}(\tilde{O}(\mathbf{k} - \mathbf{k}_i)\tilde{P}(\mathbf{k}))|^2, \quad (3.1)$$

where  $\mathbf{k}_i$  is the spatial frequency of the incident light,  $\tilde{P}(\mathbf{k})$  is the system pupil function,  $\tilde{O}(\mathbf{k})$  is the object Fourier spectrum, and  $\mathcal{F}$  is the 2D Fourier transformation operation, valid for shift-invariant systems. Intensity images are captured at the sensor plane, corresponding to auto-correlation in the Fourier domain:

$$\begin{aligned} \tilde{I}_i(\mathbf{k}) &= \mathcal{F}(|O(\mathbf{r})e^{-j\mathbf{k}_i\mathbf{r}} * P(\mathbf{r})|^2) \\ &= \tilde{O}(\mathbf{k} - \mathbf{k}_i)\tilde{P}(\mathbf{k}) \star \tilde{O}(\mathbf{k} - \mathbf{k}_i)\tilde{P}(\mathbf{k}), \end{aligned} \quad (3.2)$$

where  $*$  denotes convolution and  $\star$  denotes auto-correlation.  $\tilde{O}(\mathbf{k} - \mathbf{k}_i)\tilde{P}(\mathbf{k})$  corresponds to the shifted spectrum of the object within the circle  $|\mathbf{k}| \leq \frac{2\pi NA_{obj}}{\lambda}$  and 0 everywhere else. The auto-correlation operation essentially scans two copies of  $\tilde{O}(\mathbf{k} - \mathbf{k}_i)\tilde{P}(\mathbf{k})$  across each other, coherently summing at each shift to give  $\tilde{I}_i(\mathbf{k})$ . Typically, the object spectrum has a large zero-order (DC) term that decays sharply towards higher frequencies. In the brightfield region, when the DC term at  $\mathbf{k}_i$  is within the pupil's passband, the auto-correlation effectively scans this DC term across the conjugate spectrum, giving high values where the DC term overlaps with the conjugate pupil and negligible signal elsewhere. This interference between the DC term and pupil in the auto-correlation creates two distinct circles centered at  $\mathbf{k}_i$  and  $-\mathbf{k}_i$  in the intensity spectrum amplitude (Fig. 3.1). Hence, we can calibrate the illumination angle by finding these circle centers. For darkfield images, the DC term is outside  $\frac{2\pi NA_{obj}}{\lambda}$  and so we do not observe clearly defined circles in  $|\tilde{I}_i|$  (Fig.3.1(b)), making calibration more complicated.

Our algorithm relies on analysis of the raw intensity Fourier transform to recover illumination angles. Fourier domain analysis of intensity images has been used previously to deduce aberrations [201] and determine the center of diffraction patterns [24, 43] for system calibration. We show here that the individual Fourier spectra can be used to accurately determine illumination angles in both the brightfield and darkfield regime.

### 3.2.1 Brightfield Calibration

Locating the center of the circles in the amplitude of a Fourier spectrum is an image processing problem. Previous work in finding circles in images uses the Hough transform, which relies on an accurate edge detector as an initial step [46, 235]. In practice, however, we find that edge detectors do not function well on our datasets due to speckle noise, making the Hough transform an unreliable tool for our purpose. Therefore, we propose a new method which we call *circular edge detection*.

Intuitively, circular edge detection can be understood as performing edge detection (*i.e.* calculating image gradients) along a circular arc around a candidate center point in  $k$ -space (the Fourier domain). To first approximation, we assume  $|\tilde{I}_i|$  is a binary function that is 1 inside the two circles and 0 everywhere else. Our goal is to find the strong binary edge in order to locate the circle center. We need only consider one of the circles, since the intensity image is real-valued and so its Fourier transform is symmetric. Based on information we have about our illumination set-up, we *expect* the illumination spatial frequency (and therefore circle center) for spectrum  $\tilde{I}_i$  to be at  $\mathbf{k}_{i,0} = (k_{x,i,0}, k_{y,i,0})$  (polar coordinates  $\mathbf{k}_{i,0} = (d_{i,0}, \theta_{i,0})$ ) (Fig. 3.2(a)). If this is the *correct* center  $\mathbf{k}'_i$ , we expect there to be a sharp drop in  $|\tilde{I}_i|$  at radius  $R$  along any radial line  $f(r, \phi_n)$  out from  $\mathbf{k}'_i$  (Fig. 3.2(b)). This amplitude edge will appear as a peak at  $r = R$  in the first derivative of each radial line with respect to  $r$ ,  $f'(r, \phi_n)$  (Fig. 3.2(d)). Here  $(r, \phi_n)$  are the polar coordinates of the radial line with respect to the center  $\mathbf{k}_i$ , considering the  $n^{\text{th}}$  of  $N$  radial lines.

We identify the correct  $\mathbf{k}'_i$  by evaluating the summation of the first derivative around the circular arc at  $r = R$  from several candidate  $\mathbf{k}_i = (d_i, \theta_i)$  positions:

$$E_1(R, d_i, \theta_i) = \sum_{n=1}^N f'(r = R, \phi_n, d_i, \theta_i). \quad (3.3)$$

When  $\mathbf{k}_i$  is incorrect, the edges do not align and the derivative peaks do not add constructively at  $R$  (Fig. 3.2(c)). The derivatives at  $R$  are all maximized *only* at the correct center  $\mathbf{k}'_i$  (Fig. 3.2(d)), creating a peak in  $E_1$  (Fig. 3.2(e)). This is analogous to applying a classic edge filter in the radial direction from a candidate center and accumulating the gradient values at radius  $R$ .

In order to bring our data closer to our binary image approximation, we divide out the average spectrum  $\text{mean}_i(|\tilde{I}_i|)$  across all  $i$  spectra. Because the object remains constant across images while the angles of illumination change, the average spectrum is similar in form to the object's auto-correlation spectrum, with a sharp central peak decaying towards

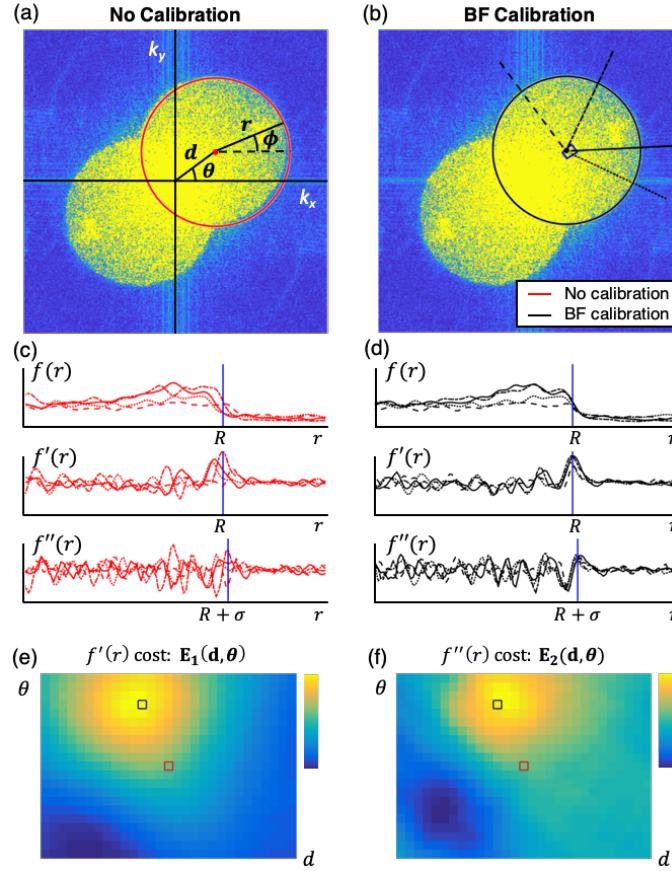


Figure 3.2: Circular edge detection on brightfield images finds circle centers, giving illumination angle calibration. (a,b) Comparison of uncalibrated (red) and calibrated (black) illumination  $\mathbf{k}_i$ . The blue box in (b) indicates the search range for  $\mathbf{k}_i$ . (c,d)  $\tilde{I}_i$  along radial lines,  $f(r, \phi_n)$ , and derivatives with respect to  $r$ . (e,f)  $E_1$  and  $E_2$ , sums of the derivatives at known radii  $R$  and  $R + \sigma$ , peak near the correct center. Boxes show uncalibrated (red) and calibrated (black)  $\mathbf{k}_i$  centers.

higher frequencies. The resulting normalized spectra contain near-constant circles on top of background from higher-order terms. We then convolve with a Gaussian blur kernel with standard deviation  $\sigma$  to remove speckle noise (Alg. 2.1-2). Experimentally, we choose  $\sigma = 2$  pixels, which balances blurring speckle noise and maintaining the circular edge. Under this model, the radial line  $f(r, \phi_n)$  from our correct center  $\mathbf{k}'_i$  can be modeled near the circular edge as a binary step function convolved with a Gaussian:

$$f(r, \phi_n, d'_i, \theta'_i) = \text{rect}\left(\frac{r}{2R}\right) * \frac{1}{\sqrt{2\pi}\sigma} e^{-\frac{r^2}{2\sigma^2}}. \quad (3.4)$$

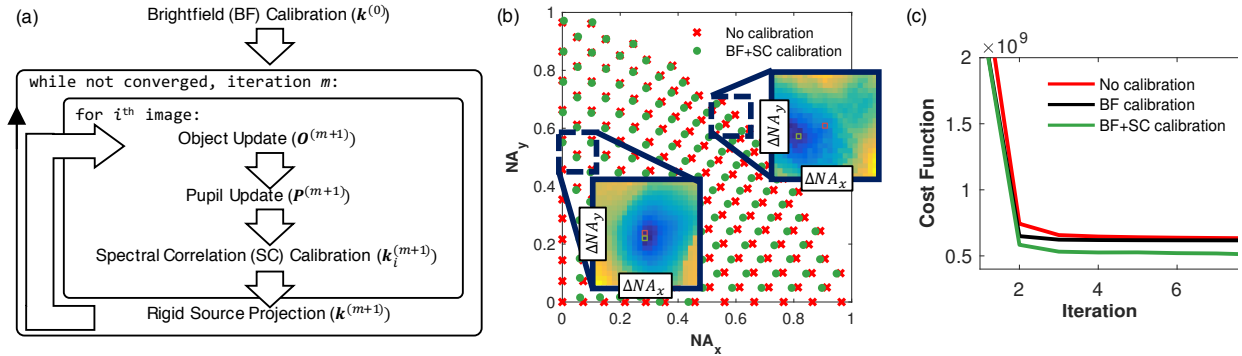


Figure 3.3: BF calibration uses a fast pre-processing step to estimate illumination angles, then SC calibration iteratively refines them within the FPM solver. (a) Algorithm block diagram, (b) uncalibrated (red) and BF + SC calibrated (green) illumination angle map. Insets are example search spaces, showing local convexity. (d) FPM convergence plot for different methods.

By differentiating through  $f'''(r, \phi_n)$  and setting equal to zero, we find the peak of  $f'(r, \phi_n)$  still occurs at  $r = R$ . Additionally, we find that the second derivative  $f''(r, \phi_n)$  has a maximum at  $r = R + \sigma$ . Experimentally, we have found that considering both the first *and* second derivatives increases our accuracy and robustness to noise across a wide variety of datasets. We therefore calculate a second derivative metric,

$$E_2(R + \sigma, d_i, \theta_i) = \sum_{n=1}^N f''(r = R + \sigma, \phi_n, d_i, \theta_i), \quad (3.5)$$

which is jointly considered with Eq. 3.3. We identify candidate centers  $\mathbf{k}_i$  that occur near the peak of *both*  $E_1$  and  $E_2$  (Fig. 3.2(e-f)), then use a least-squares error metric to determine the final calibrated  $\mathbf{k}'_i$  (Alg. 2.5-9). In practice, we also only consider the non-overlapping portion of the circle's edge, bounding  $\phi$ .

Until now, we have assumed that the precise radius  $R$  of the pupil is known. However, in pixel units,  $R$  is dependent on the pixel size of the sensor,  $p_s$ , and the system magnification,  $mag$ :

$$R = \frac{NA_{obj} p_s * M}{\lambda mag}, \quad (3.6)$$

as well as  $NA_{obj}$  and  $\lambda$ , where  $\tilde{I}_i$  is dimension  $M \times M$ . Given that  $mag$  and  $NA_{obj}$  are often imprecisely known but are unchanged across all images, we calibrate the radius by finding the  $R'$  which gives the maximum gradient peak  $E_1$  across multiple images before calibrating  $\mathbf{k}'_i$  (Alg. 2.3). A random subset of images may be used to decrease computation time.

**Algorithm 2** Brightfield Calibration

- 
- 1:  $\tilde{I}_f \leftarrow |\tilde{I}| / \text{mean}_i(|\tilde{I}_i|)$  ▷ Divide out mean spectrum
  - 2:  $\tilde{I}_f \leftarrow \text{gauss}(\tilde{I}_f, \sigma)$  ▷ Smooth speckle
  - 3:  $R' \leftarrow \text{argmax}_R E_1(R, d_i, \theta_i), \text{subset}(\tilde{I}_{f,i})$  ▷ Calibrate radius
  - 4: **for**  $i$  image **do** ▷ Circular edge detection
  - 5:      $\mathbf{k}_{i,1} \leftarrow (d_i, \theta_i)$  where  $E_1$  near max (within 0.1 std)
  - 6:      $\mathbf{k}_{i,2} \leftarrow (d_i, \theta_i)$  where  $E_2$  near max
  - 7:      $\mathbf{k}_i \leftarrow \mathbf{k}_{i,1} \cap \mathbf{k}_{i,2}$  ▷ Consider both metrics
  - 8:      $\mathbf{k}'_i \leftarrow \text{argmin}_{\mathbf{k}_i} \|I_i - \mathcal{F}(\tilde{I}_i \cdot \tilde{P}(\mathbf{k} - \mathbf{k}_i))\|_2$  ▷ Evaluate  $\mathbf{k}_i$
  - 9: **end for**
  - 10:  $A, i_{\text{outliers}} \leftarrow \text{RANSAC}(A = \mathbf{k}'_i / \mathbf{k}_{i,0})$  ▷ Identify outliers
  - 11:  $\mathbf{k}_{\text{inliers}}^{(0)} \leftarrow \mathbf{k}'_{\text{inliers}}$  ▷ Initialize for FPM
  - 12:  $\mathbf{k}_{\text{outliers}}^{(0)} \leftarrow A \mathbf{k}_{\text{outliers},0}$
  - 13:  $\mathbf{k}_{\text{darkfield}}^{(0)} \leftarrow A \mathbf{k}_{\text{darkfield},0}$
- 

Finally, once all images are calibrated, we want to remove outliers and extrapolate the correction to the darkfield images. Outliers occur due to: 1) little high-frequency image content and therefore no defined circular edge; 2) strong background; or 3) shifts such that the conjugate circle center  $-\mathbf{k}_i$  is identified as  $\mathbf{k}'_i$ . In these cases, we cannot recover the correct center based on a single image and must rely on the overall calibrated change in the illuminator’s position. We find outliers based on an illuminator-specific transformation  $A$  (*e.g.*, rigid motion) between the expected initial guess of circle centers  $\mathbf{k}_{i,0}$  (*e.g.*, the LED array map) and the calibrated centers  $\mathbf{k}'_i$  using a RANSAC-based method [91]. This transformation is used to correct outliers and darkfield images (Alg. 2.10-13), serving as an initialization for our spectral correlation (SC) method.

### 3.2.2 Spectral Correlation Calibration

While the brightfield (BF) calibration method localizes illumination angles using intrinsic contrast from each measurement, this contrast is not present in high-angle (darkfield) measurements (Fig. 3.1(b)). Therefore, we additionally solve a more general joint estimation problem to refine the initialization provided by BF calibration, where the object  $O(\mathbf{r})$ , pupil  $P(\mathbf{k})$ , and illumination angles  $\mathbf{k}_i$  are optimized within the FPM algorithm. At each inner iteration, we estimate the  $i^{\text{th}}$  illumination angle by minimizing the FPM objective function with respect to illumination angle (Fig. 3.3(a)). This step finds the relative k-space location of the current spectrum  $\tilde{I}_i$  relative to the overall object, providing an estimate  $\mathbf{k}_i^{(m)}$  relative

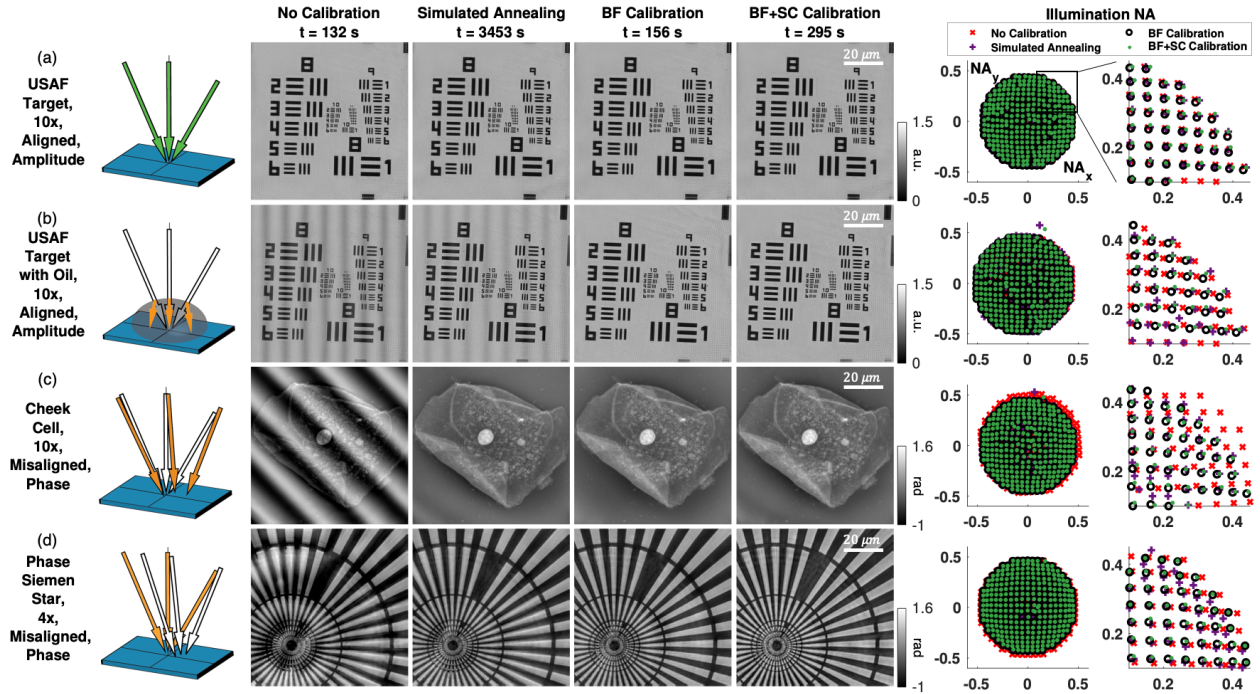


Figure 3.4: Experimental results with an LED array microscope, comparing reconstructions with no calibration (average reconstruction time 132 seconds), simulated annealing (3453 s), our BF calibration (156 s), and our BF + SC calibration (295 s). (a) Amplitude reconstructions of a USAF target in a well-aligned system. (b) Amplitude reconstructions of the same USAF target with a drop of oil placed on top of the sample to simulate sample-induced aberrations. (c) Phase reconstructions of a human cheek cell with computationally misaligned illumination, and (d) a Siemens star phase target with experimentally misaligned illumination.

to the other illuminator angles  $\mathbf{k}_j^{(m)}$ ,  $j \neq i$ . We call this the spectral correlation method because this optimization implicitly finds  $\mathbf{k}_i^{(m)}$  which best aligns the  $i^{\text{th}}$  spectrum with the estimated object spectrum  $\tilde{O}(\mathbf{k})^{(m)}$ .

Unlike previous joint estimation methods [210, 233], we constrain  $\mathbf{k}_i$  to exist on the k-space grid defined by the our image sampling. Our k-space resolution is band-limited by the size of the image patch,  $\mathbf{s} = (s_x, s_y)$ , across which the illumination can be assumed coherent. This coherent area size is determined by the van Cittert-Zernike theorem, which can be simplified [18] to show that the coherence length  $l_c$  of illumination with mean source wavelength  $\bar{\lambda}$  produced by a source of size  $\rho$  at a distance  $R$  is determined by:

$$l_c = \frac{0.61R\bar{\lambda}}{\rho}. \quad (3.7)$$

For example, a 300  $\mu\text{m}$  wide LED placed 50 mm above the sample with  $\bar{\lambda} = 530 \text{ nm}$  gives  $l_c = 53.8 \mu\text{m}$ , which provides an upper bound on the size of image patch used in the FPM reconstruction,  $(s_x, s_y) \leq l_c$ . This limitation imposes a minimum resolvable discretization of illumination angles  $\Delta\mathbf{k} = 2\pi\frac{2}{s}$  due to the Nyquist criterion. Since we cannot resolve finer angle changes, we need only perform a local grid search over integer multiples of  $\Delta\mathbf{k}$ , which makes our joint estimation SC method much faster than previous methods.

SC calibration is cast as an iterative optimization of discrete perturbations of the estimated angle using a local grid search. At each FPM iteration, we solve for the optimal perturbation of illumination angle  $\mathbf{k}_i^{(m)}$  over integer multiples  $\mathbf{n} = (n_x, n_y)$  of k-space resolution-limited steps  $\Delta\mathbf{k}$  such that the updated illumination position  $\mathbf{k}_i^{(m+1)} = \mathbf{k}_i^{(m)} + \mathbf{n} \cdot \Delta\mathbf{k}$  minimizes the  $\ell_2$  distance between the object and illumination angle estimates and measurements,

$$\begin{aligned} \underset{\mathbf{n}}{\operatorname{argmin}} \quad & \| |I_i - |O^{(m+1)} e^{-j(\mathbf{k}_i^{(m)} + \mathbf{n}\Delta\mathbf{k})\tilde{\mathbf{r}}} * P^{(m+1)}|^2 \|_2^2 \\ \text{subject to } \quad & \mathbf{n} = (n_x, n_y), \quad (n_x, n_y) \in [-1, 0, 1]. \end{aligned} \quad (3.8)$$

This grid search is performed iteratively within each sequential iteration of an FPM reconstruction until  $\mathbf{k}_i$  converges, giving a lower reconstruction cost than BF calibration alone (Fig. 3.3(b-c)).

The choice of  $\mathbf{n} = (n_x, n_y)$  to search can be tuned to match the problem. In most experimental cases, we find that a search of the immediate locality of the current estimate ( $(n_x, n_y) \in [-1, 0, 1]$ ) gives a good balance between speed and gradient performance when paired with the close initialization from our BF calibration. A larger search range (e.g.  $(n_x, n_y) \in [-2, -1, 0, 1, 2]$ ) may be required in the presence of noise or without a close initialization, but the number of points searched will increase with the square of the search range, causing the algorithm to slow considerably.

Including prior information about the design of the illumination source can make our calibration problem more well-posed. For example, we can include knowledge that an LED array is a rigid, planar illuminator in our initial guess of the illumination angle map,  $\mathbf{k}_{i,0}$ . By forcing the current estimates  $\mathbf{k}_i^{(m)}$  to fit a transformation of this initial angle map at the end of each FPM sub-iteration, we can use this knowledge to regularize our optimization (Fig. 3.3(a)). The transformation model used depends on the specific illuminator. For example, our quasi-dome LED array is composed of five circuit boards with precise LED positioning within each board but variable board position relative to each other. Thus, imposing an affine transformation from the angle map of each board to the current estimates  $\mathbf{k}_i^{(m)}$  significantly reduces the problem dimensionality and mitigates noise across LEDs, making the reconstruction more stable.

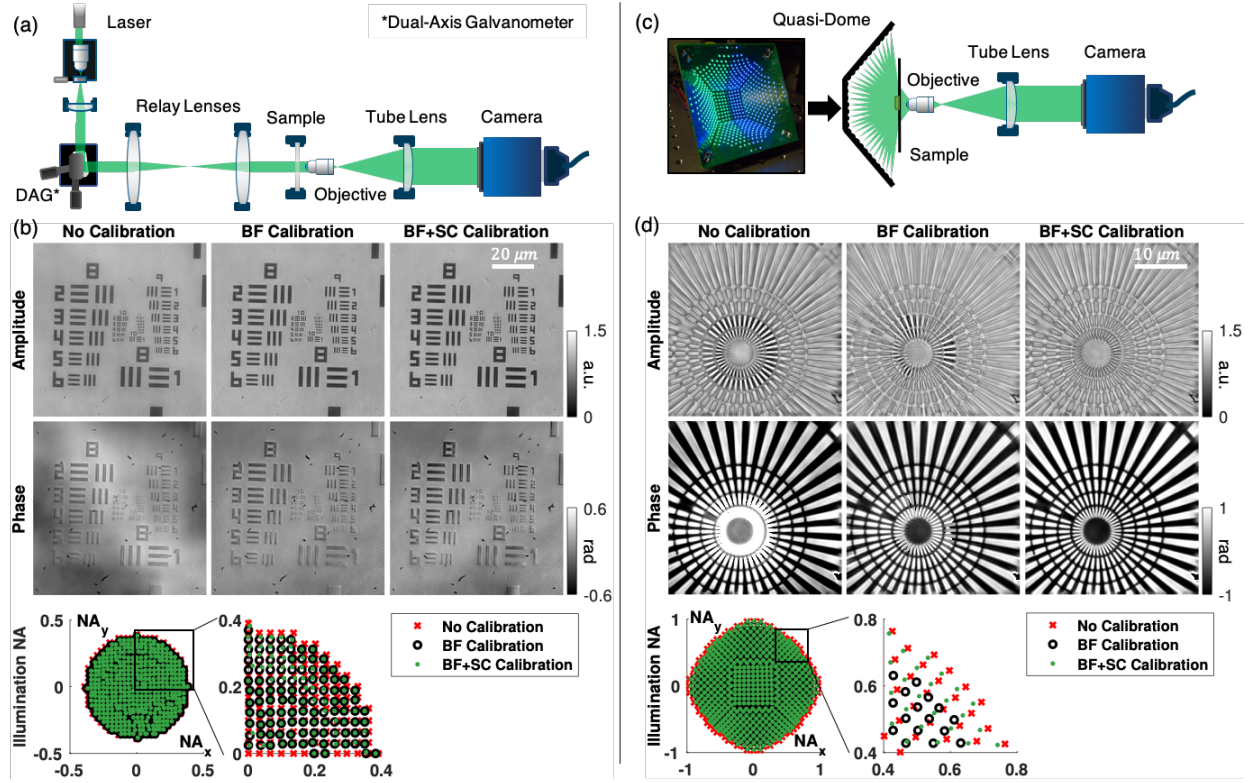


Figure 3.5: Experimental angle calibration in laser and high-NA quasi-dome illumination systems. (a) Laser illumination is steered by a dual-axis galvanometer. The angled beam is relayed to the sample by 4", 80 mm focal length lenses. (b) Our calibration method removes low-frequency reconstruction artifacts. (c) The quasi-dome illuminator enables up to 0.98  $NA_{illum}$  using programmable LEDs. (d) Our 1.23 NA reconstruction provides isotropic 425 nm resolution with BF + SC calibration.

## 3.3 Results

### 3.3.1 Planar LED Array

We first show experimental results from a conventional LED array illumination system with a  $10\times$ , 0.25 NA and a  $4\times$ , 0.1 NA objective lens at  $\lambda = 514\text{nm}$  and  $NA_{illum} \leq 0.455$  (Fig. 3.4). We compare reconstructions with simulated annealing, our BF pre-processing alone, and our combined BF+SC calibration method. All methods were run in conjunction with EPRY pupil reconstruction [156]. We include results with and without the SC calibration to illustrate that the BF calibration is sufficient to correct for most misalignment of the LED array since we can accurately extrapolate LED positions to the darkfield region when the LEDs fall on a planar grid. However, when using a low NA objective ( $NA_{obj} \leq 0.1$ ),

as in Fig. 3.4(d), the SC method becomes necessary because the BF calibration is only able to use 9 images (compared to 69 brightfield images with a  $10\times$ , 0.25 NA objective, as in Fig. 3.4(a-c)).

Our method is object-independent, so can be used for phase and amplitude targets as well as biological samples. All methods reconstruct similar quality results for the well-aligned LED array with the USAF resolution target (Fig. 3.4(a)). To simulate an aqueous sample, we place a drop of oil on top of the resolution target. The drop causes uneven changes in the illumination, giving low-frequency artifacts in the uncalibrated and simulated annealing cases which are corrected by our method (Fig. 3.4(b)). Our method is also able to recover a  $5^\circ$  rotation, 0.02 NA shift, and  $1.1\times$  scaled computationally-imposed misalignment on well-aligned LED array data for a cheek cell (Fig. 3.4(c)), and gives a good reconstruction of an experimentally misaligned LED array for a phase Siemens star (Benchmark Technologies, Inc.) (Fig. 3.4(d)). In contrast to simulated annealing, which on average takes  $26\times$  as long to process as FPM without calibration, our brightfield calibration only takes an additional 24 seconds of processing time and the combined calibration takes roughly only  $2.25\times$  as long as no calibration.

### 3.3.2 Steered Laser

Laser illumination can be used instead of LED arrays to increase the coherence and light efficiency of FPM [41, 111]. In practice, laser systems are typically less rigidly aligned than LED arrays, making them more difficult to calibrate. To verify the performance of our method, we constructed a laser-based FPM system using a dual-axis galvanometer to steer a 532 nm, 5 mW laser, which is focused on the sample by large condenser lenses (Fig. 3.5(a)). This laser illumination system allows finer, more agile illumination control than an LED array, as well as higher light throughput. However, the laser illumination angle varies from the expected value due to offsets in the dual-axis galvanometer mirrors, relay lens aberrations, and mirror position misestimations when run at high speeds. Our method can correct for these problems in a fraction of the time of previous methods (Fig. 3.5(b)).

### 3.3.3 Quasi-Dome

Since the FPM resolution limit is set by  $NA_{obj} + NA_{illum}$ , high-NA illuminators are needed for large space-bandwidth product imaging [173, 211]. To achieve high-angle illumination with sufficient signal-to-noise ratio in the darkfield region, the illuminators must become more dome-like, rather than planar [172]. We previously developed a novel programmable quasi-dome array made of five separate planar LED arrays that can illuminate up to 0.98 NA [173]. This device uses discrete LED control with RGB emitters ( $\bar{\lambda} = [475 \text{ nm}, 530 \text{ nm}, 630 \text{ nm}]$ ) and can be easily attached to most commercial inverted microscopes (Fig. 3.5(c)).

As with conventional LED arrays, we assume that the LEDs on each board are rigidly placed as designed. However, each circuit board may have some relative shift, tilt, or rotation since the final joining of the five boards is performed by hand. LEDs with high-angle

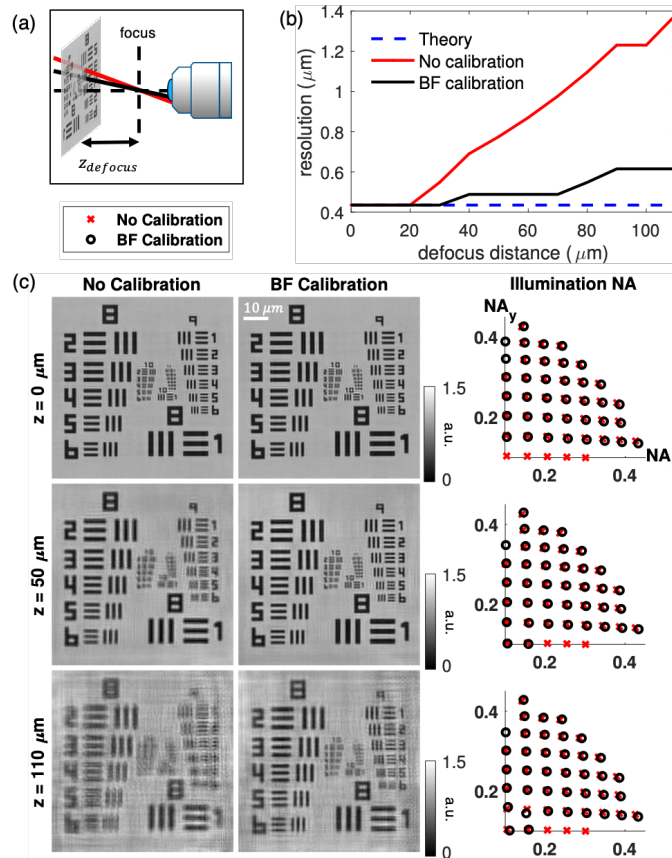


Figure 3.6: Even small calibration errors degrade 3D FPM resolution severely when defocus distances are large. (a) Experiment schematic for a USAF target placed at varying defocus distances. (b) Measured reconstruction resolution degrades with defocus distance; our calibration algorithm reduces this error significantly. (c) Amplitude reconstructions for selected experimental defocus distances, with and without calibration of the illumination angles.

incidence are both harder to calibrate and more likely to suffer from misestimation due to the dome geometry, so the theoretical reconstruction NA would be nearly impossible to reach without self-calibration. Using our method, we obtain the theoretical resolution limit available to the quasi-dome (Fig. 3.5(d)). The SC calibration is especially important in the quasi-dome case since it typically has many darkfield LEDs.

### 3.3.4 3D FPM

Calibration is particularly important for 3D FPM. Even small changes in angle become large when they are propagated to large defocus depths, leading to reduced resolution and reconstruction artifacts [57, 215]. For example, using a well-aligned LED array, [215] was

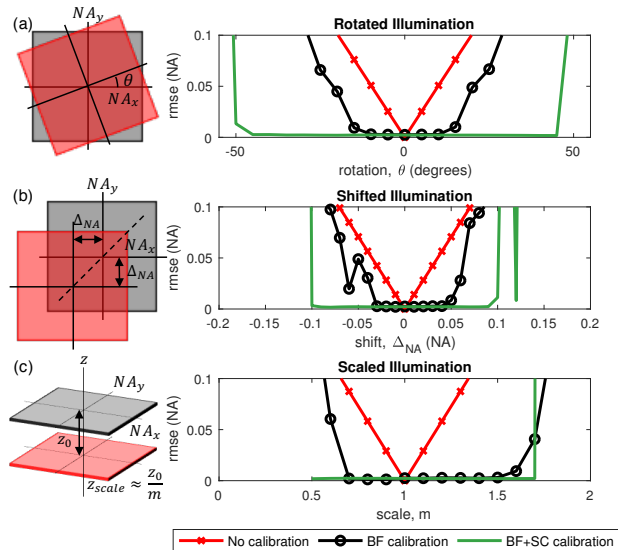


Figure 3.7: Our calibration methods are robust to large mismatches between estimated and actual LED array position. Simulation of misaligned illumination by (a) rotation, (b) shift, and (c) scale. Our calibration recovers the illumination with  $< 0.005$  NA error for rotations of  $-45^\circ$  to  $45^\circ$ , shifts of  $-0.1$  to  $0.1$  NA, and scalings of  $0.5\times$  to  $1.75\times$  before diverging.

unable to reconstruct high-resolution features of a resolution target defocused beyond  $30\ \mu\text{m}$  due to angle misestimation; using the same dataset, our method allows us to reconstruct high-resolution features of the target even when it is  $70\ \mu\text{m}$  off-focus (Fig. 3.6).

Since iterative angle estimation (including our SC calibration) unfeasibly increases the computational complexity of 3D FPM, we use BF calibration only. While we do not attain the theoretical limits for all defocus depths, we offer significant reconstruction improvement. Our calibration only slightly changes the angles of illumination (Fig. 3.6(c)), highlighting that small angular changes have a large effect on 3D reconstructions. Experimental resolution was determined by resolvable bars on the USAF resolution target in Fig. 3.6(c), where we declare a feature as “resolved” when there is a  $> 20\%$  dip between  $I_{max}$  and  $I_{min}$ .

### 3.4 Discussion

Our calibration method offers significant gains in speed and robustness as compared to previous methods. BF calibration enables these capabilities by obtaining a good calibration that needs to be calculated only once in pre-processing, reducing computation. Since an estimation of a global shift in the illuminator based only on the brightfield images provides such a close initialization for the rest of the illumination angles, we can use a quicker, easier joint estimation computation in our SC calibration than would be otherwise possible. Jointly,

these two methods work together to create fast and accurate reconstructions.

3D FPM algorithms are slowed an untenable amount by iterative calibration methods, since they require the complicated 3D forward model to be calculated multiple times during each iteration. Combined with 3D FPM’s reliance on precise illumination angles to obtain a good reconstruction, it has previously been difficult to obtain accurate reconstruction of large volumes with 3D FPM. However, since BF calibration occurs outside the 3D FPM algorithm, we can now correct for the angle misestimations that have degraded these reconstructions in the past, allowing 3D FPM to be applied to larger volumes.

We analyze the robustness of our method to illumination changes by simulating an object illuminated by a grid of LEDs with  $NA_{illum} < 0.41$ , with LEDs spaced at  $0.041NA$  intervals. We define the system to have  $\lambda = 532$  nm, with a  $10\times$ ,  $0.25$  NA objective, a  $2\times$  system magnification, and a camera with  $6.5\mu\text{m}$  pixels. While the actual illumination angles in the simulated data remain fixed, we perturb the expected angle of illumination in typical misalignment patterns for LED arrays: rotation, shift, and scale (analogous to LED array distance from sample). We then calibrate the unperturbed data with the perturbed expected angles of illumination as our initial guess.

Our method recovers the actual illumination angles with error less than  $0.005$  NA for rotations of  $-45^\circ$  to  $45^\circ$  (Fig. 3.7(a)); shifts of  $-0.1$  to  $0.1$  NA, or approximately a displacement of  $\pm 2$  LEDs (Fig. 3.7(b)); and scalings of  $0.5\times$  to  $1.75\times$  (or LED array height between  $40$ - $140$  cm if the actual LED array height is  $70$  cm) (Fig. 3.7(c)). In these ranges, the average error is  $0.0024$  NA, less than the k-space resolution of  $0.0032$  NA. Hence, our calibrated angles are very close to the actual angles even when the input expected angles are extremely far off. This result demonstrates that our method is robust to most misalignments in the illumination scheme.

### 3.5 Conclusion

We have presented a novel two-part calibration method for recovering the illumination angles of a computational illumination system for Fourier ptychography. We have demonstrated how this self-calibrating method makes Fourier ptychographic microscopes more robust to system changes and aberrations introduced by the sample. The method also makes it possible to use high-angle illuminators, such as the quasi-dome, and non-rigid illuminators, such as laser-based systems, to their full potential. Our pre-processing brightfield calibration further enables 3D multislice Fourier ptychography to reconstruct high-resolution features across larger volumes than previously possible. These gains were all made with minimal additional computation, especially when compared to current state-of-the-art methods. Efficient self-calibrating methods such as these are important to make computational imaging methods more robust and available for broad use in the future. Open source code is available at [www.laurawaller.com/opensource](http://www.laurawaller.com/opensource).

## Chapter 4

# Practical 3D Refractive Index Imaging Systems

3D refractive index imaging provides quantitative structural information about biological sample morphology, and thus has great potential for a wide variety of biological research applications. However, these systems are often difficult to build and use, and require large amounts of measured data and long computational reconstruction times. 3D refractive index imaging is therefore an important area to focus on for designing more robust and practical computational imaging systems.

The main contribution of this chapter is to introduce previous work in 3D refractive index imaging and give practical guidance for the design and operation of intensity-only optical diffraction tomography (ODT) 3D RI imaging systems. I present a review of 3D RI imaging methods and a comparison of forward light propagation models for use in 3D RI reconstruction algorithms. I also present practical guidance on how to build and use an angle-scanning, dual-objective intensity-only ODT imaging system, which I hope will be useful to those who wish to build and use 3D RI imaging systems. In addition, I present a comparison of field- and amplitude-based 3D RI reconstructions, concluding that field-based ODT measurements contain a similar degree of diverse phase information as the pupil-coded intensity ODT measurements described in detail in Chapter 5. Further methods for increasing the robustness of intensity-only ODT are discussed in Chapter 5, with the introduction of pupil-coded intensity ODT, and Chapter 6, with the application of physics-based machine learning system optimization.

### 4.1 Introduction to 3D Refractive Index Imaging

In biological microscopy, the ability to measure the morphology of transparent samples is useful to advance scientific understanding of cells, tissue, and small organisms. While many biological researchers use fluorescent labeling or staining to render biological sample structures and functions visible under the microscope [10, 47, 184], label-free phase imaging methods

rely on the sample's natural interaction with light to provide image contrast [164]. Label-free methods are beneficial because they do not require time-intensive labeling processes, yet still capture structural information about the sample. More recently, 2D quantitative phase imaging (QPI) [138, 164, 186, 187, 216, 240] and 3D refractive index (RI) imaging [33, 36, 98, 126, 150] methods have been developed to reconstruct quantitative phase information, which can be useful in imaging samples that cannot be stained, such as stem cell organoids [123] or developing embryos [29, 150]; calculating cell dry mass [6] and other cell properties [7]; or in tandem with fluorescent imaging methods to simultaneously gather functional and structural information [38, 106, 139, 232]. 3D RI imaging in particular can provide 3D morphological information useful in interpreting sample structure and function, or could be used to better model microscopic organisms' interaction with light, which could be important for reducing uncertainty in climate models when applied to phytoplankton or snow algae [44, 114].

Since biological samples are usually transparent, QPI and 3D RI imaging systems typically rely on manipulation of the light on either the illumination-side or the detection-side of the microscope to measure phase contrast information in the collected images, using the sample's innate interaction with light to make its structure visible. Illumination-side coding includes annular illumination [122, 237], angled plane wave illumination [33, 36, 65, 105, 113, 150, 213, 215, 225], or otherwise patterned illumination sources [29]. Detection-side coding includes manipulation of the pupil function [72], including the simplest case of blocking the DC component of the sample spectrum in the Fourier plane, as in Zernike phase contrast microscopy [237]; scanning through focus [29, 48, 66, 68, 94, 141, 143, 200, 204, 226, 244] (which can be formulated as a pupil function manipulation but is often implemented by physically moving the object or imaging system through focus); or through interference with a reference beam that has not passed through the sample (*i.e.*, interferometry) [90, 150]. In addition, 3D information can be captured by rotating the sample relative to the imaging system [14, 27, 80, 190]. In all cases, the intensity of the electric field  $u_i$  is measured at the camera plane. These measured images are then processed computationally to reconstruct quantitative 2D phase or 3D refractive index, usually using an optimization algorithm which reconstructs the object  $O$  that best explains the measurements  $I_i$  given the imaging system parameters and light scattering model. In interferometric imaging systems, the amplitude and phase of the electric field  $u_i$  is usually first reconstructed from the intensity measurements before the quantitative object  $O$  is recovered.

3D RI reconstruction quality is determined by both the amount of high-contrast 3D phase information captured through the imaging system in the measurements  $I_i$  and by the efficacy of the computational algorithm in reconstructing an accurate object  $O$  from these measurements. In particular, the accuracy of the forward light scattering model, which models how light propagates through the sample, is important for the efficacy of the reconstruction algorithm [58]. While the physics of light scattering can be described with Maxwell's equations, reducing to the Helmholtz equation under the scalar wave assumption, calculating light scattering in a computationally feasible way is computationally expensive, especially as 3D RI reconstruction algorithms are often iterative and require many repetitions of the forward light scattering model. Many 3D RI methods therefore use the Born

approximation [113, 126, 213], which limits samples to a single-scattering approximation, or the Rytov approximation [33], which limits samples to be smoothly varying in phase. More recently, multiple-scattering models, such as the multislice model, have been developed for 3D RI imaging [31, 98, 99, 129, 215] which better account for multiple scattering involved in thicker, more scattering samples.

In this chapter, we review multislice-model based intensity-only ODT. We present a comparison of four forward scattering models for use in 3D RI imaging, including the Born approximation, a series-expanded Born algorithm called SEAGLE, the multislice model, and a rigorous finite-difference time-domain (FDTD) method. In addition, we present alignment techniques for intensity-only ODT systems and a comparison between simulated intensity-based and field-based 3D RI reconstructions.

## 4.2 Intensity-only Optical Diffraction Tomography

In a 3D intensity-only ODT microscope [36, 98, 215], a refractive index sample  $O(\mathbf{r})$  with low absorption is illuminated sequentially by coherent plane waves at different incident angles up to the numerical aperture (NA) of the imaging objective lens,  $NA_{obj}$ . The  $i^{th}$  measured intensity is given by

$$I_i(\mathbf{r}) = |\mathcal{F}^{-1} \{ \mathcal{F} \{ S_i(O(\mathbf{r})) \} P(\mathbf{k}) \}|^2, \quad (4.1)$$

where  $\mathcal{F} \{ \cdot \}$  and  $\mathcal{F}^{-1} \{ \cdot \}$  are the Fourier transform and inverse Fourier transform, respectively;  $\mathbf{r}$  and  $\mathbf{k}$  are image- and spatial frequency-space coordinates;  $S_i(\cdot)$  is the forward light scattering operator of the  $i^{th}$  angled plane wave illumination; and  $P(\mathbf{k})$  is the pupil function of the imaging system. Many forward scattering models have been used for 3D quantitative phase imaging, including the linear Born and Rytov models [33, 126, 213], a series-expanded Born model called SEAGLE [129], multislice [42], and the recently developed multi-layer Born and multi-layer Rytov models [31]. Several of these methods are discussed in Sec. 4.3 below.

In this work, we selected the multislice algorithm as our forward light scattering model  $S_i(\cdot)$ , as it allows for multiple scattering of the light inside the reconstructed volume, which allows thicker, more scattering objects to be reconstructed than single-scattering models. The multislice algorithm is also computationally feasible for our selected object sizes [58]. In the multislice algorithm, the incident angled plane wave electric field is defined as

$$u_0(\mathbf{r}) = \exp(j\mathbf{k}_i \cdot \mathbf{r}), \quad (4.2)$$

where  $\mathbf{k}_i = (k_{i,x}, k_{i,y})$  is the spatial frequency of the  $i^{th}$  illumination angle and  $j$  here denotes the imaginary unit. The incident electric field  $u_0$  is multiplied by the transmission matrix of the 1<sup>st</sup> object slice, then is propagated by a distance  $z_1$  to the 2<sup>nd</sup> layer using the angular spectrum propagation kernel [73]. The resultant electric field  $u_m$  is successively multiplied by the  $m^{th}$  object slice and propagated by a distance  $z_m$  to the  $(m+1)^{th}$  layer of the volume.

This process is repeated through all  $M$  slices of the object volume, producing output electric field  $u_M(\mathbf{r})$  which is then filtered by the microscope's pupil function and imaged onto the camera plane.

In intensity-only ODT, quantitative 3D refractive index is recovered by formulating an iterative optimization problem that minimizes the error between the modeled and measured image amplitudes given an estimated RI volume  $\hat{O}(\mathbf{r})$ ,

$$\hat{O}(\mathbf{r}) = \arg \min_{O(\mathbf{r})} \sum_i \left\| \left| \mathcal{F}^{-1} \{ \mathcal{F} \{ S_i(O(\mathbf{r})) \} P(\mathbf{k}) \} \right| - \sqrt{I_i(\mathbf{r})} \right\|_2^2 + \alpha \mathcal{P}(O(\mathbf{r})), \quad (4.3)$$

where  $\mathcal{P}(O(\mathbf{r}))$  is a prior penalty that can be chosen to constrain the solution space of  $O(\mathbf{r})$ , and  $\alpha$  is a tunable regularization parameter. In 3D RI imaging, some common choices for  $\mathcal{P}(O(\mathbf{r}))$  are to enforce the assumptions that  $\hat{O}(\mathbf{r})$  is purely real (*i.e.*, the sample does not absorb any light), strictly positive (*i.e.*, the sample's refractive index is strictly greater than that of background media), or that it is smoothly varying and therefore has low-valued first-derivatives, often enforced through a total variation regularizer which forces the reconstruction to be piecewise constant [25, 192, 207]. The optimization problem is nonlinear due to the choice of the multislice scattering operator  $S_i(\cdot)$ , so must be solved iteratively.

In addition, this optimization problem is highly nonconvex, meaning that many local minima exist that can satisfy the data consistency penalty but may produce sub-optimal reconstructions that do not accurately represent the sample's true refractive index distribution. Experimentally, we find that the most common local minima in traditional ODT reconstructions capture the high spatial frequencies (*i.e.*, the high-resolution edges) of the object  $O$  well but do not capture the low spatial frequencies (*i.e.*, the internal RI values). In particular, in angle-coded intensity-only ODT, the reconstructions under a low-angle illumination constraint do not reconstruct low spatial frequencies well, giving inaccurate reconstructions. A low-angle illumination constraint exists when the maximum angle of illumination is approximately 85% or lower than the numerical aperture of the imaging objective,  $NA_{illum,max} < \sim 0.85 NA_{obj}$ . As discussed in Chapter 5, intensity-only ODT therefore requires high-angle illumination (*i.e.*,  $NA_{illum,max} \approx NA_{obj}$ ) for high-quality reconstructions, increasing the complexity of the imaging system to guarantee these high illumination angles, which in turn can make the imaging system more constrained and difficult to use.

### 4.3 3D Coherent Light Propagation Models

3D RI imaging systems require accurate forward models<sup>1</sup> to reconstruct high-quality 3D RI results. With thick refractive index samples, the forward model must simulate the propagation of coherent light through the 3D object, taking into account both interference and diffraction effects. 3D RI reconstruction methods [36, 49, 88, 98, 215] often use iterative algorithms that require re-evaluating the forward model many times as the object estimate is updated. In order to build practical 3D RI imaging systems, the forward model must therefore also

be computationally efficient, to reduce both the memory footprint and computation time required for reconstructions. Here, we compare the computational complexity and accuracy for large amounts of scattering for the finite-difference time-domain (FDTD), multislice, first Born approximation, and series-expanded Born (SEAGLE) simulation methods.

The finite-difference, time-domain (FDTD) method is the most accurate wave optics simulation method available. However, the memory and time requirements of FDTD grow as  $N^3$  and  $N^4$ , respectively, where the simulation volume is  $N \times N \times N$  [8]. Hence, FDTD works well as a ground truth simulation for small objects, but is not practical for iterative algorithms where the forward model must be computed many times. To avoid excessive computation, many models make assumptions about the object, illumination, or imaging system. For example, the Born approximation assumes that variations in refractive index are small and scattering is weak [18, 213]. The multislice model (beam propagation method) can account for multiple scattering, but assumes there is no back-scattered light [42]. The recently developed series-expanded Born SEAGLE method also accounts for multiple scattering, but has increased computational complexity. In this chapter, we compare the tradeoffs in time vs. accuracy for forward models of a biological cell phantom via FDTD, multislice, first Born approximation, and SEAGLE methods.

### 4.3.1 Finite-Difference Time-Domain

The finite-difference time-domain (FDTD) method is a numerical analysis technique for finding solutions to differential equations. The FDTD method can model electromagnetic wave propagation through a refractive material by iteratively solving Maxwell's equations (Fig. 4.1(a)). The object, described by a distribution of dielectric constants, is gridded into finite points. The electric and magnetic fields are solved at each point by stepping through small time increments. As the increment size decreases, the FDTD algorithm more closely approximates the solution to the continuous Maxwell's equations. We use FDTD simulations computed using the freely available software package MEEP [8]) as the ground-truth forward model for light propagation through a 3D phase object.

### 4.3.2 Multislice

The multislice method (also known as the beam propagation method) models a 3D object as a series of thin 2D slices separated by homogeneous medium [42]. The incident wave propagates through the volume from slice to slice. Each slice acts as a complex transmission mask that modulates the incident electric field (Fig. 4.1(b)). After each slice, the field is propagated to the next slice using Fresnel or angular spectrum propagation [73]. The multislice algorithm

---

<sup>1</sup>Sec. 4.3 represents work done in collaboration with Nicole Repina and Michael Chen. It is drawn primarily from [58] Regina Eckert, Nicole Repina, Michael Chen, Yishuang Liang, Ren Ng, Laura Waller, "Modeling Light Propagation in 3D Phase Objects," in *Imaging and Applied Optics 2017*, OSA Technical Digest (Optical Society of America, 2017), paper DW2F.2.

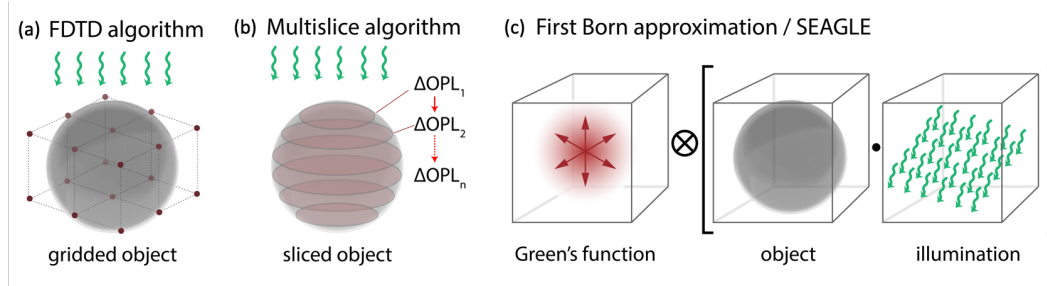


Figure 4.1: Four forward models for coherent light propagation through a refractive object are studied. (a) FDTD: Maxwell’s equations are evaluated at each time step and volume grid point. (b) Multislice: the object is modeled as a stack of 2D slices with complex transmission masks, and light is propagated from slice to slice through the volume. (c) Born approximations: the perturbation of the object on the incident light is propagated across the volume via convolution with a Green’s function, either under a single-scattering approximation (First Born approximation) or a full-scattering, series-expanded approach (SEAGLE).

divides a 3D sample into lateral slices of a defined thickness, which impart a phase shift to an incoming electric field based on the refractive index of the preceding material.

For a phase object, the refractive index distribution  $n$  along path  $s$  determines the phase delay  $\Delta\phi$  imparted to the incident wave at each slice:

$$\Delta\phi = \frac{2\pi}{\lambda}\Delta OPL = \frac{2\pi}{\lambda}\sum_{m=1}^M n_m s_m, \quad (4.4)$$

where  $\lambda$  is the illumination wavelength and  $\Delta OPL$  is the change in optical path length caused by each slice. The multislice algorithm assumes forward scattering by the sample. Model accuracy is improved by decreasing the distance between slices, which should be smaller than the depth-of-field of the microscope system.

The incoming field,  $u_{m-1}(x, y)$  is multiplied by the phase shift and then propagated to the next slice using using near-field free-space propagation

$$u_m(x, y) = (u_{m-1}(x, y) \cdot A_{m-1}(x, y)e^{j\phi_{m-1}(x, y)}) * h_z(x, y), \quad (4.5)$$

where  $A_{m-1}(x, y)$  and  $\phi_{m-1}(x, y)$  are the amplitude and phase of the  $(m-1)^{th}$  slice’s transmission mask,  $h_z(x, y)$  is the diffraction impulse response, and  $*$  denotes convolution. Practically, this convolution is implemented as a multiplication in the Fourier domain. The angular spectrum kernel  $H_{angular}(\mathbf{k})$  is used when  $z$  is small and Fresnel propagation kernel  $H_{Fresnel}(\mathbf{k})$  is used when  $z$  is larger. They are given by the equations [73]

$$\begin{aligned}
H_{angular}(\mathbf{k}) &= e^{jz\sqrt{\frac{4\pi^2}{\lambda^2} - k_x^2 - k_y^2}} \\
H_{Fresnel}(\mathbf{k}) &= e^{j\frac{2\pi}{\lambda}z} e^{-j\pi\lambda z \frac{1}{4\pi^2}(k_x^2 + k_y^2)},
\end{aligned}$$

where  $\mathbf{k} = (k_x, k_y)$  are the spatial frequency-space coordinates.

### 4.3.3 First and Series-Expanded Born (SEAGLE) Approximations

The scalar Helmholtz equation defines the resultant field of a wave scattered from an inhomogeneous volume as:

$$u(\mathbf{r}) = u_i(\mathbf{r}) + \int G(|\mathbf{r}' - \mathbf{r}|)V(\mathbf{r})u(\mathbf{r})d\mathbf{r}, \quad (4.6)$$

where  $V(\mathbf{r}) = \frac{4\pi^2}{\lambda^2}(n(\mathbf{r})^2 - n_0^2)$  is the scattering potential of the volume,  $n(\mathbf{r})$  is the refractive index distribution,  $u_i$  is the incident field, and  $G(|\mathbf{r}' - \mathbf{r}|)$  is the Green's function describing how a perturbation at  $\mathbf{r}$  affects point  $\mathbf{r}'$ . We take the Green's function to be a spherical point spread function (PSF)  $G(\mathbf{r}) = \frac{1}{4\pi} \frac{e^{jk_0|\mathbf{r}|}}{|\mathbf{r}|}$ , where  $k_0 = \frac{2\pi}{\lambda_0}$  is the wavenumber in vacuum. we define  $G(\mathbf{r} = 0)$  numerically based on the grid size of our simulation to avoid division by zero.

$$G(0) = \frac{1}{k_0^2} [(1 - jk_0R)e^{jk_0R} - 1] \quad (4.7)$$

where

$$R = \left(\frac{3}{4\pi} \Delta x \Delta y \Delta z\right)^{\frac{1}{3}} \quad (4.8)$$

is the radius of the sphere around the center, given grid spacing  $\Delta x$ ,  $\Delta y$ , and  $\Delta z$ .

The field  $u(\mathbf{r})$  forms an inherently recursive definition of the scattering of light through the volume. The first Born approximation replaces the recursive reliance on the resultant field  $u(\mathbf{r})$  with the incident field  $u_i(\mathbf{r})$ , reducing computational complexity:

$$u(\mathbf{r}) = u_i(\mathbf{r}) + \int G(|\mathbf{r}' - \mathbf{r}|)V(\mathbf{r})u_i(\mathbf{r})d\mathbf{r}. \quad (4.9)$$

This effectively approximates the sample  $V(\mathbf{r})$  as scattering an unperturbed volumetric incident field  $u_i(\mathbf{r})$ . Scattering effects are propagated in 3D by convolving the perturbed field with  $G(\mathbf{r})$ , which spreads the effect of each perturbation across the volume. This gives us the first-order approximation of the scattered field, which assumes that the surfaces closest to the source do not substantially scatter the incoming plane wave such that the field incident on the interior surfaces is approximately a plane wave. This is an accurate approximation when the changes in refractive index across a sample are low and the scattering is weak.

Higher-order estimations of the scattered field can be obtained by directly using the recursive definition of  $u(\mathbf{r})$  in the recursive Born approximation. SEAGLE, a series-expanded Born method, was developed from this concept for more accuracy in highly scattering objects and is implemented using accelerated-gradient optimization[129].

#### 4.3.4 Comparison of 3D Light Propagation Models

The 3D phase object used in our simulations (Fig. 4.3) is designed to have the same refractive index variations as a mammalian cell [13]. It is a  $10 \times 12 \times 6 \mu\text{m}$  ellipsoid and contains a nucleus with a  $5.2 \mu\text{m}$  diameter. Two organelles ( $800 \text{ nm}$  diameter,  $0.8 \mu\text{m}$  apart, refractive index  $n = 1.1$ ) are in the plane of focus, while a third organelle is  $1.8 \mu\text{m}$  behind focus. A thin plasma membrane ( $100 \text{ nm}$  thick,  $n = 1.1$ ) surrounds the cell and nucleus. The cell is placed in a uniform background  $n = 1.0$ , while the cell cytoplasm has a slightly higher index of refraction due to solubilized proteins ( $n = 1.03$ ). This phantom maintains the relative refractive index of these cell components, with a background value of  $n = 1.0$  chosen for simplicity rather than the more accurate aqueous background  $n = 1.33$ . However, since the primary differences in forward scattering model accuracy are due to the differences in refractive index  $\Delta n$ , as seen in Fig. 4.3, the choice of background value  $n = 1.0$  is not expected to affect the results of this comparison.

For each forward model, we simulated illuminating the cell from three different angles (Fig. 4.2): on-axis brightfield ( $(\theta_x, \theta_y) = (0^\circ, 0^\circ)$ ), off-axis brightfield ( $8.6^\circ, 8.6^\circ$ ), and darkfield ( $25.8^\circ, 25.8^\circ$ ). We also modeled image formation with increasing refractive index values of the cell parameters to simulate increased scattering (Fig. 4.3). The cell was imaged with a  $0.6 \text{ NA}$ ,  $40\times$  objective focused at the cell's center. All images are scaled to their background intensities. Both the multislice and SEAGLE methods match the FDTD results well, excepting that multislice has slightly lighter cell features when normalized (implying a brighter background). The first Born approximation exhibits large differences in brightfield and a brighter cell interior in darkfield, especially for larger refractive index differences  $\Delta n$ . These large differences are expected for the first Born approximation, since it is a single-scattering model of a multiply-scattering object. Small differences in the multislice results can be largely attributed to lack of backscattered light and in SEAGLE to the possibility that the algorithm had not fully converged.

On average, each illumination angle took the following computation time for the base cell refractive index values: FDTD 1980 seconds, multislice 0.8 seconds, first Born approximation 1.4 seconds, SEAGLE 240 seconds (Fig. 4.4). Considering the lengthy simulation times of FDTD and SEAGLE, as well as the poor applicability of the first Born approximation to highly scattering objects, we conclude that multislice is a good choice for quick, accurate simulation of 3D cells and objects that have relatively little backscattered light. The SEAGLE algorithm considers backscattered light and is orders of magnitude faster than FDTD, making it more useful for highly backscattering objects. However, SEAGLE's computation time increases with the degree of scattering inside the modeled object since it is based on an optimization algorithm, as seen in Fig. 4.4. On-going work may accelerate the SEAGLE

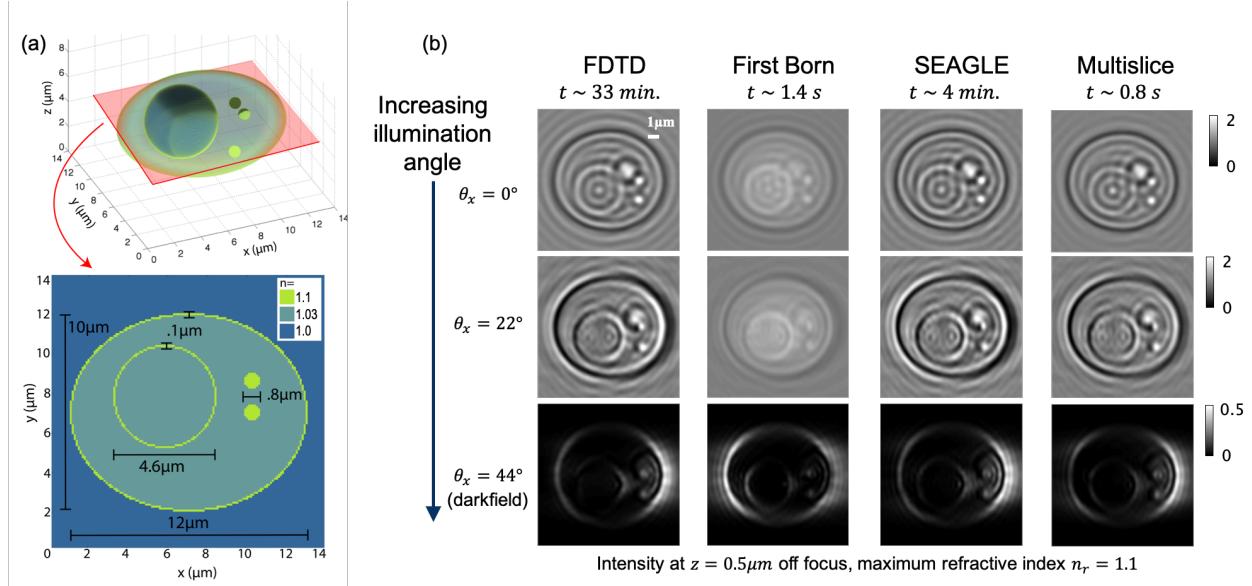


Figure 4.2: Forward model comparison across illumination angle. (a) 3D visualization and cross-section of the simulated mammalian cell model for comparing forward models. (b) Simulated 2D intensity at center focus for three different illumination angles. Considering FDTD as the ground truth ( $0.05 \mu\text{m}$  resolution), the multislice and series-expanded Born (SEAGLE) methods provide a close approximation, whereas the first Born approximation method deviates in the brightfield cases (all  $0.1 \mu\text{m}$  resolution). Grid artifacts from refocusing in FDTD are negligible and can be solved with a larger simulation volume.

algorithm, which would make it competitive with the multislice algorithm for speed and accuracy.

Not included in this comparison are the Rytov model [213], the recursive Born method [97], which calculates the forward-scattered field through multiple iterations of the Helmholtz equation in Eq. 4.6, and the multi-Born model [31], which divides the sample into small axial sections and applies the Born approximation to each section iteratively to model both the forward and reverse scattering of the light. Future work to compare these and other coherent light propagation models would prove useful in the determination of the best forward scattering model to use for 3D RI imaging of thicker, more scattering samples.

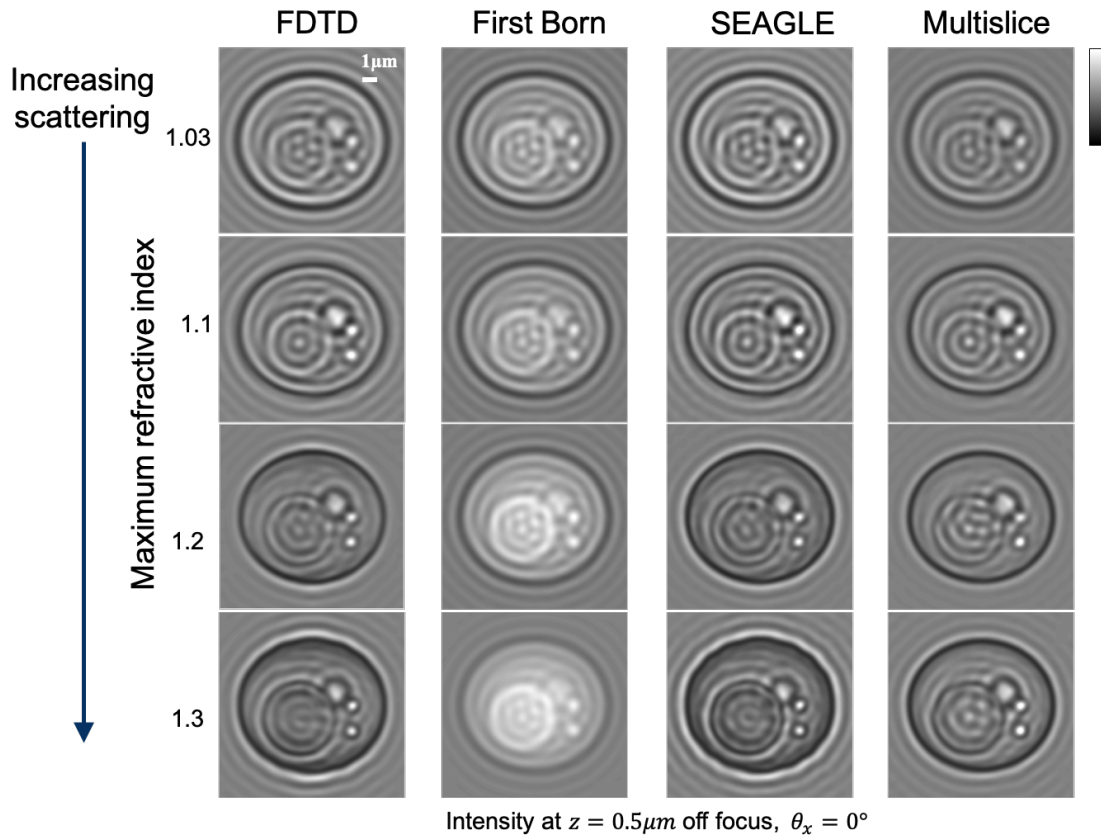


Figure 4.3: Forward model comparison across  $\Delta n$  for on-axis illumination. The background refractive index  $n_{bk} = 1.0$  for all simulations while the cell body  $n_{cell} = [1.01, 1.03, 1.06, 1.09]$  and organelle  $n_{organelle} = [1.03, 1.1, 1.2, 1.3]$  are changed in each row. This greater disparity in RI is related to increased scattering in the volume. The SEAGLE model best matches the ground truth FDTD simulations across all scattering levels, closely followed by the multislice model. The First Born approximation performs well for low  $\Delta n$  but poorly at high  $\Delta n$ .

## 4.4 Intensity-only ODT System Design and Alignment

### 4.4.1 Illumination System and Objective Lens Design

Angle-scanning ODT systems scan the angle of incident plane wave illumination at the sample plane in the same manner as Fourier ptychographic microscopy (FPM). Therefore, the same illumination source designs described in Sec. 2.2.1 can be used for ODT systems. However, since ODT is a 3D imaging method, ODT systems have different imaging system

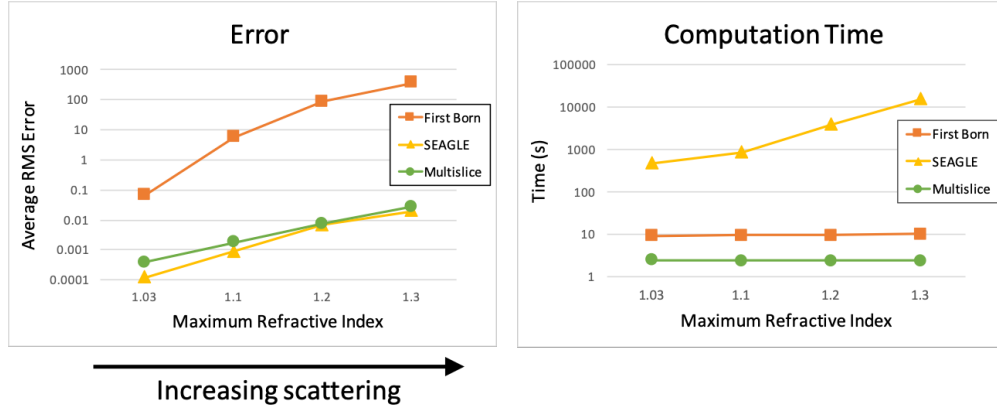


Figure 4.4: Comparison of model computation time and overall error shown across increasing  $\Delta n$ . The SEAGLE and multislice RMS error is similar across scattering levels, while the First Born approximation’s error is higher and increases more with higher  $\Delta n$ . The computation time is much higher for SEAGLE, and increases with object complexity. The computation time for both multislice and First Born are relatively low and do not depend on object complexity.

design considerations than 2D FPM.

While darkfield images could theoretically be used in 3D reconstructions, they typically are not because of the large intensity difference between brightfield and darkfield images, which can cause reconstruction instability.<sup>2</sup> Typically, therefore, the maximum  $NA_{illum,max} \leq NA_{obj}$ , measuring all brightfield images, where the DC term of the scattered field’s Fourier spectrum is passed through the pass-band of the imaging objective lens.

In 3D imaging, we also desire  $NA_{obj}$  to be as large as possible, unlike in FPM, since the axial resolution of the 3D reconstruction scales with the square of the objective  $NA_{obj}$ . Typically, we select  $NA_{obj} \geq 0.7$  for high-quality 3D reconstructions.<sup>3</sup> In intensity-only ODT systems, the majority of the low-frequency information comes from the high-NA illumination angles. Therefore, a high-NA illumination source must be chosen (typically a dual-objective lens design) with attendant constraints on the physical system design and use. As discussed in Chapter 5 below, our proposed pupil-coded intensity ODT system relaxes this constraint by capturing low-frequency content in low-NA illumination angle images, which allows for different, less constrained illumination sources to be used. This results in a large gain in 3D RI imaging system practicality, since the high-NA illumination angles often introduce the

<sup>2</sup>However, this remains an open area of inquiry.

<sup>3</sup>We note that the multislice algorithm may limit the maximum illumination angle possible for reconstruction [188]. In practice, we have stopped down the pupil plane to  $NA \approx 0.7$  in air, even in high-resolution systems [36], to avoid model mismatch with the multislice algorithm. However, given a forward light propagation model that works well at high NA, this constraint would be relaxed.

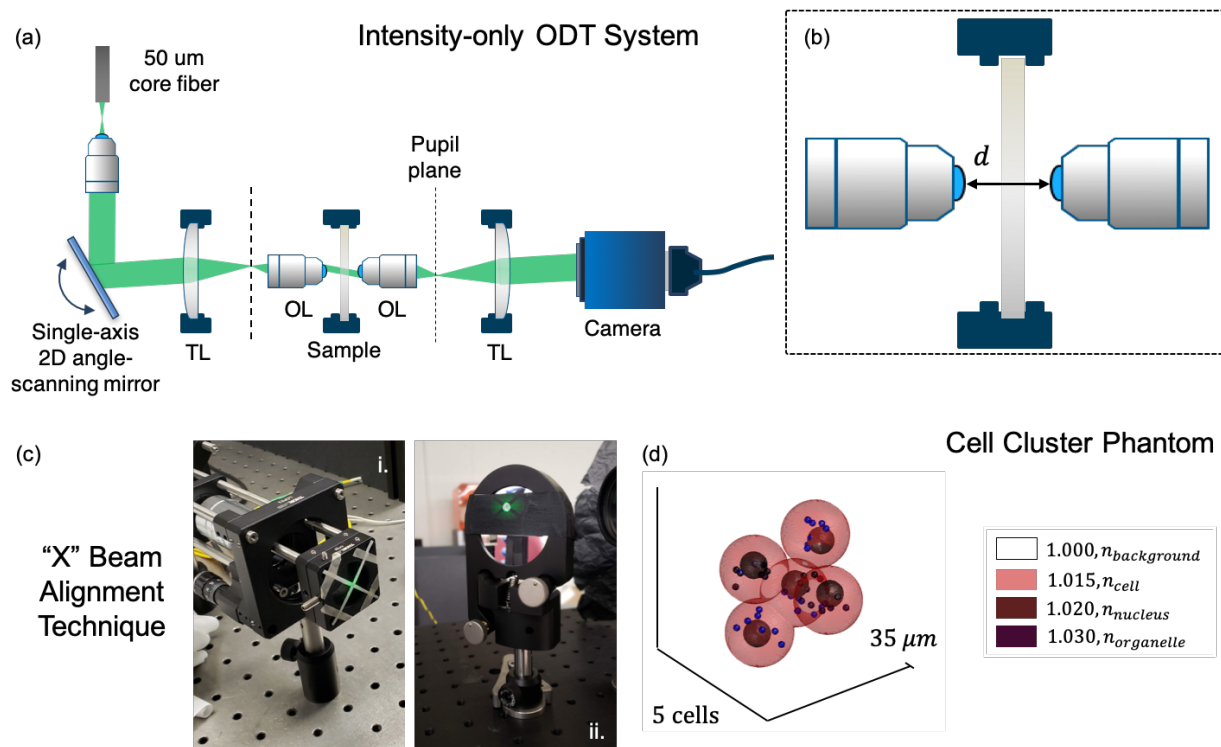


Figure 4.5: Intensity-only ODT system overview. (a) Intensity-only ODT system diagram. An objective lens collimates the fiber-coupled LED beam and relays it onto a scanning mirror, which relays the light through tube lenses (TL) and objective lenses (OL) to image the sample at the camera plane. (b) Dual-objective systems have a short distance  $d = WD_{illum} + WD_{im}$  between them for the sample, defined by the working distance ( $WD$ ) of the illumination and imaging objectives, respectively. (c) Pictures of the “X” beam alignment technique. (d) Cell cluster phantom used for field and amplitude reconstruction comparisons.

most constraints on the system design.

#### 4.4.2 Dual-Objective Alignment Methods

While most ODT system alignment can be done with standard optical alignment techniques and tools<sup>4</sup>, the alignment of the dual-objective system necessary for intensity-only ODT is more complex and is important for correct system functionality.

In the dual-objective angled illumination system, collimated light is relayed onto a computer-controlled angle scanning mirror at back focal plane of the illumination objective’s

<sup>4</sup>Including though not limited to use of a centered “X” in the beam path to determine beam alignment; use of centered irises at different axial locations to determine beam size and alignment; use of reflections to check alignment; and use of a shearing plate interferometer to check beam collimation.

tube lens. The tube lens is placed roughly a focal length away from the illumination-side objective. This first objective is aligned axially by placing it at a position where it will make the finest possible spot. If a centered “X” is placed in the beam path, as seen in Fig. 4.5(c), it should be as sharp as possible when the objective is at the correct axial position. The objective is aligned laterally by shifting the objective to center the beam path “X” on a fiducial marker that was placed in the beam prior to the insertion of the lenses, also shown in Fig. 4.5(c).

Alignment of the second objective (the imaging objective) is done iteratively. First, we align the imaging objective so that it is approximately the correct distance away from the illumination objective based on the combined working distance of the two objective lenses (Fig. 4.5(b)). When we do this, we place the same glass thickness (*i.e.*, two 0.17 mm thick #1.5 coverslips) between the two objectives that are expected for the sample, since the optical thickness of glass is different than of air and affects the axial alignment. We then align the imaging tube lens so that the output beam is collimated, as determined by a shearing plate interferometer. The camera is placed a focal distance from the tube lens. If the system allows access to an intermediate image plane, we place a resolution target at the intermediate image plane, a focal distance from the imaging tube lens. The camera placement can then be fine-tuned by finding the camera position which results in the best-focused image with the highest resolution features.

Now that the imaging objective has been initially aligned, we can determine how to fine-tune its axial alignment. To do this, we scan the angles of illumination at relatively large  $NA_{illum}$  and observe the images at the camera plane. If the centered “X” in the beam path do not move as the illumination angle is scanned, then the imaging objective is at the correct axial location. We repeat this process until the circular boundary and centered “X” do not move as the illumination angle is scanned. Then we repeat the alignment steps for the imaging tube lens and camera placement described above, especially if large changes of the objective’s axial position were needed. While this procedure could include many iterations if the imaging objective was initially extremely misaligned, we find in practice that using a single fine-tune alignment of the imaging objective, tube lens, and camera is sufficient for high-quality system operation.

### 4.4.3 Hardware Synchronization

Hardware synchronization is important for both ODT and FPM, as the  $i^{th}$  camera measurement must correspond with the  $i^{th}$  illumination angle. In the pupil-coded intensity ODT system discussed in Chapter 5, this synchronization is even more important because three pieces of hardware must work in tandem: the illumination angle control, the spatial light modulator display, and the camera capture system. One of the most difficult parts of building a computational imaging microscope is finding a platform where all necessary hardware can be simultaneously controlled. While the examples given here are not exhaustive, they are hopefully useful for identifying available hardware synchronization platforms.

The three basic options for hardware synchronization across many different devices are:

1. Dedicated hardware control, such as a microcontroller, FPGA, or DAQ
2. Device advanced programming interfaces (API's) accessed through general programming languages, such as Python or Matlab
3. Micro-Manager<sup>5</sup> [60, 59] and Pycro-Manager<sup>6</sup> [175] for microscopy-specific, open source control

If devices are purchased through the same company, it is possible that their software might allow joint control of the hardware. However, this is generally not true. In addition, some devices allow for trigger signals to be sent to the device to trigger an action (*e.g.*, a camera exposure), which is useful for fast synchronization but might require a chain of devices. For example, a DAQ or Raspberry Pi microcontroller can be used to send TTL signals to trigger a PCO Edge 5.5 camera exposure, rather than directly controlling the camera exposure from the computer. Overall, camera API's have a speed and functionality reduction from what is offered in the camera software, since the camera's software is usually specifically designed for fast imaging speeds. This reduction can be avoided by controlling the camera through trigger signals and capturing with the camera software, if this functionality is available.

*Dedicated hardware control* is the best choice for enabling extremely fast imaging, but restricts the control logic to a pre-programmed set of options, requires hardware programming experience, and can be opaque to new users. In addition, it can be difficult to alter if system parameters or devices change. It is usually easier to control hardware programmatically, unless high imaging speeds are needed. There are two main ways to do this. First, *device API's for general programming languages*, such as Python or Matlab, may be available open source or from the device manufacturer. Second, *open source Micro-Manager API's* may also be available for the device. Micro-Manager is an open source company dedicated to making microscopy systems easier to build by providing a common hardware and software operating platform [60, 59]. While base versions of Micro-Manager restrict the control and logic design functionality of the microscope system to a pre-designed set of commands, recently developed Pycro-Manager works directly with Python [175]. Using Python (and Pycro-Manager) or Matlab to synchronize hardware allows for extreme system flexibility, which is especially important for research-level computational imaging systems. However, this might come at the cost of reduced speed. In addition, not all devices are easy to control through these interfaces. It is therefore useful to review the available control systems before purchasing different controllable hardware devices in order to determine how easy they would be to synchronize with the rest of the system.

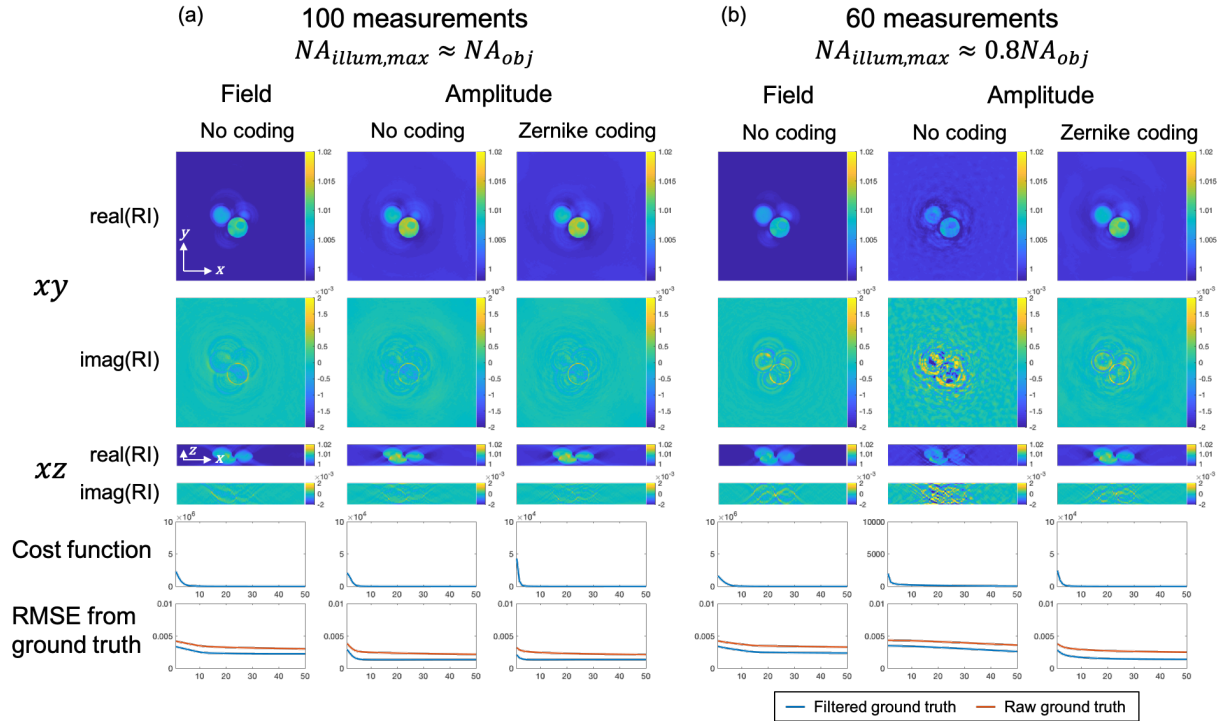


Figure 4.6: Comparison of simulated field- and amplitude-based 3D RI reconstructions. Reconstructions from simulated field and amplitude measurements at (a) 100 images, with  $NA_{illum,max} \approx NA_{obj}$  and (b) 60 images, with  $NA_{illum,max} \approx 0.8NA_{obj}$  show that field-based reconstructions are similar to amplitude-based reconstructions. While the field-based reconstruction in the (b) limited illumination case is better than the amplitude-based reconstruction without pupil coding, the field-based results are similar to the pupil-coded amplitude-based results (Zernike coding), which similarly introduce increased phase information into each measurement. Cost functions show that all reconstructions have converged. RMSE from NA-filtered and raw ground truth values show that the pupil-coded amplitude-based results are best in the (b) limited illumination case and equivalent to the amplitude-based results in (a) the full illumination case.

## 4.5 Comparison of Field- and Amplitude-Based 3D RI Reconstructions

Many 3D RI imaging systems have been created in recent years, as discussed in Sec. 1.3.2. We have chosen to focus on angle-scanning systems such as ODT because illumination angle

<sup>5</sup>See <https://micro-manager.org/>.

<sup>6</sup>See <https://github.com/micro-manager/pycro-manager>.

scanning is much more practical to implement than sample or system rotation, provides more diverse and higher-NA measurements than focal scanning, and allows for multiple scattering of the light, unlike methods that involve coherence-gating, which reject multiply scattered light.

As stated previously, traditional ODT systems use interferometric measurements to encode field information into the measured intensity images at the camera plane [33, 113, 150, 213]. In these interferometric systems, the intensity images are first processed to recover the complex scattered electric field for each illumination angle. These recovered fields are then processed to reconstruct the 3D RI volume. Interferometric systems introduce optical complexity, however, and may degrade multiple-scattered signal that could be used in the reconstruction. We opt to use an intensity-only ODT system which does away with the optical interferometric component and reconstructs the 3D RI volume directly from intensity measurements. We note that both of these systems only measure intensity images; the interferometric systems merely pre-process the data to obtain scattered field amplitude and phase information, which is central to traditional ODT algorithms such as filtered back-projection. While the interferometric system provides a useful method for encoding phase information in intensity measurements across illumination angles, it is unclear that the intermediate step of recovering field data is useful for the reconstruction. We use simulated data from field measurements and from intensity measurements to investigate how 3D RI reconstructions compare when field information is available to the 3D RI reconstruction algorithm.

We simulated a cluster of five  $10\text{ }\mu\text{m}$ -diameter,  $n_{cell} = 1.015$  refractive index cells in a volume of refractive index  $n_{bk} = 1.0$ . Each cell had one randomly-placed  $4\text{ }\mu\text{m}$ -diameter nucleus ( $n_{nucleus} = 1.01$ ) and ten randomly-placed  $1\text{ }\mu\text{m}$ -diameter organelles ( $n_{organelle} = 1.02$ ), as shown in Fig. 4.5(d). These values were drawn from typical cell characteristics [13], with a focus on maintaining the relative refractive index difference  $\Delta n$  between cell components, as this controls the accuracy of the light propagation model (see Sec. 4.3 above for more details). We used the multislice model to simulate the propagation of light through the volume at  $0.12\text{ }\mu\text{m}$  resolution in all dimensions, with wavelength  $\lambda = 532\text{ nm}$ , objective NA 0.45, and camera pixel size  $d_{cam} = 2.4\text{ }\mu\text{m}$ . We simulated a total of 100 illumination angles with maximum  $NA_{illum,max} = 0.45$ . This forward simulation produced the complex field exiting the volume for each illumination angles.

We used these simulated complex field measurements  $u_i(\mathbf{r})$  to reconstruct the 3D volumetric RI of the sample under three different imaging cases:

1. Field-based reconstruction, where the simulated field measurements  $u_i(\mathbf{r})$  were used directly in the reconstruction to simulate an ideal interferometric ODT system
2. Amplitude-based reconstruction, where the amplitude measurements  $|u_i(\mathbf{r})|$  were used to simulate use of an intensity-only ODT system
3. Pupil-coded amplitude-based reconstruction, where the field was additionally modulated by a random pupil coding mask  $\tilde{M}_i(\mathbf{k})$ , then converted to amplitude via intensity

measurement, giving  $|u_i(\mathbf{r}) * \mathcal{F}(\tilde{M}_i(\mathbf{k}))|$ , where  $*$  denotes convolution. This simulates use of the pupil-coded intensity ODT system described in Chapter 5.

For all of these imaging cases, the volume was reconstructed at lateral resolution  $0.24\ \mu\text{m}$  and axial resolution  $0.7314\ \mu\text{m}$  with a multislice-based FISTA optimization reconstruction algorithm, as described in Sec. 4.2. We note that this is a comparison of field- and amplitude-based reconstruction given this specific reconstruction algorithm, since field-based 3D RI reconstructions are usually done with different algorithms than the results presented here. However, we believe this still represents a good comparison for the amount of phase information encoded into each of these measurement systems that can be utilized by an optimization-based reconstruction algorithm. Additionally, given that the optimization reconstruction framework can be used with light propagation models that incorporate multiple-scattering, while traditional field-based reconstruction algorithms are built around single-scattering approximations, such as the Born or Rytov approximations, we argue that this is an important comparison to make to understand the usefulness of field measurements when reconstructing 3D RI volumes using these more general frameworks.

We compare these three imaging cases in two imaging conditions. First, we reconstruct with all 100 measurements with maximum  $NA_{illum,max} = 0.45$ , as seen in Fig. 4.6(a). In this case, all reconstructions produce reasonable results, with a good reconstruction of low-spatial frequency RI. Second, we reconstruct with a limited illumination condition, where we only use 60 measurements to reconstruct with a maximum  $NA_{illum,max} = 0.36$ , as seen in Fig. 4.6(b). As discussed in detail in Chapter 5, the excluded high-angle measurements provide the majority of the phase information for the amplitude-based reconstruction without pupil-coding. When pupil-coding is introduced to the amplitude-based reconstruction, more phase information is included in the low-angle measurements. Therefore, we see that the amplitude-based reconstruction without pupil coding has a poor reconstruction in the limited illumination angle case, with the recovered RI at much lower values than expected, while the pupil-coded amplitude-based reconstruction still provides good results. The field-based reconstruction provides similar good-quality results in this limited illumination angle condition. This suggests that both field measurements and pupil-coded amplitude measurements introduce diverse phase information into the measurements across illumination angle, allowing for good-quality reconstructions even in this limited illumination condition.

## Chapter 5

# Measurement Diversity for Improved 3D Refractive Index Imaging

3D refractive index microscopy has great potential to provide quantitative, structural data to biological researchers, but currently available methods become less accurate as sample volume, thickness, and scattering increase. Recent algorithms have been developed that extend 3D refractive index imaging to use models that better account for multiple-scattering. However, in order to tackle large, complicated samples, these methods require large amounts of data for high-quality reconstructions. In this chapter, we present a novel system for 3D refractive index imaging which we term pupil-coded intensity optical diffraction tomography (ODT) that utilizes both illumination- and detection-side coding to encode complex three-dimensional refractive index information into intensity-only images.

In the proposed system, angled coherent illumination is used to measure different 3D Fourier space regions of the object spectrum, as in previously presented ODT methods. This illumination-side coding is additionally augmented by random phase pupil coding applied on the detection side. We show that joint illumination- and detection-side coding better encodes diverse phase information into each measurement, leading to better simulated and experimental refractive index reconstructions that require less measured data and computation time than previous methods. We present simulated and experimental reconstructions showing these improvements. Our results show that the glass-induced spherical aberrations in an uncorrected objective lens can be used as a static pupil coding element, offering similar 3D RI imaging improvements to dynamic pupil coding introduced by a spatial light modulator. We present a transfer function analysis of the proposed system showing that the additional detection-side coding improves the transfer of low-spatial frequency information into the measured images. We additionally introduce a spatial entropy metric, which could be used to directly compare the measurement diversity across different 3D RI imaging systems.

## 5.1 Introduction

Current methods for 3D refractive index imaging suffer from long capture times that limit allowable sample motion; long computation times and large data requirements for high-quality RI recovery; inaccurate reconstructions for samples that are too thick or too highly scattering; and many constraints on the imaging system design. Recent work has aimed to reduce the capture and computation time through better system design [37], improve the results by using higher-resolution objectives [36]<sup>1</sup>, and incorporate multiple-scattering into the computational model to extend the reconstruction to thicker samples [98, 99, 215]. Even with these improvements, challenges still remain. In this chapter, we introduce a novel imaging system called pupil-coded intensity ODT that uses joint illumination- and detection-side coding to increase encoding of diverse phase information into all intensity measurements, which in turn reduces the capture time, computation time, and data requirements for high-quality RI recovery, and also reduces optical constraints on the illumination system.

High-quality 3D RI reconstructions depend on capturing sufficient 3D phase information through the imaging system. From general principles, a high numerical aperture (NA) objective should be used for 3D imaging since the axial resolution increases with the square of the objective NA. Beyond general principles, 3D imaging systems are difficult to directly optimize, however, as there are many possible configurations with different physical and practical limitations. Therefore, instead of directly optimizing the imaging system for 3D RI imaging, we focus on increasing the system’s *measurement diversity*. We observe that a 3D RI imaging system will require the least amount of measured data when each measurement introduces diverse, non-redundant 3D phase information to the reconstruction algorithm. One of the motivating factors in this chapter is addressing how we can increase this measurement diversity for 3D RI imaging.

In previous 3D RI imaging work, Ewald sphere analyses [62, 63] have been made for various 3D RI capturing methods [163], showing the 3D Fourier space coverage of different measurement systems under a single-scattering assumption. This analysis suggests high-angle illumination and high-NA objectives should be used and the object rotated to cover as much 3D Fourier space as possible. Transfer function analysis of different illumination patterns under linear, single-scattering models have been used to optimize the illumination pattern for phase imaging [126, 142]. This analysis shows that low-spatial frequency phase information is not transferred into measurements in current 3D RI imaging systems except when the incident illumination is at or near the NA of the imaging objective. Thus, high-NA illumination is needed, which increases imaging system complexity, data requirements, and

---

<sup>1</sup>Which, however, leads to increases in measured data, reconstructed volume size, and therefore computation times in intensity-only ODT. The measured data is increased because the angle scanning-only intensity-only ODT method requires the maximum illumination angle to be near the NA of the imaging objective,  $NA_{illum,max} \approx NA_{obj}$ , so more measured data is required as  $NA_{obj}$  increases. Additionally, as the effective pixel size decreases (since higher NA usually implies increased magnification), the volume size will also increase to cover the same physical area. Both of these effects increase the computation time of the reconstruction.

capture time when working with multiply-scattering samples. Related work in phase diversity has shown that measuring two images with different, known phase delays breaks the ambiguity of intensity measurements, leading to more efficient wavefront recovery [72, 92]. The phase diversity concept has been applied to diffraction-limited imaging [147] and generally illustrates the importance of capturing diverse phase information in each measurement for improved complex field reconstructions.

In this chapter, we introduce a novel 3D RI imaging microscope which combines illumination-side coherent plane wave angle scanning with detection-side phase pupil coding using an LCOS phase-only spatial light modulator (Fig. 5.1). We use the multislice forward light scattering model to allow for thicker, more complex samples and reconstruct with an iterative optimization algorithm. Our method builds on previous, intensity-only optical diffraction tomography (ODT) systems [36] that use angle-scanned illumination without pupil coding to capture 3D RI information. In our proposed system, however, the addition of different random pupil phase masks for each angle of illumination increases our system’s measurement diversity and more effectively encodes phase information across measurements. We find that the low spatial frequencies of the 3D refractive index are encoded into low-angle illumination measurements under the proposed system’s increased measurement diversity, unlike in methods without pupil coding. This increased measurement of diverse 3D phase across all measurements simplifies high-angle illumination constraints, leading to more practical imaging systems, and reduces data capture requirements, thus reducing capture time. In addition, we find that the system’s increased measurement diversity leads to faster 3D RI reconstruction convergence, shortening computation times. We present simulated and experimental results showing the improved reconstructions under low-NA illumination and limited computation conditions with the proposed system. We analyze the transfer functions of the proposed system to show that it encodes more low spatial frequency information across measurements, and present a spatial entropy metric to visualize the increased measurement diversity compared to prior imaging systems. Finally, we show that with a properly selected pupil phase, only a single, static pupil phase mask is needed across all angles of illumination for these 3D RI imaging improvements. We demonstrate a highly effective static phase mask experimentally using a highly aberrated, off-the-shelf uncorrected objective lens without additional pupil coding, showing the benefits of joint illumination- and detection-side coding in a simple imaging system. This static pupil-coded system further reduces imaging system complexity by eliminating the need for the spatial light modulator required for dynamic pupil coding.

## 5.2 Methods

In the novel proposed measurement diversity 3D phase imaging system, an additional phase spatial light modulator (SLM) coding element is added in the pupil plane of a traditional 3D intensity-only ODT microscope, as shown in Fig. 5.1. For each  $i^{th}$  angle of plane wave illumination through a refractive index volume  $O(\mathbf{r})$ , a different known phase mask

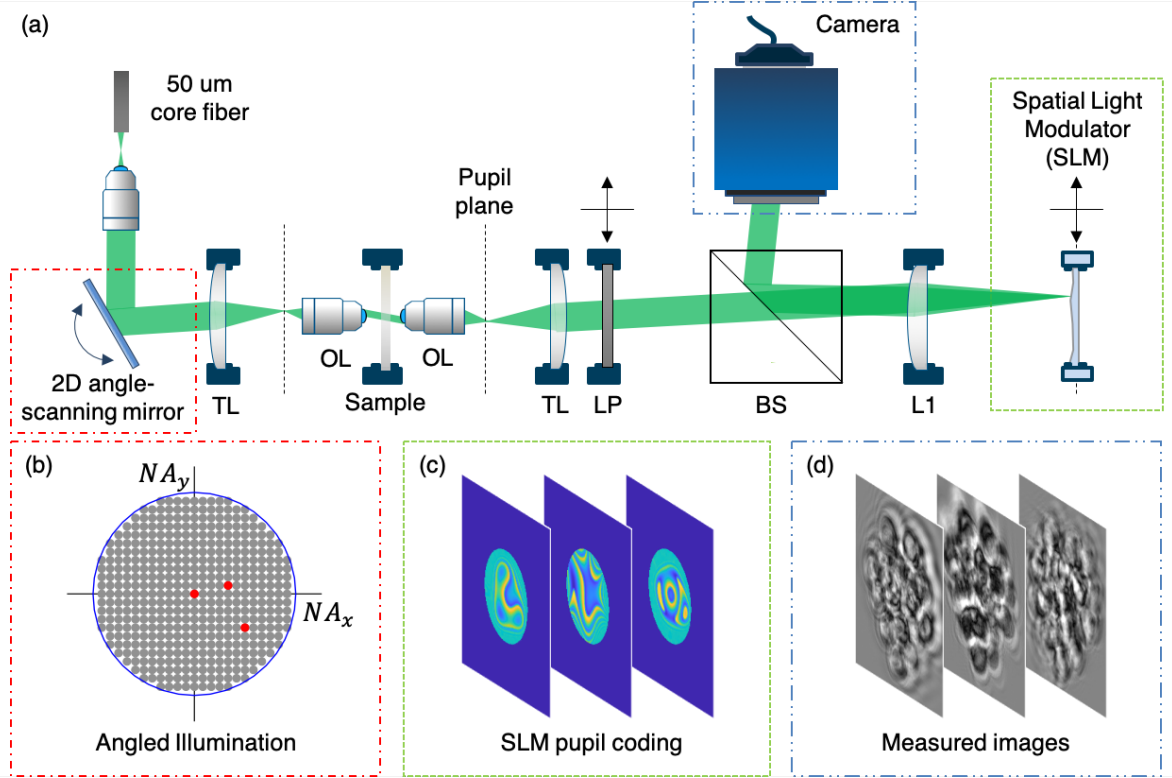


Figure 5.1: Joint illumination- and detection-side coding captures diverse measurements for improved 3D refractive index reconstructions. (a) A 2D angle-scanning servo mirror assembly provides angled illumination through a  $50\times$ , 0.8 numerical aperture (NA) objective lens (OL) and 180 mm tube lens (TL). An identical  $50\times$ , 0.8 NA objective and 180 mm tube lens are used to image the sample. A linear polarizer (LP) selects the polarization aligned to the modulation axis of the LCOS phase spatial light modulator (SLM). The light passes through a beamsplitter (BS) and through a 300 mm lens (L1), which Fourier transforms the signal. The SLM is modulated to code the phase of the conjugate pupil plane, and the final signal is reflected, Fourier transformed at L1, and imaged at the camera plane. (b) A map of simulated angled illumination, with three representative angles shown in red and the objective NA shown in blue. (c) Three representative random Zernike basis pupil phase coding masks displayed on the SLM. (d) Three representative simulated measurements showing measurement diversity.

$\tilde{M}_i(\mathbf{k}) = \exp j\phi_i(\mathbf{k})$  is displayed in the pupil plane, introducing a unique pupil coding for each measurement, where  $\mathbf{r}$  and  $\mathbf{k}$  are image- and spatial frequency-space coordinates. Under this system, the  $i^{th}$  measured intensity  $I_i(\mathbf{r})$  is given by:

$$I_i(\mathbf{r}) = |\mathcal{F}^{-1} \left\{ \mathcal{F} \{S_i(O(\mathbf{r}))\} \tilde{P}(\mathbf{k}) \tilde{M}_i(\mathbf{k}) \right\}|^2 \quad (5.1)$$

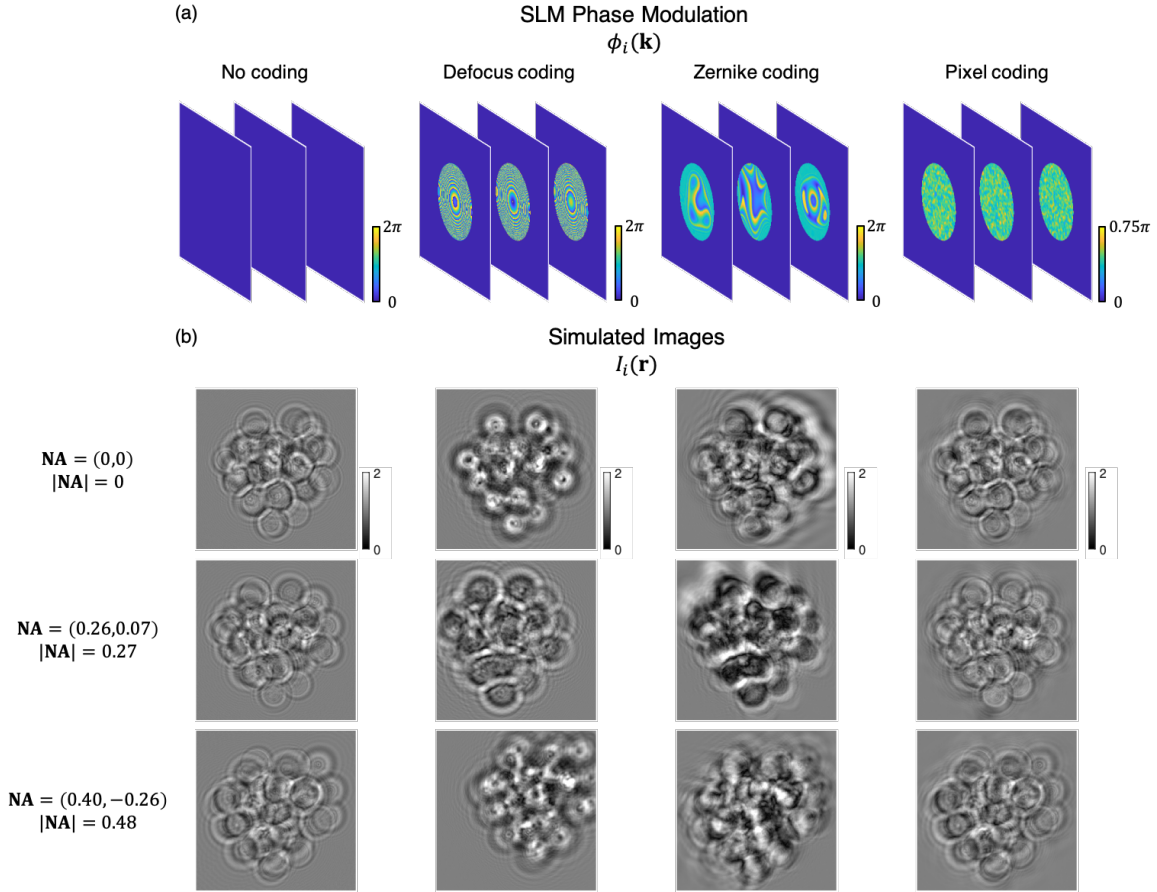


Figure 5.2: (a) Example SLM phase masks  $\phi_i(\mathbf{k})$  and (b) respective simulated measured images  $I_i(\mathbf{r})$  at illumination NA's 0, 0.27, 0.48 are displayed for no coding, random pixel coding, random Zernike coding, and random defocus coding.

where  $\mathcal{F}\{\cdot\}$  and  $\mathcal{F}^{-1}\{\cdot\}$  are the Fourier transform and inverse Fourier transform, respectively;  $S_i(\cdot)$  is the forward light scattering operator of the  $i^{\text{th}}$  angled plane wave illumination; and  $P(\mathbf{k})$  is the pupil function of the imaging system. We use the multislice forward propagation algorithm for the scattering operator  $S_i(\cdot)$  to allow for thicker objects with more scattering, as described in Chapter 4.

The object reconstruction algorithm is given by the optimization problem

$$\hat{O}(\mathbf{r}) = \operatorname{argmin}_{O(\mathbf{r})} \sum_i \left\| \left\| \mathcal{F}^{-1} \left\{ \mathcal{F} \{ S_i(O(\mathbf{r})) \} \tilde{P}(\mathbf{k}) \tilde{M}_i(\mathbf{k}) \right\} - \sqrt{I_i(\mathbf{r})} \right\|_2 \right\|^2 + \alpha \mathcal{P}(O(\mathbf{r})), \quad (5.2)$$

where  $\mathcal{P}(O(\mathbf{r}))$  is a prior penalty that can be chosen to constrain the solution space of  $O(\mathbf{r})$ , and  $\alpha$  is a tunable regularization parameter. We solve this optimization problem using a fast

iterative shrinkage-thresholding algorithm (FISTA) [15]. We also utilize a joint optimization of the objective pupil function  $\tilde{P}(\mathbf{k})$ , which we find improves experimental results, as the objective pupil function is imperfectly known.

This optimization problem is highly nonconvex, meaning that many local minima exist that can satisfy the data consistency penalty but may produce sub-optimal reconstructions that do not accurately represent the sample’s true refractive index distribution. Experimentally, we find that the most common local minima in traditional ODT reconstructions capture the high spatial frequencies (i.e., the high-resolution edges) of the object  $O$  well but do not capture the low spatial frequencies (i.e., the internal RI values). In particular, in angle-coded intensity-only ODT, the reconstructions under a low-angle illumination constraint do not reconstruct low spatial frequencies well, giving inaccurate reconstructions. A low-angle illumination constraint exists when the maximum angle of illumination is approximately 85% or lower than the numerical aperture of the imaging objective,  $NA_{illum,max} < \sim 0.85NA_{obj}$ . As discussed in Chapter 5, intensity-only ODT therefore requires high-angle illumination (i.e.,  $NA_{illum,max} \approx NA_{obj}$ ), increasing the complexity of the imaging system to guarantee these high illumination angles, which in turn can make the imaging system more constrained and difficult to use.

This optimization problem is highly nonconvex, meaning that many local minima exist that satisfy the data consistency penalty but produce sub-optimal reconstructions that do not represent the true refractive index distribution well. Experimentally, we find that the most common local minima in traditional ODT reconstructions capture the high spatial frequencies (i.e., the high-resolution edges) of the object  $O$  well but do not capture the low spatial frequencies (i.e., the internal RI values). In particular, in traditional, angle-coded only intensity ODT, the reconstructions under a low-angle illumination constraint do not reconstruct low spatial frequencies well, giving inaccurate reconstructions. A low-angle illumination constraint exists when the maximum angle of illumination is approximately 85% or lower than the numerical aperture of the imaging objective,  $NA_{illum,max} < \sim 0.85NA_{obj}$ .<sup>2</sup> This means that the traditional intensity-only ODT imaging system requires high-angle illumination (i.e.,  $NA_{illum,max} \approx NA_{obj}$ ), increasing the complexity of the imaging system and making it more difficult to use in practical settings. Conversely, the proposed pupil-coded intensity ODT system removes this constraint and can reconstruct low spatial frequencies even when limited to low angles of illumination.

When faced with an optimization reconstruction that is converging to a sub-optimal local minima for a given sample, there are two main approaches to improving the reconstruction result. First, a prior penalty  $\mathcal{P}(O(\mathbf{r}))$  that is well-matched to the sample parameters can be applied to further constrain the optimization and eliminate spurious local minima. However, these penalties are object-specific and therefore are not always sufficient or applicable, especially thicker, more complex samples. Second, more diverse data can be measured to make

---

<sup>2</sup>The maximum value of  $NA_{illum,max}$  where the traditional intensity-only ODT reconstruction degrades is given as  $\sim 0.85NA_{obj}$  because it will change depending on the sample and the regularization parameters used in the reconstruction. However, we have observed that across objects and regularization parameters,  $NA_{illum,max} = 0.85NA_{obj}$  typically results in degraded results for traditional intensity-only ODT.

the reconstruction more well-conditioned. In traditional ODT systems, however, collecting more data is analogous to taking images at more densely packed angles of illumination. Intuitively, we can see that there are diminishing returns in this system as we add more closely-spaced angles of illumination because these angles encode very similar information about the object, which is sub-optimal for improved reconstructions. The addition of a dynamic coding element in pupil-coded intensity ODT increases the controllable degrees of freedom available in the system for increasing the diversity of measurements from a given sample. This system produces higher contrast, more diverse measurements  $I_i$  for better-conditioned reconstructions across a wide variety of samples.

In this chapter, we demonstrate the pupil-coded intensity ODT method with sets of phase masks based on random defocus values, random coefficients on a Zernike basis, and random pixel values, respectively, to explore the best pupil phase mask properties for 3D RI imaging (Fig. 5.2(a)). Across all three phase mask types, we find that including dynamic detection-side pupil coding increases the diversity of our measurements, as seen by the increased contrast across representative images in each dataset in Fig. 5.2(b) and corroborated by a spatial entropy metric discussed in Sec. 5.5.2. This increased measurement diversity means that fewer images at lower maximum angles of illumination are required for high-quality reconstructions with pupil-coded intensity ODT. We also find that optimization of these 3D RI reconstructions converges faster than the traditional intensity-only ODT method due to the system’s increased measurement diversity.

### 5.2.1 Phase Mask Formulation

We investigated the proposed pupil-coded intensity ODT method with phase masks from random coefficients on the defocus, Zernike polynomial, and pixel bases. Each set of phase masks is formulated separately, as discussed below. Within each set of phase masks, an  $[N_{im} \times N_{im}]$  pixel phase mask  $\phi_i(\mathbf{k})$  are generated for each  $i^{th}$  angle of illumination, where the  $N_{im}$  is the lateral pixel dimension of the reconstruction volume. The phase mask coefficients for each basis are drawn from a uniform distribution to ensure high measurement diversity. The pupil coding masks are given by  $\tilde{M}_i(\mathbf{k}) = \exp(j\phi_i(\mathbf{k}))$ . The phase generation process for each mask type is given below. For each basis, the scaling of the uniform distribution is chosen heuristically. Typical values are given below. Example masks and simulated measurements from each set of phase mask types are shown in Fig. 5.2.

The phase masks are generated with the constraints of the LCOS phase-only SLM used to modulate the pupil function. The phase masks are first generated at the lateral reconstruction dimension,  $[N_{im} \times N_{im}]$ , where typically  $N_{im} = 500$  pixels. All experimental masks are wrapped to  $(0, 2\pi)$  radians to fit within the SLM’s modulation range and then Gaussian filtered, typically with  $\sigma = 4$ , to avoid fringing field effects on the SLM [81, 146, 167, 189], which result in nonidealities in the displayed phase at large phase changes due to physical properties of the SLM’s pixelated liquid-crystal display. The phase masks are then upsampled to the SLM dimension,  $[1024 \times 1280]$  by a factor of  $du_{camera}/du_{SLM}$ , giving the SLM

display phase  $\Phi_i(\mathbf{k})$ . The reconstruction and SLM frequency space pixel size are given by

$$\begin{aligned} du_{camera} &= \frac{1}{N \frac{d_{camera}}{mag}} \\ du_{SLM} &= \frac{d_{SLM} \cdot mag}{\lambda \cdot f_{SLM}}, \end{aligned}$$

where  $d_{camera}$  and  $d_{SLM}$  are the pixel size of the camera and SLM, respectively;  $mag$  is the system magnification;  $f_{SLM}$  is the focal length of the Fourier transform lens before the SLM; and  $\lambda$  is the wavelength of the illumination. In experiment, SLM phase masks  $\Phi_i(\mathbf{k})$  are then translated to SLM grey levels via an experimentally calibrated phase mapping process described in Sec. 5.4.1.

### Defocus Basis

Defocus basis mask phases are created using the angular spectrum propagation kernel [73] for a set of distances  $d_i$  chosen from the uniform random distribution,  $d_i \in U(-15 \mu\text{m}, 15 \mu\text{m})$ .

$$\phi_{\text{defocus},i}(\mathbf{k}) = 2\pi d_i \sqrt{\lambda^{-2} - \mathbf{k}^2} \quad (5.3)$$

The total depth of  $30 \mu\text{m}$  was chosen because it provided for a relatively large focus change, leading to high contrast between measurements, but small enough that signal was primarily kept within the chosen field of view. Phase masks were blurred with a Gaussian filter  $\sigma = 4$  in experiment.

### Zernike Basis

Zernike basis phase masks are generated by multiplying uniform random coefficients  $c_{p,i} \in U$  by Zernike polynomials for  $p_z = 15$  Zernike modes, giving

$$\phi_{\text{zernike},i}(\mathbf{k}) = \sum_{p=0}^{p_z} c_{p,i} Z_p(\rho, \theta), \quad (5.4)$$

where  $Z_p(\rho, \theta)$  are the Zernike polynomials,  $\rho$  and  $\theta$  are polar coordinates, and  $p$  is the linear index of the polynomials, which are typically denoted by two indices  $(n, m)$ .<sup>3</sup> Following the implementation in [224], we define:

$$\begin{aligned} n &= \text{ceil}\left(\frac{-3 + \sqrt{9 + 8p}}{2}\right) \\ m &= 2p - n(n + 2) \\ Z_n^{m < 0}(\rho, \theta) &= R_n^m(\rho) \sin(|m|\theta) \\ Z_n^{m \geq 0}(\rho, \theta) &= R_n^m(\rho) \cos(|m|\theta) \end{aligned}$$

---

<sup>3</sup> $n$  here is disambiguated from the other usages in this chapter, where it denotes refractive index.

where the radial functions  $R_n^m(\rho)$  are given by

$$R_n^m(\rho) = \begin{cases} \sum_{l=0}^{(n-m)/2} \frac{(-1)^l (n-l)!}{l! [\frac{1}{2}(n+m)-l]! [\frac{1}{2}(n-m)-l]!} \rho^{n-2l}, & \text{for } n-m \text{ even} \\ 0, & \text{for } n-m \text{ odd} \end{cases}$$

In simulation, typically  $c_{p,i} \in U(-\pi, \pi)$ . However, in experiment we found these large coefficient values led to many phase wrapping points between 0 and  $2\pi$ , which in turn created many experimental nonidealities due to fringing field effects on the SLM. In experiment, we therefore chose  $c_{p,i} \in U(-0.5, 0.5)$  and additionally scaled the NA and pixel size used in the creation of the Zernike polynomials by a factor of 1.2 to effectively zoom in on the center of the Zernike polynomials. This eliminated the edge of the high-NA Zernikes, which tend to exhibit large phase wrapping and therefore large experimental SLM model mismatch, while still providing phase modulation for the full  $NA_{obj}$  on the SLM. Phase masks were blurred with a Gaussian filter  $\sigma = 4$  in both simulation and experiment.

### Pixel Basis

Each random pixel phase mask is generated by Gaussian filtering a random matrix from the continuous uniform distribution,  $U(0, 2\pi)$ , where  $*$  denotes convolution and  $g_\sigma(x, y) = \frac{1}{2\pi\sigma} e^{-\frac{x^2+y^2}{2\sigma^2}}$ .

$$\phi_{pixel,i}(\mathbf{k}) = U(0, 2\pi)(\mathbf{k}) * g_\sigma(\mathbf{k}) \quad (5.5)$$

We find in both simulation and experiment that  $\sigma = 4$  provides sufficiently diverse measurements without amplifying noise.

### 5.2.2 Utilizing Randomness

The choice of random coefficients for the pupil phase masks presented in this chapter was based on many recent imaging systems designed under compressed sensing principles [12, 55, 112, 208, 230], which use random coding mechanisms. These compressed sensing systems exploit signal sparsity and sensing system incoherence, which is often obtained through random coding mechanisms, to guarantee reconstruction with a lower data sampling rate than suggested by Shannon-Nyquist sampling theorem [23]. However, we note that proposed pupil-coding ODT system proposed in this chapter does not directly utilize compressed sensing, which requires that object sparsity be enforced in the reconstruction.

## 5.3 Simulation Results

In order to investigate the effectiveness of the proposed pupil-coded intensity ODT method for thick objects, a structured refractive index phantom was simulated with similar features as cell clusters in embryo growth [123], as seen in Fig. 5.3. Cell clusters of varying size were simulated to observe the effect of increased multiple scattering, but similar results

were observed across all simulated cell cluster sizes. Results are shown for a cluster of 40 spherical cells positioned inside a  $55\ \mu\text{m}$  cube using Poisson disk sampling [22], which provides a random, non-overlapping packing of the cells in 3D. An additional constraint that the cells be packed within a sphere centered within the volume was imposed to ensure the phantom was tightly clustered. Each cell were simulated with a  $10\ \mu\text{m}$  diameter cell body of refractive index  $n = 1.345$ , a randomly placed  $4\ \mu\text{m}$  diameter nucleus ( $n = 1.34$ ), and ten randomly placed  $1\ \mu\text{m}$  diameter organelles ( $n = 1.35$ ) in a uniform aqueous background ( $n = 1.33$ ) [13, 131, 197]. The cells were simulated with  $100\ \text{nm}$  resolution.

The multislice (a.k.a beam propagation) forward model was used to simulate angled coherent plane-wave illumination at  $\lambda = 0.532\ \mu\text{m}$  through the simulated RI volume. The forward simulation was performed at full,  $100\ \text{nm}$  pixel size inside a  $2\times$  padded volume to reduce circular boundary artifacts and ensure that the forward simulation was done at a more accurate size scale than the reconstruction. Forward simulations were performed for a grid of illumination angles  $(\theta_x, \theta_y)$ , related to numerical aperture (NA) by  $NA = n \sin(\theta)$  and spatial frequency by  $k = 2\pi \frac{NA}{\lambda} = 2\pi \frac{n \sin \theta}{\lambda}$ , where  $n$  is the refractive index. The maximum illumination angle was simulated at  $NA = 0.8$  with the spacing between illumination grid points  $\Delta NA = 0.05$ .

This forward simulation produced electric fields  $u_i(\mathbf{r})$  at the last plane of the simulated phantom volume, which were then simulated through objectives with various numerical apertures. The magnification of these virtual objectives were chosen to avoid aliasing with camera pixel size  $d_{camera} = 6.5\ \mu\text{m}$ . The magnification was rounded up to a multiple of 5 for simplicity. In particular, we here present results from a  $0.8\ \text{NA}$ ,  $mag = 40\times$  objective and a  $0.5\ \text{NA}$ ,  $mag = 25\times$  objective. The electric fields were filtered by the objective's low-pass filter in Fourier space, then downsampled to the pixel size of the reconstruction,  $d_{recon} = d_{camera}/mag$ . For each  $i^{th}$  angle of illumination, the  $i^{th}$  SLM pupil mask  $\tilde{M}_i(\mathbf{k})$  was applied via a Fourier space multiplication. New sets of random masks were generated for each reconstruction with the three chosen pupil coding bases (*i.e.*, defocus, Zernike, and pixel). For the comparison case with no SLM coding, a phase mask of all zeros was applied to each illumination angle. The intensity of the electric field was then taken as the measured image at the camera plane,  $I_i(\mathbf{r})$ . This process was also performed for a constant background volume of refractive index  $n = 1.33$  to give background intensity measurements  $I_{bk,i}(\mathbf{r})$ . The measured amplitude through the sample  $|I_i(\mathbf{r})|$  was divided by the background amplitude  $|I_{bk,i}(\mathbf{r})|$  to reduce spurious structured background artifacts created by FFT boundary conditions and to scale each measured amplitude to have a background value of roughly unity. Random Gaussian noise with standard deviation  $\sigma$  was then added to each simulated measurement. Example simulated measurements can be seen in Fig. 5.2(b).

Reconstructions based on these simulated measurements were performed following Eq. 5.2. We compare these reconstructed RI volumes to ground truth under a variety of illumination, reconstruction, and pupil coding conditions, discussed below, to investigate the improvements offered by the proposed system.

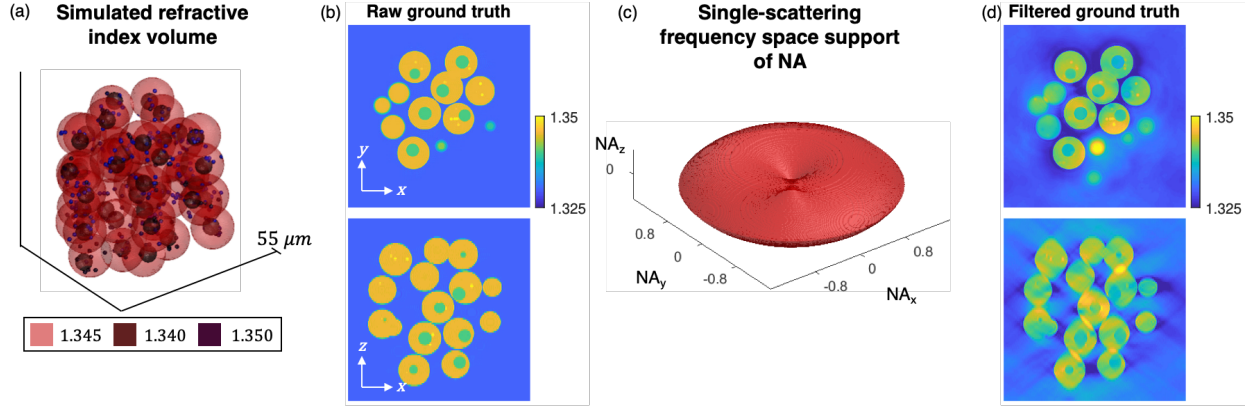


Figure 5.3: 3D refractive index of a simulated sample consisting of a 40 cell cluster. (a) 3D view of simulated cell cluster RI distribution. (b)  $xy$  and  $xz$  slices of ground truth RI volume. (c) Maximum 3D frequency space support for a 0.8 NA objective ( $\lambda = 0.532 \mu\text{m}$ ) under an under an Ewald sphere single-scattering assumption with  $NA_{illum,max} = NA_{obj}$ . (d) Filtered ground truth RI, representing the best possible reconstruction with the chosen objective and illumination scanning under a single-scattering assumption.

### 5.3.1 Ground Truth Comparisons

We calculated the root-mean-squared error (RMSE) of each reconstruction to the raw ground truth refractive index to quantify the reconstruction quality. The raw ground truth RI volume was downsampled to the reconstruction size, shown for the 0.8 NA objective system in Fig. 5.3(b).

We note that due to the “missing cone” problem in 3D RI imaging, wherein high axial spatial frequencies are not captured at low lateral spatial frequencies due to the lowpass filtering by the objective lens, a better comparison volume is the NA-filtered ground truth refractive index, shown in Fig. 5.3(d). This NA-filtered ground truth volume reflects the best possible reconstruction under a single-scattering assumption for a given objective NA. We construct the NA-filtered Fourier support of our system by considering an Ewald sphere formulation [62, 63, 148]. Under this formulation, the 3D Fourier space support of a plane wave at angle  $(NA_x, NA_y)$  scattered through an object and imaged by an objective of numerical aperture  $NA_{obj}$  is described by an arc in 3D  $\mathbf{k}$ -space with spherical radius  $k_m = \frac{2\pi n}{\lambda}$ , lateral radius  $2\pi \frac{NA_{obj}}{\lambda}$  (defining the maximum angle imaged through the system), and centered at

$$\begin{aligned}
k_x &= \frac{2\pi n}{\lambda} NA_x \\
k_y &= \frac{2\pi n}{\lambda} NA_y \\
k_z &= \frac{2\pi n}{\lambda} (1 - \sqrt{1 - NA_x^2 - NA_y^2})
\end{aligned}$$

Scanning illumination angles is analogous to scanning this arc in 3D Fourier space, with a captured image at a certain illumination angle containing information from that region of Fourier space. Assuming an illumination angle-scanning system where the maximum possible illumination angle is the same as the objective NA,  $NA_{obj}$ , the maximum possible frequency support is therefore described by the overlap of two toroids given by:

$$\left( \frac{2\pi NA_{obj}}{\lambda_n} - \sqrt{\mathbf{k}_x^2 + \mathbf{k}_y^2} \right)^2 + \left( \mathbf{k}_z \pm \frac{2\pi}{\lambda_n} \sqrt{1 - NA_{obj}^2} \right)^2 \leq \left( \frac{2\pi}{\lambda_n} \right)^2 \quad (5.6)$$

where  $\lambda_n = \frac{\lambda}{n}$  is the wavelength in the medium. The resulting 3D Fourier space support for a 0.8 NA objective is shown in Fig. 5.3(c). We note that since the reconstructions presented in this chapter are based off of the multiple-scattering multislice model, it is theoretically possible that more information can be reconstructed with the multislice model than the NA-filtered ground truth volume shown here, given that multiple scattering can send high spatial frequency information through the lowpass filter of an objective lens [34, 35, 182, 234]. However, in general the NA-filtered ground truth presents a reasonable comparison for simulations performed with the relevant objective NA. We therefore also present the RMSE of the reconstructions compared to the NA-filtered ground truth RI volume.

### 5.3.2 Limited Illumination

With illumination angles up to the NA of the objective ( $NA_{illum,max} = NA_{obj}$ ), sufficient optimization algorithm iterations to reach convergence of the cost function (150 iterations), and low noise conditions ( $\sigma = 0.001$ ), we show in Fig. 5.4(a) that both the previous, no SLM coding method and the proposed SLM pupil coding methods achieve reconstructions comparable to the NA-filtered ground truth. The convergence to both the filtered and raw ground truth occurs faster using the proposed pupil-coding method, and the Zernike coding basis has the lowest RMSE across all datasets, as seen in Fig. 5.4(c-d).

As these results show, traditional intensity-only ODT method without pupil coding requires high illumination angles to measure and reconstruct low spatial frequency information about the sample's 3D RI distribution. Unfortunately, designing an illumination system that can create coherent plane waves at angles with  $NA_{illum,max} = NA_{obj}$  creates large design constraints, especially in systems with high-NA objectives for better axial resolution. While

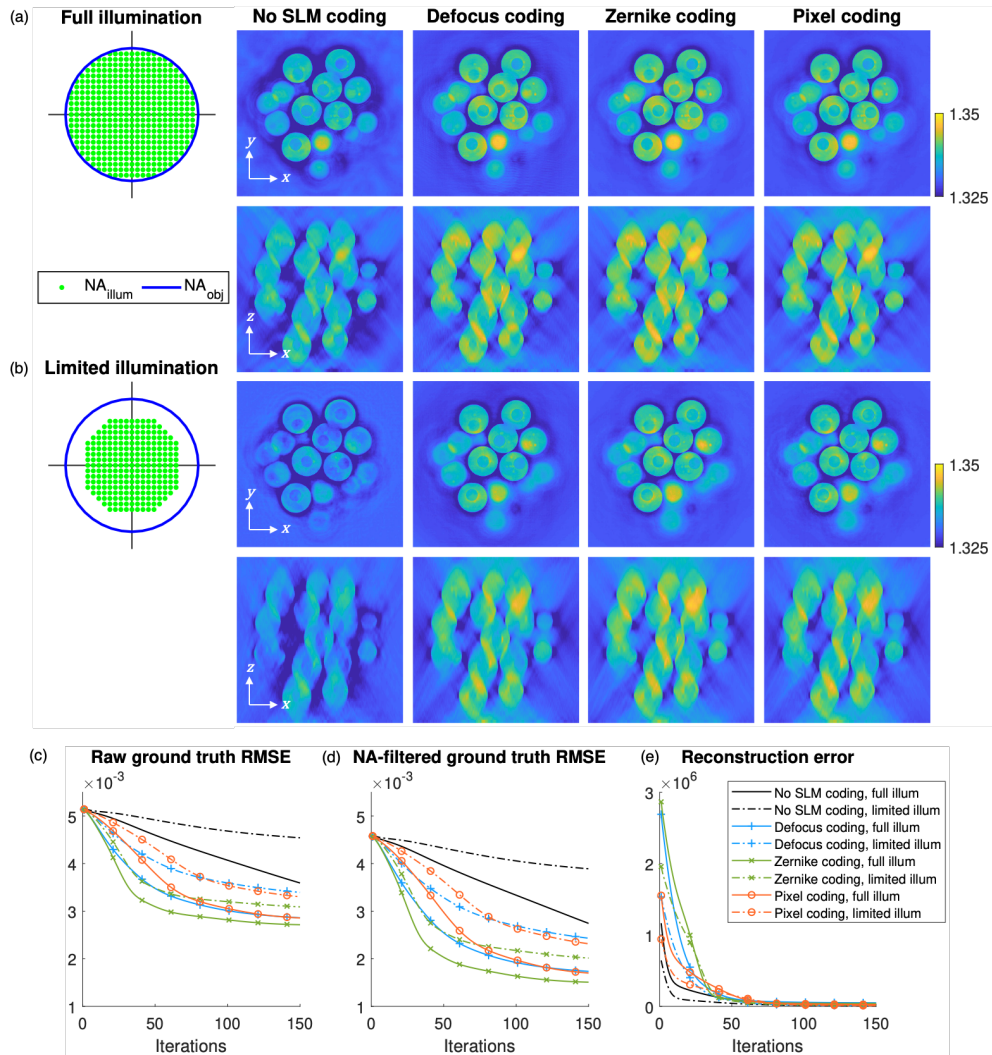


Figure 5.4: Reconstructed simulated volumes under (a) full, high-angle illumination and (b) limited, low-angle illumination conditions for the traditional system (no SLM coding) and proposed system (defocus, Zernike, and pixel coding).  $xy$  and  $xz$  slices into the volumes are shown for each. Reconstructions have more accurate low spatial frequency content (i.e. better refractive index estimation) when pupil coding is used, and the difference is especially stark in the limited illumination condition (b). The plots of RMSE from the raw ground truth volume (c) and filtered ground truth volume (d) show this improved reconstruction, and also show that a reasonable reconstruction is obtained with fewer iterations under the proposed system, regardless of pupil coding basis. (e) The reconstruction cost function shows that all reconstructions converge. All simulations were run with a 0.8 NA,  $40\times$  objective, and  $\lambda = 0.532\ \mu\text{m}$  for 150 iterations and  $\sigma = 0.001$  of additive Gaussian noise.

planar LED arrays could provide high-NA illumination, they have a large illumination intensity fall-off at high incident angles. A domed illumination source [159, 173, 172, 198], such as the quasi-dome LED array [173], can provide high-NA illumination without this intensity fall-off. In practice, however, we find that the quasi-dome LED array has relatively low-intensity illumination, requiring prohibitively long exposure times for high-NA objectives in the proposed system. Therefore a dual-objective lens system, with two objectives on either side of the sample as seen in Fig. 5.1, is often the most practical for simultaneously illuminating and detecting at high-NA. But as objective working distance generally decreases with increasing NA, using identical objectives on either side of the sample in order to obtain high-NA illumination constrains the physical extent of the sample and can be therefore be practically difficult to use.

Reducing the requirement that the maximum illumination angle must be near the NA of the imaging objective for high-quality RI reconstructions would therefore be extremely helpful in 3D RI imaging system design. We see in Fig. 5.4(b) that this goal is obtained with the proposed method. Under a limited, low-angle illumination condition where the maximum illumination  $NA_{illumination} \leq 0.75NA_{obj}$ , we see that good reconstructions are obtained using the defocus, Zernike, and pixel random pupil coding. Conversely, the traditional intensity-only ODT system without SLM coding performs poorly, particularly failing to reconstruct the low spatial frequencies of the sample. While the RMSE from the ground truth is higher in all cases under the limited illumination condition, the proposed method reconstructions have lower RMSE after 150 iterations than the traditional, no coding method across both the full- and limited-illumination conditions (Fig. 5.4(c)). This reduction in the requirement for high-angle illumination reduces constraints on the imaging system, which could make 3D RI imaging systems easier to use.

The proposed method’s improved reconstruction under the limited illumination condition also represents a reduction in the measured data, from 437 images in the full illumination condition to 249 images in the limited illumination condition. This data reduction leads to a commensurate reduction in capture time and processing time, which scales with the dataset size. This means that under the proposed system, since we are better capturing the data we need for the reconstruction, we can get better reconstructions with less data, capture time, and processing time, while also making the system more robust to changes in the maximum available angle of illumination  $NA_{illum,max}$ . The proposed system therefore offers significant improvements to practical 3D RI imaging. However, we note that the limited illumination reconstructions cannot reach the same low RMSE offered by the proposed method under the full illumination, since the axial resolution is reduced by limiting the illumination NA.

### 5.3.3 Limited Computation

We show that the proposed method approaches the ground truth refractive index in fewer iterations than the previous method without pupil coding. In Fig. 5.5(a), we present reconstructed 3D RI volumes at 50 iterations of the optimization algorithm under the full, high-angle illumination condition, representing a limited-computation condition where the

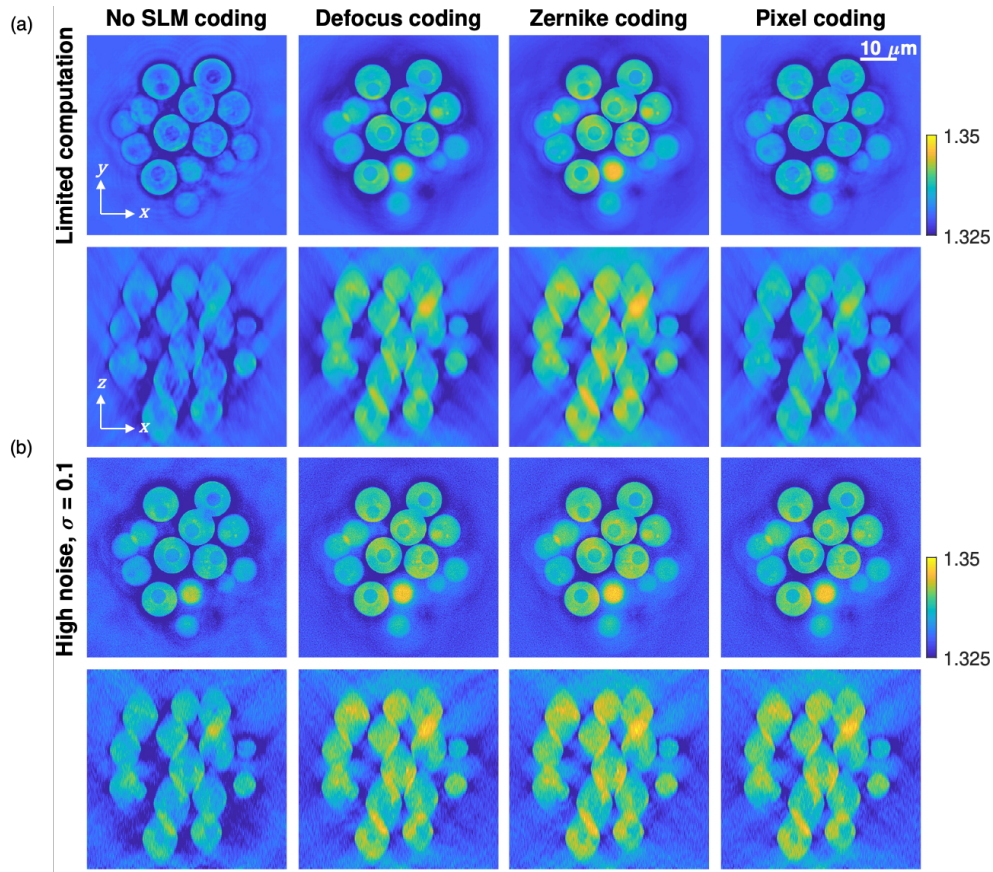


Figure 5.5: Reconstructed simulated volumes under (a) a 50 iteration, limited-computation condition with low noise ( $\sigma = 0.001$ ) and (b) a full-computation (150 iterations), high-noise condition with  $\sigma = 0.1$  of Gaussian noise added to each measurement. Both (a) and (b) were reconstructed under the full, high-angle illumination condition for  $\text{NA} = 0.8$ ,  $\lambda = 0.532 \mu\text{m}$ . (a) shows that all pupil coding bases under the proposed method reconstruct low spatial frequency components sooner in the iterative optimization process, and thus begin to converge to ground truth values with less required computation compared to the previous system without pupil coding. (b) shows that increased additive Gaussian noise equally affects reconstructions with and without pupil coding.

optimization algorithm is stopped early. We see in this case that the proposed method has better reconstructions than the previous, no coding method. The Zernike coding basis shows particularly good results. This test demonstrates that the proposed method is better-conditioned to reconstruct the low spatial frequency components of the 3D RI volume, since it converges more quickly to a high-quality result. Additionally, this result could be used to reduce the computation time required for large volumes via early stopping of the

optimization algorithm.

### 5.3.4 High Noise

We also present reconstructions with high,  $\sigma = 0.1$  additive Gaussian noise in Fig. 5.5(b). These reconstructions were performed with full, high-angle illumination and full, 150 iteration computation. We see that while the noise degrades the resultant reconstructions, it does so evenly across the different methods, showing that noise is not disproportionately amplified by the reconstruction under the proposed method.

### 5.3.5 Mask Diversity Requirements

We hypothesized that having a diverse set of random phase masks under the proposed method increases the proposed system’s measurement diversity, giving the reconstruction improvements shown above. While clearly the addition of random phase masks has beneficial consequences, it is unclear how many distinct random masks are needed to provide these benefits.

We simulated measurements for different numbers of distinct masks for each pupil coding basis under a limited, low-angle illumination condition to see how many distinct phase masks are required for high-quality reconstructions in pupil-coded intensity ODT. For each simulation,  $C$  distinct phase masks of the relevant pupil coding basis were generated and randomly assigned to each  $i^{\text{th}}$  measurement  $I_i$ . We simulated reconstructions for  $C = [1, 2, 5, 10, 25, 50, 75, 97]$  distinct masks across 97 images with 97 distinct angles of illumination. To reduce the computational cost of the simulation, we simulated with a 0.5 NA, 25 $\times$  objective lens.

Reconstructions are shown in Fig. 5.6. Both visual inspection and RMSE plots show that only one distinct random mask is needed to obtain a good-quality reconstruction under the limited illumination condition for the Zernike and pixel bases, while the defocus bases requires  $\approx 5$  or more distinct masks for good-quality reconstructions. This is a surprising result, as it suggests that only a single phase mask of certain properties is needed to obtain the necessary measurement diversity in the dataset, unlike phase diversity systems, which require two distinct phase masks. We theorize that this is due to the object spectrum being scanned across the pupil plane by the angled plane-wave illumination under the Fourier shift theorem. If the chosen single pupil phase mask varies widely across the pupil plane, the effective pupil coding applied to the object spectrum at each angle will be effectively diverse across measurements. We further explore this result by analyzing the system transfer functions for a single, static pupil phase mask in Sec. 5.5.1.

This result also has large practical implications. In order to achieve dynamic pupil coding experimentally, we must use a spatial light modulator in the pupil plane of the imaging system, which increases the imaging system complexity. However, this simulated result suggests that we could augment a traditional angle-scanning ODT system with a single phase aberration, which could be applied through an engineered or off-the-shelf transmission

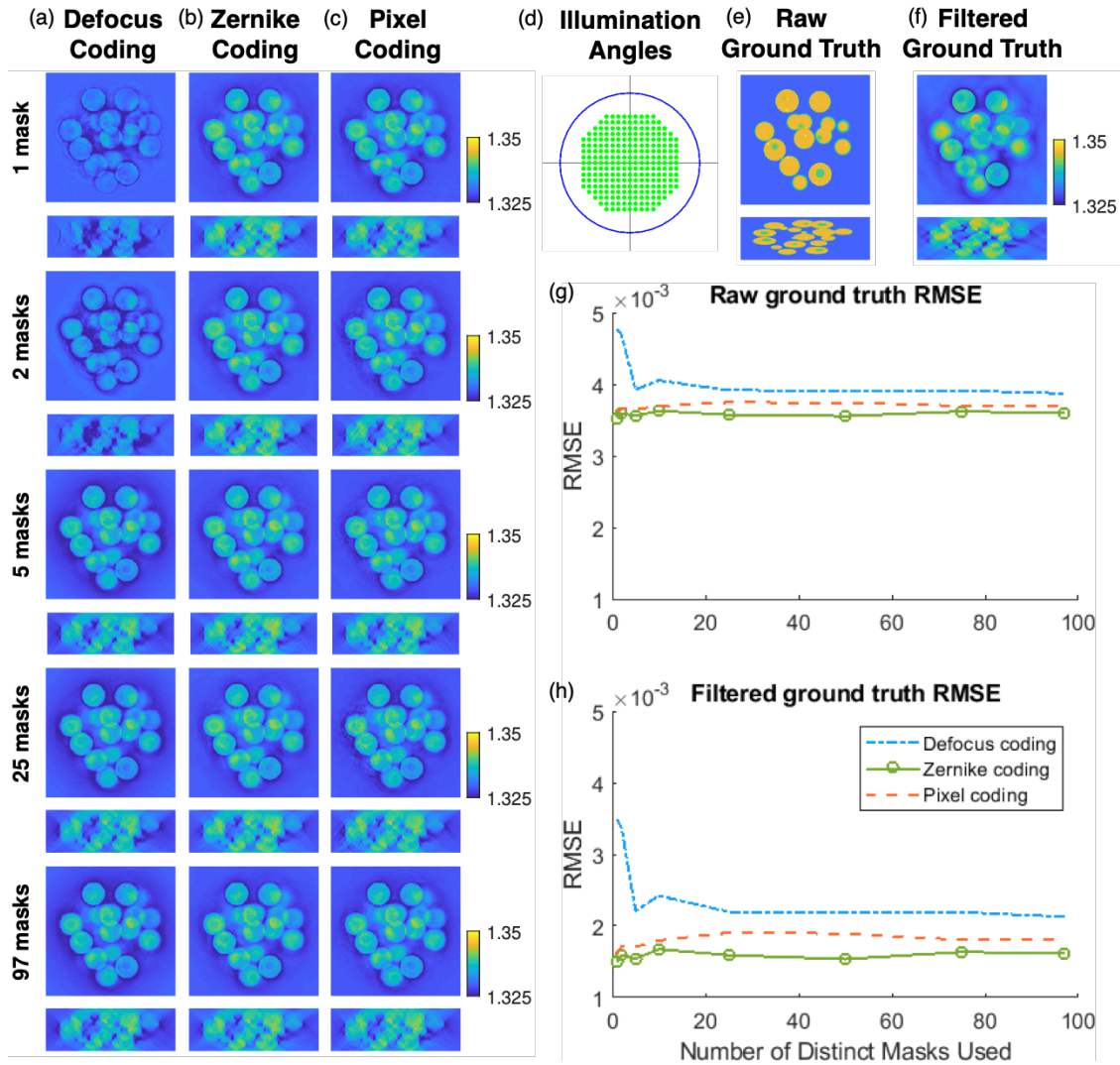


Figure 5.6: Reconstructed simulated volumes under a limited, low-angle illumination condition to evaluate the importance of number of distinct random phase masks used for each (a) defocus, (b) Zernike polynomial, and (c) pixel coding basis. All reconstructions are run with 150 iterations for a 0.5 NA objective,  $\lambda = 0.532 \mu\text{m}$ , with  $\sigma = 0.001$  of additive Gaussian noise. Comparative ground truth RI volume slices are shown in (d). The final RMSE of each reconstruction against the (e) filtered ground truth RI and (f) raw ground truth RI across number of distinct masks used in the simulation are shown. For the (a) defocus basis, we see that more than 25 distinct random phase masks are needed to reconstruct a high-quality result under the limited illumination condition. However, for the (b) Zernike polynomial basis and (c) pixel basis, only one distinct random mask is necessary for a high-quality reconstruction.

phase mask, or even using the native aberrations present in an objective lens. We explore the experimental implications further in the following section.

## 5.4 Experimental Results

A 50  $\mu\text{m}$  fiber-coupled LED source (Thorlabs M530F2) with wavelength  $\lambda = 530 \text{ nm}$  is beam-expanded and collimated using a Nikon Plan Apochromatic  $2\times$ , 0.1 NA objective, as shown in Fig. 5.1. A dual-axis mirror mount with DC servo motors (Thorlabs Z812 with Kinesis brushed motor controller) is used to angle the collimated beam at a conjugate imaging plane. The angled beam is relayed through the illumination-side objective (0.8 NA,  $50\times$ , working distance (w.d.) 1 mm Olympus M Plan Fluorite air objective) and 180 mm tube lens assembly to illuminate the sample with a coherent, angled plane wave. The light is modulated by the sample and imaged with the imaging objective and tube lens assembly. We opted for high-NA imaging and illumination objective lenses to obtain high resolution reconstructions in both the comparison reconstructions without SLM coding and the proposed system with SLM coding.

We used two imaging objective lenses in our experiments. A 0.75 NA,  $40\times$  Nikon Plan Fluorite, glass aberration-corrected air objective lens (w.d. 0.66 mm) with a 200 mm tube lens was used as the imaging objective for the comparison (no SLM coding) case. An uncorrected 0.8 NA,  $50\times$  Olympus M Plan Fluorite air objective with a 180 mm tube lens was used as the imaging objective for the proposed method with SLM pupil coding. This uncorrected objective lens exhibits strong aberrations when a #1.5 coverslip (0.17 mm thick glass) is placed on top of the sample (Fig. 5.7(i-j)). We present results with the aberrated 0.8 NA,  $50\times$  objective without SLM pupil coding to show that these glass-induced aberrations act as a single, well-chosen Zernike pupil phase coding that improves 3D RI reconstructions under low-angle illumination as predicted by simulations in Sec. 5.3.5.

A linear polarizer is placed close to the tube lens to linearly polarize the collimated light in the same direction as the SLM's modulation axis. A  $f_{L1} = 300 \text{ mm}$  lens performs a Fourier transform between the imaging plane and the pupil plane at the SLM's surface. The focal length  $f_{L1}$  focal length was chosen to increase the area modulated at the SLM from the objective's native pupil diameter to make the greatest possible use of the SLM's [12.8 mm  $\times$  16 mm] active area. An objective's native pupil diameter is given by

$$d_{obj} = 2NA_{obj} \frac{f_{tube}}{mag}, \quad (5.7)$$

where  $f_{tube}$  is the focal length of the tube lens. The  $f_{L1} = 300 \text{ mm}$  Fourier transform lens magnifies the pupil diameter, giving the pupil diameter at the SLM plane as

$$d_{obj \text{ at } SLM} = 2NA_{obj} \frac{f_{tube}}{mag} \left( \frac{f_{L1}}{f_{tube}} \right) = 2NA_{obj} \frac{f_{L1}}{mag}. \quad (5.8)$$

For the 0.75,  $40\times$  objective,  $d_{obj \text{ at } SLM, 0.75NA} = 11.25 \text{ mm}$ . For the 0.8,  $50\times$  objective,  $d_{obj \text{ at } SLM, 0.8NA} = 9.6 \text{ mm}$ .

The LCOS SLM (Hamamatsu X13138-01) modulates the phase of the incident light, which is then reflected and Fourier transformed again by the  $f_{L1} = 300$  mm lens. A beam-splitter (Thorlabs BS031) redirects the modulated signal to the camera (PCO Edge 5.5), where the intensity image is measured. For each  $i^{th}$  illumination angle, a different upsampled phase coding mask  $\Phi_i(\mathbf{k})$  is displayed in the pupil plane on the SLM for each coding basis. In the cases without applied SLM coding (both the comparison case and the case where the objective lens' native aberration supplies the phase coding element), the SLM displays a calibrated pattern corresponding to a uniform phase of 0 radians.

### 5.4.1 Calibration Methods

It is important that the experimental system be properly calibrated (*i.e.*, accurately represented in the reconstruction algorithm) for any computational imaging system to succeed. One of the primary sources of error in computational imaging systems is “model mismatch”, where the computational system model does not match the physical system, introducing error. One of the main sources of model mismatch comes from inaccurate representation of how the optical system modulates the light, which will be addressed in this section. Another source of model mismatch in 3D RI imaging is due to the light scattering model, which might trade off proper modeling of the light scattering physics through the object for computationally feasibility. Addressing model mismatch due to the choice of forward light scattering model is outside the scope of this chapter, but is an important area of inquiry.<sup>4</sup>

Calibrating the physical optical system has many practical challenges, described below. In particular, we describe how we calibrated the mapping between digital LCOS display values on the SLM to phase delays of the incident field; SLM fringing field effects [81, 146, 167, 189]; and the lateral, axial, and tilt positions of the SLM surface. Additionally, we describe how to calibrate other system parameters such as angle of illumination and the overall system pupil function, which predominantly includes aberrations from the imaging objective lens.

The success of the proposed method in part relies on the fact that we are introducing additional, known information into the reconstruction algorithm with pupil coding. As in traditional intensity-only ODT, we enforce that the angle of illumination for each measurement is known in the reconstruction algorithm. In the proposed method, we are additionally enforcing that each measurement was pupil-coded with a known unique phase mask. We theorize that this additional constraint on the measurement increases the ability of the optimization algorithm to infer important information about the sample being imaged with fewer overall measurements.

---

<sup>4</sup>See recent works that seek to reduce this model mismatch by developing new forward models [31, 129].

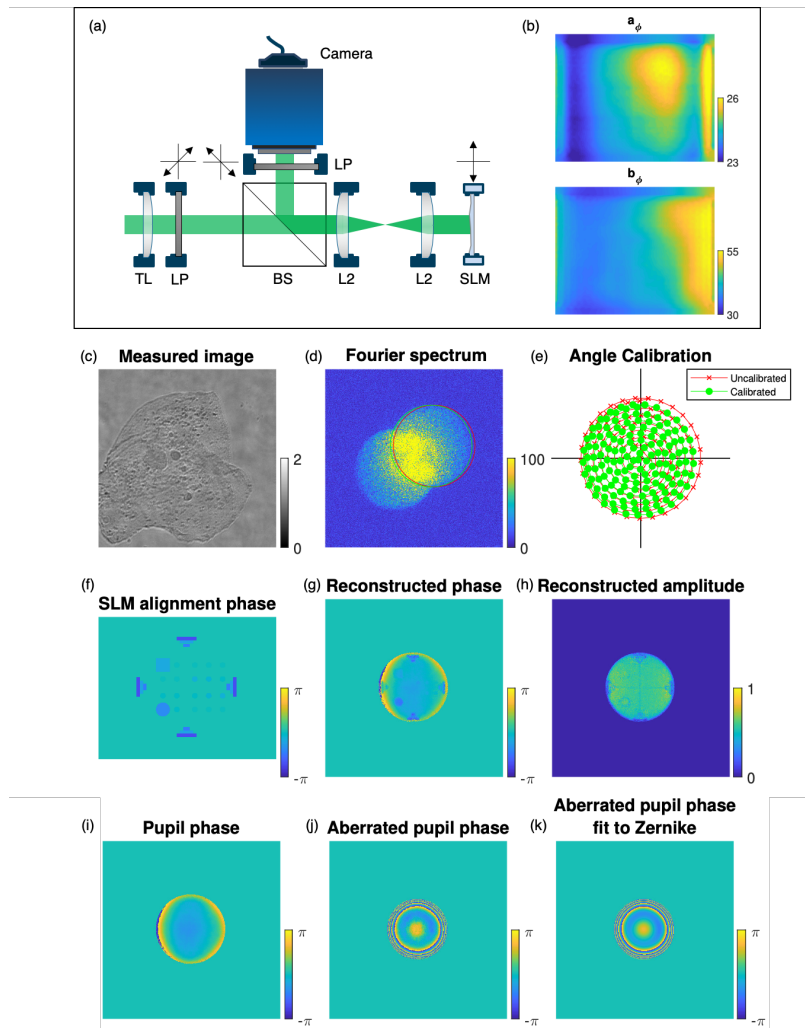


Figure 5.7: Calibration of the SLM, angled illumination, and objective pupil aberrations are needed for accurate reconstructions. (a) Modified set-up for calibration of the pixelated phase mapping parameters shown in (b), which map from desired phase delay  $\Phi$  to SLM grey levels  $\Phi_{SLM}$ . (c) Example data from cheek cell used to calibrate illumination angles via circle-finding in the Fourier spectrum (d), as well as recover pupil functions (f-k). (e) Illumination angle calibration corrects for angle misestimation. (f) Phase of alignment target  $\Phi$  displayed on SLM to calibrate SLM position. (g,h) Reconstructed pupil phase and amplitude using Fourier ptychography, used to align SLM position. (i) Reconstructed objective pupil phase aberration without coverslip in place (no coding, no aberrations). (j) Reconstructed objective pupil phase aberration with no. 1.5 coverslip in place (no coding, with aberrations), due to uncorrected objective. (k) Aberrated pupil phase from (j) fit to Zernike polynomials with 15 modes for smoothing.

### SLM Response Calibration

The SLM response is controlled by integer display values  $s \in [0, 255]$ , which are translated to phase values  $\Phi$  by the relationship

$$\Phi = a_{\Phi}s + b_{\Phi}. \quad (5.9)$$

A modified set-up is used to measure the pixelated SLM phase response maps given by  $a_{\Phi}$  and  $b_{\Phi}$ , as seen in Fig. 5.7(a). Two 150 mm lenses are placed between the beamsplitter and the SLM, forming conjugate image planes at the SLM and camera planes. An on-axis plane wave at wavelength  $\lambda = 530$  nm illuminates the entire SLM surface. Two linear polarizers are placed with crossed polarization axes, one in the illumination path and the other in the detection path. Both are at 45° to the modulation axis of the SLM. This set-up turns the phase-modulation SLM into an amplitude-modulation SLM, with measured intensity  $I$  at the camera plane related to SLM phase delay  $\Phi$  by

$$I = A_0^2 \sin^2\left(\frac{\Phi}{2}\right) \quad (5.10)$$

where  $A_0$  is an arbitrary constant. We display a uniform grey level  $s$  on the SLM with values from 0 to 255, capturing an image at each display value, giving intensity measurements across  $s$ ,  $I(s)$ . We then reorder the relation to give

$$\Phi(s) = 2 \sin^{-1} \left( \sqrt{\frac{I(s) - I_{min}}{I_{max} - I_{min}}} \right) \quad (5.11)$$

where  $I_{min}$  and  $I_{max}$  are the minimum and maximum values per pixel across all  $I(s)$ . This normalization step effectively accounts for the arbitrary  $A_0$  constant from Eq. 5.10. We use Eq. 5.11 to recover the phase delay value  $\Phi$  associated with the display value  $s$  for each image pixel by normalizing, phase-unwrapping, and then performing linear regression on the measured data to recover  $a_{\Phi}$  and  $b_{\Phi}$ . The scalar  $a_{\Phi}$  and offset  $b_{\Phi}$  mappings shown in Fig. 5.7(b) have additionally been resampled to fit the size of the SLM, with interpolation performed for edge values that were not measured at the camera plane. We note that the objective pupil is relayed to the center of the SLM's surface in pupil-coded intensity ODT, so interpolation at the edges has no bearing on the presented results. The relative camera pixel and SLM pixel position was determined by displaying known patterns on the SLM in the amplitude-coding mode and determining the relative rotation, shift, and scaling between the camera and SLM planes.

### System Calibration

The remaining system calibration is performed with the system in the experimental configuration shown in Fig. 5.1. We utilize a previously developed illumination angle calibration technique [56] which finds the illumination angle-defined offset of the circular pupil in the

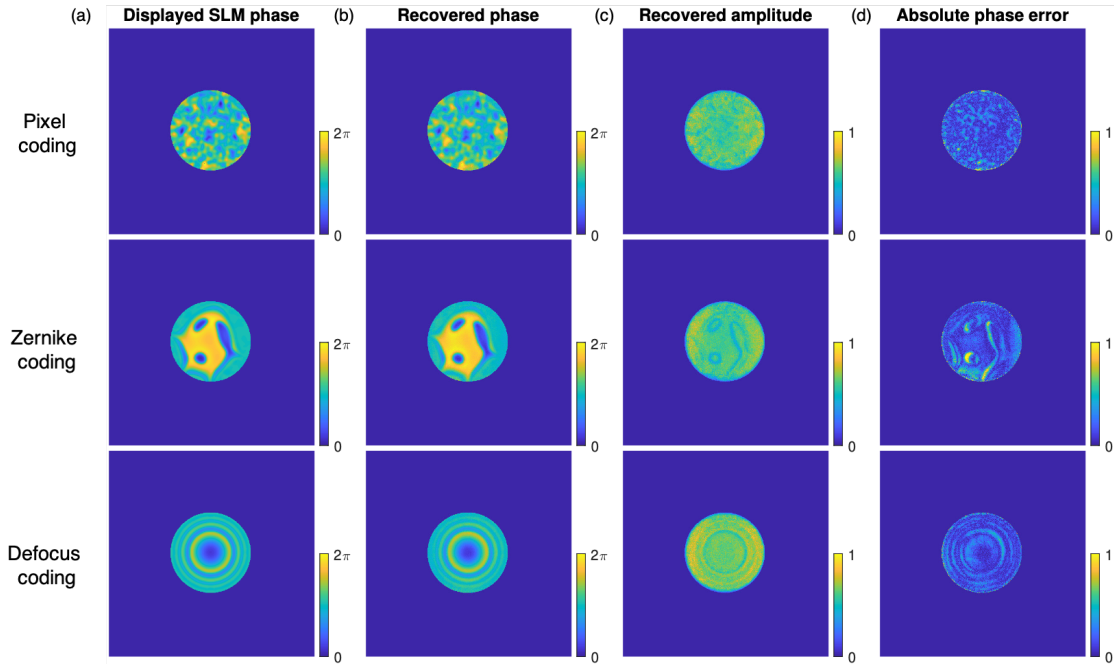


Figure 5.8: Fourier ptychography is used to recover pupil phase to verify SLM coding for representative phase masks across the pixel, Zernike, and defocus bases. (a) Expected phase  $\Phi$  displayed on SLM. (b) Recovered SLM pupil phase via Fourier ptychography, after objective pupil phase aberration subtraction. (c) Recovered SLM pupil amplitude via Fourier ptychography. Amplitude effects can be seen and are believed to be related to SLM fringing field effects. (d) RMSE of recovered SLM pupil phase (b) compared to displayed phase (a), showing that the SLM correctly displays the expected phase values.

Fourier spectrum of each brightfield image in order to directly calibrate the angle of illumination from measured data, as seen in Fig. 5.7(d-e).

We also make use of the fact that Fourier ptychographic microscopy (FPM) [240], a method to recover high-resolution images from low-NA, high field-of-view objective lenses, uses the same angled illumination system as intensity ODT. We reconstruct a two-dimensional sample, such as a phase USAF resolution target (Benchmark Technologies Quantitative Phase Microscopy Target [170]) or cheek cell (Fig. 5.7(c)) using FPM, leveraging the reduced dimensionality of the reconstructed object to also reconstruct a high-fidelity system pupil function under the EPR algorithm [156]. Using EPR’s pupil recovery capabilities, we can estimate the microscope’s base pupil aberrations when the SLM displays a uniform phase of 0 radians (Fig. 5.7(i)). When using the 0.8 NA, 50 $\times$  Olympus imaging objective lens that is not corrected for glass coverslips, we can also estimate the glass-induced aberrations of the imaging system by placing a #1.5 coverslip (0.17 mm thick glass) on top of the phase resolution target or cheek cell sample and performing an FPM reconstruction to recover the

aberrated pupil function (Fig. 5.7(j)). Since this aberration is large, it takes more iterations to recover an accurate pupil phase. We additionally fit the recovered aberrated pupil phase to a Zernike polynomial basis to smooth out the edges of the estimated pupil function, which tend to be noisy (Fig. 5.7(k)).

We designed a custom alignment phase SLM display pattern that involves a central cross pattern (Fig. 5.7(f)). By displaying this pattern on the SLM and performing an FPM reconstruction, we can experimentally calibrate the lateral location of the SLM with respect to the rest of the imaging system (Fig. 5.7(g-h)). We calibrate the axial position of the SLM by using a shearing interferometer in front of the camera plane while aligning the system. The tilt position of the SLM is verified by placing a pinhole at the center of the 300 mm Fourier transform lens and ensuring the reflected light from the SLM returns through the pinhole.

Finally, we verify the SLM displayed phase by capturing FPM datasets of the phase USAF target with a single phase mask of each type (*i.e.*, pixel, Zernike, and defocus) across all images (Fig. 5.8). Each dataset was reconstructed using FPM to recover the complex pupil function. We see that the recovered pupil phase matches the expected SLM displayed phase in Fig. 5.8(a-b) when the system’s base pupil aberrations are subtracted. Additionally, the FPM pupil reconstruction has reduced amplitude along sharp phase jumps in the phase pattern (Fig. 5.8(c)), due to diffraction at the SLM’s surface and the SLM fringing field effect [81, 146, 167, 189]. In order to reduce the effect of SLM diffraction, we smoothed all experimental phase masks with a Gaussian filter,  $\sigma = 4$ , to maintain the equivalency between the expected pupil phase, which is used in the reconstruction algorithm, and the actual pupil phase used to physically encode the measurements. As seen in Fig. 5.8(c), this is not adequate to remove all amplitude effects imparted by the SLM.

## 5.4.2 Results

We experimentally demonstrate the usefulness of the proposed method on benchmark objects, including polystyrene beads and a fabricated 3D refractive index object [243]. For all results, we captured 100 images of the object for each reconstruction, with the highest angles of illumination occurring at 0.685 NA, near the NA of the imaging objectives, which were 0.75 NA and 0.8 NA, respectively. We note, however, that the experimentally observed NA of the uncorrected 0.8 NA, 50 $\times$  objective in the presence of a #1.5 coverslip was 0.69 NA, due to the objective’s extreme glass aberrations. This resulted in the functional limitation of the  $NA_{illum,max} = 0.685$ , as an identical objective lens was used as the illumination objective in all presented results.

For the polystyrene bead reconstructions, we observe that the results with the pupil coding are of similar quality to the results without pupil coding when all images are used for the reconstruction. However, when the maximum illumination NA is reduced to  $NA_{illum,max} = 0.6$ , we see that the refractive index reconstruction without pupil coding suffers while the pupil-coded datasets still obtain high-quality reconstructions. Conversely, for the fabricated 3D RI object, the reconstruction without pupil coding fails to recover the background RI

even with all 100 images, since the maximum illumination NA (0.685 NA) is still 9% lower than the imaging NA (0.75 NA) without pupil coding. These results are discussed in detail below. Besides showcasing an avenue for reducing data requirements for 3D refractive index imaging, these results show that the proposed system could greatly simplify the current physical limitations of 3D RI imaging systems by reducing the required maximum incident angle at the sample plane.

Given that 3D refractive index is a quantity that cannot be directly measured, but must be inferred through optimization procedures such as those presented in this work, it is important to use benchmark objects to demonstrate the efficacy of 3D RI recovery. We stress, however, that the presented method is object-dependent, so successful reconstruction of these benchmark objects does not necessarily translate to successful reconstruction of biological samples. The fabricated 3D cell phantom from [243] is especially useful because it was fabricated using Nanoscribe photolithography to mimic typical biological cell features and refractive index differences, and also includes lateral and axial resolution target features to benchmark system performance. We therefore might expect successful reconstruction of this cell phantom to indicate successful reconstruction of biological samples.

Each dataset of 100 images was captured sequentially, scanning through the angles of illumination. For the aberration-corrected (NA 0.75 objective) and uncorrected glass aberration (NA 0.8 objective) datasets without SLM pupil coding, the SLM displayed a uniform phase of 0 radians, obtained using the calibrated SLM mapping shown in Fig. 5.7(b). For the datasets with pupil coding (i.e. the defocus, Zernike, and pixel basis datasets), each  $i^{th}$  pupil coding mask was mapped to the SLM grey levels using the calibrated SLM mapping and shifted according to the calibrated SLM alignment shift to align the center of the pupil to the imaging axis before being displayed on the SLM. A control loop ensured that the mirror controlling the angle of illumination was at the proper tilt position and that the SLM was displaying the correct phase value before the intensity image was captured at the camera.

A separate dataset was captured with two blank #1.5 coverslips at the sample plane to obtain data on the background intensity at each angle. This background dataset was Gaussian filtered with  $\sigma = 4$  to remove effects from dust on the blank coverslips. Before processing, the captured datasets were divided by the Gaussian-smoothed background dataset to remove bulk background effects from the processing pipeline.

### Polystyrene Beads

8  $\mu\text{m}$  diameter polystyrene beads ( $n = 1.596$  at  $\lambda = 530$  nm [239]) were suspended in Cargille  $n = 1.564$  immersion oil ( $n = 1.57$  at  $\lambda = 530$  nm), placed between two #1.5 coverslips, and imaged with both the 0.75 NA, glass-corrected objective without pupil coding (Fig. 5.9(a)) and the 0.8 NA, uncorrected objective with dynamic pupil coding on the SLM (Fig. 5.9(b-d)). In addition, the beads were imaged with the 0.8 NA, uncorrected objective without pupil coding (Fig. 5.9(e)) to demonstrate the effect of using the imaging objective's aberrations as a static pupil coding element. The difference in the magnification and field of view between the different objectives is apparent in Fig. 5.9.

We reconstructed the 3D refractive index of the beads under four different illumination conditions, with maximum illumination NA's of 0.685, 0.6, 0.5, and 0.4 NA, respectively, to test performance. All reconstructions used the prior  $\mathcal{P}$  that the 3D RI reconstruction was purely real and strictly greater than the background RI  $n = 1.57$ . The results without SLM coding have high refractive index for the  $NA_{illum,max} = 0.685$  illumination condition, but the reconstruction degrades as the maximum illumination NA decreases. In particular, the center of the bead becomes much darker without pupil coding under limited illumination conditions, as the low spatial frequencies are not reconstructed. Conversely, both the dynamically pupil-coded and glass-aberrated results maintain the flat bead RI structure across all illumination angle conditions, even when  $NA_{illum,max} = 0.4$ . We note that the bead refractive index value reconstructed by the 0.8 NA system is lower than expected ( $n \approx 1.58$ ), but that this value is consistent across reconstructions.

We notice also that the axial bead extent is larger for the 0.8 NA system; this is likely due to the NA of the system being functionally restricted to  $\approx 0.69$  by the objective's glass aberrations from empirical observation. Ideally, the 0.75 NA imaging objective system would have used a larger maximum illumination NA than functionally available in this system ( $NA_{illum,max} = 0.685$ , which is 91% of the imaging objective's 0.7 NA), but was limited by experimental constraints. The decent reconstruction with the 0.75 NA imaging objective without SLM coding at  $NA_{illum,max} = 0.685$  is therefore partially due to the strong prior constraint that the object is purely real and strictly greater than the background RI.

### Fabricated 3D Cell Phantom

A fabricated refractive index cell phantom target [243] was placed between two #1.5 coverslips with Cargille  $n = 1.52$  immersion oil ( $n = 1.5247$  at  $\lambda = 530$  nm). We expect the unexposed USAF lines to be  $n = 1.5241$ , the nucleus background to be  $n = 1.5353$ , and the cell body and nucleoli to be  $n = 1.5476$  at  $\lambda = 530$  nm. We again imaged with both the 0.75 NA, glass-corrected objective without pupil coding (Fig. 5.10(a)) and the 0.8 NA, uncorrected objective with dynamic pupil coding on the SLM (Fig. 5.10(b-d)) and without pupil coding, to demonstrate the effect of the objective's glass aberrations (Fig. 5.10(e)).

We reconstructed with the same range of limited illumination conditions described above, with maximum illumination NA's of 0.685, 0.6, 0.5, and 0.4 NA. We did not use any regularization in the reconstruction. Since we did not use prior constraints, the 0.75 NA objective system without pupil coding is unable to reconstruct the object's background RI values even at the highest possible experimental angle of illumination,  $NA_{illum,max} = 0.685$ , as seen in Fig. 5.10(a). While the high-spatial frequency cell features are reconstructed, the low-spatial frequencies are not reconstructed without pupil coding, showing how reliant intensity-only ODT systems without pupil coding are on high-NA illumination angles for good-quality reconstructions. Conversely, the results with pupil coding (Fig. 5.10(b-d)) show high-quality, flat reconstructions of the cell background and features, as expected for maximum illumination NA's of 0.685, 0.6, and 0.5. At maximum illumination NA 0.4, the amount of data is decreased to 37 images and so reconstruction instabilities occur, as in the case of the Zernike

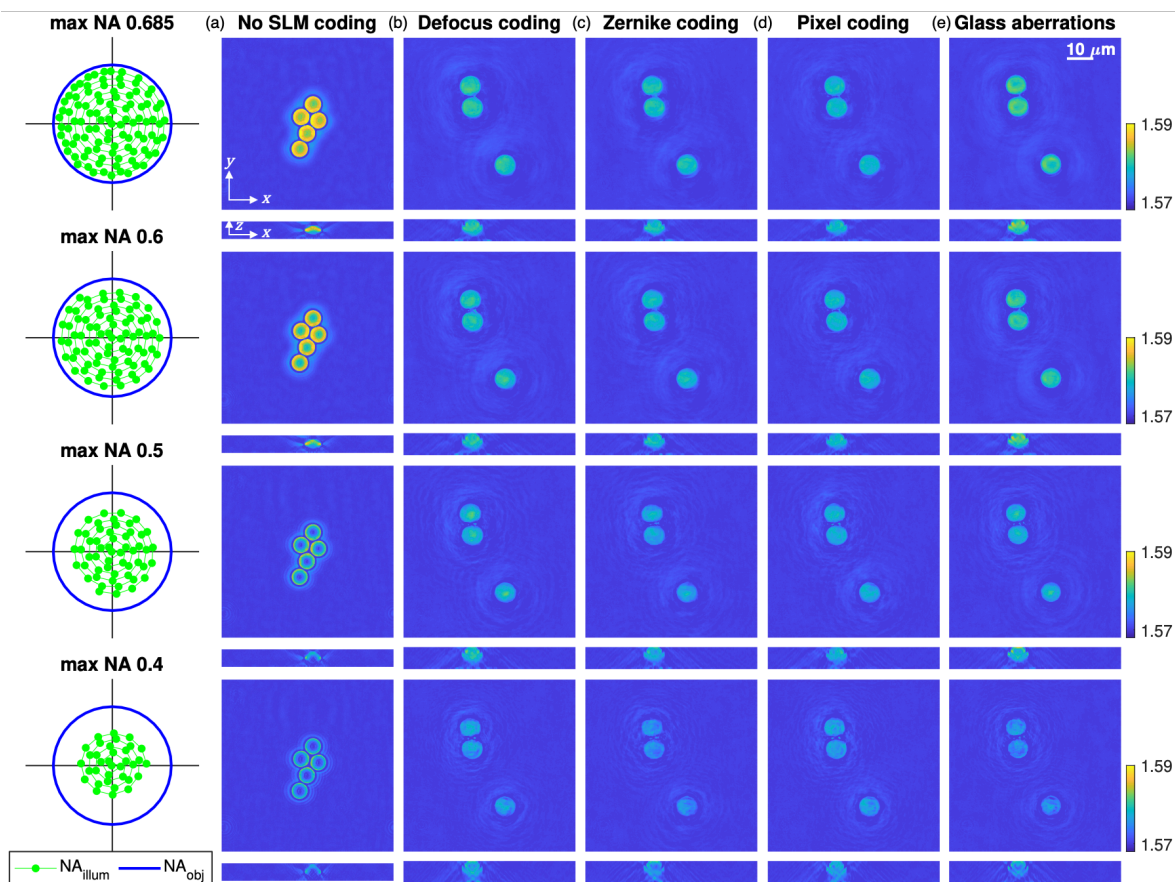


Figure 5.9: Reconstruction of polystyrene beads shows improved reconstructions for limited NA illumination for defocus, zernike, and pupil coding (b-d) over no coding, no aberration case (a). Additional reconstructions using the imaging objective’s extreme glass aberrations (e) also show good-quality reconstructions. Regularization was applied to enforce that  $O$  was purely real and strictly greater than the background RI.



## 5.5 Analysis

Due to the nonlinear and nonconvex nature of the multiple-scattering 3D RI imaging problem, it is difficult to theoretically analyze improvements in 3D RI reconstructions under the proposed system. In this section, we therefore present an analysis of a linearized form of the 3D RI imaging problem, which uses a single-scattering Born approximation rather than the multislice method used in the reconstructions presented above. We also discuss a more general spatial entropy analysis that could be used as a measure of dataset measurement diversity across different imaging system designs.

Overall, we theorize that the improvement in the proposed system is provided by increased transfer of low spatial frequency phase information into the measured intensity images. This is achieved because the pupil coding couples different parts of the scattering electric field phase into the electric field amplitude across all angles, which is then measured in the intensity images at the camera. We thus expect the measured intensity image  $I_i$  with pupil coding to include phase information from electric field  $u_i$  that would not be captured without pupil coding. This is similar to the analysis of phase diversity methods [72, 92, 147], which shows that imaging with different phase delays in the measurement path breaks the ambiguity of intensity measurements with the introduction of additional phase information.

However, we note that the phase encoding of an arbitrary pupil function is not the only mechanism for the proposed system’s improvement. If it were, we would expect that imaging with two distinct defocus masks across all illumination angles would provide an equal reconstruction improvement as having a different random mask for each illumination angle. We see in Fig. 5.6, however, that at least 5 distinct defocus masks are needed for reconstruction improvement from pupil coding. Moreover, this theory also fails to explain why, under the Zernike and pixel coding bases, only one distinct pupil phase mask is needed for the reconstruction improvement, as seen in simulation in Fig. 5.6 and verified in experiment in Fig. 5.10(e) and Fig.-5.9(e).

We theorize that the *diversity* of the phase encoding across images is important for the success of the proposed system. We explore this through a transfer function weight matrix analysis and a spatial entropy metric of measured data under the proposed system.

### 5.5.1 Transfer Function Weight Matrix Analysis

While the 3D RI imaging problem is nonconvex, making it difficult to analyze, the choice of forward light scattering model  $S(\cdot)$  can range from linear forward models, such as the Born single scattering approximation, to nonlinear models, such as the multislice algorithm. As noted above, we choose in this chapter to use the multislice algorithm in our reconstructions, as this allows for more complicated objects to be reconstructed. However, in order to analyze the usefulness of random phase coding in 3D RI imaging, we find it useful to turn to a linear, single-scattering Born approximation [18, 29, 30, 142, 217] to better understand why random-phase encoded measurements give simulated and experimental reconstruction improvements. While the change in forward light scattering models means the analysis below does not

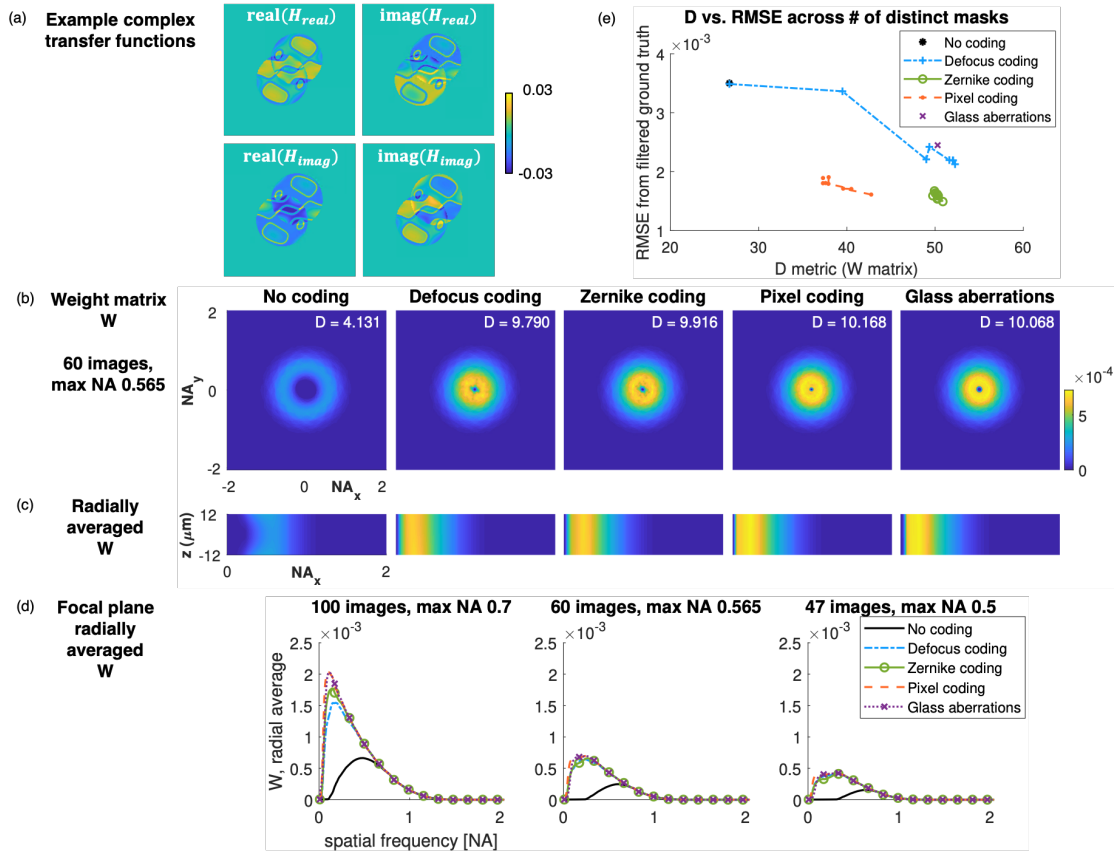


Figure 5.11: A transfer function weight matrix reveals the measurement system’s frequency space weighting. (a) Example complex transfer functions  $H_{re}$  and  $H_{im}$  calculated under a single-scattering Born approximation for a random Zernike pupil phase at an off-axis angle of illumination. (b) Weight matrix  $W$  at the focal plane for 60 images (maximum illumination NA 0.565) across pupil coding types. Metric  $D$  across axial planes is displayed for each dataset.  $W$  shows how the introduction of pupil coding weights the low spatial frequencies in the measurements much higher than the case with no pupil coding. This is true even with a single, aberration-induced pupil code. (c) Radial average of  $W$  (laterally), displayed across axial planes for all pupil coding types under the low-angle, maximum NA 0.565, 60 image measurement condition. Pupil coding introduces low spatial frequency coverage across axial planes. (d) Radial average of  $W$  for  $z = 0$  across different illumination angle conditions. As the maximum illumination angle nears the NA of the imaging objective, the traditional, no pupil coding system includes low spatial frequency weighting. At all measurement conditions shown, the low spatial frequency weighting is better under the proposed, pupil-coded system. (e) Higher  $D$  values correspond to lower RMSE from filtered ground truth for simulated datasets across different numbers of distinct pupil coding masks.

capture any multiple-scattering phenomena in the system, the single-scattering light makes up a large part measured signal even for the multislice model for the presented samples.

We refer to the formulations in [29, 30, 142] which utilize the Born approximation to the Helmholtz equation to model the 3D scattering of light through a volume with scattering potential  $V(\mathbf{r})$ . In short, this formulation allows us to write the linear process of light scattering through the sample volume using real and imaginary transfer function matrices,  $H_{re}(\mathbf{k})$  and  $H_{im}(\mathbf{k})$ , which operate on the real and imaginary parts of the 3D Fourier spectrum of the scattering potential, as denoted by:

$$\tilde{I}_i(\mathbf{k}) = H_{re, i}(\mathbf{k})\tilde{V}_{re}(\mathbf{k}) + H_{im, i}(\mathbf{k})\tilde{V}_{im}(\mathbf{k}) \quad (5.12)$$

where  $\tilde{I}_i(\mathbf{k})$  is the Fourier spectrum of the measured intensity image. Given the angle of illumination, objective pupil support  $\tilde{P}(\mathbf{k})$  and applied SLM pupil mask  $\tilde{M}_i = \exp(j\phi_i(\mathbf{k}))$ , we can calculate the transfer functions via

$$\begin{aligned} \Psi_i(\mathbf{k}) &= \mathcal{F}_{xy} \left\{ S_{flip, i} \tilde{M}_i \tilde{P} 2\pi \sqrt{\frac{n^2}{\lambda} - \mathbf{k}_x^2 - \mathbf{k}_y^2} \right\} \\ &\quad \cdot \text{conj} \left( \mathcal{F}_{xy} \left\{ \tilde{M}_i \tilde{P} 2\pi \sqrt{\frac{n^2}{\lambda} - \mathbf{k}_x^2 - \mathbf{k}_y^2} \cdot \text{real} \left( \frac{\tilde{P}}{4\pi \sqrt{\frac{n^2}{\lambda} - \mathbf{k}_x^2 - \mathbf{k}_y^2}} \right) \right\} \right) \\ H_{re, i}(\mathbf{k}) &= j \mathcal{F}_{xy}^{-1} \{ j \text{imag}(\Psi_i(\mathbf{k})) \} \\ H_{im, i}(\mathbf{k}) &= - \mathcal{F}_{xy}^{-1} \{ \text{real}(\Psi_i(\mathbf{k})) \} \end{aligned}$$

where  $S_{flip, i}$  contains a Dirac delta at the conjugate location of the illumination angle at  $(k_{x, i}, k_{y, i})$ , as given in [29, 30].

We follow the formulation in [142], which defines an overall transfer matrix

$$\mathbf{H} = \begin{bmatrix} H_{re}[1, 1] & \dots & H_{re}[q_z, 1] & H_{im}[1, 1] & \dots & H_{im}[q_z, 1] \\ \vdots & \ddots & \vdots & \vdots & \ddots & \vdots \\ H_{re}[1, N] & \dots & H_{re}[q_z, N] & H_{im}[1, N] & \dots & H_{im}[q_z, N] \end{bmatrix} \quad (5.13)$$

containing the real and imaginary transfer functions for  $q = 1 \dots q_z$   $z$  planes and  $i = 1 \dots N$  images. Following from the work in [142], the SVD of  $\mathbf{H}[q]$ , the system transfer function for each axial plane, renders a weight matrix  $W$  given by:

$$\begin{aligned} W[q] &= \left( \sum_i |H_{re}[q, i]|^2 \right) \left( \sum_i |H_{im}[q, i]|^2 \right) \\ &\quad - \left( \sum_i H_{re}^*[q, i] H_{im}[q, i] \right) \left( \sum_i H_{re}[q, i] H_{im}^*[q, i] \right) \end{aligned}$$

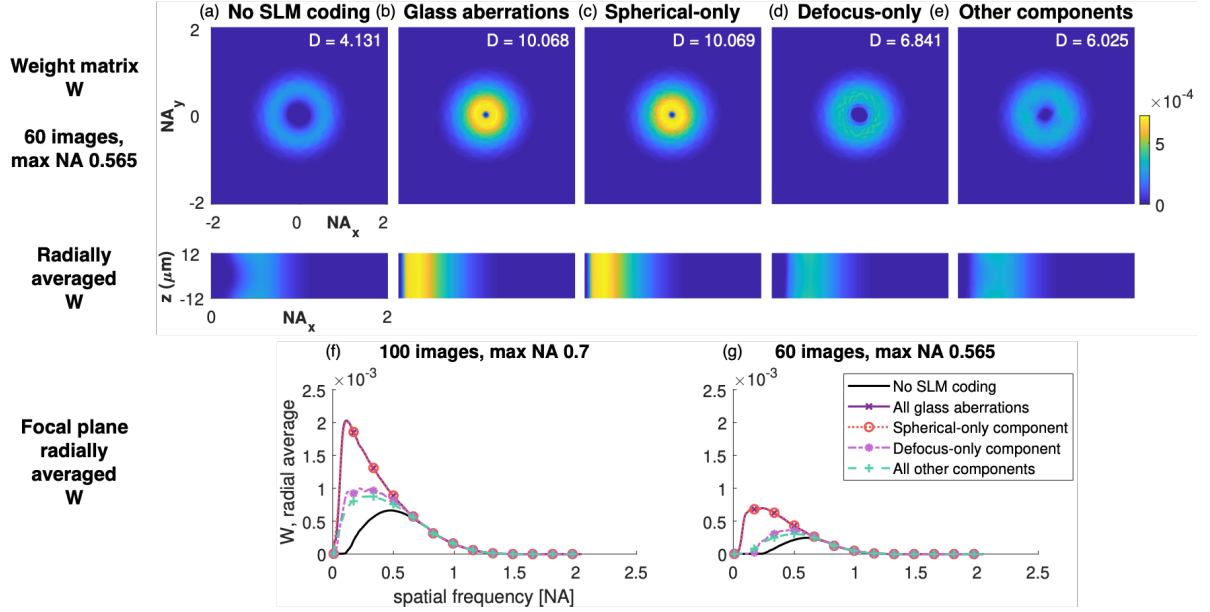


Figure 5.12: Transfer function weight matrix analysis shows that the primary pupil-coding improvement of objective glass aberrations are due to high spherical aberrations. The focal plane weight matrix  $W$  and radial average of  $W$  across depth are shown for a system with 60 images with  $NA_{illum,max} = 0.565$  and (a) no pupil coding and (b) glass aberrations experimentally derived from an uncorrected objective lens, as well as the (c) the spherical component, (d) defocus component, and (e) all other components of the glass aberrations. The radial average of  $W$  at the focal plane for (f)  $NA_{illum,max} = 0.7$  and (g)  $NA_{illum,max} = 0.565$  show that the high spherical aberration is the primary cause for increased low spatial frequency weighting observed in measurements with an uncorrected objective lens.

where  $q$  indexes into axial position and  $i$  indexes image number.  $W$  is related to the Tikhonov regularization weighting factor in 3D differential phase contrast algorithms [29, 30, 142, 217] and describes the relative weighting of the different Fourier space regions by the transfer functions of the imaging system. Broadly speaking, the spatial frequencies with higher values in  $W$  have increased weighting across all measured images captured by the imaging system. It does not strictly match measured information, but rather shows what regions of Fourier space are relatively well-represented by the measurement system. We adopt a similar metric  $D$  to that used in [142], defined as

$$D = \frac{\sum W|_{W \geq \alpha}}{\sum W|_{W < \alpha}} \quad (5.14)$$

to evaluate the weighting  $W$  across all available regions of Fourier space.

The weight matrix  $W$  at the focal plane across the five different measurement systems

under consideration is shown in Fig. 5.11(b) for a low-angle, limited illumination condition (60 images, with maximum illumination NA 0.565) for a 0.8 NA, 50 $\times$  imaging objective lens. We see that under this limited illumination condition, the system without pupil coding resembles a wide donut, where the low-spatial frequency components are not well-represented in the system measurements. This matches previous research in LED array pattern design for phase imaging, which finds that low-spatial frequency phase information is best captured in high-angle measurements, with the angle of illumination near the NA of the imaging objective [64, 116, 216]. However, when we include random pupil coding, much of the low-spatial frequency region has increased weighting. This is also true for the single-mask Zernike case where we use the objective aberrations to directly provide pupil coding, as seen in Fig. 5.12. Subsequently, the  $D$  metric is higher under the proposed system with pupil coding, showing that the pupil coding provides better weighting in the Fourier domain in all available regions.

Given that the  $W$  matrices are reasonably radially symmetric, we present the lateral radial average of  $W$  across all  $z$  positions for comparison in Fig. 5.11(c). We see that the proposed pupil coding system exhibits improved weighting of low spatial frequency components across all  $z$  positions. We compare the radial average of the focal plane  $W$  (at  $z = 0$ ) in Fig. 5.11(d) for different illumination conditions. We see that for the high-angle illumination condition (100 images, maximum illumination NA 0.7), the low-spatial frequency weighting is improved for the classic, no-coding ODT system. As the maximum angle of illumination drops, so too does the low-spatial frequency weighting. However, for the proposed system with pupil coding, the low-spatial frequency weighting is high even with very low angles of illumination. In Fig. 5.11(e), we see that higher values of metric  $D$  is related to lower reconstruction RMSE from the NA-filtered ground truth for the simulated multislice-based reconstructions presented in Fig. 5.6, showing that the  $D$  metric and transfer function analysis is useful for predicting improved multislice-based 3D RI reconstructions. This analysis matches our experimentally-derived observations that by simultaneously scanning illumination angle and randomly phase coding at the Fourier transform plane, we can better reconstruct low-spatial frequency 3D phase information even with limited illumination angles, leading to large experimental improvements.

We note that the improvement in the single-Zernike phase aberration directly provided by the objective lens glass aberrations is driven by the large spherical aberration component, as seen in Fig. 5.12. This relates to our argument that the *diversity* of the phase coding across angles of illumination is what matters to improve results. When we calculate the weight matrix  $W$  for the limited illumination case for the defocus-only component of the objective aberration, we see some improvement in low spatial frequency weighting. However, this is far surpassed by the improvement in low spatial frequencies in  $W$  for the spherical-only component. By deconstructing the calculation of the weight matrix  $W$  in these two cases (Fig. 5.13), we can begin to uncover how phase coding patterns result in improved low-frequency weightings. We view the components of the focal plane weight matrix for the first 10 measurements with the lowest illumination angles to build intuition. First of all, the term

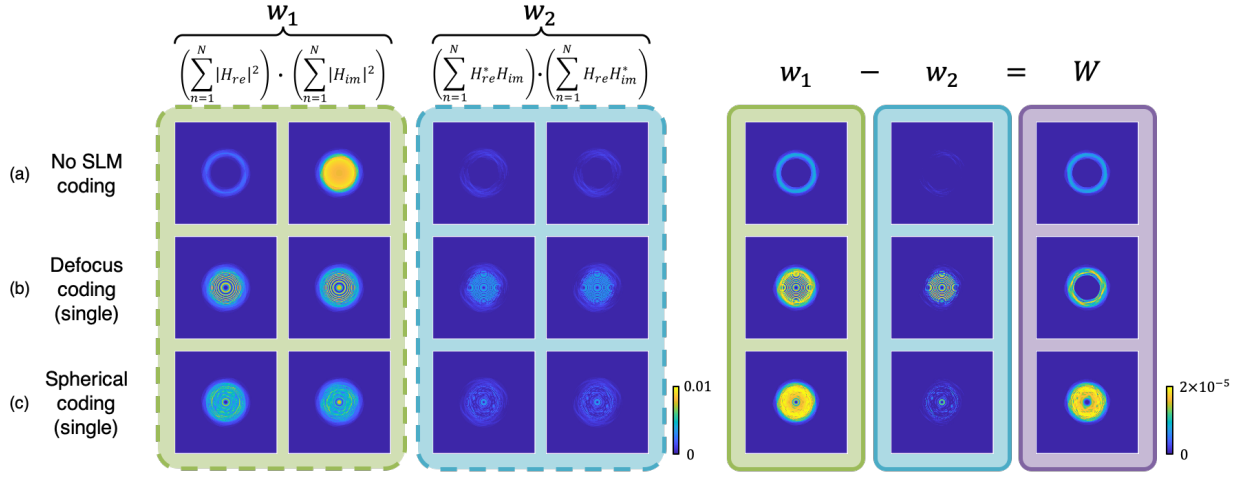


Figure 5.13: Transfer function analysis shows encoding of diverse phase information with well-chosen pupil coding. Components of the transfer function  $W$  matrix are shown for the 10 images with the lowest illumination NA. (a) With no pupil coding, the phase transfer function  $H_{re}$  is low-valued for low spatial frequencies, resulting in low values for the final  $W$  in the low spatial frequencies. (b) With a single defocus pupil code across illumination angles, both the phase and amplitude transfer functions have high amplitudes. However, a lack of diversity in this phase encoding means  $w_1$  and  $w_2$  are identical in the low spatial frequencies, resulting in low values for the final  $W$  in this region. (c) With a single spherical aberration, diverse phase information is measured by the system, resulting in a  $W$  with high values for low spatial frequencies.

given by

$$w_1 = \left( \sum_i |H_{re}[q, i]|^2 \right) \left( \sum_i |H_{im}[q, i]|^2 \right) \quad (5.15)$$

must have low-spatial frequency content in both the  $\sum |H_{re}|^2$  and  $\sum |H_{im}|^2$  components. In the no-coding case, we see that while the  $\sum |H_{im}|^2$  term (referred to in [29] as the *absorption transfer function*) has low-spatial frequency content, the  $\sum |H_{re}|^2$  (the *phase transfer function*) does not. Therefore, when the multiplication of the two terms occurs, the low spatial frequency weighting is near zero for the first term, as seen in Fig. 5.13(a). However, when we introduce phase coding, we see that both transfer function terms have high values in the low spatial frequency regions (Fig. 5.13(b-c)). This is related to the intuition that pupil coding couples phase information into the intensity measurements.

However, this cannot be the only improvement required, otherwise we would expect the defocus phase coding to prove as effective as spherical phase coding (which is proven false in

Fig. 5.12). We must also consider the second, cross-term in the calculation of  $W$ , given by

$$w_2 = \left( \sum_i H_{re}^*[q, i] H_{im}[q, i] \right) \left( \sum_i H_{re}[q, i] H_{im}^*[q, i] \right) \quad (5.16)$$

which is subtracted from the first term  $w_1$ . We want this term to be as low-valued as possible, suggesting that the pupil phase should be incoherent between measurements in the low-spatial frequency regions around the object spectrum's DC term, which is scanned across the pupil plane by the changing angle of illumination. We find that in the defocus-only phase encoded case, the low-spatial frequency phase term is similar across illumination angles. Thus, the second, cross-term  $w_2$  is high-valued in the low-spatial frequencies, which results in lower overall low-spatial frequency weighting in  $W$  when subtracted from the first term (Fig. 5.13(b)). However, for the spherical-only phase encoded case, the low frequency terms are dissimilar across angles of illumination, even at low NA. Thus, this cross-term is low-valued, resulting in a high-valued  $W$  matrix in the low-spatial frequency regions (Fig. 5.13(c)).

We can understand this result by visualizing the scanning of the electric field spectrum across the pupil coding plane. In the single-mask defocus-only case with a single mask, the coding does not change much across low-NA illumination angles, so the phase information coupled into the intensity measurements is roughly the same across all images. However, in the single-mask spherical-only case, the spherical coding varies a large amount across even low-NA illumination angles. Therefore, as the electric field spectrum is scanned across low-NA angles, the modulation at each angle by the spherical aberration phase is incoherent across measurements, especially when the spherical aberration coefficient is large, as in the presented results. The measurements will thus have diverse phase information, and will therefore collectively better weight low spatial frequencies across measurements. This intuition would suggest that a single random pixel or large-coefficient random Zernike mask, which have large variation in all parts of the pupil plane, would also perform well as pupil coding bases with a sufficiently diverse single mask, which matches the simulated results presented in Fig. 5.6 and the experimental results presented in Fig. 5.9-5.10.

Transfer function analysis builds shows that the proposed pupil-coded intensity ODT system has increased measurement of diverse phase information, leading to improved recovery of 3D RI low-spatial frequency components. Though the weight matrix  $W$  does not directly apply to the multislice-based reconstruction algorithm as it does to 3D differential phase contrast imaging, the presented transfer function analysis matches the multislice-based simulated and experimental results, giving confidence applicability of the analysis framework. This transfer function analysis could be used in future work to explore further improvements to 3D RI measurement systems.

## 5.5.2 Spatial Entropy Metric for Measurement Diversity

A more general way to approach the analysis of the proposed system is through the lens of measurement diversity. Phase diversity systems have been mathematically shown to break

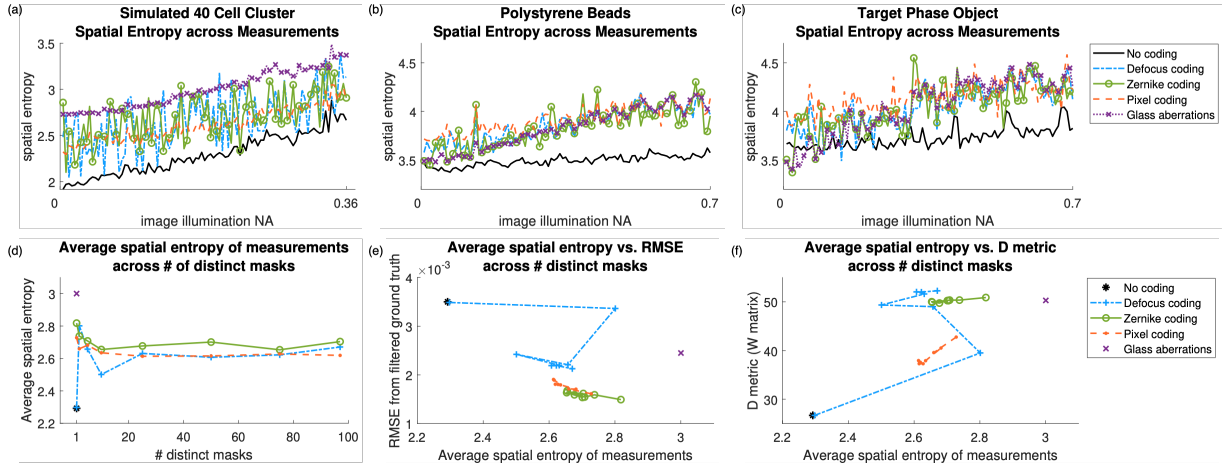


Figure 5.14: Spatial entropy across measurements is used to calculate measurement diversity. Image spatial entropy across illumination angle for (a) simulated 40 cell cluster, (b) experimental polystyrene beads, and (c) experimental fabricated phase object. In all cases, we see that the traditional, no-coding data has the lowest spatial entropy, while the pupil-coded and glass-aberrated data have much higher spatial entropy, which increases as the image’s illumination angle increases. (d) Average spatial entropy across number of distinct masks used for each pupil coding basis. (e) Average spatial entropy for simulated datasets is compared to NA-filtered ground truth under a limited, low-angle illumination condition, showing that higher average spatial entropy relates to lower RMSE, with some exceptions. (f) Similarly, average spatial entropy is related positively with the  $D$  metric calculated from the transfer function weight matrix  $W$ . While  $D$  can only be calculated theoretically, average spatial entropy is calculated directly from measured data, so could be used to compare measurement diversity across imaging systems.

the ambiguity of intensity-only measurements when recovering wavefront phase information by introducing diverse phase delays between measurements [72, 92, 147]. A related concept is random encoding in compressed sensing systems, which guarantee recovery at sub-Nyquist sampling rates for sparse systems with incoherent (often random) measurement systems [12, 23, 55, 112, 208, 230]. These concepts argue for diverse measurements in optimization systems, and suggest that using random coefficients on the presented pupil coding bases could be useful for pupil-coded intensity ODT. We have shown heuristically that the measurements obtained under the proposed system with random pupil coding are more diverse (*i.e.*, have higher contrast measurements) than measurements measured without pupil coding. We here present an information-theoretic spatial entropy metric to quantify and compare this measurement diversity across datasets.

Information-theoretic entropy can be thought of as a generalized standard deviation

calculation that can be justly compared across all types of probability function shapes.<sup>5</sup> If we calculate the histogram of all pixel values across  $h$  bins as  $\text{hist}_h(I_i)$  in a single background-normalized measured image  $I_i$ , we can calculate a proxy to the probability mass function governing the distribution of pixel values in the image as

$$p_h = \frac{\text{hist}_h(I_i)}{\sum_h \text{hist}_h(I_i)}. \quad (5.17)$$

We term this the *spatial probability distribution* of pixels, since it describes the variation of pixels in the spatial domain (*i.e.*, inside a single image, rather than across images). We calculate the spatial entropy for the  $i^{\text{th}}$  image as

$$H_{\text{entropy}} = - \sum_h p_h \log p_h. \quad (5.18)$$

Using this basic calculation of image statistics, we can compare the measurement diversity across different imaging systems. In Fig. 5.14(a-c), we see that pupil coding provides higher spatial entropy, and therefore higher contrast, measurements than the traditional angle-scanning-only ODT system across different types of samples in both simulation and experiment. We see in Fig. 5.14(d-f) how this metric relates to reconstruction RMSE and transfer function weight matrix  $D$  metric to verify its usefulness as a experimental measure of measurement diversity, all based on the simulated reconstructions with different numbers of distinct pupil coding masks described in Sec. 5.3.5. We observe that increased average spatial entropy of the measurements is related to decreased reconstruction RMSE and increased weight metric  $D$  metric, suggesting that average spatial entropy may be a good proxy function to evaluate a system's measurement diversity and related reconstruction efficacy.

Theoretically speaking, a measure of pointwise mutual information would be more directly useful in measuring the information content of the measured images to determine which measurements are more useful for reconstruction. However, this measure is computationally untenable to calculate. Conversely, spatial entropy is simple to calculate for any dataset, but is a less accurate measure of diverse information content. Increased spatial entropy might as easily come from increased noise as increased information content about the object. For example, we can see that the measurements for random defocus coding with two distinct masks has high spatial entropy in Fig. 5.14(d) but also high reconstruction error in Fig. 5.14(e). While in general higher spatial entropy correlates with increased measurement diversity, and therefore better reconstructions, it also correlates to higher noise, and so is not a good proxy for measurement diversity in all cases. Thus, spatial entropy should only be compared across similar noise conditions if this metric is used to compare measurement systems.

---

<sup>5</sup>Whereas the standard deviation is only applicable to Gaussian distributions.

## 5.6 Conclusion

In this chapter, we have presented a novel 3D RI imaging framework called pupil-coded intensity ODT which utilizes joint plane wave illumination angle-scanning and detection-side pupil coding. We have shown in both simulation and experiment that introducing pupil coding improves 3D RI imaging reconstructions under low-angle, limited illumination and limited computation conditions due to the increase in diverse phase encoding in the intensity measurements. This improvement has several practical system-level implications which could be used to make high-resolution 3D RI imaging systems easier to use in real-world settings.

While 3D RI imaging is a promising imaging technique with a wide array of applications, we are only beginning to understand the best way to measure 3D RI information. When determining what measurements are optimal, we must both consider reconstruction accuracy and stability as well as data requirements, imaging speed, and computation time; practical optical system complexity and constraints; and availability of robust calibration. We have shown in simulation and experiment that the proposed system encodes more diverse phase information in each measurement, thus allowing for stable 3D RI reconstructions with less measured data. This reduced data requirement leads to increased imaging speed and decreased computation time, since fewer measurements need to be measured and used in the optimization algorithm. Additionally, we have shown that the proposed system increases the low-spatial frequency content across measurements, which leads to better convergence to ground truth 3D RI in fewer iterations, also reducing required computation time for high-quality results.

While practical optical system constraints are necessarily system-specific, we find the proposed system to be a promising direction for practical real-world 3D RI imaging systems. 3D RI imaging systems that utilize illumination angle scanning to collect 3D information are less complicated than systems that utilize sample rotation, which either require the imaging system to rotate around the sample or the sample to be manipulated with optical tweezers [80] or placed on a minutely controlled object like a pipette tip [27], which limits the samples that can be imaged. However, high-resolution angle-scanning 3D RI imaging systems require both high-NA illumination and detection objective lenses located on either side of the sample, which results in a very small working distance between the two lenses, making nonexpert use of the system infeasible. Under the proposed system, the highest angle of illumination no longer needs to be near the NA of the imaging objective for high-quality reconstructions, allowing the illumination-side objective to be a lower cost, longer working distance, low-NA objective. The reduced constraint on the maximum NA of illumination thus translates into greater ease in the design, building, and use of an angle-scanned 3D RI imaging system. In addition, our system utilizes a non-interferometric system, encoding phase information into intensity measurements that is directly processed by the optimization algorithm, also resulting in reduced system complexity by eliminating the need for an interferometric reference arm.

The downside of the proposed system is the inclusion of a phase spatial light modulator (SLM) in the conjugate Fourier plane of the imaging objective, which is used to create

dynamic pupil phase coding. The SLM adds system complexity, increases system space requirements, and requires more complex alignment and calibration steps. However, we have shown in simulation and experiment that introducing a *single* well-chosen phase mask in the Fourier plane is sufficient to increase the measurement diversity in an angle-scanning ODT system. Under this finding, we have shown it is possible to improve the 3D RI reconstructions under the proposed system using only the glass-induced aberrations of an uncorrected objective lens, given proper calibration procedures, simplifying the proposed system implementation greatly. An even more promising, as yet unexplored avenue would be to fabricate a single, known phase mask to place in the optical path, thus eliminating the need for the SLM while also including a known, pre-calibrated modulation element for the desired pupil phase coding.

In addition to the proposed system improvements, we demonstrated the use of a transfer function-based weight matrix analysis and spatial entropy metric to compare 3D RI imaging methods. The transfer function weight matrix analysis drawn from work in 3D differential phase contrast [29, 30, 142] shows how the proposed joint illumination- and detection-side coding increases the weighting of low-spatial frequency components of the single-scattered light due to diverse electric field phase encoding across all angles of illumination. The spatial entropy metric was used to analyze simulated and experimental data, showing that the measured images under the proposed system have measurably higher contrast than the traditional angle-scanning ODT system. In general, higher spatial entropy across measurements was shown to correlate with increased measurement diversity and decreased reconstruction error in simulated datasets. While spatial entropy can also indicate higher amounts of imaging noise, this relationship between increased spatial entropy and lower reconstruction RMSE suggests that spatial entropy could be used as a metric to optimize 3D RI reconstruction across imaging systems, as long as datasets are correctly normalized for noise.

3D RI imaging is a promising imaging technique with a wide variety of applications across biological research, as well as in improved scattering models of small organisms for climate-related modeling. We have shown that by increasing the measurement diversity in an angle-scanning tomography system, we can improve our 3D RI reconstructions in many dimensions, which we hope will lead to increased usability of 3D RI imaging systems in the future.

## Chapter 6

# Machine Learning for Pupil-Coded 3D Refractive Index Imaging

Computational imaging aims to jointly leverage the strengths of computation and optics, suggesting a need to explore the intersection of these two fields. In the last few years, data-driven approaches have been used for the joint optimization of optical and computational parameters for computational imaging. In this chapter, we apply a data-driven, physics-based machine learning algorithm to optimize experimental design for 3D refractive index microscopic imaging. 3D refractive index imaging recovers quantitative structural information about biological samples, and thus has the potential to be extremely useful for biological imaging applications. However, it is both an experimentally and computationally difficult problem to solve, since neither three-dimensional nor refractive index information can be measured directly using available technology. 3D RI imaging therefore requires multiple, diverse measurements of a sample to be captured, which are then synthesized with a computational algorithm to reconstruct the sample's volumetric refractive index distribution. In Chapter 5, we introduced a novel 3D RI imaging system called pupil-coded intensity ODT, which uses joint illumination- and detection-side coding to capture more diverse measurements, leading to reduced imaging constraints and faster, more robust reconstructions. In this chapter, we investigate the use of physics-based machine learning methods to find more optimal ways to encode 3D RI information in captured images by optimizing the pupil coding masks used in pupil-coded intensity ODT.<sup>1</sup> We present simulated and experimental results and apply a transfer function analysis on the learned pupil coding masks. We conclude that the learned pupil coding masks under the proposed algorithm produce similar-quality results to randomly-generated pupil coding masks.

While the presented learned pupil coding masks do not improve upon randomly-generated masks, physics-based machine learning has improved imaging parameters for many other computational imaging systems [51, 103, 102, 185]. These physics-based, data-driven optimization algorithms are an exciting tool for computational imaging system design, as they

---

<sup>1</sup>Chapter 6 represents currently-unpublished work done in collaboration with Michael Kellman.

allow direct joint optimization of both the imaging and computational system parameters. However, there is no guarantee that the results produced from physics-based machine learned design will necessarily improve upon previous imaging system parameters, especially if the learning algorithm must be trained on simulated data, which is often the case. Care should therefore be taken when using these resource-intensive algorithms.

## 6.1 Introduction

The goal at the heart of computational imaging is to leverage the joint strength of optical and computational systems to image properties of interest in the most accurate, most robust, easiest, and fastest manner with the least amount of data. Computational imaging generally approaches imaging problems from a signal processing standpoint, treating the optical system as an encoder of desired information and the computational algorithm as a decoder that reconstructs the desired signal.

The choice of how to best encode and decode the desired information in an optical system depends highly on the imaging application. Computational imaging system design has either been made through the application of theoretical optical principles, human intuition backed by empirical evidence, or optimization over reconstruction parameters or heuristic metrics [12, 64, 140, 142, 181]. More recently, attention has been turned to the power of data-driven approaches as a way to evaluate and optimize optical system designs for joint use with computational reconstruction algorithms [51, 103, 102, 185]. This approach follows on an explosion of computer vision machine learning in recent years, where large convolutional neural networks are trained on image datasets to perform a wide array of tasks, beginning with the revolutionary use of AlexNet for image classification in 2012 [110]. Similarly, in computational imaging, these deep neural networks can be trained to perform reconstruction [120, 121, 145, 151, 229] or classification [87, 149] tasks using measured data from the optical system as inputs. Neural networks have also been used to regularize the output of a traditional reconstruction method by forming statistical image priors [5, 20], denoising [183], and using the properties of untrained neural networks [19, 85]. However, applying neural networks directly as the reconstruction method for computational imaging, while promising, does not guarantee that a reconstruction will not hallucinate a reasonable result that is not physically accurate, though methods of quantifying learning-based reconstruction accuracy are beginning to be adopted [209, 228]. These deep learning networks would also require vast training datasets in order to learn useful reconstructions. Large experimental datasets with ground truth reconstructions do not currently exist for most microscopy applications, and synthetic training data is of limited use, as it may not generalize to experimental datasets. In addition, deep neural networks for direct reconstructions usually discard the physics-based knowledge available about the system, instead learning a data-driven mapping between image inputs and reconstruction outputs that are difficult for the human user to interrogate and understand. This differs from traditional methods which are based strictly in the physics of the problem at hand and may have mathematical reconstruction guarantees.

Physics-based machine learning leverages many of the benefits of both machine learning and traditional, physics-based reconstruction algorithms, allowing for data-driven optimization of computational imaging systems [51, 87, 103, 102, 149, 185]. These methods typically work by unrolling a fixed-iteration traditional, physics-based iterative optimization algorithm, treating each iteration (i.e. gradient step) of the traditional algorithm as a layer in a neural network. In this unrolled form, the raw input measurements are mapped through a fixed number of optimization algorithm iterations to reconstruct the desired output. Unlike in traditional reconstructions, however, the error between the reconstructed object and a ground truth object can be backpropagated through the optimization algorithm to update both imaging system and computational algorithm parameters for improved reconstructions. This framework allows computational imaging to use both accurate physics-based modeling and the statistics of real data to create better imaging system designs.

However, physics-based machine learning is a resource-intensive process, requiring large amounts of GPU memory, long training times, and high energy consumption. Unlike deep neural networks, unrolled algorithms cannot be easily parallelized, and so must usually fit in the memory of a single GPU, which is currently practically limited to a memory footprint of 10-16 Gigabytes. Since the unrolled algorithms directly process image data at every iteration, the memory footprint of the algorithm can quickly grow. This is especially true for 3D reconstruction algorithms, where each gradient-based layer updates a memory-intensive 3D volume. Therefore, memory-efficient learning methods [70, 74, 104] have been developed, which selectively save certain parameters throughout the network in a method called *checkpointing*, then recalculate the discarded parameters when needed, trading off memory footprint for computational speed and complexity. These methods also selectively load data into GPU memory for processing, which also trades memory footprint for processing time.

In this chapter, we apply physics-based machine learning to the pupil-coded intensity optical diffraction tomography (ODT) system proposed in Chapter 5 for improved 3D refractive index (RI) imaging. In pupil-coded intensity ODT, joint illumination- and detection-side coding is used to capture diverse measurements of thick biological samples. This data is processed by a gradient-based optimization algorithm that reconstructs the sample's volumetric refractive index, revealing useful structural information about the sample without requiring staining or fluorescent tagging. In pupil-coded intensity ODT, the coherent, plane wave illumination is scanned through different angles while, simultaneously, the Fourier-space pupil plane is simultaneously coded with phase masks. This joint illumination- and detection-side coding encodes diverse phase information into the measured images, reducing imaging constraints and data requirements, as well as increasing computational reconstruction speed, as it requires fewer iterations for good-quality 3D RI reconstructions. In this chapter, we apply an unrolled, physics-based machine learning algorithm to this pupil-coded intensity ODT system to investigate the efficacy of data-driven learning to improve the pupil coding masks over those drawn from random coefficients. We use the MELD open source memory-efficient learning kit developed by Kellman et al. [104] to allow us to apply physics-based machine learning to 3D refractive index imaging, which would otherwise require an infeasible amount of GPU memory. In this chapter, we compare the physics-based learned pupil coding

masks to random pupil coding masks in simulation and experiment, and present a transfer function-based analysis of the learned masks. We find that the learned and random pupil coding masks perform equally well in simulation and experiment.

## 6.2 Methods

### 6.2.1 Pupil-Coded Intensity Optical Diffraction Tomography

Pupil-coded intensity ODT is a 3D refractive index imaging method that uses joint illumination- and detection-side coding. In pupil-coded intensity ODT, a volumetric RI object  $O(\mathbf{r})$  is illuminated sequentially by a coherent plane wave incident at different angles and simultaneously coded in the Fourier-space pupil plane, as seen in Fig. 6.1. This pupil coding might be done dynamically using a spatial light modulator (SLM), or might involve a static, single coding element, such as the use of native glass-based aberrations in an uncorrected objective lens. The system's  $i^{\text{th}}$  intensity measurement is given by

$$I_i(\mathbf{r}) = \left| \mathcal{F}^{-1} \left\{ \mathcal{F} \{S_i(O(\mathbf{r}))\} \tilde{P}(\mathbf{k}) \tilde{M}_i(\mathbf{k}) \right\} \right|^2 \quad (6.1)$$

where  $\mathcal{F} \{ \cdot \}$  is the Fourier transform,  $\mathbf{r}$  and  $\mathbf{k}$  are image- and spatial frequency-space coordinates,  $S_i(\cdot)$  is the forward light scattering operator,  $\tilde{P}(\mathbf{k})$  is the pupil function of the imaging system, and  $\tilde{M}_i(\mathbf{k})$  is the  $i^{\text{th}}$  pupil coding mask applied at the Fourier plane using the SLM. We choose to use the multislice forward scattering operator [42] for  $S_i(\cdot)$  to account for thick samples with multiple-scattering light. The refractive index volume  $O(\mathbf{r})$  is recovered using an iterative optimization algorithm given by

$$\hat{O}(\mathbf{r}) = \operatorname{argmin}_{O(\mathbf{r})} \sum_i \left\| \left| \mathcal{F}^{-1} \left\{ \mathcal{F} \{S_i(O(\mathbf{r}))\} \tilde{P}(\mathbf{k}) \tilde{M}_i(\mathbf{k}) \right\} \right|^2 - I_i(\mathbf{r}) \right\|_2^2 \quad (6.2)$$

which seeks to minimize the difference between the modeled intensity given the current volumetric RI estimate  $\hat{O}(\mathbf{r})$  and the measured intensity  $I_i(\mathbf{r})$ .

Combined illumination- and detection-side coding in pupil-coded intensity ODT increases the diversity of phase information encoded into each measured image. This system thus requires less data and less optimization algorithm iterations for good-quality 3D RI reconstructions. Additionally, this system discards the requirement that the maximum illumination angle must be near the NA of the imaging objective for good results, which is necessary in traditional, angle scanning-only intensity ODT. Pupil-coded intensity ODT makes the reconstructions more robust and reduces the constraints on the imaging system by allowing the maximum illumination angles to be smaller than the imaging objective NA. In Chapter 5, we presented results from this system with pupil coding phase masks using random coefficients on the defocus, Zernike polynomial, and pixel bases. In this chapter, we investigate the use of physics-based machine learning to improve upon these results by optimizing the pupil coding phase masks for improved reconstructions.

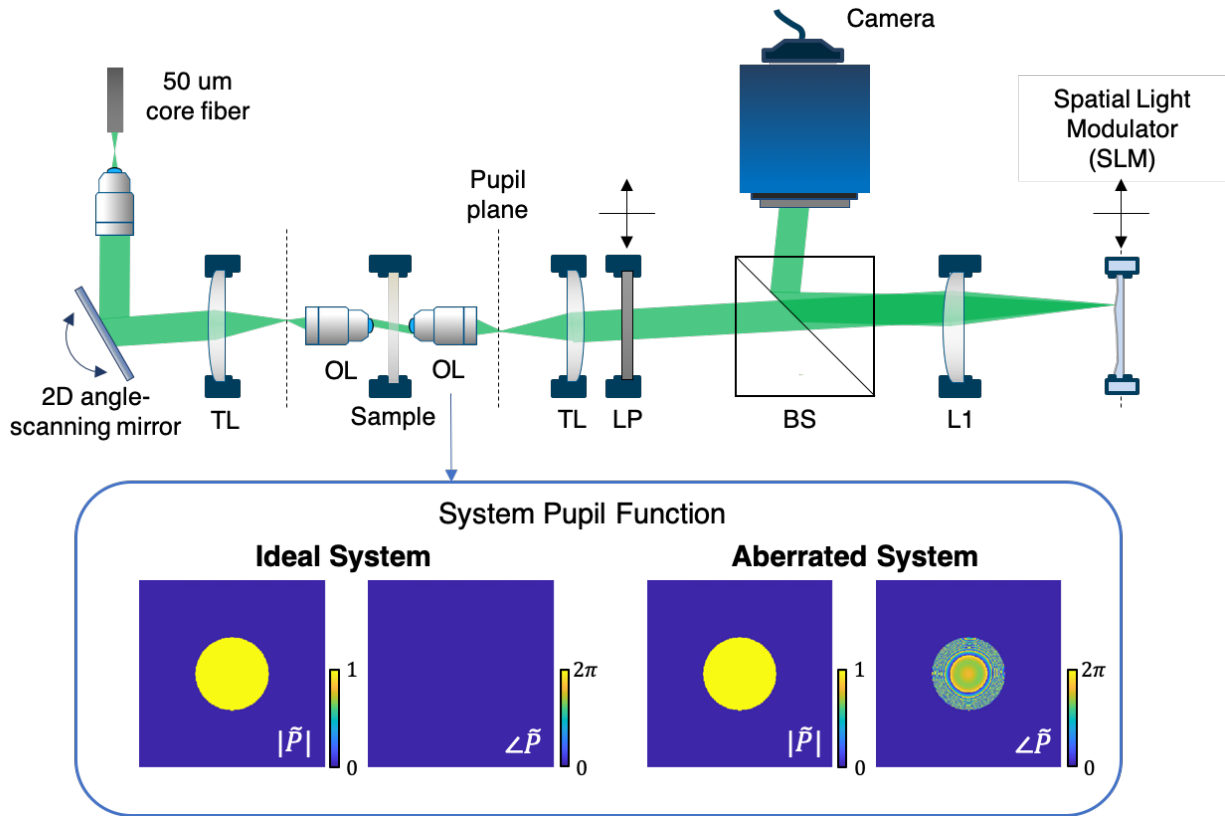


Figure 6.1: Pupil-coded intensity ODT uses simultaneous illumination-side and detection-side coding to increase measurement diversity for 3D RI imaging. A collimated LED beam is angled by a 2D angle-scanning mirror and relayed through a tube lens (TL) and objective lens (OL) to the sample plane. The sample-modulated light is detected by an illumination-side objective lens assembly and passed through a linear polarizer (LP) and Fourier transform lens (L1) to a spatial light modulator (SLM) at the pupil plane, which modulates the pupil phase. The light is reflected, Fourier transformed at L1, and passed through a beamsplitter (BS) to be imaged on the camera focal plane. The imaging objective lens pupil function  $P(\mathbf{k})$  is modeled in two ways: as ideal, aberration-free lens and with experimentally derived glass-based aberrations.

### 6.2.2 Physics-Based Machine Learning Algorithm

In physics-based machine learning, a fixed-length optimization algorithm is unrolled to treat every gradient step operation in the algorithm as a layer in a neural network. Certain imaging system and computational reconstruction parameters are denoted in the algorithm as *learnable parameters*, which are then updated by the algorithm to improve the reconstruction quality based on a comparison to a ground truth object. The method is data-driven because

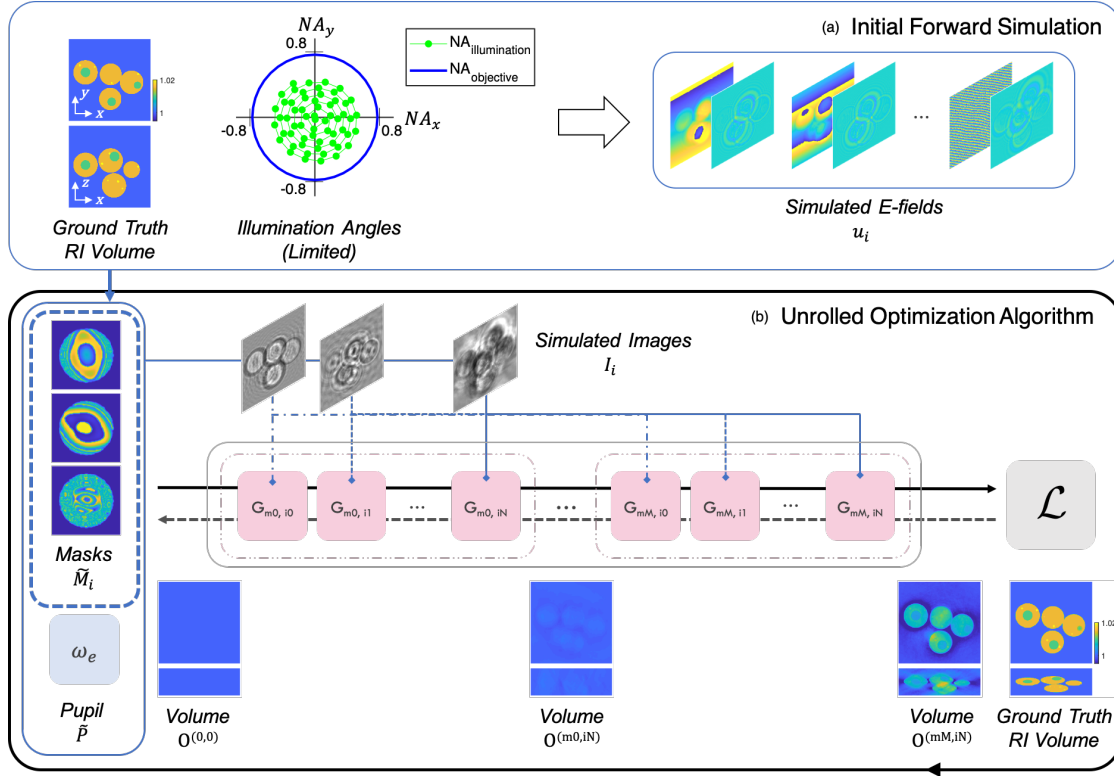


Figure 6.2: Overview of physics-based machine learning algorithm. (a) Angled plane wave illumination is scattered through a ground truth refractive index volume to produce  $N = 60$  simulated electric fields  $u_i(\mathbf{r})$ . A limited illumination condition is used with  $NA_{illum,max} = 0.565$ . (b) Each gradient step  $G$  of the fixed  $M$  iteration physics-based optimization algorithm is treated as a layer in a neural network. The electric fields  $u_i(\mathbf{r})$  are filtered by the system pupil  $\tilde{P}(\mathbf{k})$  and learnable masks  $\tilde{M}_i(\mathbf{k})$  to create simulated images  $I_i(\mathbf{r})$ , with the  $i^{th}$  image initializing each  $G_{m,i}$  gradient step for each  $m^{th}$  iteration.  $\omega_e$  represents noise and other nonidealities in the system used to initialize the network. After each gradient step, the reconstructed RI volume  $O^{(m,i)}$  is updated. The RMSE between the final reconstructed volume  $O^{(M,N)}$  is backpropagated through the network to update the learnable masks  $\tilde{M}_i(\mathbf{k})$ . This process is repeated for a set number of epochs to produce learned pupil masks.

it uses the properties of example data and reconstructions to optimize the system's learnable parameters. This process is limited by the need for a ground truth comparison object, which is often difficult or impossible to obtain for experimental data. Therefore, simulated data is often used for the machine learning training process, since the ground truth object is readily available for simulated data.

To form the pupil-coded intensity ODT physics-based machine learning algorithm, we unrolled Eq. 6.2 with a fixed number of  $M$  iterations, treating each gradient step  $G_{m,i}$  in

the optimization algorithm as a layer in a neural network, as seen in Fig. 6.2. For a system with  $N$  input images, the  $m^{\text{th}}$  optimization algorithm iteration over the  $i^{\text{th}}$  input image  $I_i$  is associated with gradient step  $G_{m,i}$ , for a total of  $N \cdot M$  network layers. This algorithm operates in the same way as the traditional gradient descent algorithm described in Eq. 6.2 in that it takes input measured images  $I_i$  and system parameters (such as angles of illumination  $\mathbf{NA}_i$ , system pupil function  $\tilde{P}$ , and pupil coding masks  $\tilde{M}_i$ ) to reconstruct a 3D refractive index volume  $O(\mathbf{r})$ . This is beneficial, as the unrolled algorithm retains all of the important physical models of both the optical system and light propagation that would be lost in a typical deep learning algorithm. However, this unrolled algorithm is different from the traditional gradient descent optimization algorithm because it has a fixed number of iterations and because it allows a loss function on the reconstructed volume to be backpropagated through the system to optimize the system parameters for improved reconstructions. We used this algorithm to update the pupil coding phase mask  $\tilde{M}_i(\mathbf{k}) = \exp j\phi_i(\mathbf{k})$  for each image under a limited illumination angle condition with maximum illumination NA 0.565 for an imaging system with objective NA 0.8, which requires pupil coding for high-quality 3D RI reconstructions.

We separately investigated learning the pupil phase masks coefficients on the defocus, Zernike polynomial, and pixel bases. For the defocus and Zernike bases, the pupil phase was defined by the Zernike coefficients  $c_{p,i}$  on the Zernike polynomials  $Z_p(\rho, \theta)$ ,

$$\phi_{zernike,i}(\mathbf{k}) = \sum_{p=0}^{p_z-1} c_{p,i} Z_p(\rho, \theta), \quad (6.3)$$

where  $\rho$  and  $\theta$  are the polar coordinates,  $p$  is the linear Zernike index, and  $p_z$  is the number of Zernike polynomial modes used following the Zernike polynomial implementation given in [224], as detailed in Chapter 5. For the defocus basis pupil functions, we used only the  $p = 4$  Zernike index, while for the Zernike basis pupils, we use the first  $p_z = 15$  Zernike modes. For the defocus and Zernike basis phase masks, the Zernike coefficients  $c_{p,i}$  were denoted as the learnable parameters updated by the machine learning algorithm. Under the pixel basis, the raw pixels of the pupil phase  $\phi_{pixel,i}(\mathbf{k})$  were denoted as the learnable parameters and were directly updated by the machine learning algorithm. The defocus-based masks have the least degrees of freedom, as a single defocus value is optimized for each mask. The Zernike-based masks have more degrees of freedom, with  $p_z = 15$  coefficients per mask, while the pixel-based masks have the most degrees of freedom, with 7869 pixels inside the pass-band of the imaging objective.

In order to increase the efficacy of the learned pupil phase masks when applied to the experimental pupil-coded intensity ODT system, we additionally included experimental constraints in our physics-based machine learning algorithm. As seen in Fig. 6.1, we used a phase-only LCOS SLM to create dynamic pupil coding in the experimental system. This SLM required that the applied phase profile be smoothly varying to avoid fringing field effects [81, 146, 167, 189] and that the phase be within the modulation range of approximately  $[0, 2\pi]$ . After each update step of the machine learning algorithm, we therefore  $2\pi$ -wrapped

the modeled pupil mask phase  $\phi_i(\mathbf{k})$  and blurred it with a Gaussian blur kernel ( $\sigma = 1$  pixel), giving

$$\tilde{M}_i(\mathbf{k}) = \exp j(\text{mod}(\phi_i(\mathbf{k}), 2\pi) * g_1(\mathbf{k})) \quad (6.4)$$

where  $g_\sigma(k_x, k_y) = \frac{1}{2\pi\sigma} e^{-\frac{k_x^2 + k_y^2}{2\sigma^2}}$  and the  $\text{mod}(\cdot, 2\pi)$  operator indicates that the phase has been wrapped to range  $[0, 2\pi]$ . We note that we observed better results from the learning algorithm in preliminary investigations without the Gaussian blurring, as blurring reduces the high spatial frequency features of the masks.

### 6.2.3 Physics-Based Machine Learning Training Procedure

We optimized the pupil coding phase masks using simulated data, as ground truth data does not exist experimentally for 3D RI imaging. Structured refractive index phantoms were simulated with similar refractive index differences to typical biological cells [13], as seen in Fig. 6.3(d). We simulated cell clusters of 5 to 6 spherical cells positioned using Poisson disk sampling [22]. Each cell had a 10  $\mu\text{m}$  diameter cell body ( $n = 1.015$ ), a randomly placed 4  $\mu\text{m}$  diameter nucleus ( $n = 1.01$ ), and ten randomly placed 1  $\mu\text{m}$  diameter organelles ( $n = 1.02$ ), in a uniform background ( $n = 1.0$ ). The cells were simulated with 0.065  $\mu\text{m}$  resolution. Following from previous work [103, 102], we used a single cell cluster object  $O_{train}(\mathbf{r})$  to train the system, with a second testing object  $O_{test}(\mathbf{r})$  to evaluate the efficacy of the learning process without updating the learnable parameters. Since the objects in use are high-dimensional and the algorithm is updating a handful of parameters, one object is usually sufficient for good-quality results. We note that when more objects were used in the training set, the learned masks did not change significantly.

The multislice (a.k.a. beam propagation) forward model [42] was used to simulate coherent plane-wave illumination through the phantom at illumination angles  $\theta_i$  to produce forward scattered electric fields  $u_i(\mathbf{r}) = S_i(O(\mathbf{r}))$ . The angle of illumination  $\theta_i = (\theta_x, \theta_y)$  is related to the illumination's numerical aperture (NA) by the relation  $NA = n \sin(\theta)$ , where  $n$  is the background refractive index. We restricted the algorithm to  $N = 60$  illumination angles with max illumination NA of 0.565, or approximately 70% of the imaging objective's 0.8 NA.

The forward scattered electric fields  $u_i(\mathbf{r})$  across images were downsampled to 0.13  $\mu\text{m}$  resolution and given as inputs to the machine learning algorithm. Pre-computing the forward scattered electric fields reduced the algorithm's computational complexity and allowed the initial forward scattering operation to be processed at a  $2\times$  pixel size compared to the reconstruction algorithm, leading to a higher-fidelity forward scattering model. In each iteration of the machine learning algorithm, the intensity fed into each layer was initialized by

$$I_i(\mathbf{r}) = |\mathcal{F}^{-1} \{ \mathcal{F} \{ u_i(\mathbf{r}) \} \tilde{P}(\mathbf{k}) \tilde{M}_i(\mathbf{k}) \}|^2 \quad (6.5)$$

The images  $I_i(\mathbf{r})$  were designed to be  $256 \times 256$  pixels at 0.13  $\mu\text{m}$  lateral pixel size, defining a  $33.28 \mu\text{m} \times 33.28 \mu\text{m}$  field of view. The axial pixel size was reduced to 0.3915  $\mu\text{m}$ . The

reconstructed object  $O(\mathbf{r})$  was therefore dimension  $256 \times 256 \times 85$  pixels. Given the high memory footprint of 3D RI imaging and unrolled algorithms, we used the MELD open-source memory-efficient learning kit [104] to enable this algorithm to fit on a 12 Gigabyte NVIDIA Titan X GPU.

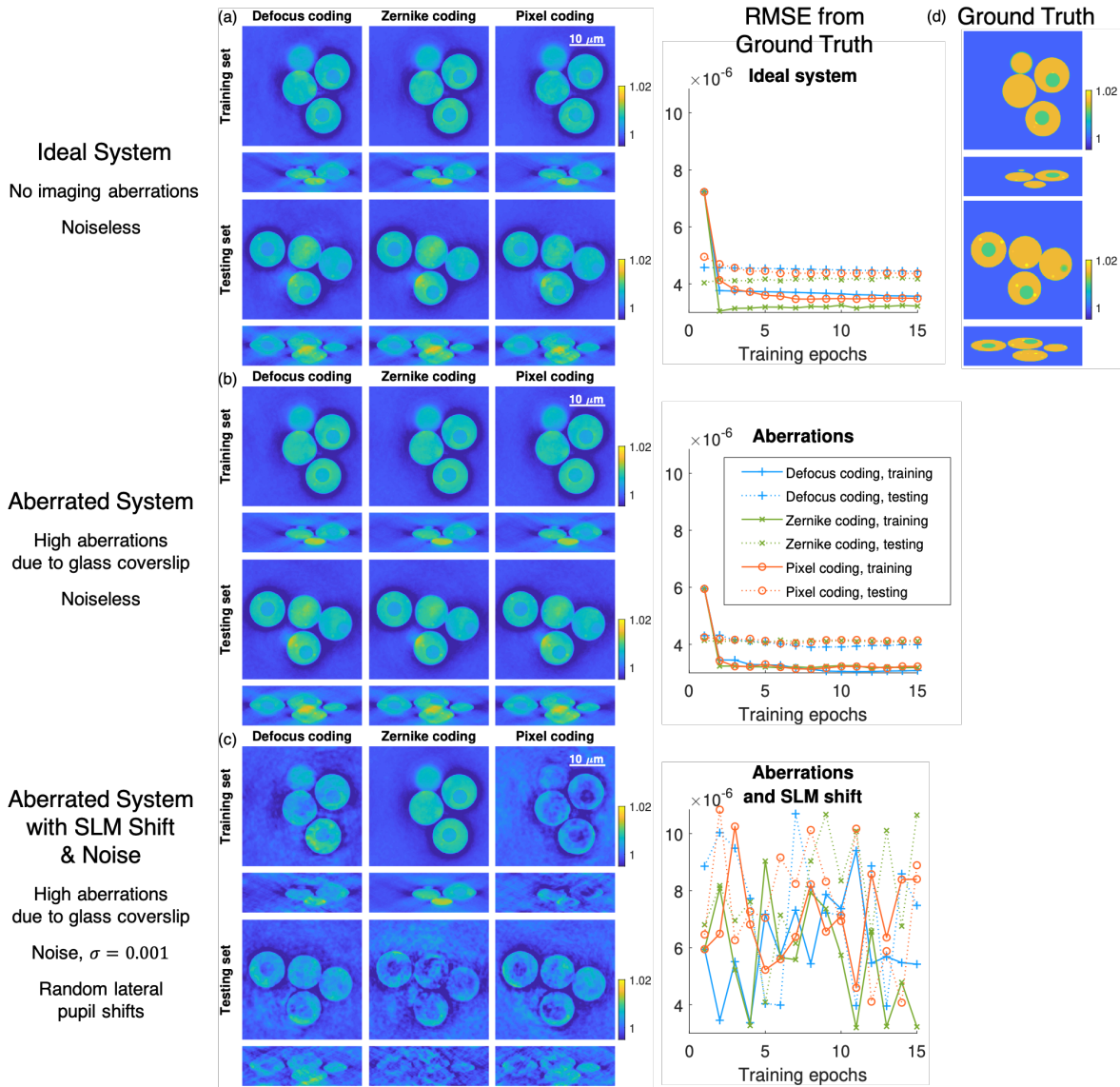


Figure 6.3: Final reconstructed RI volumes for the training and testing set for an (a) ideal, noiseless system; (b) glass-aberrated, noiseless system; and (c) glass-aberrated system with random SLM lateral shifts and additive Gaussian noise ( $\sigma = 0.001$ ). The RMSE from the (d) ground truth volumes are shown for each system across training epochs.

We defined the imaging parameters of our simulated data based on our experimental system, with a 0.8 NA, 50 $\times$  imaging objective and a camera with pixel size 6.5  $\mu\text{m}$ . We trained the learned pupil coding masks under three different system configurations, as seen in Fig. 6.3. In System 1, we simulated an ideal, noiseless system with a binary amplitude pupil function  $\tilde{P}(\mathbf{k})$  to simulate the pass-band of the imaging objective. In System 2, we simulated a noiseless system with glass-induced aberrations in the pupil function  $\tilde{P}(\mathbf{k})$ , based on the aberrations present in our experimental uncorrected objective lens when imaging through a 0.17 mm thick #1.5 glass coverslip. In System 3, we simulated a glass-aberrated system with Gaussian noise ( $\sigma = 0.001$ ) added to each image  $I_i$  and SLM lateral position shifts of 1 – 2 pixels, which changed randomly across training epochs. The two system pupil functions used are shown in Fig. 6.1(b). The final training and testing set reconstructed volumes  $O^{(M,N)}$  for the last training epoch are shown in Fig. 6.3 for each of these cases, along with the RMSE from the ground truth volume for each epoch. We can see from these results that both the ideal (Fig. 6.3(a)) and glass-aberrated (Fig. 6.3(b)) systems show decreases in RMSE for both the training and testing sets across all pupil coding bases through the machine learning optimization algorithm. However, the random shifts of the SLM position mean that the aberrated system with SLM shifts and additive noise (Fig. 6.3(c)) does not have good-quality reconstructions for either the training or the testing set, even as the pupils are updated.

## 6.3 Results

We present the learned pupil coding masks under the machine learning algorithm, as well as simulation and experimental reconstructions using the learned pupil masks. Our results indicate that the random coefficients on the different pupil coding bases perform as well as the learned coefficients in simulation, and that the random coefficients produce better results than the learned coefficients in experiment. This suggests that randomly chosen coefficients are in general useful for the pupil-coded intensity ODT system, though further investigation of the physics-based machine learning algorithm may prove useful to improve the learned pupil mask results.

### 6.3.1 Learned Masks

We ran the physics-based machine learning algorithm with  $N = 60$  illuminations and  $M = 25$  iterations within the optimization algorithm, for a total of 900 neural network layers. In each epoch, the unrolled algorithm was run to reconstruct the final layer’s reconstructed volume,  $O^{(M,N)}$ , and the error was backpropagated to update the pupil coding masks  $\tilde{M}_i$  for each  $i^{\text{th}}$  illumination. We ran the training algorithm for 15 epochs, when the learned masks appeared to reach convergence. The Adam optimizer was used with a learning stepsize of 10 and a gradient descent optimization stepsize of  $\alpha = 0.0001$ . The system was configured for a 0.8 NA, 50 $\times$  objective lens. All masks and associated coefficients were initialized with a flat

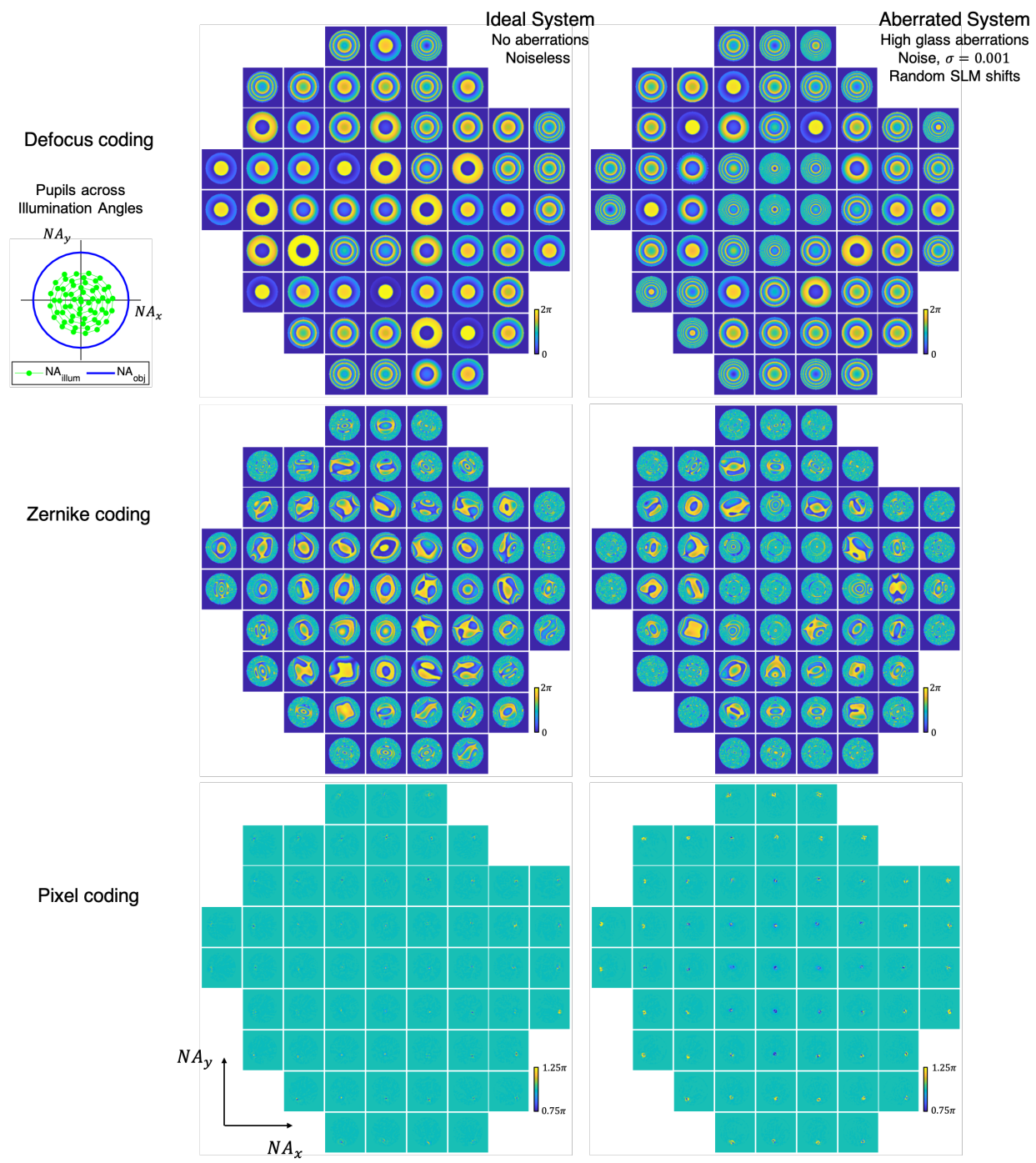


Figure 6.4: Map of learned masks across pupil bases for ideal, noiseless system and aberrated system with noise and SLM shifts. Each mask is displayed at the approximate location in Fourier space as its corresponding angle of illumination.

phase profile. For the defocus and Zernike bases, the Zernike coefficients for the defocus index  $p = 4$  and for the first 15 Zernike indices were updated by the algorithm, respectively. These coefficients were then used to create the pupil phase masks  $\tilde{M}_i = \exp(j\phi_i)$ , which were in turn used to create the simulated images  $I_i$  for the next training epoch. For the pixel basis, the pixelated phase mask  $\phi_i$  was updated by the algorithm directly. Given the need to match experimental constraints of the SLM, after each epoch mask update step, each mask's phase  $\phi_i$  was wrapped to be within  $[0, 2\pi]$  and smoothed with a Gaussian filter with  $\sigma = 1$  pixel. This allowed the masks to fit within the dynamic range of the SLM and to avoid fringing field effects [81, 146, 167, 189] after the optimization. We note that different experimental conditions will have different nonidealities that should be included in the optimization algorithm in this way, and that results might improve if the Gaussian blurring for the SLM could be avoided, allowing the trained masks to have sharper features.

For the ideal system (System 1), the system pupil function  $\tilde{P}$  was set to be a binary amplitude mask representing the lowpass filter of the objective lens (Fig 6.1(b)). For the aberrated system (System 2), the system pupil function was set to be an experimentally-derived pupil function from an uncorrected objective lens imaging through a 0.17 mm thick glass #1.5 coverslip, which is primarily driven by spherical aberration, as seen in Fig. 6.1(b). For the aberrated system with noise and SLM shifts (System 3), the same aberrated system pupil function was used as in System 2 and random Gaussian noise with  $\sigma = 0.001$  was added to each image  $I_i$  before each training epoch. Additionally, the masks  $\tilde{M}_i$  were shifted laterally by a random shift  $(\beta_x, \beta_y) = \text{round}(\mathcal{N}(\mu = 0, \sigma = 1))$  in the creation of the simulated images  $I_i$  while the known masks used inside the training algorithm were not shifted. This simulated a relative shift between the experimental placement of the SLM and the estimated SLM position in the reconstruction. The shift  $(\beta_x, \beta_y)$  was the same within each training epoch, but varied randomly across epochs. The random additive Gaussian noise  $\sigma = 0.001$  did not appear to greatly affect the training process in separate tests not shown here. However, the inclusion of glass-induced aberrations made large differences to the learned masks across all pupil coding bases, and the random SLM shifts made a large difference in the pixel basis learned masks. Given that the training was done on  $256 \times 256$  pixel images with pixel size  $0.13 \mu\text{m}$ , a single pixel shift of the SLM in the training process is the equivalent to a 7.6 pixel shift of the experimental SLM, or approximately  $95 \mu\text{m}$ , which is entirely feasible for a manually aligned experimental set-up.

The pupil coding masks learned through this training algorithm for the defocus, Zernike, and pixel bases are shown in Fig. 6.4 for the ideal system (System 1) and aberrated system with noise and SLM shifts (System 3). The learned coefficients for the defocus and Zernike bases are shown for all three system configurations in Fig. 6.5. A combined plot of the pixel basis pupil masks are also shown for each system in Fig. 6.5.

In general, we note that the coefficients and pixel coding amplitudes are much lower for the ideal system (System 1) than for the two systems with glass aberrations (Systems 2-3) across all coding bases. From Fig. 6.5, we see that the two systems with glass aberrations produce very similar results for the noiseless case and the case with noise and random SLM shifts for the defocus and Zernike bases, while the results for the pixel coding have

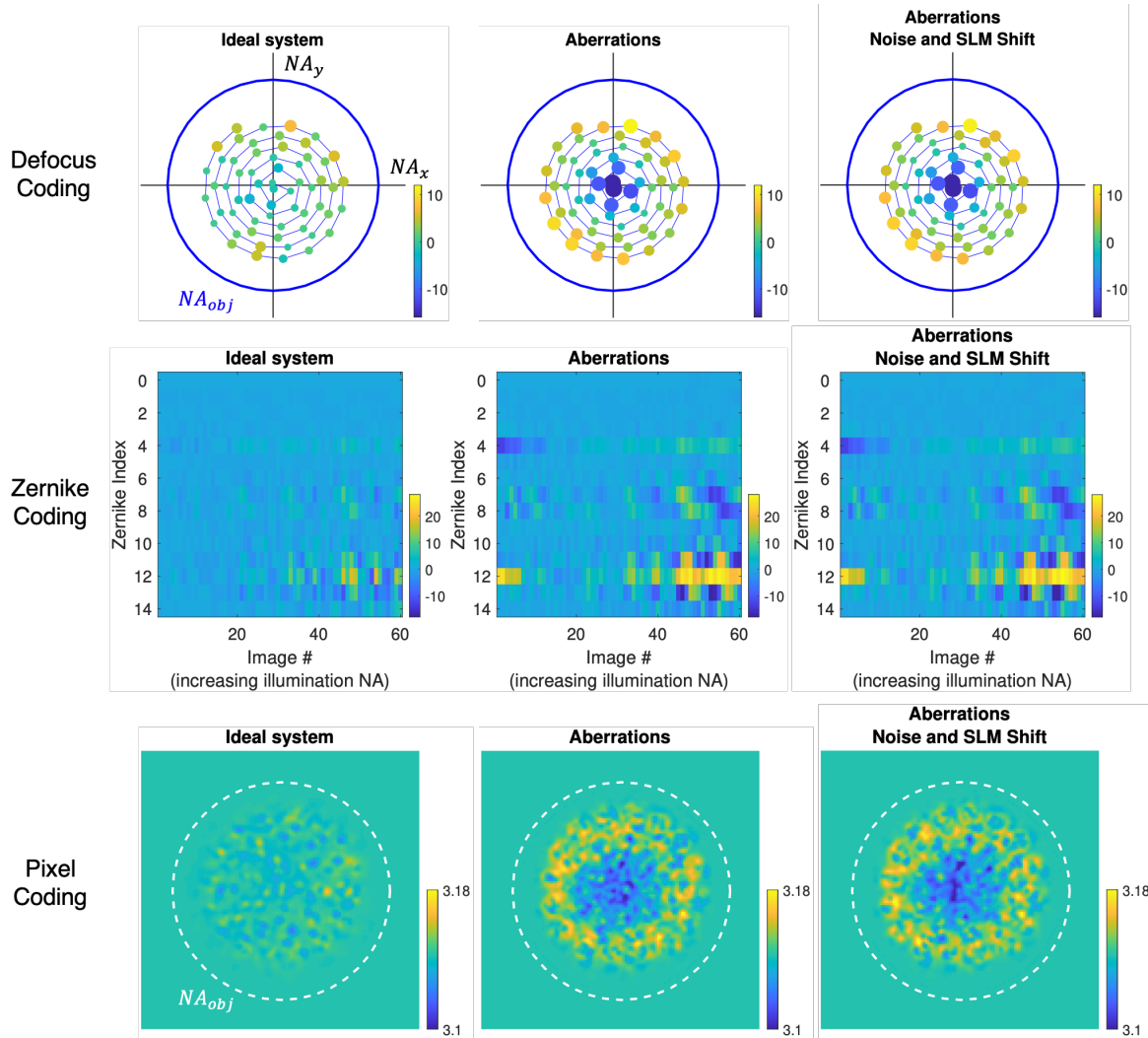


Figure 6.5: Comparison of learned masks across the (a) defocus, (b) Zernike, and (c) pixel pupil coding bases for the ideal system, aberrated system, and aberrated system with noise and SLM shift. (a) The learned defocus distance in microns is displayed for each angle of illumination, with the plotted circle size corresponding to absolute distance from focus and color corresponding to defocus distance. (b) The learned Zernike coefficient weights are displayed for each image. Coefficient values generally increase in magnitude as the image’s illumination NA increases. (c) The learned pixel coding is averaged to create a composite image, as each learned pattern is generally confined to a small area around the spectrum’s angle of illumination-based shift. The learned coefficients for the ideal system are generally lower magnitude than for the aberrated systems. The learned Zernike and defocus coefficients are similar for the noiseless and noisy aberrated systems, while the learn pixel basis masks differ across all modeled systems.

slightly wider and more rounded features in the case with SLM shifts (System 3) than without (System 2). This is due to the algorithm compensating for the random shifts in the SLM position between training epochs. Since the defocus and Zernike bases already have widespread structure, small shifts in the SLM location make less difference than in the pixel basis case, where small shifts can lead to very different results.

For the defocus basis, we see in Fig. 6.5 that the images at low- and high-illumination angles typically have larger amounts of defocus, while the middle-illumination angles have smaller amounts of defocus. For the Zernike basis, we see that the defocus ( $p = 4$ ), coma ( $p = 7, 8$ ), secondary astigmatism ( $p = 11, 13$ ), and spherical ( $p = 12$ ) components have the largest magnitudes in all three systems. From Fig. 6.4, we can see how the Zernike basis masks appear to rotate as the illumination changes, tracking the shifted object spectrum. In the ideal system, the Zernike basis masks at the low- and middle-illumination angles have lower coefficients and less phase-wrapping, while the high-angle masks generally exhibit high coefficients and high phase-wrapping. In the aberrated system, only the middle-illumination angles have lower coefficients, and both the low- and high-angles exhibit high coefficients with high phase-wrapping. In both the defocus and Zernike cases, there is a diversity of low- and high-coefficient masks in all modeled systems, demonstrating a need for diverse masks across angle of illumination.

In the pixel basis masks, the learned masks are generally a flat  $\pi$  phase value except in a local area around the mask’s corresponding angle of illumination. In this local area, where the object spectrum’s DC term will be shifted by the angle of illumination, the phase is modulated differently to produce higher contrast intensity images. Since the modulation is confined to a local area, we can average all 60 masks to create a combined mask for ease of viewing the resultant learned masks, as seen in Fig. 6.5. The dotted white line represents the NA of the imaging objective. For the ideal system, the modulation phase has smaller magnitude values than for the glass-aberrated systems. Seemingly random low-phase speckles, similar to Zernike phase contrast imaging [122, 237], are apparent, especially at mid-to-high illumination angles, with a fewer number of high-phase speckles. In the glass-aberrated systems, the patterns show primarily low-phase speckles at low-illumination angles and high-phase speckles at high-illumination angles. The features in the glass-aberrated system with noise and random SLM shifts (System 3) have larger, smoother features in general than the glass-aberrated system without noise (System 2), but otherwise exhibit similar features.

### 6.3.2 Simulation Results

After the learned masks were obtained from the physics-based machine learning algorithm, we tested them on larger simulated objects, reconstructing  $O(\mathbf{r})$  with a traditional, FISTA-based optimization algorithm. A cell cluster volume was simulated with 10 spherical cells positioned using Poisson disk sampling [22] inside a  $33.28\ \mu\text{m}$  cube. Each cell has a  $10\ \mu\text{m}$  diameter cell body ( $n = 1.345$ ), a randomly placed  $4\ \mu\text{m}$  diameter nucleus ( $n = 1.34$ ), and ten randomly placed  $1\ \mu\text{m}$  diameter organelles ( $n = 1.35$ ), in a uniform aqueous background

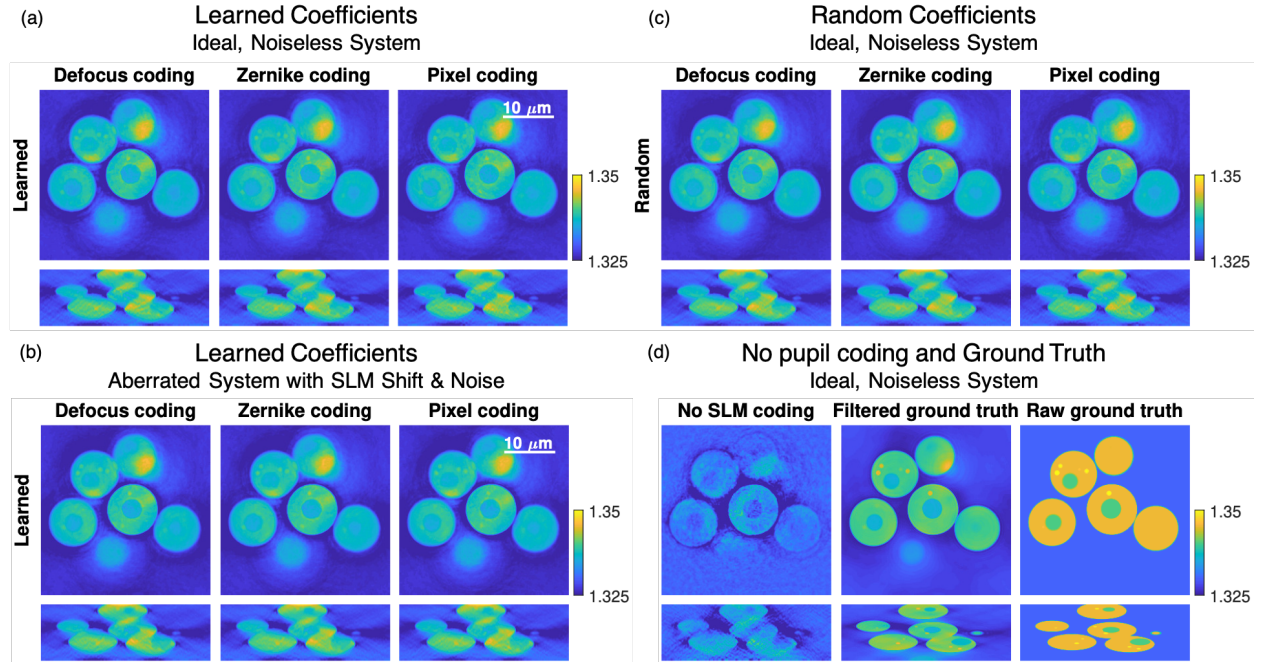


Figure 6.6: Simulated reconstruction results in the limited illumination condition with (a) mask coefficients learned on an ideal, noiseless system, (b) mask coefficients learned on a glass-aberrated system with noise and SLM shifts, (c) random coefficients, and (d) no pupil coding, with NA-filtered and raw ground truth RI volumes for comparison. All learned and random masks produce similar reconstruction results, and show great improvement over the reconstruction without pupil coding.

( $n = 1.33$ ), as seen in Fig. 6.6(d). The multislice algorithm was used for the forward propagation of angled light through the volume at  $0.065 \mu\text{m}$  resolution. The resultant electric fields were downsampled by a factor of 2 to a  $0.13 \mu\text{m}$  resolution, to match the pixel size of a  $d_{\text{pixel}} = 6.5 \mu\text{m}$  camera with a  $50\times$  objective lens. The fields were then filtered by the system pupil  $\tilde{P}(\mathbf{k})$  and pupil coding masks  $M_i(\mathbf{k})$  and the intensity images  $I_i(\mathbf{r})$  were taken at the camera plane. This procedure was repeated for an empty volume with background  $n = 1.33$  to produce background images  $I_{bk,i}(\mathbf{r})$ , which were then divided out of the measured intensity images  $I_i(\mathbf{r})$  to remove simulation artifacts and provide a uniform background across all images. Random Gaussian noise with  $\sigma = 0.001$  was added to each image. The simulations were done under a limited illumination condition with 60 images and  $NA_{\text{illum,max}} = 0.565$  for a  $0.8 \text{ NA}$ ,  $50\times$  imaging objective.

We performed the forward simulation for the learned defocus, Zernike, and pixel basis pupil masks from the three systems discussed above (ideal, glass-aberrated, and glass-aberrated with noise and SLM shift). For each forward simulation, we reconstructed a 3D

refractive index volume with a traditional, FISTA-based optimization algorithm. The reconstruction results for the ideal system (System 1) learned pupil masks and glass-aberrated system with noise and SLM shift (System 3) pupil masks are shown in Fig. 6.6(a-b). Results from the glass-aberrated system without noise (System 2) pupil masks are not shown, as they are similar to results from System 1 and 3. We compared to simulations with random coefficients drawn from the uniform random distribution on the same scale as the learned coefficients (Fig. 6.6(c)) and for the case without pupil coding (Fig. 6.6(d)). All simulations were done without glass-induced objective aberrations. The raw ground truth and NA-filtered ground truth refractive index volumes are shown for comparison in Fig. 6.6(d).

Given the limited illumination condition, the reconstruction without pupil coding does not produce good-quality results. Conversely, the results from all learned masks and all random masks show high-quality reconstructions, with very little difference in reconstruction quality across all sets of masks. This suggests that the learned coefficients and random coefficients perform equally well for encoding greater amounts of diverse phase information in the system’s measurements for improved 3D refractive index reconstructions.

### 6.3.3 Experimental Results

We tested the effectiveness of the learned pupil coding masks in an experimental setup shown in Fig. 6.1. A  $\lambda = 530$  nm wavelength LED is fiber-coupled into a 50  $\mu\text{m}$  fiber, then beam-expanded and collimated using a Nikon Plan Apochromatic  $2\times$ , 0.1 NA objective. A dual-axis mirror mount with DC servo motors (Thorlabs Z812 with Kinesis brushed motor controller) is used to angle the collimated beam at a conjugate imaging plane. The angled beam is relayed through the illumination-side objective (0.8 NA,  $50\times$ , working distance (w.d.) 1 mm Olympus M Plan Fluorite air objective) and 180 mm tube lens assembly to illuminate the sample with a coherent, angled plane wave. The light is modulated by the sample and imaged by an identical 0.8 NA,  $50\times$  objective lens and 180 mm tube lens assembly. This objective has a long working distance, making it practically easier to use in this dual-objective configuration. However, it is not corrected for imaging through glass and therefore exhibits high glass-induced aberrations when imaging samples beneath a coverslip, as in all experimental results shown here.

The light is relayed through a linear polarizer aligned to the modulation axis of the LCOS spatial light modulator. A 300 mm lens Fourier transforms the light incident at the SLM’s modulation plane, allowing pupil phase coding by the SLM (Hamamatsu X13138-01). The light reflects from the back surface of the SLM and is Fourier transformed again by the 300 mm lens before being deflected by a beamsplitter to be imaged at the camera’s focal plane.

We aligned and calibrated this experimental system in the same fashion as Sec. 5.4.1-5.4.1. In addition, we had to ensure that the experimental angle of illumination matched the angle of illumination used to produce the learned pupil masks, since the each learned mask relies heavily on the corresponding angle of illumination, especially for masks on the pixel and Zernike bases. In order to faithfully reproduce the desired angles of illumination

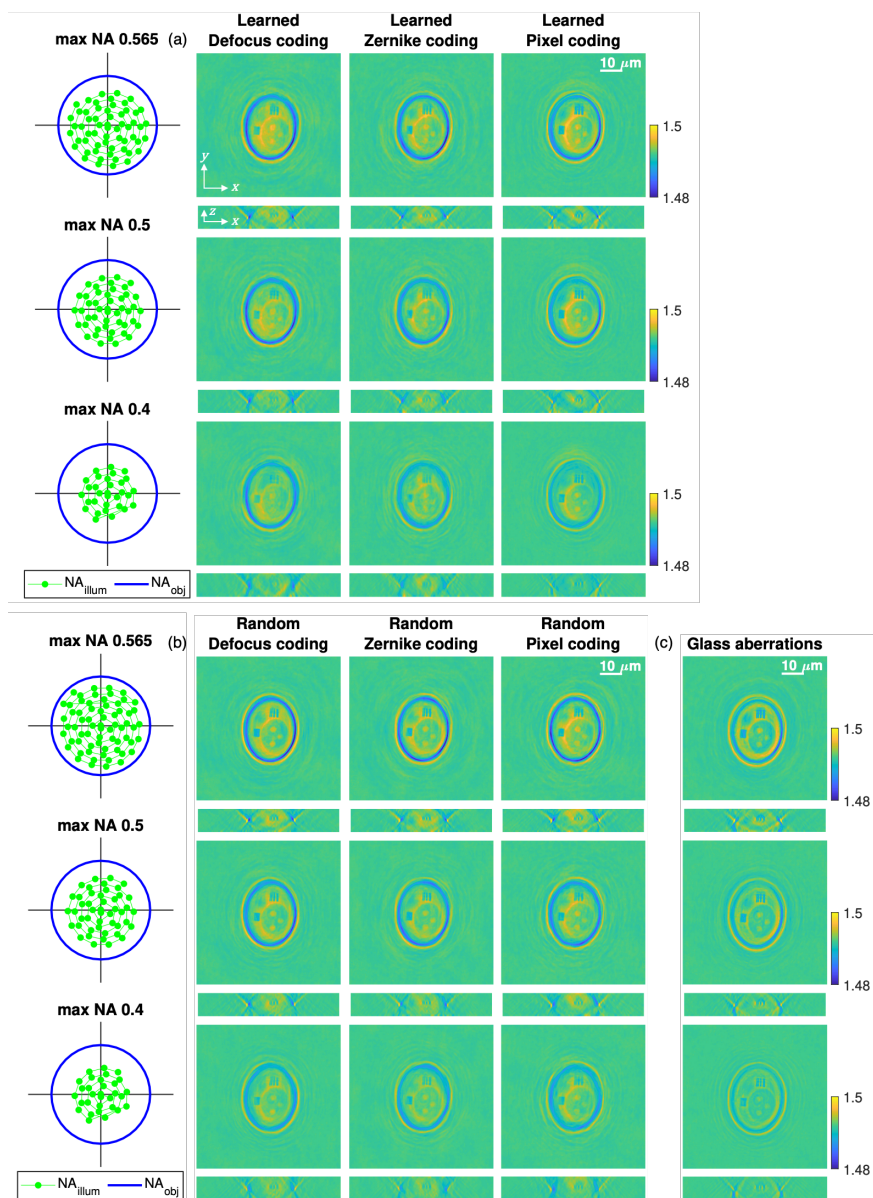


Figure 6.7: Experimental results on a fabricated phase object in  $n = 1.4917$  immersion oil across three limited illumination conditions, with maximum illumination NA 0.565, 0.5, and 0.4, respectively. Results are similar for (a) mask coefficients learned on a glass-aberrated system with noise and SLM shifts and (b) random coefficients. Results for (c) a glass-aberrated system without SLM pupil coding exhibit more artifacts, but still show a decent reconstruction. No regularization was used in the reconstruction.

$\mathbf{NA}_{illum,desired}$ , we first imaged a cheek cell (without a glass coverslip, to avoid the objective's aberrations) with an initial set of angled mirror voltages  $\mathbf{v}_{init}$  and calibrated the corresponding angles of illumination  $\mathbf{NA}_{illum,init}$  with the calibration described in [56]. We placed both vectors in homogeneous coordinates

$$\mathbf{v}_{H,init} = \begin{bmatrix} v_{init}^{(0,0)} & v_{init}^{(0,1)} & \dots & v_{init}^{(0,N)} \\ v_{init}^{(1,0)} & v_{init}^{(1,1)} & \dots & v_{init}^{(1,N)} \\ 1 & 1 & \dots & 1 \end{bmatrix} \quad (6.6)$$

$$\mathbf{NA}_{H,illum,init} = \begin{bmatrix} NA_{illum,init}^{(0,0)} & NA_{illum,init}^{(0,1)} & \dots & NA_{illum,init}^{(0,N)} \\ NA_{illum,init}^{(1,0)} & NA_{illum,init}^{(1,1)} & \dots & NA_{illum,init}^{(1,N)} \\ 1 & 1 & \dots & 1 \end{bmatrix} \quad (6.7)$$

to define the homographic transformation between mirror voltage and angle of illumination given by

$$\mathbf{v}_{H,init} = \mathbf{C} \mathbf{NA}_{H,illum,init}. \quad (6.8)$$

The homography given by  $\mathbf{C}$  was calculated from a least-squares fit and applied to the desired illumination angles  $\mathbf{NA}_{H,illum,desired}$  to obtain the corresponding control voltages for the mirror  $\mathbf{v}_{H,desired}$ . This process was iterated through twice to ensure that the proper voltages were applied to obtain the correct angles of illumination. We additionally ensured that the signal at the camera appeared to be modulated when the learned pixel basis masks were in use, as the modulation area for the pixel-basis masks was small and located around the angle of illumination-derived spectral shift in the Fourier plane. However, while we were able to ensure that the angle of illumination was highly similar to that used in the training algorithm, instabilities in the system and mirror control mean that the angle of illumination varies slightly for each dataset, so we expect some error may have been introduced due to small differences in the angle of illumination, as well as error in the SLM lateral positioning. We present results for two objects: a fabricated refractive index phantom [243], shown in Fig. 6.7, and a two-layer stack of 8  $\mu\text{m}$  diameter polystyrene beads, shown in Fig. 6.8. All learned results shown were captured using the defocus, Zernike, and pixel basis pupil masks derived from the glass-aberrated system with noise and SLM shifts (System 3), as this matches the experimental system parameters most closely. However, data was also captured with the pupil masks created under the ideal system (System 1) and glass-aberrated, noiseless system (System 2), with similar reconstruction results to those shown. We also imaged with masks based on random coefficients chosen from the uniform random distribution. Additionally, we imaged the samples without any dynamic SLM pupil coding, using instead the native aberrations of the uncorrected objective lens to provide a static pupil coding.

The fabricated refractive index phantom developed by Ziemczonok et al. [243] was placed between two 0.17 mm thick #1.5 glass coverslips with  $n = 1.488$  Cargille immersion oil ( $n = 1.4917$  at  $\lambda = 530$  nm). We expect the unexposed USAF lines to be  $n = 1.5241$ , the nucleus background to be  $n = 1.5353$ , and the cell body and nucleoli to be  $n = 1.5476$  at  $\lambda = 530$  nm, representing a relatively large difference in refractive index between the

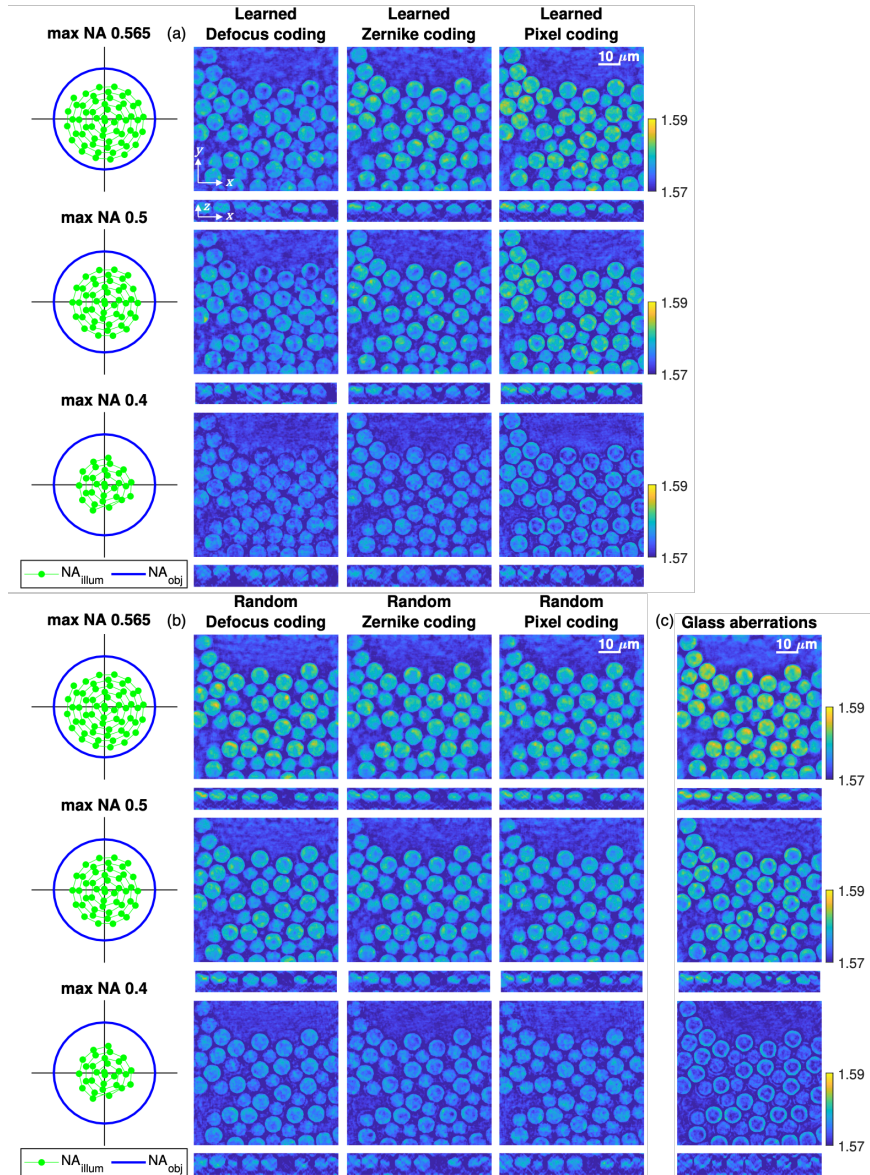


Figure 6.8: Experimental results on a two-layer stack of  $8 \mu\text{m}$   $n = 1.596$  polystyrene beads in  $n = 1.57$  immersion oil across three limited illumination conditions, with maximum illumination NA 0.565, 0.5, and 0.4, respectively. Results are similar for (a) mask coefficients learned on a glass-aberrated system with noise and SLM shifts and (b) random coefficients, excepting the learned defocus coding, which shows poor results. Results for (c) a glass-aberrated system without SLM pupil coding have a better reconstruction when  $NA_{illum,max} = 0.565$ , but exhibit a loss of low-spatial frequencies in the reconstruction for  $NA_{illum,max} = 0.5$  and below. Regularization enforced that the reconstruction was purely real and had larger values than the background.

sample and background immersion oil. We reconstructed under three limited illumination conditions without any regularization, with maximum illumination NA's of 0.565, 0.5, and 0.4, as seen in Fig. 6.7. In all reconstructions, the expected phase object's refractive indices were not reproduced, due to the high mismatch with the background RI. However, the relative refractive index across the sample was maintained, especially in the learned and random reconstructions with maximum illumination NA's of 0.565 and 0.5. In general, the reconstruction quality is similar between the learned and random pupil masks. The reconstructions without SLM pupil coding, using only the objective's aberrations for pupil coding, exhibit higher ringing artifacts and lose low-spatial frequency information as the maximum illumination NA is decreased.

Two layers of 8  $\mu\text{m}$  diameter polystyrene beads ( $n = 1.596$  [239]) were immersed in Cargille  $n = 1.564$  immersion oil ( $n = 1.57$  at  $\lambda = 530$  nm) and placed between two #1.5 coverslips. The reconstruction algorithm used regularization to enforce prior knowledge that the reconstructed volume was purely real and had larger values than the background refractive index. We see in Fig. 6.8 that the learned and random pupil coding-based datasets all reconstructed the two layers of beads well for the  $NA_{illum,max} = 0.565$  and  $NA_{illum,max} = 0.5$  limited illumination conditions, with the exception of the learned defocus pupil coding, which did not provide good-quality reconstructions. The learned pixel coding and random defocus, Zernike, and pixel coding datasets all reconstructed similar bead RI values for the  $NA_{illum,max} = 0.565$  condition, with the glass-aberration coded dataset reconstructing the highest bead RI, though none were close to the expected RI value of  $n = 1.596$ . However, the glass-aberration-based dataset with no SLM pupil coding had significantly degraded reconstructions for the  $NA_{illum,max} = 0.5$  and lower, as the low spatial frequencies of the bead centers are not reconstructed. Overall, the random pupil coding appears to provide the best reconstructions for the polystyrene bead sample.

## 6.4 Analysis

We compare the learned and random pupil coding masks using the transfer function weight matrix analysis from Sec. 5.5.1. As seen in Fig. 6.9, both the learned and random pupil coding masks promote the transfer of low-spatial frequencies into the measured images for 3D RI reconstruction under limited illumination conditions, improving on the case without pupil coding. While the learned defocus and Zernike coding weight matrices  $W$  are more uniform and have a slightly higher  $D$  metric value than their random counterparts, the improvement is slight. Conversely, the learned pixel coding exhibits lower weighting and a lower  $D$  metric value than its random pixel counterpart, though still transfers the low-spatial frequencies through the imaging system well.

In both simulated results and the transfer function analysis, we have seen that the reconstructions derived from learned pupil coding masks are of the same quality as random pupil coding masks. This suggests that random coefficient-based pupil coding masks should be used in pupil-coded intensity ODT instead of the learned masks presented here, to eliminate

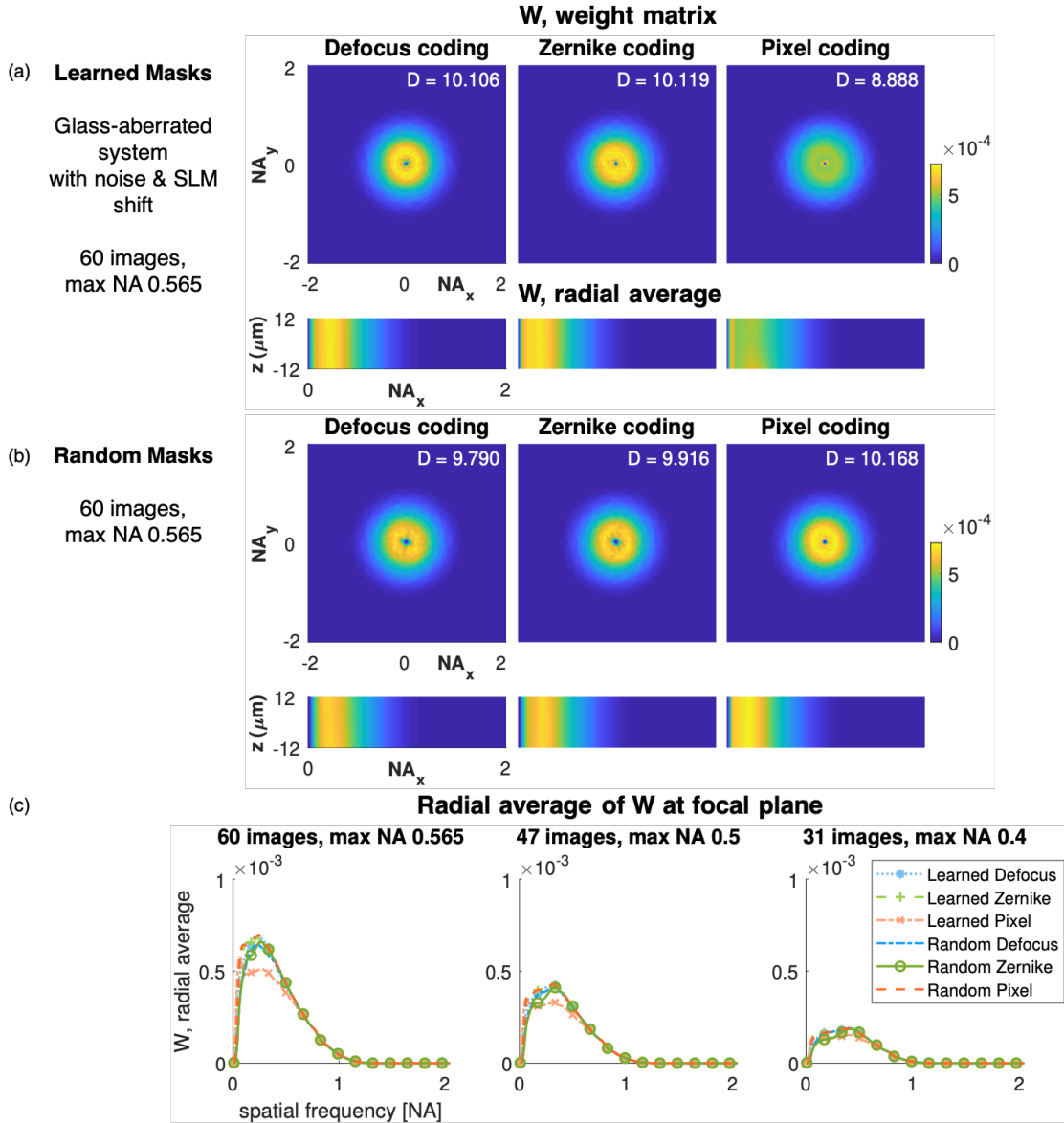


Figure 6.9: Transfer function analysis of learned and random pupil coding masks. The transfer function weight matrix  $W$  at the focal plane and the radial average of  $W$  at each  $z$  plane are shown for (a) learned masks and (b) random masks for  $N = 60$  images under limited illumination NA. (c) The radial average of the focal plane  $W$  is compared across mask types for different limited illumination conditions. All masks support transfer of low spatial frequencies into the measurements, even at very limited illumination NA.

the need for the extra training and rigorous illumination angle alignment process required by the learned pupil coding masks.

The experimental reconstructions with learned pupil coding masks can additionally be worse quality than random pupil coding masks, as seen in Fig. 6.8. There are a few possible causes for this reduction in reconstruction quality for the learned masks. First, the learned masks rely upon rigorous illumination angle and SLM alignment, which is difficult to perform experimentally. Second, the learned masks were defined on a much smaller scale than the phase masks applied at the SLM surface and in the experimental reconstructions, since the learning algorithm had to operate on a small enough volume to fit inside GPU memory. Therefore, the masks were upsampled from  $256 \times 256$  pixel images (pixel size  $0.13 \mu\text{m}$ ; Fourier plane pixel size  $0.024 \mu\text{m}^{-1}$ ) to be displayed on the  $1024 \times 1280$  pixel SLM surface (physical pixel size  $12.5 \mu\text{m}$ ; Fourier plane pixel size  $0.0031 \mu\text{m}^{-1}$ ; total upsampling factor  $7.6\times$ ) and for use in the reconstruction algorithm ( $500 \times 500$  pixel images; pixel size  $0.13 \mu\text{m}$ ; Fourier plane pixel size  $0.012 \mu\text{m}^{-1}$ ; total upsampling factor  $1.95\times$ ). The upsampling process might have created differences between the original learned mask and the pupil phase displayed at the SLM, as well as in the reconstruction algorithm's phase mask, creating model mismatch that degrades reconstruction quality. In addition, while the original pupil phase masks were Gaussian blurred with  $\sigma = 1$ , translating to a larger blur factor at the SLM plane, this blurring might have been insufficient to avoid fringing field effects at the SLM, another important source of model mismatch. More attention to the upsampling process might reduce this source of model mismatch and improve experimental results with learned pupil coding masks.

## 6.5 Conclusion

We have presented a physics-based machine learning algorithm that optimizes the dynamic pupil coding masks for pupil-coded intensity ODT. We have presented learned pupil coding masks for defocus, Zernike, and pixel bases across three system configurations. Simulated results show that these learned pupil coding masks perform as well as random pupil coding masks, and experimental results corroborate this finding, though show better performance of the random pupil coding masks over learned masks in some cases. A transfer function analysis reveals that the learned pupil coding masks have slight improvements over their random counterparts in theory for the defocus and Zernike bases, but verify that the learned and random pupil coding masks have similar performance for 3D refractive index imaging using pupil-coded intensity ODT. These results suggest that random pupil coding masks should be used instead of the presented learned pupil coding masks.

However, we believe there is great potential for further exploration of physics-based machine learning system optimization for pupil-coded intensity ODT. There are many unexplored avenues for investigation, including joint learning of the ideal illumination pattern and pupil coding masks for 3D RI imaging. We note as well that the constraints introduced by the experimental LCOS SLM may have effected the efficacy of the learned pupil coding

masks. In particular, the limitation to smoothly varying phase values (to avoid fringing field effects) within the modulation range  $[0, 2\pi]$  of the SLM meant that the learned masks were constrained to low phase values without high-resolution features. In preliminary investigations without phase mask blurring, we observed more improvement in the learned masks over the random masks in simulated reconstructions. If a better pupil coding mechanism could be devised without the blurring requirement of the LCOS SLM, the learned pupil coding might show more improvement over random pupil coding.

Another area where improvement is possible is by further reduction of the number of images or reduction of the number of distinct pupil coding masks used across all images. In particular, the native glass aberrations of an uncorrected objective are able to improve the reconstruction of experimental objects in limited illumination conditions over corrected objectives without pupil coding. Using the proposed machine learning algorithm to learn optimal single pupil coding masks (or a small number of pupil coding masks) is a promising avenue to pursue. This is particularly true since a single pupil coding mask such as a ground glass plate could be fabricated specifically for 3D RI imaging and inserted in the imaging system easily, getting rid of many of the constraints introduced by the spatial light modulator for dynamic pupil coding.

Overall, physics-based machine learning presents an exciting new option for optimizing computational imaging system parameters in a data-driven way. By combining the computational algorithm with experimental parameters, this method may be very useful in finding new, unexpected imaging gains by optimizing optical and computational system parameters for reconstruction quality. However, caution should also be taken when using these algorithms, as they are resource-intensive, and may only provide equal performance to randomly generated coefficients, as in the work presented here.

# Chapter 7

## Conclusion

Computational imaging systems are in use across a wide variety of domains, from medical imaging systems such as CT, ultrasound, and MRI, to biological imaging, astronomical imaging, and in consumer phone cameras. Computational imaging has a large design space in which to leverage the power of both optical and computational systems, but designing computational imaging systems for robust operation is not always straightforward. In this dissertation, I have presented three methods for designing robust computational imaging systems, with a particular focus on 2D and 3D quantitative phase imaging systems. While the presented algorithms and systems were specific to quantitative phase imaging, the presented self-calibration, increased system measurement diversity, and physics-based data-driven system design methods are applicable to computational imaging systems beyond quantitative phase imaging.

In Chapter 3, I presented a self-calibration algorithm that efficiently calculates the illumination angle of incident plane waves in a microscope system directly from measured data. This self-calibration algorithm enables robust and simple calibration of coherent imaging systems without requiring additional calibration steps, which has enabled novel microscope systems to be used for FPM [4, 96, 173], intensity-only ODT [36], and aberration correction methods [76]. Overall, self-calibration is a useful principle for designing robust computational imaging systems. By definition, self-calibrating algorithms retrieve important system parameters directly from the measured data. This joint use of the measured data for calibration and reconstruction ensures that the retrieved calibration parameters are as accurate as possible for each reconstruction. Pre-calibration procedures do not have this guarantee, as system instabilities could create system misalignment before the measured data is captured. In addition, self-calibration algorithms are easier to use, as they do not require additional alignment or data capture steps beyond those routinely done in the capture of the measured data. Therefore, it is useful to design computational imaging systems with the understanding of how different system parameters might be self-calibrated in order to build more robust systems.

In Chapter 5, I presented a novel pupil-coded intensity optical diffraction tomography (ODT) 3D refractive index imaging system based on increased measurement diversity. By

adding joint detection-side pupil-coding element to the traditional illumination-side coding of ODT, pupil-coded intensity ODT measurements contained more diverse information about the sample, leading to improved reconstructions. Through simulation and experimental results, we found that the proposed method improved the robustness of 3D RI reconstructions in limited-illumination and limited-computation conditions. We presented a transfer function analysis that showed the increased coupling of diverse phase information into all measured intensity images under the proposed system. This increased diverse phase information in the measured images leads to a higher weighting of low-spatial frequency information in the pupil-coded intensity ODT system, leading to more robust reconstructions and reduced system constraints. Measurement diversity has also been shown to be important across many other imaging systems, from phase diversity [72, 92, 147] and compressed sensing-based imaging systems [12, 23, 55, 112, 208, 230], to the diverse data required for training better machine learning algorithms [71]. Measurement diversity is a useful design principle for computational imaging systems, as it encourages designers to think about how to reduce the redundancy of measured data and introduce useful degrees of freedom into the imaging system, potentially breaking through many of the trade-offs typically seen in traditional optical systems.

Finally, in Chapter 6, I presented a physics-based machine learning algorithm that used data-driven techniques to design the pupil-coding masks used in pupil-coded intensity ODT. The presented learned pupil coding masks showed similar performance to randomly-generated pupil coding masks in 3D RI imaging simulations and experiments, as well as under a transfer function analysis. Despite this result, physics-based machine learning is still a useful tool for exploring the joint optimization of optical and computational parameters in computational imaging systems, and it has been successfully applied in a wide variety of imaging systems [51, 103, 102, 185]. Care should be taken in using this tool, however, as there is no guarantee that it will provide better imaging parameters, as in the work presented here. As with all machine learning methods, it is additionally resource-intensive, requiring large amounts of data, computation time, and energy.

In addition to these frameworks for robust computational imaging system design, I have also presented practical advice for the building and operation of quantitative phase imaging systems to aid the increased adoption of these systems. In Chapter 2, I gave an overview of Fourier ptychographic microscopy (FPM) systems for high-resolution, wide field-of-view 2D quantitative phase imaging. This chapter included a description of illumination system designs for angled, coherent illumination, which is applicable to both 2D FPM and 3D ODT imaging systems. In addition, practical advice for FPM system design, reconstruction initialization, background removal, and vignetting artifact mitigation were presented, alongside a verification of joint system pupil recovery using FPM. In Chapter 4, I presented an overview of intensity-only ODT systems for 3D refractive index imaging, including a comparison of three forward light propagation models used for 3D reconstructions. I also gave practical advice for the illumination system design and alignment for intensity-only ODT systems, as well as a more generally applicable description of hardware synchronization techniques for systems with many controllable hardware elements such as ODT. A comparison of field-

based and intensity-based ODT reconstructions was also presented, showing that field-based ODT measurements appear to encode similarly diverse phase information as the pupil-coded intensity ODT system proposed in Chapter 5.

Throughout this work, I have demonstrated that by using the frameworks of algorithmic self-calibration, increased system measurement diversity, and physics-based machine learning for computational imaging system design, we can develop more robust quantitative phase imaging systems that are practical for real-world use. Overall, I hope that the work presented in this dissertation will prove useful in the future design of more robust computational imaging systems. Increased robustness of quantitative phase imaging microscopes is a particularly exciting goal, as it will allow for wide adoption of this useful imaging modality for a wide range of biological research applications.

## 7.1 Funding Information

This material is based upon work supported by the National Science Foundation Graduate Research Fellowship Program under Grant No. DGE 1106400; Gordon and Betty Moore Foundation's Data-Driven Discovery Initiative through Grant GBMF4562 to Laura Waller (UC Berkeley); Packard Fellowship for Science and Engineering; and Office of Naval Research N00014-17-1-2401.

# Bibliography

- [1] Sara Abrahamsson et al. “Multifocus microscopy with precise color multi-phase diffractive optics applied in functional neuronal imaging”. In: *Biomed. Opt. Express* 7.3 (Mar. 2016), pp. 855–869. DOI: 10.1364/BOE.7.000855. URL: <http://www.osapublishing.org/boe/abstract.cfm?URI=boe-7-3-855>.
- [2] Mortimer Abramowitz and Michael W. Davidson. *Troubleshooting Microscope Configuration and Other Common Errors*. Ed. by Olympus. URL: <https://www.olympus-lifescience.com/en/microscope-resource/primer/photomicrography/errors/> (visited on ).
- [3] Jesse K. Adams et al. “Single-frame 3D fluorescence microscopy with ultraminiature lensless FlatScope”. In: *Science Advances* 3.12 (2017). DOI: 10.1126/sciadv.1701548. eprint: <https://advances.sciencemag.org/content/3/12/e1701548.full.pdf>. URL: <https://advances.sciencemag.org/content/3/12/e1701548>.
- [4] Tomas Aidukas et al. “Low-cost, sub-micron resolution, wide-field computational microscopy using opensource hardware”. In: *Scientific Reports* 9.1 (2019), p. 7457. ISSN: 2045-2322. DOI: 10.1038/s41598-019-43845-9. URL: <https://doi.org/10.1038/s41598-019-43845-9>.
- [5] Kazunori Akiyama et al. “First M87 Event Horizon Telescope Results. IV. Imaging the Central Supermassive Black Hole”. In: *The Astrophysical Journal. Letters* 875.1 (Apr. 2019). DOI: 10.3847/2041-8213/ab0e85.
- [6] Sherazade Aknoun et al. “Living cell dry mass measurement using quantitative phase imaging with quadriwave lateral shearing interferometry: an accuracy and sensitivity discussion”. In: *Journal of Biomedical Optics* 20.12 (2015), pp. 1–15. DOI: 10.1117/1.JBO.20.12.126009. URL: <https://doi.org/10.1117/1.JBO.20.12.126009>.
- [7] Sherazade Aknoun et al. “Quantitative phase microscopy for non-invasive live cell population monitoring”. In: *Scientific Reports* 11.1 (2021), p. 4409. ISSN: 2045-2322. DOI: 10.1038/s41598-021-83537-x. URL: <https://doi.org/10.1038/s41598-021-83537-x>.
- [8] Ardavan F. Oskooi et al. “MEEP: A flexible free-software package for electromagnetic simulations by the FDTD method”. In: *Computer Physics Communications* 181 (Jan. 2010), pp. 687–702. DOI: doi:10.1016/j.cpc.2009.11.008.

- [9] Emma Alexander et al. “Focal Flow: Velocity and Depth from Differential Defocus Through Motion”. In: *International Journal of Computer Vision* 126.10 (2018), pp. 1062–1083. ISSN: 1573-1405. DOI: 10.1007/s11263-017-1051-5. URL: <https://doi.org/10.1007/s11263-017-1051-5>.
- [10] Hani A Alturkistani, Faris M Tashkandi, and Zuhair M Mohammedsaleh. “Histological Stains: A Literature Review and Case Study”. eng. In: *Global journal of health science* 8.3 (June 2015), pp. 72–79. ISSN: 1916-9736. DOI: 10.5539/gjhs.v8n3p72. URL: <https://pubmed.ncbi.nlm.nih.gov/26493433%20https://www.ncbi.nlm.nih.gov/pmc/articles/PMC4804027/>.
- [11] Andor, ed. *Multi-Wavelength Imaging*. Andor, an Oxford Instruments Company. URL: <https://andor.oxinst.cn/assets/uploads/products/andor/documents/Multi-Wavelength-Brochure.pdf> (visited on ).
- [12] Nick Antipa et al. “DiffuserCam: lensless single-exposure 3D imaging”. In: *Optica* 5.1 (Jan. 2018), pp. 1–9. DOI: 10.1364/OPTICA.5.000001. URL: <http://www.osapublishing.org/optica/abstract.cfm?URI=optica-5-1-1>.
- [13] R. Barer and S. Joseph. “Refractometry of Living Cells”. In: *Journal of Cell Science* s3-95.32 (1954), pp. 399–423. ISSN: 0021-9533. eprint: <http://jcs.biologists.org/content/s3-95/32/399.full.pdf>. URL: <http://jcs.biologists.org/content/s3-95/32/399>.
- [14] A Barty et al. “Quantitative phase tomography”. In: *Optics Communications* 175.4-6 (2000), pp. 329–336.
- [15] Amir Beck and Marc Teboulle. “A Fast Iterative Shrinkage-Thresholding Algorithm for Linear Inverse Problems”. In: *SIAM J. Img. Sci.* 2.1 (Mar. 2009), pp. 183–202. DOI: 10.1137/080716542. URL: <https://doi.org/10.1137/080716542>.
- [16] Liheng Bian et al. “Motion-corrected Fourier ptychography”. In: *Biomed. Opt. Express* 7.11 (Nov. 2016), pp. 4543–4553. DOI: 10.1364/BOE.7.004543. URL: <http://www.osapublishing.org/boe/abstract.cfm?URI=boe-7-11-4543>.
- [17] Zichao Bian, Siyuan Dong, and Guoan Zheng. “Adaptive system correction for robust Fourier ptychographic imaging”. In: *Opt. Express* 21.26 (Dec. 2013), pp. 32400–32410. DOI: 10.1364/OE.21.032400. URL: <http://www.opticsexpress.org/abstract.cfm?URI=oe-21-26-32400>.
- [18] M. Born and E. Wolf. *Principles of Optics: Electromagnetic Theory of Propagation, Interference and Diffraction of Light*. 7th ed. Cambridge University Press, 1999.
- [19] Emrah Bostan et al. “Deep phase decoder: self-calibrating phase microscopy with an untrained deep neural network”. In: *Optica* 7.6 (June 2020), pp. 559–562. DOI: 10.1364/OPTICA.389314. URL: <http://www.osapublishing.org/optica/abstract.cfm?URI=optica-7-6-559>.

- [20] Katherine L. Bouman et al. “Computational Imaging for VLBI Image Reconstruction”. In: *Proceedings of the IEEE Conference on Computer Vision and Pattern Recognition (CVPR)*. June 2016.
- [21] Stephen Boyd et al. “Distributed Optimization and Statistical Learning via the Alternating Direction Method of Multipliers”. In: *Found. Trends Mach. Learn.* 3.1 (Jan. 2011), pp. 1–122. ISSN: 1935-8237. DOI: 10.1561/2200000016. URL: <https://doi.org/10.1561/2200000016>.
- [22] Robert Bridson. “Fast Poisson Disk Sampling in Arbitrary Dimensions”. In: *ACM SIGGRAPH 2007 Sketches*. SIGGRAPH '07. San Diego, California: Association for Computing Machinery, 2007, 22–es. ISBN: 9781450347266. DOI: 10.1145/1278780.1278807. URL: <https://doi.org/10.1145/1278780.1278807>.
- [23] Emmanuel J Candès and Michael B Wakin. “An introduction to compressive sampling”. In: *IEEE signal processing magazine* 25.2 (2008), pp. 21–30.
- [24] Julien Cauchie, Valerie Fiolet, and Didier Villers. “Optimization of an Hough transform algorithm for the search of a center”. In: *Pattern Recognition* 41.2 (2008), pp. 567–574. ISSN: 0031-3203. DOI: <http://dx.doi.org/10.1016/j.patcog.2007.07.001>. URL: <http://www.sciencedirect.com/science/article/pii/S0031320307003160>.
- [25] Antonin Chambolle. “An Algorithm for Total Variation Minimization and Applications”. In: *Journal of Mathematical Imaging and Vision* 20.1 (2004), pp. 89–97. ISSN: 1573-7683. DOI: 10.1023/B:JMIV.0000011325.36760.1e. URL: <https://doi.org/10.1023/B:JMIV.0000011325.36760.1e>.
- [26] Julie Chang et al. “Hybrid optical-electronic convolutional neural networks with optimized diffractive optics for image classification”. In: *Scientific reports* 8.1 (2018), pp. 1–10.
- [27] Florian Charrière et al. “Living specimen tomography by digital holographic microscopy: morphometry of testate amoeba”. In: *Opt. Express* 14.16 (Aug. 2006), pp. 7005–7013. DOI: 10.1364/OE.14.007005. URL: <http://www.opticsexpress.org/abstract.cfm?URI=oe-14-16-7005>.
- [28] Chen Chen et al. “Spectral tomographic imaging with aplanatic metalens”. In: *Light: Science & Applications* 8.1 (2019), p. 99. ISSN: 2047-7538. DOI: 10.1038/s41377-019-0208-0. URL: <https://doi.org/10.1038/s41377-019-0208-0>.
- [29] Michael Chen, Lei Tian, and Laura Waller. “3D differential phase contrast microscopy”. In: *Biomed. Opt. Express* 7.10 (Oct. 2016), pp. 3940–3950. DOI: 10.1364/BOE.7.003940. URL: <http://www.osapublishing.org/boe/abstract.cfm?URI=boe-7-10-3940>.

- [30] Michael Chen, Lei Tian, and Laura Waller. “3D differential phase contrast microscopy”. In: *Quantitative Phase Imaging II*. Ed. by Gabriel Popescu and YongKeun Park. Vol. 9718. International Society for Optics and Photonics. SPIE, 2016, pp. 245–251. URL: <https://doi.org/10.1117/12.2211817>.
- [31] Michael Chen et al. “Multi-layer Born multiple-scattering model for 3D phase microscopy”. In: *Optica* 7.5 (May 2020), pp. 394–403. DOI: 10.1364/OPTICA.383030. URL: <http://www.osapublishing.org/optica/abstract.cfm?URI=optica-7-5-394>.
- [32] Zhongtao Cheng et al. “Practical phase unwrapping of interferometric fringes based on unscented Kalman filter technique”. In: *Opt. Express* 23.25 (Dec. 2015), pp. 32337–32349. DOI: 10.1364/OE.23.032337. URL: <http://www.opticsexpress.org/abstract.cfm?URI=oe-23-25-32337>.
- [33] Wonshik Choi et al. “Tomographic phase microscopy”. In: *Nature Methods* 4.9 (2007), pp. 717–719. ISSN: 1548-7105. DOI: 10.1038/nmeth1078. URL: <https://doi.org/10.1038/nmeth1078>.
- [34] Youngwoon Choi et al. “Optical Imaging With the Use of a Scattering Lens”. In: *IEEE Journal of Selected Topics in Quantum Electronics* 20.2 (2014), pp. 61–73. DOI: 10.1109/JSTQE.2013.2275942.
- [35] Youngwoon Choi et al. “Overcoming the Diffraction Limit Using Multiple Light Scattering in a Highly Disordered Medium”. In: *Phys. Rev. Lett.* 107 (2 July 2011), p. 023902. DOI: 10.1103/PhysRevLett.107.023902. URL: <https://link.aps.org/doi/10.1103/PhysRevLett.107.023902>.
- [36] Shwetadwip Chowdhury et al. “High-resolution 3D refractive index microscopy of multiple-scattering samples from intensity images”. In: *Optica* 6.9 (Sept. 2019), pp. 1211–1219. DOI: 10.1364/OPTICA.6.001211. URL: <http://www.osapublishing.org/optica/abstract.cfm?URI=optica-6-9-1211>.
- [37] Shwetadwip Chowdhury et al. “Large-scale computational recovery of 3D refractive-index in multiple-scattering biology”. In: *Biophotonics Congress: Biomedical Optics 2020 (Translational, Microscopy, OCT, OTS, BRAIN)*. Optical Society of America, 2020, STh4D.5. DOI: 10.1364/OTS.2020.STh4D.5. URL: <http://www.osapublishing.org/abstract.cfm?URI=OTS-2020-STh4D.5>.
- [38] Shwetadwip Chowdhury et al. “Structured illumination multimodal 3D-resolved quantitative phase and fluorescence sub-diffraction microscopy”. In: *Biomed. Opt. Express* 8.5 (May 2017), pp. 2496–2518. DOI: 10.1364/BOE.8.002496. URL: <http://www.osapublishing.org/boe/abstract.cfm?URI=boe-8-5-2496>.
- [39] Jaebum Chung et al. “Counting white blood cells from a blood smear using fourier ptychographic microscopy”. In: *PLoS ONE* 10.7 (2015), pp. 1–10. ISSN: 19326203. DOI: 10.1371/journal.pone.0133489.

- [40] Jaebum Chung et al. “Wide field-of-view fluorescence image deconvolution with aberration-estimation from Fourier ptychography”. In: *Biomed. Opt. Express* 7.2 (Feb. 2016), pp. 352–368. DOI: 10.1364/BOE.7.000352. URL: <http://www.osapublishing.org/boe/abstract.cfm?URI=boe-7-2-352>.
- [41] Jaebum Chung et al. “Wide-field Fourier ptychographic microscopy using laser illumination source”. In: *Biomed. Opt. Express* 7.11 (Nov. 2016), pp. 4787–4802. DOI: 10.1364/BOE.7.004787. URL: <http://www.osapublishing.org/boe/abstract.cfm?URI=boe-7-11-4787>.
- [42] J. M. Cowley and A. F. Moodie. “The scattering of electrons by atoms and crystals. I. A new theoretical approach”. In: *Acta Crystallographica* 10.10 (Oct. 1957), pp. 609–619. DOI: 10.1107/S0365110X57002194. URL: <https://doi.org/10.1107/S0365110X57002194>.
- [43] Christoph Dammer et al. “Use of the Hough transform to determine the center of digitized X-ray diffraction patterns”. In: *Nuclear Instruments and Methods in Physics Research Section B: Beam Interactions with Materials and Atoms* 132.1 (1997), pp. 214–220. ISSN: 0168-583X. DOI: [http://dx.doi.org/10.1016/S0168-583X\(97\)00440-0](http://dx.doi.org/10.1016/S0168-583X(97)00440-0). URL: <http://www.sciencedirect.com/science/article/pii/S0168583X97004400>.
- [44] Veronika Dashkova et al. “Imaging flow cytometry for phytoplankton analysis”. In: *Methods* 112 (2017). Flow Cytometry, pp. 188–200. ISSN: 1046-2023. DOI: <https://doi.org/10.1016/j.ymeth.2016.05.007>. URL: <https://www.sciencedirect.com/science/article/pii/S104620231630130X>.
- [45] P. Davidovits and M. D. Egger. “Scanning Laser Microscope for Biological Investigations”. In: *Appl. Opt.* 10.7 (July 1971), pp. 1615–1619. DOI: 10.1364/AO.10.001615. URL: <http://ao.osa.org/abstract.cfm?URI=ao-10-7-1615>.
- [46] E.R. Davies. *Machine Vision: Theory, Algorithms and Practicalities*. 3rd ed. Royal Holloway, University of London: Morgan Kaufmann Publishers, Dec. 2004. Chap. 10. ISBN: 0-12-206093-8.
- [47] Karl Deisseroth. “Optogenetics: 10 years of microbial opsins in neuroscience”. In: *Nature Neuroscience* 18.9 (2015), pp. 1213–1225. DOI: 10.1038/nn.4091. URL: <https://app.dimensions.ai/details/publication/pub.1049870880%20and%20http://europepmc.org/articles/pmc4790845?pdf=render>.
- [48] A Descloux et al. “Combined multi-plane phase retrieval and super-resolution optical fluctuation imaging for 4D cell microscopy”. In: *Nature Photonics* 12.3 (2018), pp. 165–172. ISSN: 1749-4893. DOI: 10.1038/s41566-018-0109-4. URL: <https://doi.org/10.1038/s41566-018-0109-4>.
- [49] A.J. Devaney. “Generalized projection-slice theorem for fan beam diffraction tomography”. In: *Ultrasonic imaging* 7.3 (1985), pp. 264–275.

- [50] Jianglei Di et al. “High resolution digital holographic microscopy with a wide field of view based on a synthetic aperture technique and use of linear CCD scanning”. In: *Appl. Opt.* 47.30 (Oct. 2008), pp. 5654–5659. DOI: 10.1364/AO.47.005654. URL: <http://ao.osa.org/abstract.cfm?URI=ao-47-30-5654>.
- [51] Benedict Diederich et al. “Using Machine-Learning to Optimize phase contrast in a Low-Cost Cellphone Microscope”. In: *PLOS ONE* 13 (Dec. 2017). DOI: 10.1371/journal.pone.0192937.
- [52] Siyuan Dong et al. “FPscope: a field-portable high-resolution microscope using a cellphone lens”. In: *Biomedical Optics Express* 5.10 (2014), p. 3305. ISSN: 2156-7085. DOI: 10.1364/BOE.5.003305. URL: <https://www.osapublishing.org/boe/abstract.cfm?uri=boe-5-10-3305>.
- [53] Siyuan Dong et al. “Sparsely sampled Fourier ptychography”. In: *Opt. Express* 22.5 (Mar. 2014), pp. 5455–5464. DOI: 10.1364/OE.22.005455. URL: <http://www.opticsexpress.org/abstract.cfm?URI=oe-22-5-5455>.
- [54] Jiantai Dou et al. “Iterative autofocusing strategy for axial distance error correction in ptychography”. In: *Optics and Lasers in Engineering* 98.Supplement C (2017), pp. 56–61. ISSN: 0143-8166. DOI: <https://doi.org/10.1016/j.optlaseng.2017.06.003>. URL: <http://www.sciencedirect.com/science/article/pii/S0143816617301409>.
- [55] Marco F. Duarte et al. “Single-pixel imaging via compressive sampling”. In: *IEEE Signal Processing Magazine* 25.2 (2008), pp. 83–91. DOI: 10.1109/MSP.2007.914730.
- [56] Regina Eckert, Zachary F. Phillips, and Laura Waller. “Efficient illumination angle self-calibration in Fourier ptychography”. In: *Appl. Opt.* 57.19 (July 2018), pp. 5434–5442. DOI: 10.1364/AO.57.005434. URL: <http://ao.osa.org/abstract.cfm?URI=ao-57-19-5434>.
- [57] Regina Eckert, Lei Tian, and Laura Waller. “Algorithmic Self-calibration of Illumination Angles in Fourier Ptychographic Microscopy”. In: *Imaging and Applied Optics 2016*. Optical Society of America, 2016, CT2D.3. DOI: 10.1364/COSI.2016.CT2D.3. URL: <http://www.osapublishing.org/abstract.cfm?URI=COSI-2016-CT2D.3>.
- [58] Regina Eckert et al. “Modeling light propagation in 3D phase objects”. In: *OSA Imaging and Appl. Optics*. 2017, DW2F.2. DOI: 10.1364/3D.2017.DW2F.2. URL: <http://www.osapublishing.org/abstract.cfm?URI=3D-2017-DW2F.2>.
- [59] Arthur D Edelstein et al. “Advanced methods of microscope control using  $\mu$ Manager software”. In: *Journal of biological methods* 1.2 (2014).
- [60] Arthur Edelstein et al. “Computer control of microscopes using  $\mu$ Manager”. In: *Current protocols in molecular biology* 92.1 (2010), pp. 14–20.
- [61] Rolf Erni et al. “Atomic-Resolution Imaging with a Sub-50-pm Electron Probe”. In: *Phys. Rev. Lett.* 102 (9 Mar. 2009), p. 096101. DOI: 10.1103/PhysRevLett.102.096101. URL: <https://link.aps.org/doi/10.1103/PhysRevLett.102.096101>.

- [62] P. P. Ewald. “Die Berechnung optischer und elektrostatischer Gitterpotentiale”. In: *Annalen der Physik* 369.3 (1921), pp. 253–287. DOI: <https://doi.org/10.1002/andp.19213690304>. eprint: <https://onlinelibrary.wiley.com/doi/pdf/10.1002/andp.19213690304>. URL: <https://onlinelibrary.wiley.com/doi/abs/10.1002/andp.19213690304>.
- [63] P. P. Ewald. “Introduction to the dynamical theory of X-ray diffraction”. In: *Acta Crystallographica Section A* 25.1 (1969), pp. 103–108. DOI: <https://doi.org/10.1107/S0567739469000155>. eprint: <https://onlinelibrary.wiley.com/doi/pdf/10.1107/S0567739469000155>. URL: <https://onlinelibrary.wiley.com/doi/abs/10.1107/S0567739469000155>.
- [64] Yao Fan et al. “Optimal illumination scheme for isotropic quantitative differential phase contrast microscopy”. In: *Photon. Res.* 7.8 (Aug. 2019), pp. 890–904. DOI: 10.1364/PRJ.7.000890. URL: <http://www.osapublishing.org/prj/abstract.cfm?URI=prj-7-8-890>.
- [65] Reto Fiolka et al. “Simplified approach to diffraction tomography in optical microscopy”. In: *Opt. Express* 17.15 (July 2009), pp. 12407–12417. DOI: 10.1364/OE.17.012407. URL: <http://www.opticsexpress.org/abstract.cfm?URI=oe-17-15-12407>.
- [66] Greg Gbur and Emil Wolf. In: *Opt. Lett.* 27.21 (Nov. 2002), pp. 1890–1892. DOI: 10.1364/OL.27.001890. URL: <http://ol.osa.org/abstract.cfm?URI=ol-27-21-1890>.
- [67] Adam Geva et al. “X-ray computed tomography through scatter”. In: *Proceedings of The European Conference on Computer Vision (ECCV)*. 2018, pp. 34–50.
- [68] David J. Glugla et al. “Transport-of-intensity-based phase imaging to quantify the refractive index response of 3D direct-write lithography”. In: *Opt. Express* 26.2 (Jan. 2018), pp. 1851–1869. DOI: 10.1364/OE.26.001851. URL: <http://www.opticsexpress.org/abstract.cfm?URI=oe-26-2-1851>.
- [69] T. M. Godden et al. “Ptychographic microscope for three-dimensional imaging”. In: *Opt. Express* 22.10 (May 2014), pp. 12513–12523. DOI: 10.1364/OE.22.012513. URL: <http://www.opticsexpress.org/abstract.cfm?URI=oe-22-10-12513>.
- [70] Aidan N Gomez et al. “The Reversible Residual Network: Backpropagation Without Storing Activations”. In: *Advances in Neural Information Processing Systems*. Ed. by I. Guyon et al. Vol. 30. Curran Associates, Inc., 2017. URL: <https://proceedings.neurips.cc/paper/2017/file/f9be311e65d81a9ad8150a60844bb94c-Paper.pdf>.
- [71] Zhiqiang Gong, Ping Zhong, and Weidong Hu. “Diversity in Machine Learning”. In: *IEEE Access* 7 (2019), pp. 64323–64350. ISSN: 2169-3536. DOI: 10.1109/access.2019.2917620. URL: <http://dx.doi.org/10.1109/ACCESS.2019.2917620>.
- [72] Robert A. Gonsalves. In: *Optical Engineering* 21 (1982), pp. 21 - 21 - 4. DOI: 10.1117/12.7972989. URL: <https://doi.org/10.1117/12.7972989>.

- [73] J.W. Goodman. *Introduction to Fourier Optics*. 2nd ed. McGraw-Hill, 1996.
- [74] Andreas Griewank and Andrea Walther. *Evaluating Derivatives*. Second. Society for Industrial and Applied Mathematics, 2008. DOI: 10.1137/1.9780898717761. eprint: <https://epubs.siam.org/doi/pdf/10.1137/1.9780898717761>. URL: <https://epubs.siam.org/doi/abs/10.1137/1.9780898717761>.
- [75] Manuel Guizar-Sicairos and James R. Fienup. “Phase retrieval with transverse translation diversity: a nonlinear optimization approach”. In: *Opt. Express* 16.10 (May 2008), pp. 7264–7278. DOI: 10.1364/OE.16.007264. URL: <http://www.opticsexpress.org/abstract.cfm?URI=oe-16-10-7264>.
- [76] Gautam Gunjala et al. “Aberration recovery by imaging a weak diffuser”. In: *Opt. Express* 26.16 (Aug. 2018), pp. 21054–21068. DOI: 10.1364/OE.26.021054. URL: <http://www.opticsexpress.org/abstract.cfm?URI=oe-26-16-21054>.
- [77] Kaikai Guo et al. “Microscopy illumination engineering using a low-cost liquid crystal display.” In: *Biomedical optics express* 6.2 (2015), pp. 574–9. ISSN: 2156-7085. DOI: 10.1364/B OE.6.000574. URL: <http://www.pubmedcentral.nih.gov/articlerender.fcgi?artid=4354584%7B%5C%26%7Dtool=pmcentrez%7B%5C%26%7Drendertype=abstract>.
- [78] Kaikai Guo et al. “Optimization of sampling pattern and the design of Fourier ptychographic illuminator”. In: *Opt. Express* 23.5 (Mar. 2015), pp. 6171–6180. DOI: 10.1364/OE.23.006171. URL: <http://www.opticsexpress.org/abstract.cfm?URI=oe-23-5-6171>.
- [79] Qi Guo et al. “Compact single-shot metalens depth sensors inspired by eyes of jumping spiders”. In: *Proceedings of the National Academy of Sciences* 116.46 (2019), pp. 22959–22965. ISSN: 0027-8424. DOI: 10.1073/pnas.1912154116. eprint: <https://www.pnas.org/content/116/46/22959.full.pdf>. URL: <https://www.pnas.org/content/116/46/22959>.
- [80] Mor Habaza et al. “Tomographic phase microscopy using optical tweezers”. In: *Advanced Microscopy Techniques IV; and Neurophotonics II*. Optical Society of America, 2015, 95360H. DOI: 10.1364/ECBO.2015.95360H. URL: <http://www.osapublishing.org/abstract.cfm?URI=ECBO-2015-95360H>.
- [81] Emil Hallstig et al. “Fringing fields in a liquid crystal spatial light modulator for beam steering”. In: *Journal of Modern Optics* 51.8 (2004), pp. 1233–1247. DOI: 10.1080/09500340408230419. eprint: <https://doi.org/10.1080/09500340408230419>. URL: <https://doi.org/10.1080/09500340408230419>.
- [82] DK Hamilton and CJR Sheppard. “Differential phase contrast in scanning optical microscopy”. In: *Journal of microscopy* 133.1 (1984), pp. 27–39. DOI: 10.1111/j.1365-2818.1984.tb00460.x/full.

- [83] G. Harding, J. Kosanetzky, and U. Neitzel. “X-ray diffraction computed tomography”. In: *Medical Physics* 14.4 (1987), pp. 515–525. DOI: <https://doi.org/10.1118/1.596063>. eprint: <https://aapm.onlinelibrary.wiley.com/doi/pdf/10.1118/1.596063>. URL: <https://aapm.onlinelibrary.wiley.com/doi/abs/10.1118/1.596063>.
- [84] Kuan He et al. “Computational multifocal microscopy”. In: *Biomed. Opt. Express* 9.12 (Dec. 2018), pp. 6477–6496. DOI: 10.1364/BOE.9.006477. URL: <http://www.osapublishing.org/boe/abstract.cfm?URI=boe-9-12-6477>.
- [85] Reinhard Heckel and Paul Hand. “Deep Decoder: Concise Image Representations from Untrained Non-convolutional Networks”. In: *CoRR* abs/1810.03982 (2018). arXiv: 1810.03982. URL: <http://arxiv.org/abs/1810.03982>.
- [86] S. Hell et al. “Aberrations in confocal fluorescence microscopy induced by mismatches in refractive index”. In: *Journal of Microscopy* 169.3 (1993), pp. 391–405. ISSN: 1365-2818. DOI: 10.1111/j.1365-2818.1993.tb03315.x. URL: <http://dx.doi.org/10.1111/j.1365-2818.1993.tb03315.x>.
- [87] Roarke Horstmeyer et al. *Convolutional neural networks that teach microscopes how to image*. 2017. arXiv: 1709.07223 [cs.CV].
- [88] Roarke Horstmeyer et al. “Diffraction tomography with Fourier ptychography”. In: *Optica* 3.8 (Aug. 2016), pp. 827–835. DOI: 10.1364/OPTICA.3.000827. URL: <http://www.osapublishing.org/optica/abstract.cfm?URI=optica-3-8-827>.
- [89] Roarke Horstmeyer et al. “Overlapped Fourier coding for optical aberration removal”. In: *Opt. Express* 22.20 (Oct. 2014), pp. 24062–24080. DOI: 10.1364/OE.22.024062. URL: <http://www.opticsexpress.org/abstract.cfm?URI=oe-22-20-24062>.
- [90] D Huang et al. “Optical coherence tomography”. In: *Science* 254.5035 (1991), pp. 1178–1181. ISSN: 0036-8075. DOI: 10.1126/science.1957169. eprint: <https://science.sciencemag.org/content/254/5035/1178.full.pdf>. URL: <https://science.sciencemag.org/content/254/5035/1178>.
- [91] Matt Jacobson. “Absolute Orientation Matlab package”. In: *Matlab Central File Exchange* (2015). URL: <https://www.mathworks.com/matlabcentral/fileexchange/26186-absolute-orientation-horn-s-method>.
- [92] Stuart M. Jefferies et al. “Sensing wave-front amplitude and phase with phase diversity”. In: *Appl. Opt.* 41.11 (Apr. 2002), pp. 2095–2102. DOI: 10.1364/AO.41.002095. URL: <http://ao.osa.org/abstract.cfm?URI=ao-41-11-2095>.
- [93] Ellen C. Jensen. “Overview of Live-Cell Imaging: Requirements and Methods Used”. In: *The Anatomical Record* 296.1 (2013), pp. 1–8. DOI: <https://doi.org/10.1002/ar.22554>. eprint: <https://anatomypubs.onlinelibrary.wiley.com/doi/pdf/10.1002/ar.22554>. URL: <https://anatomypubs.onlinelibrary.wiley.com/doi/abs/10.1002/ar.22554>.

- [94] Zhong Jingshan et al. “Transport of Intensity phase imaging by intensity spectrum fitting of exponentially spaced defocus planes”. In: *Opt. Express* 22.9 (May 2014), pp. 10661–10674. DOI: 10.1364/OE.22.010661. URL: <http://www.opticsexpress.org/abstract.cfm?URI=oe-22-9-10661>.
- [95] Peter M. Joseph and Robin D. Spital. “The effects of scatter in x-ray computed tomography”. In: *Medical Physics* 9.4 (1982), pp. 464–472. DOI: <https://doi.org/10.1118/1.595111>. eprint: <https://aapm.onlinelibrary.wiley.com/doi/pdf/10.1118/1.595111>. URL: <https://aapm.onlinelibrary.wiley.com/doi/abs/10.1118/1.595111>.
- [96] Tahseen Kamal, Lu Yang, and Woei Ming Lee. “In situ retrieval and correction of aberrations in moldless lenses using Fourier Ptychography”. In: *Opt. Express* 26.3 (Feb. 2018), pp. 2708–2719. DOI: 10.1364/OE.26.002708. URL: <http://www.opticsexpress.org/abstract.cfm?URI=oe-26-3-2708>.
- [97] Ulugbek S. Kamilov et al. “A Recursive Born Approach to Nonlinear Inverse Scattering”. In: *IEEE Signal Processing Letters* 23.8 (2016), pp. 1052–1056. DOI: 10.1109/LSP.2016.2579647.
- [98] Ulugbek S. Kamilov et al. “Learning approach to optical tomography”. In: *Optica* 2.6 (June 2015), pp. 517–522. DOI: 10.1364/OPTICA.2.000517. URL: <http://www.osapublishing.org/optica/abstract.cfm?URI=optica-2-6-517>.
- [99] Ulugbek S. Kamilov et al. “Optical Tomographic Image Reconstruction Based on Beam Propagation and Sparse Regularization”. In: *IEEE Transactions on Computational Imaging* 2.1 (2016), pp. 59–70. DOI: 10.1109/TCI.2016.2519261.
- [100] Sungsam Kang et al. “High-resolution adaptive optical imaging within thick scattering media using closed-loop accumulation of single scattering”. In: *Nature Communications* 8.1 (2017), p. 2157. ISSN: 2041-1723. DOI: 10.1038/s41467-017-02117-8. URL: <https://doi.org/10.1038/s41467-017-02117-8>.
- [101] Sungsam Kang et al. “High-resolution adaptive optical imaging within thick scattering media using closed-loop accumulation of single scattering”. In: *Nature Communications* 8.1 (2017), p. 2157. DOI: 10.1038/s41467-017-02117-8. URL: <https://doi.org/10.1038/s41467-017-02117-8>.
- [102] Michael R. Kellman et al. “Physics-Based Learned Design: Optimized Coded-Illumination for Quantitative Phase Imaging”. In: *IEEE Transactions on Computational Imaging* 5.3 (2019), pp. 344–353. DOI: 10.1109/TCI.2019.2905434.
- [103] Michael Kellman et al. “Data-Driven Design for Fourier Ptychographic Microscopy”. In: *2019 IEEE International Conference on Computational Photography (ICCP)*. 2019, pp. 1–8. DOI: 10.1109/ICCPHOT.2019.8747339.
- [104] Michael Kellman et al. “Memory-Efficient Learning for Large-Scale Computational Imaging”. In: *IEEE Transactions on Computational Imaging* 6 (2020), pp. 1403–1414. DOI: 10.1109/TCI.2020.3025735.

- [105] Taewoo Kim et al. “White-light diffraction tomography of unlabelled live cells”. In: *Nature Photonics* 8.3 (2014), pp. 256–263. ISSN: 1749-4893. DOI: 10.1038/nphoton.2013.350. URL: <https://doi.org/10.1038/nphoton.2013.350>.
- [106] Young Seo Kim et al. “Combining Three-Dimensional Quantitative Phase Imaging and Fluorescence Microscopy for the Study of Cell Pathophysiology”. eng. In: *The Yale journal of biology and medicine* 91.3 (Sept. 2018), pp. 267–277. ISSN: 1551-4056. URL: <https://pubmed.ncbi.nlm.nih.gov/30258314%20https://www.ncbi.nlm.nih.gov/pmc/articles/PMC6153632/>.
- [107] Pavan Chandra Konda. “Multi-Aperture Fourier Ptychographic Microscopy: development of a high-speed gigapixel coherent computational microscope”. PhD. University of Glasgow, 2018. URL: <http://theses.gla.ac.uk/id/eprint/9015> (visited on ).
- [108] Pavan Chandra Konda, Jonathan M. Taylor, and Andrew R. Harvey. “Scheimpflug multi-aperture Fourier ptychography: coherent computational microscope with gigapixels/s data acquisition rates using 3D printed components”. In: *High-Speed Biomedical Imaging and Spectroscopy: Toward Big Data Instrumentation and Management II*. Ed. by Kevin K. Tsia and Keisuke Goda. Vol. 10076. International Society for Optics and Photonics. SPIE, 2017, pp. 49–56. URL: <https://doi.org/10.1117/12.2251884>.
- [109] Pavan Chandra Konda et al. “Fourier ptychography: current applications and future promises”. In: *Opt. Express* 28.7 (Mar. 2020), pp. 9603–9630. DOI: 10.1364/OE.386168. URL: <http://www.opticsexpress.org/abstract.cfm?URI=oe-28-7-9603>.
- [110] Alex Krizhevsky, Ilya Sutskever, and Geoffrey E. Hinton. “ImageNet Classification with Deep Convolutional Neural Networks”. In: *Proceedings of the 25th International Conference on Neural Information Processing Systems - Volume 1*. NIPS’12. Lake Tahoe, Nevada: Curran Associates Inc., 2012, pp. 1097–1105.
- [111] Cuifang Kuang et al. “Digital micromirror device-based laser-illumination Fourier ptychographic microscopy”. In: *Opt. Express* 23.21 (Oct. 2015), pp. 26999–27010. DOI: 10.1364/OE.23.026999. URL: <http://www.opticsexpress.org/abstract.cfm?URI=oe-23-21-26999>.
- [112] Grace Kuo. “Exploiting Randomness in Computational Cameras and Displays”. PhD thesis. EECS Department, University of California, Berkeley, Dec. 2020. URL: <http://www2.eecs.berkeley.edu/Pubs/TechRpts/2020/EECS-2020-218.html>.
- [113] V. Lauer. “New approach to optical diffraction tomography yielding a vector equation of diffraction tomography and a novel tomographic microscope”. In: *Journal of Microscopy* 205.2 (2002), pp. 165–176. DOI: <https://doi.org/10.1046/j.0022-2720.2001.00980.x>. eprint: <https://onlinelibrary.wiley.com/doi/pdf/10.1046/j.0022-2720.2001.00980.x>. URL: <https://onlinelibrary.wiley.com/doi/abs/10.1046/j.0022-2720.2001.00980.x>.

- [114] SangYun Lee et al. “High-Resolution 3-D Refractive Index Tomography and 2-D Synthetic Aperture Imaging of Live Phytoplankton”. EN. In: *Journal of the Optical Society of Korea* 18.6 (Dec. 2014), pp. 691–697. ISSN: 1226-4776/2093-6885. DOI: 10.3807/JOSK.2014.18.6.691. URL: <https://doi.org/10.3807/JOSK.2014.18.6.691>.
- [115] Marc Levoy et al. “Light Field Microscopy”. In: *ACM SIGGRAPH 2006 Papers. SIGGRAPH '06*. Boston, Massachusetts: Association for Computing Machinery, 2006, pp. 924–934. ISBN: 1595933646. DOI: 10.1145/1179352.1141976. URL: <https://doi.org/10.1145/1179352.1141976>.
- [116] Jiaji Li et al. “Optimization analysis of partially coherent illumination for refractive index tomographic microscopy”. In: *Optics and Lasers in Engineering* 143 (2021), p. 106624. ISSN: 0143-8166. DOI: <https://doi.org/10.1016/j.optlaseng.2021.106624>. URL: <https://www.sciencedirect.com/science/article/pii/S0143816621000944>.
- [117] Jingxi Li et al. “Class-specific differential detection in diffractive optical neural networks improves inference accuracy”. In: *Advanced Photonics* 1.4 (2019), p. 046001.
- [118] Peng Li and Andrew Maiden. “Multi-slice ptychographic tomography”. In: *Scientific Reports* 8.1 (2018), p. 2049. ISSN: 2045-2322. DOI: 10.1038/s41598-018-20530-x. URL: <https://doi.org/10.1038/s41598-018-20530-x>.
- [119] Qingxiang Li et al. “Autofocus system for microscope”. In: *Optical Engineering* 41.6 (2002), pp. 1289–1294. DOI: 10.1117/1.1473639. URL: <https://doi.org/10.1117/1.1473639>.
- [120] Shuai Li et al. “Imaging through glass diffusers using densely connected convolutional networks”. In: *Optica* 5.7 (July 2018), pp. 803–813. DOI: 10.1364/OPTICA.5.000803. URL: <http://www.osapublishing.org/optica/abstract.cfm?URI=optica-5-7-803>.
- [121] Yunzhe Li, Yujia Xue, and Lei Tian. “Deep speckle correlation: a deep learning approach toward scalable imaging through scattering media”. In: *Optica* 5.10 (Oct. 2018), pp. 1181–1190. DOI: 10.1364/OPTICA.5.001181. URL: <http://www.osapublishing.org/optica/abstract.cfm?URI=optica-5-10-1181>.
- [122] Rongguang Liang, J. Kevin Erwin, and Masud Mansuripur. “Variation on Zernike’s phase-contrast microscope”. In: *Appl. Opt.* 39.13 (May 2000), pp. 2152–2158. DOI: 10.1364/AO.39.002152. URL: <http://ao.osa.org/abstract.cfm?URI=ao-39-13-2152>.
- [123] Ashley R G Libby et al. “Axial elongation of caudalized human organoids mimics aspects of neural tube development”. In: *Development* 148.12 (June 2021). ISSN: 0950-1991. DOI: 10.1242/dev.198275. URL: <https://doi.org/10.1242/dev.198275>.

- [124] JooWon Lim et al. “Comparative study of iterative reconstruction algorithms for missing cone problems in optical diffraction tomography”. In: *Opt. Express* 23.13 (June 2015), pp. 16933–16948. DOI: 10.1364/OE.23.016933. URL: <http://www.opticsexpress.org/abstract.cfm?URI=oe-23-13-16933>.
- [125] Xing Lin et al. “All-optical machine learning using diffractive deep neural networks”. In: *Science* 361.6406 (2018), pp. 1004–1008.
- [126] Ruilong Ling et al. “High-throughput intensity diffraction tomography with a computational microscope”. In: *Biomed. Opt. Express* 9.5 (May 2018), pp. 2130–2141. DOI: 10.1364/BOE.9.002130. URL: <http://www.osapublishing.org/boe/abstract.cfm?URI=boe-9-5-2130>.
- [127] Hsiou-Yuan Liu, Jingshan Zhong, and Laura Waller. “Multiplexed phase-space imaging for 3D fluorescence microscopy”. In: *Opt. Express* 25.13 (June 2017), pp. 14986–14995. DOI: 10.1364/OE.25.014986. URL: <http://www.opticsexpress.org/abstract.cfm?URI=oe-25-13-14986>.
- [128] Hsiou-Yuan Liu et al. “3D imaging in volumetric scattering media using phase-space measurements”. In: *Opt. Express* 23.11 (June 2015), pp. 14461–14471. DOI: 10.1364/OE.23.014461. URL: <http://www.opticsexpress.org/abstract.cfm?URI=oe-23-11-14461>.
- [129] Hsiou-Yuan Liu et al. “SEAGLE: Sparsity-Driven Image Reconstruction Under Multiple Scattering”. In: *IEEE Transactions on Computational Imaging* 4.1 (2018), pp. 73–86. DOI: 10.1109/TCI.2017.2764461.
- [130] Jian Liu et al. “Stable and robust frequency domain position compensation strategy for Fourier ptychographic microscopy”. In: *Opt. Express* 25.23 (Nov. 2017), pp. 28053–28067. DOI: 10.1364/OE.25.028053. URL: <http://www.opticsexpress.org/abstract.cfm?URI=oe-25-23-28053>.
- [131] PY Liu et al. “Cell refractive index for cell biology and disease diagnosis: past, present and future”. In: *Lab on a chip* 16.4 (Feb. 2016), pp. 634–644. ISSN: 1473-0197. DOI: 10.1039/c5lc01445j. URL: <https://doi.org/10.1039/c5lc01445j>.
- [132] Sheng Liu and Hong Hua. “Extended depth-of-field microscopic imaging with a variable focus microscope objective”. In: *Opt. Express* 19.1 (Jan. 2011), pp. 353–362. DOI: 10.1364/OE.19.000353. URL: <http://www.opticsexpress.org/abstract.cfm?URI=oe-19-1-353>.
- [133] Ziji Liu et al. “Real-time brightfield, darkfield, and phase contrast imaging in a light-emitting diode array microscope”. In: *Journal of Biomedical Optics* 19.10 (2014), pp. 1–5. DOI: 10.1117/1.JBO.19.10.106002. URL: <https://doi.org/10.1117/1.JBO.19.10.106002>.
- [134] Adolf W. Lohmann et al. “Space–bandwidth product of optical signals and systems”. In: *J. Opt. Soc. Am. A* 13.3 (Mar. 1996), pp. 470–473. DOI: 10.1364/JOSAA.13.000470. URL: <http://josaa.osa.org/abstract.cfm?URI=josaa-13-3-470>.

- [135] Limei Ma et al. “Three-dimensional focal stack imaging in scanning transmission X-ray microscopy with an improved reconstruction algorithm”. In: *Opt. Express* 27.5 (Mar. 2019), pp. 7787–7802. DOI: 10.1364/OE.27.007787. URL: <http://www.opticsexpress.org/abstract.cfm?URI=oe-27-5-7787>.
- [136] A. M. Maiden, M. J. Humphry, and J. M. Rodenburg. “Ptychographic transmission microscopy in three dimensions using a multi-slice approach”. In: *J. Opt. Soc. Am. A* 29.8 (Aug. 2012), pp. 1606–1614. DOI: 10.1364/JOSAA.29.001606. URL: <http://josaa.osa.org/abstract.cfm?URI=josaa-29-8-1606>.
- [137] AM Maiden et al. “An annealing algorithm to correct positioning errors in ptychography”. In: *Ultramicroscopy* 120 (2012), pp. 64–72.
- [138] Andrew M. Maiden and John M. Rodenburg. “An improved ptychographical phase retrieval algorithm for diffractive imaging”. In: *Ultramicroscopy* 109.10 (2009), pp. 1256–1262. ISSN: 0304-3991. DOI: <https://doi.org/10.1016/j.ultramic.2009.05.012>. URL: <https://www.sciencedirect.com/science/article/pii/S0304399109001284>.
- [139] Ondřej Mandula et al. “Phase and fluorescence imaging with a surprisingly simple microscope based on chromatic aberration”. In: *Opt. Express* 28.2 (Jan. 2020), pp. 2079–2090. DOI: 10.1364/OE.28.002079. URL: <http://www.opticsexpress.org/abstract.cfm?URI=oe-28-2-2079>.
- [140] Pierre Marechal and Jane J. Ye. “Optimizing Condition Numbers”. In: *SIAM Journal on Optimization* 20.2 (2009), pp. 935–947. DOI: 10.1137/080740544. eprint: <https://doi.org/10.1137/080740544>. URL: <https://doi.org/10.1137/080740544>.
- [141] Manuel Martinez-Corral et al. “Fast Axial-Scanning Widefield Microscopy With Constant Magnification and Resolution”. In: *Journal of Display Technology* 11.11 (2015), pp. 913–920. DOI: 10.1109/JDT.2015.2404347.
- [142] Alex Matlock and Lei Tian. “High-throughput, volumetric quantitative phase imaging with multiplexed intensity diffraction tomography”. In: *Biomed. Opt. Express* 10.12 (Dec. 2019), pp. 6432–6448. DOI: 10.1364/BOE.10.006432. URL: <http://www.osapublishing.org/boe/abstract.cfm?URI=boe-10-12-6432>.
- [143] Alexandre Mermillod-Blondin, Euan McLeod, and Craig B. Arnold. “High-speed varifocal imaging with a tunable acoustic gradient index of refraction lens”. In: *Opt. Lett.* 33.18 (Sept. 2008), pp. 2146–2148. DOI: 10.1364/OL.33.002146. URL: <http://ol.osa.org/abstract.cfm?URI=ol-33-18-2146>.
- [144] Nikon MicroscopyU, ed. *Polarized Light Microscopy*. Nikon MicroscopyU. URL: <https://www.microscopyu.com/techniques/polarized-light/polarized-light-microscopy> (visited on ).
- [145] Kristina Monakhova et al. “Learned reconstructions for practical mask-based lensless imaging”. In: *Opt. Express* 27.20 (Sept. 2019), pp. 28075–28090. DOI: 10.1364/OE.27.028075. URL: <http://www.opticsexpress.org/abstract.cfm?URI=oe-27-20-28075>.

- [146] Simon Moser, Monika Ritsch-Martel, and Gregor Thalhammer. “Model-based compensation of pixel crosstalk in liquid crystal spatial light modulators”. In: *Opt. Express* 27.18 (Sept. 2019), pp. 25046–25063. DOI: 10.1364/OE.27.025046. URL: <http://www.opticsexpress.org/abstract.cfm?URI=oe-27-18-25046>.
- [147] Laurent Mugnier, Amandine Blanc, and Jérôme Idier. “Phase Diversity: A Technique for Wave-Front Sensing and for Diffraction-Limited Imaging”. In: *Advances in Imaging and Electron Physics - ADV IMAG ELECTRON PHYS* 141 (Dec. 2006), pp. 1–76. DOI: 10.1016/S1076-5670(05)41001-0.
- [148] Paul Müller, Mirjam Schürmann, and Jochen Guck. *The Theory of Diffraction Tomography*. 2016. arXiv: 1507.00466 [q-bio.QM].
- [149] Alex Muthumbi et al. “Learned sensing: jointly optimized microscope hardware for accurate image classification”. In: *Biomed. Opt. Express* 10.12 (Dec. 2019), pp. 6351–6369. DOI: 10.1364/BOE.10.006351. URL: <http://www.osapublishing.org/boe/abstract.cfm?URI=boe-10-12-6351>.
- [150] Tan H Nguyen et al. “Gradient light interference microscopy for 3D imaging of unlabeled specimens”. In: *Nature Communications* 8.1 (2017), p. 210. ISSN: 2041-1723. DOI: 10.1038/s41467-017-00190-7. URL: <https://doi.org/10.1038/s41467-017-00190-7>.
- [151] Thanh Nguyen et al. “Deep learning approach for Fourier ptychography microscopy”. In: *Opt. Express* 26.20 (Oct. 2018), pp. 26470–26484. DOI: 10.1364/OE.26.026470. URL: <http://www.opticsexpress.org/abstract.cfm?URI=oe-26-20-26470>.
- [152] Nikon, ed. *Super Resolution Microscopes*. Nikon Technology and Design. URL: <https://www.nikon.com/about/technology/product/srm/index.htm> (visited on ).
- [153] Center for Nondestructive Evaluation, ed. *Visual Acuity of the Human Eye*. Iowa State University. URL: <https://www.nde-ed.org/NDETechniques/PenetrantTest/Introduction/visualacuity.xhtml> (visited on ).
- [154] Jeonghun Oh et al. “Three-dimensional label-free observation of individual bacteria upon antibiotic treatment using optical diffraction tomography”. In: *Biomed. Opt. Express* 11.3 (Mar. 2020), pp. 1257–1267. DOI: 10.1364/BOE.377740. URL: <http://www.osapublishing.org/boe/abstract.cfm?URI=boe-11-3-1257>.
- [155] WILLIAM H. OLDENDORF. “The quest for an image of brain”. In: *Neurology* 28.6 (1978), pp. 517–517. ISSN: 0028-3878. DOI: 10.1212/WNL.28.6.517. eprint: <https://n.neurology.org/content/28/6/517.full.pdf>. URL: <https://n.neurology.org/content/28/6/517>.
- [156] Xiaoze Ou, Guoan Zheng, and Changhui Yang. “Embedded pupil function recovery for Fourier ptychographic microscopy”. In: *Opt. Express* 22.5 (Mar. 2014), pp. 4960–4972. DOI: 10.1364/OE.22.004960. URL: <http://www.opticsexpress.org/abstract.cfm?URI=oe-22-5-4960>.

- [157] Xiaoze Ou et al. “High numerical aperture Fourier ptychography : principle , implementation and characterization”. In: *Optics express* 23.3 (2015), pp. 5473–5480. ISSN: 1094-4087. DOI: 10.1364/OE.23.003472.
- [158] Xiaoze Ou et al. “Quantitative phase imaging via Fourier ptychographic microscopy”. In: *Optics letters* 38.22 (2013), pp. 4845–4848.
- [159] An Pan et al. “Subwavelength resolution Fourier ptychography with hemispherical digital condensers”. In: *Opt. Express* 26.18 (Sept. 2018), pp. 23119–23131. DOI: 10.1364/OE.26.023119. URL: <http://www.opticsexpress.org/abstract.cfm?URI=oe-26-18-23119>.
- [160] An Pan et al. “System calibration method for Fourier ptychographic microscopy”. In: *Journal of Biomedical Optics* 22.9 (2017), pp. 1–11. DOI: 10.1117/1.JBO.22.9.096005. URL: <https://doi.org/10.1117/1.JBO.22.9.096005>.
- [161] An Pan et al. “Vignetting effect in Fourier ptychographic microscopy”. In: *Optics and Lasers in Engineering* 120 (2019), pp. 40–48. ISSN: 0143-8166. DOI: <https://doi.org/10.1016/j.optlaseng.2019.02.015>. URL: <https://www.sciencedirect.com/science/article/pii/S0143816618316658>.
- [162] Neal Parikh and Stephen Boyd. “Proximal Algorithms”. In: *Foundations and Trends® in Optimization* 1.3 (2014), pp. 127–239. ISSN: 2167-3888. DOI: 10.1561/2400000003. URL: <http://dx.doi.org/10.1561/2400000003>.
- [163] Chansuk Park, Seungwoo Shin, and YongKeun Park. “Generalized quantification of three-dimensional resolution in optical diffraction tomography using the projection of maximal spatial bandwidths”. In: *J. Opt. Soc. Am. A* 35.11 (Nov. 2018), pp. 1891–1898. DOI: 10.1364/JOSAA.35.001891. URL: <http://josaa.osa.org/abstract.cfm?URI=josaa-35-11-1891>.
- [164] YongKeun Park, Christian Depeursinge, and Gabriel Popescu. “Quantitative phase imaging in biomedicine”. In: *Nature Photonics* 12.10 (2018), pp. 578–589. ISSN: 1749-4893. DOI: 10.1038/s41566-018-0253-x. URL: <https://doi.org/10.1038/s41566-018-0253-x>.
- [165] Sri Rama Prasanna Pavani et al. “Three-dimensional, single-molecule fluorescence imaging beyond the diffraction limit by using a double-helix point spread function”. In: *Proceedings of the National Academy of Sciences* 106.9 (2009), pp. 2995–2999. ISSN: 0027-8424. DOI: 10.1073/pnas.0900245106. eprint: <https://www.pnas.org/content/106/9/2995.full.pdf>. URL: <https://www.pnas.org/content/106/9/2995>.
- [166] Nicolas C. Pégard et al. “Compressive light-field microscopy for 3D neural activity recording”. In: *Optica* 3.5 (May 2016), pp. 517–524. DOI: 10.1364/OPTICA.3.000517. URL: <http://www.osapublishing.org/optica/abstract.cfm?URI=optica-3-5-517>.

- [167] Martin Persson, David Engström, and Mattias Goksör. “Reducing the effect of pixel crosstalk in phase only spatial light modulators”. In: *Opt. Express* 20.20 (Sept. 2012), pp. 22334–22343. DOI: 10.1364/OE.20.022334. URL: <http://www.opticsexpress.org/abstract.cfm?URI=oe-20-20-22334>.
- [168] Mojmír Petráň et al. “Tandem-Scanning Reflected-Light Microscope\*”. In: *J. Opt. Soc. Am.* 58.5 (May 1968), pp. 661–664. DOI: 10.1364/JOSA.58.000661. URL: <http://www.osapublishing.org/abstract.cfm?URI=josa-58-5-661>.
- [169] *Phantom v2512*. Aug. 13, 2021. URL: <https://www.phantomhighspeed.com/products/cameras/ultrahighspeed/v2512>.
- [170] Zachary F. Phillips and Michael Chen. *Technical Report: Benchmark Technologies Quantitative Phase Target*. URL: <https://www.benchmarktech.com/sites/default/files/UserReport.pdf> (visited on ).
- [171] Zachary F. Phillips, Michael Chen, and Laura Waller. “Single-shot quantitative phase microscopy with color-multiplexed differential phase contrast (cDPC)”. In: *PLOS ONE* 12.2 (Feb. 2017), pp. 1–14. DOI: 10.1371/journal.pone.0171228. URL: <https://doi.org/10.1371/journal.pone.0171228>.
- [172] Zachary F. Phillips et al. “Multi-Contrast Imaging and Digital Refocusing on a Mobile Microscope with a Domed LED Array”. In: *PLoS ONE* 10.5 (May 2015), e0124938. DOI: 10.1371/journal.pone.0124938. URL: <https://doi.org/10.1371/journal.pone.0124938>.
- [173] Zachary Phillips, Regina Eckert, and Laura Waller. “Quasi-Dome: A Self-Calibrated High-NA LED Illuminator for Fourier Ptychography”. In: *Imaging and Applied Optics 2017 IS*. Optical Society of America, 2017, IW4E.5. DOI: 10.1364/ISA.2017.IW4E.5. URL: <http://www.osapublishing.org/abstract.cfm?URI=ISA-2017-IW4E.5>.
- [174] Henry Pinkard et al. “Deep learning for single-shot autofocus microscopy”. In: *Optica* 6.6 (June 2019), pp. 794–797. DOI: 10.1364/OPTICA.6.000794. URL: <http://www.osapublishing.org/optica/abstract.cfm?URI=optica-6-6-794>.
- [175] Henry Pinkard et al. “Pycro-Manager: open-source software for customized and reproducible microscope control”. In: *Nature Methods* 18.3 (2021), pp. 226–228. ISSN: 1548-7105. DOI: 10.1038/s41592-021-01087-6. URL: <https://doi.org/10.1038/s41592-021-01087-6>.
- [176] Laura Poppick. *Let us now praise the invention of the microscope*. smithsonianmag.com. Mar. 2017. URL: <https://www.smithsonianmag.com/science-nature/what-we-owe-to-the-invention-microscope-180962725/>.
- [177] Mary Potter. “Recognition and Memory for Briefly Presented Scenes”. In: *Frontiers in psychology* 3 (Feb. 2012), p. 32. DOI: 10.3389/fpsyg.2012.00032.

- [178] P. Potluri, M. R. Fetterman, and D. J. Brady. “High depth of field microscopic imaging using an interferometric camera”. In: *Opt. Express* 8.11 (May 2001), pp. 624–630. DOI: 10.1364/OE.8.000624. URL: <http://www.opticsexpress.org/abstract.cfm?URI=oe-8-11-624>.
- [179] Chrysanthe Preza and José-Angel Conchello. “Depth-variant maximum-likelihood restoration for three-dimensional fluorescence microscopy”. In: *J. Opt. Soc. Am. A* 21.9 (Sept. 2004), pp. 1593–1601. DOI: 10.1364/JOSAA.21.001593. URL: <http://josaa.osa.org/abstract.cfm?URI=josaa-21-9-1593>.
- [180] Hongbin Pu, Lian Lin, and Da-Wen Sun. “Principles of Hyperspectral Microscope Imaging Techniques and Their Applications in Food Quality and Safety Detection: A Review”. In: *Comprehensive Reviews in Food Science and Food Safety* 18.4 (2019), pp. 853–866. DOI: <https://doi.org/10.1111/1541-4337.12432>. eprint: <https://onlinelibrary.wiley.com/doi/pdf/10.1111/1541-4337.12432>. URL: <https://onlinelibrary.wiley.com/doi/abs/10.1111/1541-4337.12432>.
- [181] Friedrich Pukelsheim. *Optimal design of experiments*. SIAM, 2006. URL: <https://epubs.siam.org/doi/pdf/10.1137/1.9780898719109.bm>.
- [182] E. G. van Putten et al. “Scattering Lens Resolves Sub-100 nm Structures with Visible Light”. In: *Phys. Rev. Lett.* 106 (19 May 2011), p. 193905. DOI: 10.1103/PhysRevLett.106.193905. URL: <https://link.aps.org/doi/10.1103/PhysRevLett.106.193905>.
- [183] Tal Remez et al. *Deep Convolutional Denoising of Low-Light Images*. 2017. arXiv: 1701.01687 [cs.CV].
- [184] Malte Renz. “Fluorescence microscopy: A historical and technical perspective”. In: *Cytometry Part A* 83.9 (2013), pp. 767–779. DOI: <https://doi.org/10.1002/cyto.a.22295>. eprint: <https://onlinelibrary.wiley.com/doi/pdf/10.1002/cyto.a.22295>. URL: <https://onlinelibrary.wiley.com/doi/abs/10.1002/cyto.a.22295>.
- [185] Alexander Robey and Vidya Ganapati. “Optimal physical preprocessing for example-based super-resolution”. In: *Opt. Express* 26.24 (Nov. 2018), pp. 31333–31350. DOI: 10.1364/OE.26.031333. URL: <http://www.opticsexpress.org/abstract.cfm?URI=oe-26-24-31333>.
- [186] J. M. Rodenburg and H. M. L. Faulkner. “A phase retrieval algorithm for shifting illumination”. In: *Applied Physics Letters* 85.20 (2004), pp. 4795–4797. DOI: 10.1063/1.1823034. eprint: <https://doi.org/10.1063/1.1823034>. URL: <https://doi.org/10.1063/1.1823034>.
- [187] J.M. Rodenburg. “Ptychography and Related Diffractive Imaging Methods”. In: ed. by Hawkes. Vol. 150. *Advances in Imaging and Electron Physics*. Elsevier, 2008, pp. 87–184. DOI: [https://doi.org/10.1016/S1076-5670\(07\)00003-1](https://doi.org/10.1016/S1076-5670(07)00003-1). URL: <https://www.sciencedirect.com/science/article/pii/S1076567007000031>.

- [188] J. Van Roey, J. van der Donk, and P. E. Lagasse. “Beam-propagation method: analysis and assessment”. In: *J. Opt. Soc. Am.* 71.7 (July 1981), pp. 803–810. DOI: 10.1364/JOSA.71.000803. URL: <http://www.osapublishing.org/abstract.cfm?URI=josa-71-7-803>.
- [189] Emiliano Ronzitti et al. “LCoS nematic SLM characterization and modeling for diffraction efficiency optimization, zero and ghost orders suppression”. In: *Opt. Express* 20.16 (July 2012), pp. 17843–17855. DOI: 10.1364/OE.20.017843. URL: <http://www.opticsexpress.org/abstract.cfm?URI=oe-20-16-17843>.
- [190] Geoffrey D. Rubin. “Computed Tomography: Revolutionizing the Practice of Medicine for 40 Years”. In: *Radiology* 273.2S (2014). PMID: 25340438, S45–S74. DOI: 10.1148/radiol.14141356. eprint: <https://doi.org/10.1148/radiol.14141356>. URL: <https://doi.org/10.1148/radiol.14141356>.
- [191] H. Gunther Rudenberg and Paul G. Rudenberg. “Chapter 6 - Origin and Background of the Invention of the Electron Microscope: Commentary and Expanded Notes on Memoir of Reinhold RÅEdenberg\*\*Reinhold RÅEdenberg’s memoir begins on p. 171 of this volume”. In: *Advances in Imaging and Electron Physics*. Vol. 160. Advances in Imaging and Electron Physics. Elsevier, 2010, pp. 207–286. DOI: [https://doi.org/10.1016/S1076-5670\(10\)60006-7](https://doi.org/10.1016/S1076-5670(10)60006-7). URL: <https://www.sciencedirect.com/science/article/pii/S1076567010600067>.
- [192] Leonid I. Rudin, Stanley Osher, and Emad Fatemi. “Nonlinear total variation based noise removal algorithms”. In: *Physica D: Nonlinear Phenomena* 60.1 (1992), pp. 259–268. ISSN: 0167-2789. DOI: [https://doi.org/10.1016/0167-2789\(92\)90242-F](https://doi.org/10.1016/0167-2789(92)90242-F). URL: <https://www.sciencedirect.com/science/article/pii/016727899290242F>.
- [193] Vijay Sankaran et al. “Inspection in Semiconductor Manufacturing”. In: *Wiley Encyclopedia of Electrical and Electronics Engineering*. American Cancer Society, 1999. ISBN: 9780471346081. DOI: <https://doi.org/10.1002/047134608X.W5532>. eprint: <https://onlinelibrary.wiley.com/doi/pdf/10.1002/047134608X.W5532>. URL: <https://onlinelibrary.wiley.com/doi/abs/10.1002/047134608X.W5532>.
- [194] Guy Satat et al. “All Photons Imaging Through Volumetric Scattering”. In: *Scientific Reports* 6 (Sept. 2016), p. 33946. URL: <http://dx.doi.org/10.1038/srep33946>%20http://10.04.14/srep33946%20https://www.nature.com/articles/srep33946%7B%5C#%7Dsupplementary-information.
- [195] R Schofield et al. “Image reconstruction: Part 1; understanding filtered back projection, noise and image acquisition”. In: *Journal of Cardiovascular Computed Tomography* 14.3 (May 2020), pp. 219–225. ISSN: 1934-5925. DOI: 10.1016/j.jcct.2019.04.008. URL: <https://doi.org/10.1016/j.jcct.2019.04.008>.

- [196] Elaine F. Schumacher. *Microscopy for Materials Characterization: Illuminating Structures With Light and Electrons*. American Laboratory. Sept. 2014. URL: <https://www.americanlaboratory.com/914-Application-Notes/167499-Microscopy-for-Materials-Characterization-Illuminating-Structures-With-Light-and-Electrons/> (visited on ).
- [197] Mirjam Schürmann et al. “Cell nuclei have lower refractive index and mass density than cytoplasm”. In: *Journal of Biophotonics* 9.10 (Oct. 2016), pp. 1068–1076. ISSN: 1864-063X. DOI: <https://doi.org/10.1002/jbio.201500273>. URL: <https://doi.org/10.1002/jbio.201500273>.
- [198] Sanchari Sen et al. “Fourier ptychographic microscopy using an infrared-emitting hemispherical digital condenser”. In: *Appl. Opt.* 55.23 (Aug. 2016), pp. 6421–6427. DOI: 10.1364/AO.55.006421. URL: <http://ao.osa.org/abstract.cfm?URI=ao-55-23-6421>.
- [199] Joshua W. Shaevitz and Daniel A. Fletcher. “Enhanced three-dimensional deconvolution microscopy using a measured depth-varying point-spread function”. In: *J. Opt. Soc. Am. A* 24.9 (Sept. 2007), pp. 2622–2627. DOI: 10.1364/JOSAA.24.002622. URL: <http://josaa.osa.org/abstract.cfm?URI=josaa-24-9-2622>.
- [200] William J. Shain et al. “Extended depth-of-field microscopy with a high-speed deformable mirror”. In: *Opt. Lett.* 42.5 (Mar. 2017), pp. 995–998. DOI: 10.1364/OL.42.000995. URL: <http://ol.osa.org/abstract.cfm?URI=ol-42-5-995>.
- [201] Aamod Shanker et al. “Off-axis Aberration Estimation in an EUV Microscope Using Natural Speckle”. In: *Imaging and Applied Optics 2016*. Optical Society of America, 2016, ITh1F.2. DOI: 10.1364/ISA.2016.ITh1F.2. URL: <http://www.osapublishing.org/abstract.cfm?URI=ISA-2016-ITh1F.2>.
- [202] Cheng Shen et al. “Computational aberration correction of VIS-NIR multispectral imaging microscopy based on Fourier ptychography”. In: *Opt. Express* 27.18 (Sept. 2019), pp. 24923–24937. DOI: 10.1364/OE.27.024923. URL: <http://www.opticsexpress.org/abstract.cfm?URI=oe-27-18-24923>.
- [203] C.J.R. Sheppard and A. Choudhury. “Image Formation in the Scanning Microscope”. In: *Optica Acta: International Journal of Optics* 24.10 (1977), pp. 1051–1073. DOI: 10.1080/713819421. eprint: <https://doi.org/10.1080/713819421>. URL: <https://doi.org/10.1080/713819421>.
- [204] Colin J. R. Sheppard. “Three-dimensional phase imaging with the intensity transport equation”. In: *Appl. Opt.* 41.28 (Oct. 2002), pp. 5951–5955. DOI: 10.1364/AO.41.005951. URL: <http://ao.osa.org/abstract.cfm?URI=ao-41-28-5951>.
- [205] J. Sibarita. “Deconvolution microscopy”. In: *Advances in biochemical engineering/biotechnology* 95 (2005), pp. 201–43.
- [206] David J Stephens and Victoria J Allan. “Light microscopy techniques for live cell imaging”. In: *science* 300.5616 (2003), pp. 82–86.

- [207] David Strong and Tony Chan. “Edge-preserving and scale-dependent properties of total variation regularization”. In: *Inverse Problems* 19.6 (Nov. 2003), S165–S187. DOI: 10.1088/0266-5611/19/6/059. URL: <https://doi.org/10.1088/0266-5611/19/6/059>.
- [208] Vincent Studer et al. “Compressive fluorescence microscopy for biological and hyperspectral imaging”. In: *Proceedings of the National Academy of Sciences* 109.26 (2012), E1679–E1687. ISSN: 0027-8424. DOI: 10.1073/pnas.1119511109. eprint: <https://www.pnas.org/content/109/26/E1679.full.pdf>. URL: <https://www.pnas.org/content/109/26/E1679>.
- [209] He Sun and Katherine L. Bouman. “Deep Probabilistic Imaging: Uncertainty Quantification and Multi-modal Solution Characterization for Computational Imaging”. In: *CoRR* abs/2010.14462 (2020). arXiv: 2010.14462. URL: <https://arxiv.org/abs/2010.14462>.
- [210] Jiasong Sun et al. “Efficient positional misalignment correction method for Fourier ptychographic microscopy”. In: *Biomed. Opt. Express* 7.4 (Apr. 2016), pp. 1336–1350. DOI: 10.1364/BOE.7.001336. URL: <http://www.osapublishing.org/boe/abstract.cfm?URI=boe-7-4-1336>.
- [211] Jiasong Sun et al. “Resolution-enhanced Fourier ptychographic microscopy based on high-numerical-aperture illuminations”. In: *Scientific reports*. 2017.
- [212] Jiasong Sun et al. “Sampling criteria for Fourier ptychographic microscopy in object space and frequency space”. In: *Opt. Express* 24.14 (July 2016), pp. 15765–15781. DOI: 10.1364/OE.24.015765. URL: <http://www.opticsexpress.org/abstract.cfm?URI=oe-24-14-15765>.
- [213] Yongjin Sung et al. “Optical diffraction tomography for high resolution live cell imaging”. In: *Opt. Express* 17.1 (Jan. 2009), pp. 266–277. DOI: 10.1364/OE.17.000266. URL: <http://www.opticsexpress.org/abstract.cfm?URI=oe-17-1-266>.
- [214] Pierre Thibault et al. “Probe retrieval in ptychographic coherent diffractive imaging”. In: *Ultramicroscopy* 109.4 (2009), pp. 338–343.
- [215] Lei Tian and Laura Waller. “3D intensity and phase imaging from light field measurements in an LED array microscope”. In: *Optica* 2.2 (2015), pp. 104–111. ISSN: 2334-2536. DOI: 10.1364/OPTICA.2.000104.
- [216] Lei Tian and Laura Waller. “Quantitative differential phase contrast imaging in an LED array microscope”. In: *Opt. Express* 23.9 (May 2015), pp. 11394–11403. DOI: 10.1364/OE.23.011394. URL: <http://www.opticsexpress.org/abstract.cfm?URI=oe-23-9-11394>.
- [217] Lei Tian, Jingyan Wang, and Laura Waller. “3D differential phase-contrast microscopy with computational illumination using an LED array”. In: *Opt. Lett.* 39.5 (Mar. 2014), pp. 1326–1329. DOI: 10.1364/OL.39.001326. URL: <http://ol.osa.org/abstract.cfm?URI=ol-39-5-1326>.

- [218] Lei Tian et al. “Computational illumination for high-speed in vitro Fourier ptychographic microscopy”. In: *Optica* 2.10 (2015), p. 904. ISSN: 2334-2536. DOI: 10.1364/OPTICA.2.000904. URL: <http://www.osapublishing.org/viewmedia.cfm?uri=optica-2-10-904%7B%5C%7Dseq=0%7B%5C%7Dhtml=true>.
- [219] Lei Tian et al. “Multiplexed coded illumination for Fourier Ptychography with an LED array microscope”. In: *Biomedical optics express* 5.7 (2014), pp. 2376–89. ISSN: 2156-7085. DOI: 10.1364/BOE.5.002376. URL: <http://www.pubmedcentral.nih.gov/articlerender.fcgi?artid=4102371%7B%5C%7Dtool=pmcentrez%7B%5C%7Drendertype=abstract>.
- [220] Ting Tian, Zhaoyang Yang, and Xiaoguang Li. “Tissue clearing technique: Recent progress and biomedical applications”. In: *Journal of Anatomy* 238.2 (2021), pp. 489–507. DOI: <https://doi.org/10.1111/joa.13309>. eprint: <https://onlinelibrary.wiley.com/doi/pdf/10.1111/joa.13309>. URL: <https://onlinelibrary.wiley.com/doi/abs/10.1111/joa.13309>.
- [221] Terry M. Turpin et al. “Theory of the synthetic aperture microscope”. In: *Advanced Imaging Technologies and Commercial Applications*. Ed. by Natalie Clark and John D. Gonglewski. Vol. 2566. International Society for Optics and Photonics. SPIE, 1995, pp. 230–240. URL: <https://doi.org/10.1117/12.217378>.
- [222] Peter J Verveer et al. “High-resolution three-dimensional imaging of large specimens with light sheet-based microscopy”. In: *Nature Methods* 4.4 (2007), pp. 311–313. ISSN: 1548-7105. DOI: 10.1038/nmeth1017. URL: <https://doi.org/10.1038/nmeth1017>.
- [223] Paul van Walree. *Vignetting*. URL: <http://www.cs.cmu.edu/~sensing-sensors/readings/vignetting.pdf> (visited on ).
- [224] Eric W. Weisstein. *Zernike Polynomial*. Aug. 3, 2021. URL: <https://mathworld.wolfram.com/ZernikePolynomial.html> (visited on 08/06/2021).
- [225] Emil Wolf. “Three-dimensional structure determination of semi-transparent objects from holographic data”. In: *Optics communications* 1.4 (1969), pp. 153–156.
- [226] Sheng Xiao et al. “High-contrast multifocus microscopy with a single camera and z-splitter prism”. In: *Optica* 7.11 (Nov. 2020), pp. 1477–1486. DOI: 10.1364/OPTICA.404678. URL: <http://www.osapublishing.org/optica/abstract.cfm?URI=optica-7-11-1477>.
- [227] Beibei Xu et al. “Metalens-integrated compact imaging devices for wide-field microscopy”. In: *Advanced Photonics* 2.6 (2020), p. 066004.
- [228] Yujia Xue et al. “Reliable deep-learning-based phase imaging with uncertainty quantification”. In: *Optica* 6.5 (May 2019), pp. 618–629. DOI: 10.1364/OPTICA.6.000618. URL: <http://www.osapublishing.org/optica/abstract.cfm?URI=optica-6-5-618>.

- [229] yan yang yan et al. “Deep ADMM-Net for Compressive Sensing MRI”. In: *Advances in Neural Information Processing Systems*. Ed. by D. Lee et al. Vol. 29. Curran Associates, Inc., 2016. URL: <https://proceedings.neurips.cc/paper/2016/file/1679091c5a880faf6fb5e6087eb1b2dc-Paper.pdf>.
- [230] Kyrollos Yanny et al. “Miniscope3D: optimized single-shot miniature 3D fluorescence microscopy”. In: *Light: Science & Applications* 9.1 (2020), p. 171. ISSN: 2047-7538. DOI: 10.1038/s41377-020-00403-7. URL: <https://doi.org/10.1038/s41377-020-00403-7>.
- [231] Zahid Yaqoob, Jigang Wu, and Changhuei Yang. “Spectral domain optical coherence tomography: a better OCT imaging strategy”. In: *BioTechniques* 39.6S (2005). PMID: 20158503, S6–S13. DOI: 10.2144/000112090. eprint: <https://doi.org/10.2144/000112090>. URL: <https://doi.org/10.2144/000112090>.
- [232] Li-Hao Yeh, Shwetadwip Chowdhury, and Laura Waller. “Computational structured illumination for high-content fluorescence and phase microscopy”. In: *Biomed. Opt. Express* 10.4 (Apr. 2019), pp. 1978–1998. DOI: 10.1364/BOE.10.001978. URL: <http://www.osapublishing.org/boe/abstract.cfm?URI=boe-10-4-1978>.
- [233] Li-Hao Yeh et al. “Experimental robustness of Fourier ptychography phase retrieval algorithms”. In: *Opt. Express* 23.26 (Dec. 2015), pp. 33214–33240. DOI: 10.1364/OE.23.033214. URL: <http://www.opticsexpress.org/abstract.cfm?URI=oe-23-26-33214>.
- [234] Hasan Yilmaz et al. “Speckle correlation resolution enhancement of wide-field fluorescence imaging”. In: *Optica* 2.5 (May 2015), pp. 424–429. DOI: 10.1364/OPTICA.2.000424. URL: <http://www.osapublishing.org/optica/abstract.cfm?URI=optica-2-5-424>.
- [235] H. K. Yuen et al. “A comparative study of Hough transform methods for circle finding”. In: *Proc. 5th Alvey Vision Conf., Reading (31 Aug. 1989)*, pp. 169–174.
- [236] Howard A. Zebker and Yanping Lu. “Phase unwrapping algorithms for radar interferometry: residue-cut, least-squares, and synthesis algorithms”. In: *J. Opt. Soc. Am. A* 15.3 (Mar. 1998), pp. 586–598. DOI: 10.1364/JOSAA.15.000586. URL: <http://josaa.osa.org/abstract.cfm?URI=josaa-15-3-586>.
- [237] F. Zernike. “How I Discovered Phase Contrast”. In: *Science* 121.3141 (1955), pp. 345–349. ISSN: 0036-8075. DOI: 10.1126/science.121.3141.345. eprint: <https://science.sciencemag.org/content/121/3141/345.full.pdf>. URL: <https://science.sciencemag.org/content/121/3141/345>.
- [238] Fucui Zhang et al. “Translation position determination in ptychographic coherent diffraction imaging”. In: *Optics express* 21.11 (2013), pp. 13592–13606.
- [239] Xiaoning Zhang et al. “Complex refractive indices measurements of polymers in visible and near-infrared bands”. In: *Appl. Opt.* 59.8 (Mar. 2020), pp. 2337–2344. DOI: 10.1364/AO.383831. URL: <http://ao.osa.org/abstract.cfm?URI=ao-59-8-2337>.

- [240] Guoan Zheng, Roarke Horstmeyer, and Changhuei Yang. “Wide-field, high-resolution Fourier ptychographic microscopy”. In: *Nature Photonics* 7.9 (2013), pp. 739–745. URL: <http://www.nature.com/nphoton/journal/v7/n9/abs/nphoton.2013.187.html>.
- [241] Guoan Zheng, Christopher Kolner, and Changhuei Yang. “Microscopy refocusing and dark-field imaging by using a simple LED array”. In: *Optics letters* 36.20 (2011), pp. 3987–3989. URL: <http://www.opticsinfobase.org/abstract.cfm?URI=ol-36-20-3987>.
- [242] Guoan Zheng et al. “Concept, implementations and applications of Fourier ptychography”. In: *Nature Reviews Physics* 3.3 (2021), pp. 207–223.
- [243] Michał Ziemczonok et al. “3D-printed biological cell phantom for testing 3D quantitative phase imaging systems”. In: *Scientific Reports* 9.1 (2019), p. 18872. ISSN: 2045-2322. DOI: 10.1038/s41598-019-55330-4. URL: <https://doi.org/10.1038/s41598-019-55330-4>.
- [244] Chao Zuo et al. “High-resolution transport-of-intensity quantitative phase microscopy with annular illumination”. In: *Scientific Reports* 7.1 (2017), p. 7654. ISSN: 2045-2322. DOI: 10.1038/s41598-017-06837-1. URL: <https://doi.org/10.1038/s41598-017-06837-1>.
- [245] Chao Zuo et al. “Transport of intensity equation: a tutorial”. In: *Optics and Lasers in Engineering* 135 (2020), p. 106187. ISSN: 0143-8166. DOI: <https://doi.org/10.1016/j.optlaseng.2020.106187>. URL: <https://www.sciencedirect.com/science/article/pii/S0143816619320858>.